

Dissertation

Creep Behaviour of Discontinuously Reinforced Aluminium Alloys

ausgeführt zum Zwecke der Erlangung des akademischen Grades eines Doktors der
technischen Wissenschaften unter der Leitung von

o. Univ. Prof. Dr. H.P. Degischer

Institut für Werkstoffkunde und Materialprüfung

eingerrichtet an der Technischen Universität Wien,

Fakultät Maschinenbau

von

Dipl. Ing. Guillermo Requena

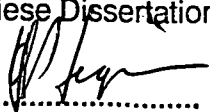
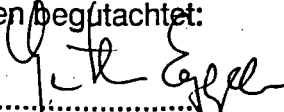
Matr. Nr.: 0027174


Lederergasse 22/3

A-1080 Wien

Wien, im April 2004

Diese Dissertation haben begutachtet:


.....

.....


.....
Guillermo Requena

Un estado, cultura, arte, ciencia o libro
no hechos para servir a la Pasión,
directa o indirectamente, no tienen explicación

Macedonio Fernández

Acknowledgements

First of all I would like to thank Prof. Degischer for his invaluable support, supervision and motivation he has given me through the whole process of development of this thesis. His never ending enthusiastic mood for working helps to keep alive the driving force necessary during the moments of exasperation which are also part of the passionate task of producing a doctoral thesis.

A very big thank goes for the one who first had the idea of giving me the possibility of carrying out this work in a renowned European university and his group of students. Thank you Prof. Julio Vivas Hohl or just “Gracias Julio!” for your trust.

I also feel in debt with Prof. Eggeler for accepting being one of the examiners of this work.

Fernando “Bebe” Lasagni, the writing of the modelling chapter and the development of the experimental method for the In Situ tensile and creep investigations would not have been possible without your work as a colleague and your support as a friend.

My friends, the old ones and the new ones had and have to carry the always unpleasant load which means supporting me at the end of a working day. Martina, Mario, the three Austrian Argentineans, the three German Argentineans, los Muchachos and Die WG are responsible for making that my day by day during these long three years far from home were not so hard 😊.

Finally, the one who really accepted the responsibility of growing me, understanding me, hearing me, emotionally and, also important, financially supporting me without ever asking anything for that: thanks Pipa, Babe and Mom. Thank you family.

Kurzfassung

Die Eigenschaften von potenziellen Hi-Tech Materialien bei erhöhter Temperatur sowie das Verständnis der zugrundeliegenden mikrostrukturellen Zustände sind von größtem wissenschaftlichem und technologischem Interesse. Die Untersuchungen der neulich entwickelten heterogenen Materialien, wie Metal Matrix Verbundwerkstoffe (MMC), haben viel versprechende mechanische Eigenschaften bei Raumtemperatur gezeigt, die sie zu aussichtsreichen Kandidaten für spezielle technische Anwendungen machen. Wegen der unterschiedlicher Temperaturabhängigkeit der Eigenschaften der Verbundwerkstoffkomponenten bedürfen die Wechselbeziehungen dieser Eigenschaften bei höheren Temperaturen unter verschiedenen mechanischen und thermischen Belastungen weiterer Analysen.

In der vorliegenden Arbeit wird die Kriechbeständigkeit einer unverstärkten und teilchenverstärkten (PRM) Aluminium Kentlegierungen (AlMg1SiCu/Al₂O₃/22p) sowie einer unverstärkten und kurzfaserverstärkten (SFRM) Aluminium Gusslegierung (AlSi12CuMgNi/Al₂O₃/10s, 15s und 20s) unter konstanter Temperatur von 300°C untersucht.

Die unverstärkte AlMg1SiCu (AA6061) Matrix zeigt eine deutlich höhere Kriechbeständigkeit als mit Teilchenverstärkung. Verantwortlich für diesen Effekt sind zusätzliche Versetzungsquellen in der Partikelumgebung, eine Zunahme des Diffusionskoeffizienten aufgrund der höheren Versetzungsdichte und der verminderten Wirkung der Mg₂Si-Ausscheidungsverstärkung. Ein Kriechexponent von $n=3$ entspricht dem Versetzungsgleiten als beherrschenden Mechanismus für die Kriechverformung im PRM. Ein ungewöhnlicher Kriechexponent von $n=2,2$ wird für die unverstärkte AA6061 Matrix beobachtet. Dies wird erklärt durch die Überalterung der Mg₂Si Ausscheidungen für Versuche die länger als 100 Stunden dauern. Die Einführung einer zeitabhängigen Schwellspannung in das Kriechgesetz für die Matrix ist notwendig, um die Abschwächung der Dehnratenabnahme bei längerer Versuchsdauer (kleinerer Belastung) darzustellen. Dieser Überalterungseffekt wird für PRM vernachlässigbar.

Alle drei SFRM zeigen bessere Kriechresistenz als die unverstärkte Gusslegierung, wobei das 15vol% kurzfaserverstärkte Material die beste Resistenz aufweist. Das SFRM mit 20vol% Kurzfasern kriecht überraschenderweise ähnlich schnell, was durch die höhere Defektdichte (Poren) vom Herstellungsprozess verursacht wird. Es werden auch Kriechversuche mit Belastungsänderungen nach dem Erreichen einer stationären Dehnrates untersucht. Dabei stellt sich heraus, dass die minimale Kriechrate bei einer bestimmten äußeren Spannung nach einer vorübergehenden Erhöhung der äußeren Spannung geringer

wird als zuvor. Dieser Effekt wird aufgrund eines örtlichen Ausgleiches der Verteilung der inneren Spannungen (Relaxation der Spannungsspitzen in der Matrix) erklärt.

Die erhaltenen Ergebnisse für isothermes Kriechen werden mit früheren Ergebnissen für dieselben Materialien unter thermozyklischem Kriechen (TCC) verglichen. Als reale Dehnungsrate für TCC Versuche wird die Maximalkriechgeschwindigkeit pro Zyklus nach dem Modell von Eshelby ermittelt. Die Werkstoffe unter isothermem Kriechen zeigen eine höhere Kriechbeständigkeit als diejenigen unter TCC. Die unverstärkte und faserverstärkte Gusslegierung besitzen eine höhere Kriechresistenz als die Knetlegierung unter TCC. Das eutektisch ausgeschiedene Si in der Gusslegierung wirkt wie eine Verstärkungskomponente.

Abstract

The high temperature behaviour of potential hi-tech engineering materials as well as the understanding of the underlying physical concepts are subjects of main scientific and technological interest. The study of recently developed new heterogeneous materials such as metal matrix composites (MMC) have shown promising room temperature mechanical properties making them candidates for demanding engineering applications. However, their properties at higher temperatures under different mechanical and thermal load conditions need still further investigations.

In this work, the creep resistance of an unreinforced and particle reinforced (PRM) aluminium wrought alloy (AlMg1SiCu/Al₂O₃/22p) and an unreinforced and short fibre reinforced (SFRM) aluminium cast alloy (AlSi12CuMgNi/Al₂O₃-Saffil/10s, 15s and 20s) was investigated at a constant temperature of 300°C.

The unreinforced AlMg1SiCu (AA6061) matrix exhibits a markedly higher creep resistance than the PRM. This is attributed to the particles acting as additional dislocation sources in the matrix, and to an increase of the apparent diffusion coefficient due to a higher dislocation density in comparison with the unreinforced matrix accelerating as well the coarsening of Mg₂Si precipitates. A creep exponent $n=3$ for the PRM is related to the creep mechanism of viscous glide of dislocations. For the AA6061 matrix, an unusual apparent creep exponent $n=2.2$ is explained by overaging of the Mg₂Si precipitates during tests for lower stresses lasting longer than 100h. A time dependant threshold stress is introduced into the creep law of the matrix to reflect the softening of the alloy during longer exposure times (i.e. at smaller applied stresses). This effect becomes negligible for the significantly higher creep rates of the PRM.

All three SFRM composites show a considerably higher creep resistance than the unreinforced matrix. Among the SFRM, the 15vol% composite exhibits the highest creep resistance. Matrix porosity owing to infiltration defects during processing is considered responsible for the relatively low creep resistance found for the 20vol% SFRM. Changes of load during the creep exposure were also tested resulting that the minimum creep rate for a given external stress is reduced after the composite has experienced a period of overloading. This is explained by local relaxation of the high ends of the internal stress distribution provoked by localised flow of matter in zones surrounding the fibres where the yield stress of the matrix is reached. A modified creep law is deduced to describe that apparent strengthening effect.

The results obtained for isothermal creep are compared with previously obtained results for the same materials under Thermal Cycling Creep (TCC) conditions. The maximum deformation rate per cycle in TCC tests is taken as the real deformation rate deduced by using the Eshelby's approximation. The materials tested under isothermal creep show a higher creep resistance than under TCC and the unreinforced and short fibre reinforced cast alloy presents a higher resistance than the PRM under the latter conditions. Thus, the eutectic Si is executing some reinforcement effect as well.

Contents

Acknowledgments	i
Kurzfassung	ii
Abstract	iv
1 Introduction	1
2 Definitions and State of the Art in Metal Matrix Composites	3
2.1 Metal Matrix Composites	3
2.1.1 Types of MMC	4
2.1.2 Processing Methods	5
2.1.2.1 Liquid phase processing	5
2.1.2.2 Solid state processing	10
2.1.3 Thermal Stresses in MMC	10
2.1.4 Isothermal Creep in discontinuously reinforced MMC	13
2.1.4.1 Strengthening Mechanisms in MMC	13
2.1.4.2 Creep Exponent and Activation Energy	14
2.1.4.3 Importance of Reinforcement Parameters	15
3 Experimental	20
3.1 Particle Reinforced Materials	20
3.1.1 Reinforcement Distribution	20
3.1.2 Thermal Treatment	21
3.1.3 Interfacial Reactions	22
3.2 Short Fibre Reinforced Materials	23
3.2.1 SFRM Production using the Squeeze Casting Process	24
3.2.2 Reinforcement Distribution	24
3.2.3 Thermal Treatment	26
3.2.4 Present Phases and Interfacial Reactions	26
3.2.5 Interaction of Si Phase with Al ₂ O ₃ Short Fibres	32
3.3 Creep Tests	33
3.3.1 Equipment Description	33
3.3.2 Sample Geometry	34
3.3.3 Creep Tests Procedure	34

3.4	In Situ Tensile Creep Tests	35
3.4.1	Sample Geometry	36
3.4.2	Metallographic Preparation of the Samples	36
3.4.3	Electrochemical Copper Deposition	36
3.4.4	In Situ Tensile/Creep Test inside a SEM	38
3.4.4.1	Creep Tests	40
3.4.5	Calculation of the Local Deformation	41
3.5	Microscopy	42
3.6	Young's Modulus Analysis	42
4	Modelling	43
4.1	The Eshelby's Method Applied to Strain Evolution in Thermal Cycling Creep (TCC)	43
4.1.1	Brief Introduction to TCC	43
4.1.2	Experimental Conditions and Results	44
4.1.3	Thermal elongation and contraction ϵ_{th}	47
4.1.4	Elastic Deformation due to Variation of Young's Modulus with Temperature $\epsilon_{\Delta E}$	47
4.1.5	Elastic Strain Produced by Internal Stresses ϵ_{ith}	48
4.1.6	Determination of the Plastic Deformation during TCC tests	50
5	Results	56
5.1	Isothermal Creep	56
5.1.1	6061 and 6061/Al ₂ O ₃ /22p	56
5.1.2	AlSi12CuMgNi, AlSi12CuMgNi/Al ₂ O ₃ /10s, AlSi12CuMgNi/Al ₂ O ₃ /15s and AlSi12CuMgNi/Al ₂ O ₃ /20s	57
5.2	Microscopic Analysis	58
5.2.1	6061 and 6061/Al ₂ O ₃ /22p	58
5.2.2	AlSi12CuMgNi, AlSi12CuMgNi/Al ₂ O ₃ /10s, AlSi12CuMgNi/Al ₂ O ₃ /15s and AlSi12CuMgNi/Al ₂ O ₃ /20s	60
5.3	Young's Modulus	62
5.4	In Situ Tensile Creep Tests	63
5.4.1	6061/Al ₂ O ₃ /10p and 6061/Al ₂ O ₃ /22p	63

5.4.2	AlSi12CuMgNi and AlSi12CuMgNi/Al ₂ O ₃ /20s	64
6	Interpretation of Results	96
6.1	Isothermal Creep	96
6.1.1	6061 and 6061/Al ₂ O ₃ /22p	96
6.1.1.1	Creep Law (σ vs $\dot{\epsilon}_{\min}$)	96
6.1.1.2	Time – Strain – Stress relationship	97
6.1.1.3	Elongation at rupture	98
6.1.2	AlSi12CuMgNi, AlSi12CuMgNi/Al ₂ O ₃ /10s, AlSi12CuMgNi/Al ₂ O ₃ /15s and AlSi12CuMgNi/Al ₂ O ₃ /20s	98
6.1.2.1	σ vs $\dot{\epsilon}_{\min}$	98
6.2	In Situ Tensile Creep Tests	99
6.2.1	6061/Al ₂ O ₃ /10p and 6061/Al ₂ O ₃ /22p	99
6.2.2	AlSi12CuMgNi and AlSi12CuMgNi/Al ₂ O ₃ /20s	100
7	Discussion	110
7.1	Isothermal Creep Mechanisms	110
7.1.1	6061 and 6061/Al ₂ O ₃ /22p	110
7.1.1.1	Creep resistance in PRM compared to the unreinforced matrix	110
7.1.1.2	Failure modes at low and high stresses	111
7.1.2	AlSi12CuMgNi, AlSi12CuMgNi/Al ₂ O ₃ /10s, AlSi12CuMgNi/Al ₂ O ₃ /15s and AlSi12CuMgNi/Al ₂ O ₃ /20s	112
7.1.2.1	Correlation with Dlouhy's Model	116
7.1.3	Isothermal Creep vs. Thermal Cycling Creep	119
8	Conclusions	122
8.1	Significance of Experimental and Modelling Methods	122
8.1.1	TCC Tests	122
8.1.2	HT In Situ Tensile Tests	122
8.1.3	Isothermal Creep Tests Performing Variations of Load	123
8.2	Significance of Results	123
8.2.1	Isothermal Creep	123
9	References	126

1 Introduction

The use of heterogeneous metal-based materials is not a new subject in the history of human civilization. Copper awls from Cayonu (Turkey) date back to about 7000BC and were made by a repeated lamination and hammering process, which gave rise to high levels of elongated non-metallic inclusions [1]. In Japan, during the 6th century, swords were produced by hammering superimposing layers of hard and soft steel which fulfilled two of the main requirements of this kind of products: the steel sword had to be at the same time hard in order to sharpen the blade and on the other side it had to present a high fracture toughness. Nowadays, the use of industrial steel, eutectic alloys, precipitation strengthened alloys, dispersion hardened alloys and other multi phase metallic materials cover a wide range of metal based materials for every-day use, structural and niche high-tech applications. In many cases, the motivation for the development of this kind of materials is based on what can be deduced from the example of the Japanese swords: by the combination of materials with different properties it may be possible to obtain a new material with macroscopically enhanced properties in comparison with the homogeneous ingredient materials. Following this principle, there has been a great interest on the development and study of the properties of the so called Metal Matrix Composites (MMC) for being used in automotive, aerospace, electronic and structural applications during the last two decades. These materials consist of a continuous metallic phase (the matrix) and an embedded reinforcing component (normally a ceramic or sometimes a metal). Thus, not only the properties of the constituents have to be appropriately selected but also their geometrical arrangement has to be tailored as well in order to achieve the highest service requirements for these composite materials to become realistic candidates in engineering applications. As mentioned above, potential fields of MMC applications are the automotive and the aerospace industries. Furthermore, MMC supersede polymer matrix composites by their resistance to elevated temperatures. Thus, the behaviour of MMC at high temperatures as well as the understanding of the underlying physical concepts are of main scientific interest in materials science and technology.

In this work, the creep behaviour of two kinds of discontinuously reinforced aluminium matrix composites will be investigated paying special attention to the role played by different aspect ratios, architectures and volume fractions of the reinforcements, the microstructure of the matrix and the influence of temperature and load changes during the test.

Chapter 2 gives the definitions of the terms involved in the study of MMC as well as an introduction to the current State of the Art of this field of materials science. The mostly used production techniques will be described. A short introduction to the physics of creep and thermomechanical properties of MMC can also be found in this chapter.

The materials investigated during the development of this thesis, the corresponding production processes as well as the methods used for their characterisation are presented in **Chapter 3**. Chemical composition of the matrices, type and volume fraction of the reinforcements, heat treatments, main microstructural characteristics, interfacial reactions between matrix and reinforcement are the subjects of this section.

Chapter 4 presents the application of the Eshelby's method in an attempt to explain quantitatively the evolution of the plastic deformation obtained when one of the discontinuously reinforced MMC studied is subjected to thermal cycling creep (TCC) conditions. This section also presents a short description of the TCC tests. The experimental results were taken from a previous work [2, 3] and the main motivation for the study developed in this section was to determine if the role played by the elastic strains due to internal stresses present in the MMC can be estimated not only qualitatively but also quantitatively using a more or a less simple approach.

The results obtained by means of the experimental methods described in Chapter 3 are presented in **Chapter 5** while their analysis and interpretation is developed in **Chapter 6**. The latter serves for the discussion of basic material behaviour in **Chapter 7**.

Finally, the conclusions for application of MMC encountered after the analysis and discussion of results are summarised in **Chapter 8**.

2 Definitions and State of the Art in Metal Matrix Composites

2.1 Metal Matrix Composites

The term composite materials refers, in a first approach, to all kinds of materials systems composed of more than one solid phase. However, if we follow this definition, any alloy with a miscibility gap would have to be considered as a composite material since it is composed of two phases. To avoid this confusion, a more general and currently accepted definition of composite material is the one provided by [4]:

A composite (or composite material) is defined as a material that consists of at least two constituents (distinct phases or combinations of phases) which are bonded together along the interface in the composite, each of which originates from a separate ingredient material which pre-exists the composite.

Following this definition, the composite is produced via a physical combination of at least two **pre-existing** ingredient materials. The so called in-situ composite materials are only those where the pre-existing ingredients change their chemical composition or their shape during mixing. Those produced by reactions between elements or between compounds within the material system [5] fall outside this definition. Although their properties can be described using composite theory (e.g. grey cast iron) they will not be considered as composite materials in the present work. As already stated, a composite presents at least two constituents, one of them may act as the matrix and the other/s one/s as the reinforcement/s. To complete our previous definition we define the components of the composite as follows:

*The **matrix** of a composite refers to the phase which presents a continuous structure and usually, but not exclusively, is the phase with highest volume fraction. The other phases of the composite are called the **reinforcement**.*

Composites can now be classified by means of the type of matrix they have. The matrices of technological interest are polymeric, metallic and ceramic matrices. Thus, we have three different types of composites:

MMC: Metal Matrix Composites

CMC: Ceramic Matrix Composites

PMC: Polymer Matrix Composites

Now, we are able to give a consistent definition of Metal Matrix Composites:

A Metal Matrix Composite (MMC) is a composite material in which one constituent, the matrix, is a metal or alloy forming at least one percolating network. The other/s pre-existing constituent/s or its/their derivative/s is/are embedded in this metal matrix and play/s the role of reinforcement phase/s. In addition, it is convenient to limit the volume fractions of the constituents to be considered as MMC [4]: matrix volume fraction > 5% and reinforcement volume fraction > 5%.

2.1.1 Types of MMC

MMC are classified according to two subgroups [6]:

- 1) Continuously reinforced MMC: where either monofilaments of approximately 0.1mm in diameter (e.g. SiC) or multifilament tows of at least some hundreds of fibres of about 0.01mm in diameter (e.g. SiC, Al₂O₃, carbon) are embedded within a rather ductile matrix. Percolating ceramic structures are considered as continuous reinforcement as well.
- 2) Discontinuously reinforced MMC: where either particulates, platelets (SiC, Al₂O₃, B₄C), short fibres of high aspect ratio (usually Al₂O₃-SiO₂) or whiskers (e.g. SiC) are embedded within high strength alloys. However, the latter have been forbidden in Europe due to their toxicity [7, 8].

The orientation of the reinforcement within the matrix will determine the degree of anisotropy of the MMC. Particle Reinforced Metals (PRM) show normally the lowest anisotropy since the shape of the particle is generally spherical, irregular or platelet-like exhibiting a shape factor smaller than 5. However, depending on the production method and post processing route they can present a certain degree of alignment in the case of irregularly shaped particles (e.g. extruded materials). In the case of short fibre reinforced metals (SFRM), the reinforcement is usually produced as preforms with the fibres randomly oriented in one plane. This means that the properties of the SFRM will normally show isotropy for directions oriented parallel to the plane of the fibres. Continuous fibre reinforced metals (CFRM) show a

high degree of anisotropy for unidirectionally aligned fibres, but to counteract this effect (in case of need) it is possible to apply layers or weaves with different fibre orientations in one plane.

2.1.2 Processing Methods

The most commonly used methods of production of MMC can be divided in two groups:

- 1) Liquid phase processes
- 2) Solid state processes

2.1.2.1 Liquid phase processing

Some characteristic problems have to be surpassed when producing a MMC using the metal matrix in the liquid state:

- 1) The melt of the metal usually does not wet the reinforcement. The two components have to be forced together in order to obtain a composite without pores and/or reinforcement clustering. This can be done by exerting a pressure on the melt or by shear forces when stirring the reinforcement (only discontinuous reinforcement) into the melt.
- 2) Most metals, which are used as matrix such as light metals, are highly reactive specially in liquid state. As soon as bonding is achieved, care has to be taken to avoid chemical reaction between the matrix and the reinforcement since these products may degrade the mechanical properties of the composite.

Stir Casting

This is the simplest process used for producing PRM. Here, a powder of ceramic particles is introduced into the molten matrix by stirring (see Figure 2.1). This can in principle be done with relatively conventional processing equipment. Due to the non-wettability between the ceramic and the metal, mixing of gas has to be prevented and only particles larger than 10µm can be introduced up to a volume fraction of about 20%. It is possible to carry out a continuous or semi-continuous production method and the obtained MMC ingots are suitable for further operations such as casting or extrusion. There are two major disadvantages in this process: the long period of molten matrix can result in interfacial reactions between

matrix and reinforcement and microstructural inhomogeneity due to particle agglomeration, gas bubble entrapment and particle segregation due to differences in densities or/and as a result of particle pushing by an advancing solidification front [9].

Commercially available PRM manufactured using this method have been successfully produced using aluminium and magnesium matrices [10, 11].

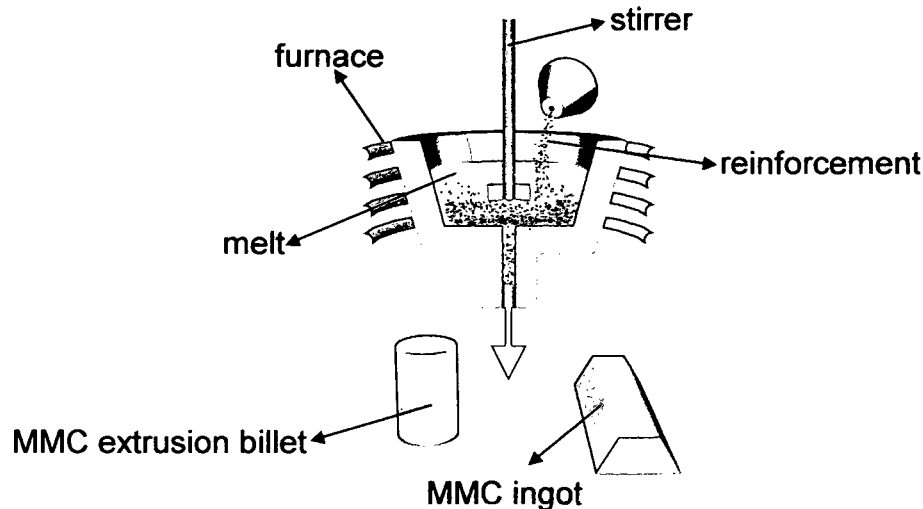


Figure 2.1. Schematic representation of the stir casting process.

Infiltration Processes

In the case of infiltration techniques, the molten unreinforced matrix will infiltrate a ceramic preform of open porosity by means of pressure provided by a piston, gas, vacuum [12] or by use of capillarity forces [13, 14] (pressureless infiltration). These methods are normally used for producing short fibre reinforced MMC and are quite common for producing continuously reinforced MMC [15, 16].

The main advantages of gas pressure or pressureless infiltration techniques are [12]:

- Much reduced mechanical degradation of the reinforcement, which is an issue when producing composites having high volume fraction of reinforcement or featuring fragile reinforcements such as low volume fraction short fibre preforms.
- Speed
- The possibility of producing a net or near-net-shape material that is generally difficult to machine.
- The possibility of producing locally reinforced parts.

Although capillarity-driven infiltration may be attractive in some instances, pressure infiltration has some significant advantages for general engineering applications [12]:

- There are fewer restrictions on the chemistry of the matrix and the reinforcement.
- Pressure speeds infiltration significantly, allowing shorter process cycles and reducing chemical interaction of the matrix with reinforcement or die tooling.
- Applied pressure permits infiltration of preforms with initial temperatures below the matrix liquidus, which can reduce further chemical interaction between matrix and reinforcement.
- Applied pressure practically eliminates the occurrence of uninfiltred portions of the preform.
- If used together with properly designed cooling for directional solidification, applied pressure can drive matrix flow through the preform to avoid matrix solidification shrinkage.
- Applied pressure increases the rate of heat removal from the casting during solidification, in turn refining the matrix microstructure and reducing the time for fibre-matrix chemical reaction in the solid state.

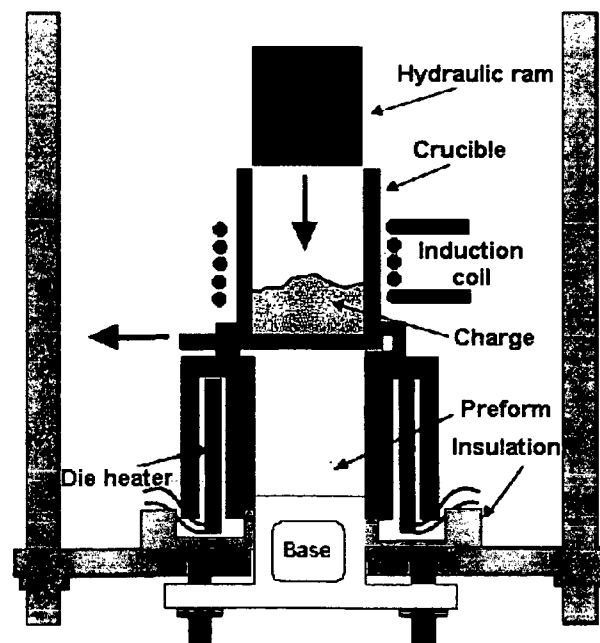


Figure 2.2. Schematic representation of the squeeze casting method [17].

Among the piston-driven infiltration processes, squeeze casting is one of the main techniques used for the production of MMC [12, 17, 18, 19, 20]. Figure 2.2 shows schematically the equipment setup used for this process. The primary distinction between this method and conventional pressure die casting is that the ram continues moving during

solidification, deforming the growing dendrite array and compensating for the freezing contraction (which is typically about 5%). In addition to this, the ram movement is usually slower, and the applied pressure often greater but rather hydrostatic, than is typical for die casting.

Several gas pressure infiltration devices have been designed [12, 15]. Figure 2.3 show four different experimental setups that have been used for producing MMC by using this method. The main disadvantages of these machines if compared to piston-driven ones is the lower available range of pressures, which implies that infiltration is slower and cooling rates are lower resulting in higher probability of reaction between matrix and reinforcement and of remaining fine pores in the MMC. However, in gas-driven techniques there is no piston that must be separated from the matrix metal, and there is greater versatility in mould design in some configurations because the die can be immersed into the chamber containing pressurized gas. This makes the stress state of the die predominantly compressive, because the pressure outside the die is higher than that inside.

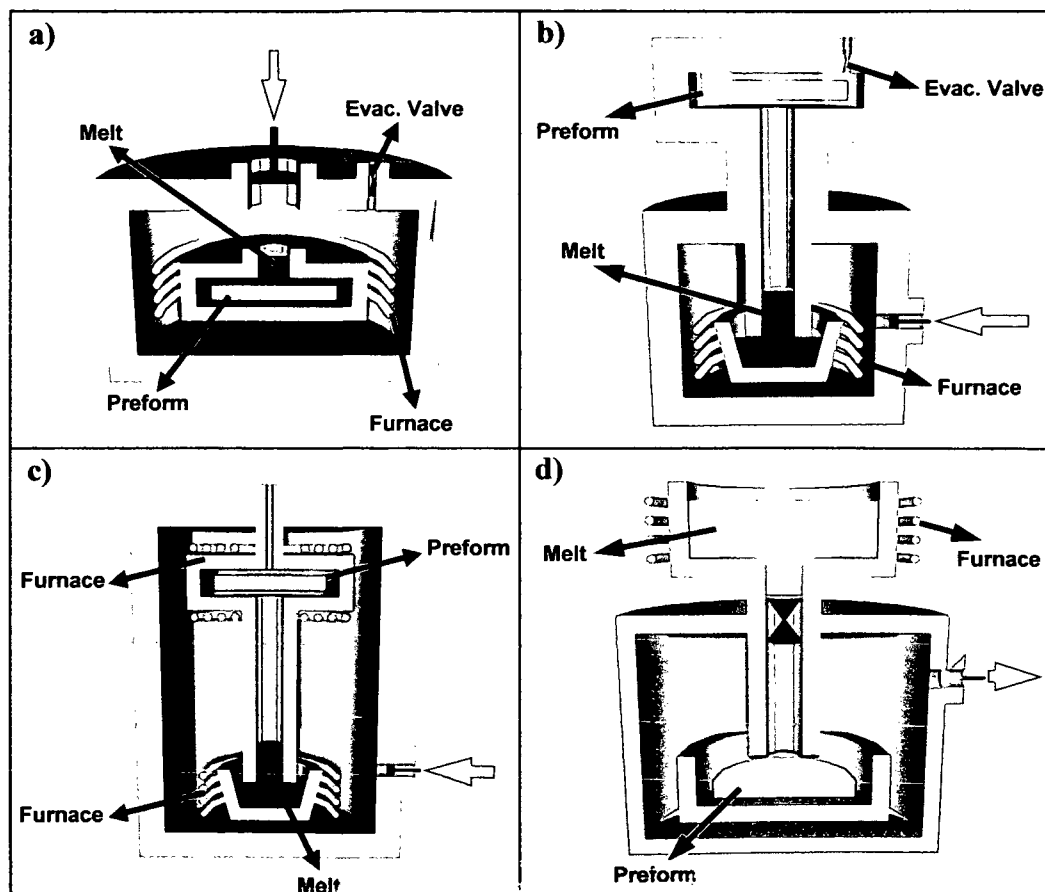


Figure 2.3. Four different experimental setups used for producing MMC by gas pressure infiltration (grey arrows represent the movement of the piston): a) the melt and the preform are both located in the autoclave during the infiltration. b) Only the melt is in the autoclave and this is injected to the preform by means of applied pressure. c) Both the melt and the preform are inside the autoclave but in different chambers before the infiltration process begins. d) The molten matrix is outside the autoclave and fed from above into the evacuated preform.

Spray Deposition

Using the principles of rapid solidification, a variety of processing techniques have been developed and emerged as attractive and viable alternatives to optimise both the microstructure and properties of particle reinforced metal matrix composites [21]. Here, a stream of metallic droplets impinges on a substrate in such a way as to build up a composite deposit. The reinforcement can be fed into the spray, if particulate, or introduced onto the substrate if fibrous. The first commercially available spray deposition technique and the most used was the **OspreyTM** (Neath, South Wales) method. The primary advantages of this technique are:

- (1) The rapid formation of a range of semi-finished products such as tubes, billets or strips directly from the melt.
- (2) Creation of composite materials which can contain up to and over 20vol% of the reinforcement by injection of particles smaller than 10µm into the atomised stream of molten alloy.
- (3) Potential for the economical manufacture of a spectrum of products as a direct consequence of the high rates of metal deposition that are available coupled with the concurrent elimination of several of the processing steps required in ingot metallurgy and powder metallurgy techniques.
- (4) The facilitation of secondary processing routes without prolonged soaking times and/or the large deformation ratios required for fine grain-size, segregation-free microstructures.

However, secondary forming (i.e. extrusion, rolling, forging) is needed to reduce the inherent porosity from deposition.

Thermal spraying refers to another group of techniques used for production of MMC by spray deposition. This involves the feeding of powder, or in some cases wire, into the hot zone of a torch, where it is heated and accelerated as separate particles by the rapid expansion of a gas. The most common thermal spraying methods are plasma spraying and the use of High Velocity Oxy-Fuel (HVOF) guns [17, 21]. Some porosity usually remains when this techniques are implemented.

2.1.2.2 Solid state processing

The characteristic problems that arise during liquid state processing such as non-wetting between matrix and reinforcement and chemical reactions can be, in principle, avoided or diminished if the materials are processed in solid state. In this case both of the components will remain in solid state during the whole production process and are bonded by diffusion.

Powder Metallurgy

This process involves the sintering of a metallic powder (the matrix) and the ceramic fibres or particles [22, 23]. The blending can be carried out dry or in liquid suspension. This is usually followed by cold compaction, canning, evacuation and a high temperature consolidation state such as HIPing or extrusion. The presence of fine oxide dispersoids coming from the precursor powders are very typical for Al based MMC and these can affect remarkably the mechanical properties such as room and high temperature strength of these materials [24, 25, 26].

Diffusion Bonding

This is the mostly used technique for the production of MFRM. Here, arrays of filaments are placed between thin metallic foils or coated by the matrix and then hot pressed at high temperature. This method is attractive for the production of monofilament reinforced Ti matrix composites because: 1) reinforcement of Ti with continuous fibres is particularly attractive (in view of the scope for significant improvements in creep resistance and stiffness), b) routes involving liquid Ti suffer from rapid interfacial chemical reaction and c) Ti is well suited to diffusion bonding operations since it dissolves its own oxide at temperatures above 700°C [27].

2.1.3 Thermal Stresses in MMC

When MMC are fabricated at high temperature, formed or heat treated at a certain elevated temperature and cooled down to room temperature, internal stresses produced by the mismatch of the thermal expansion coefficients between the matrix and the reinforcement build up and can have several consequences for the thermomechanical behaviour of a MMC component and therefore their evaluation is of fundamental interest.

Internal stress existing in a polycrystalline material depends on the history of the sample, and the final state can be expressed at various scales of interest. First order stresses

(macrostresses) are stresses that vary on a spatial scale of a large number of grains in the materials; in a composite these are considered to extend across the phases. Such stresses are caused by non-uniform mechanical, thermal treatment or as a result of a non-uniform distribution of the reinforcement causing relative deformation of different areas of the material. Second order stresses (mismatch stresses) vary on a much smaller scale than macrostresses, of the order of the grain size of the material or the interparticle spacing in a composite material. They characterise the deviation of the stresses for a particular grain from the first order value. These stresses occur because of small-scale anisotropy or heterogeneity in the material such as the above mentioned mismatch in thermal expansion coefficient, the elastic constant or the plastic flow between different phases or even individual grains of the material. Third order stresses occur on the smallest scale, over distances within individual grains, and their origins include the local stress field around crystal defects like dislocations, precipitates and point defects.

Until now, a number of models have been used to describe the elastoplastic and thermal behaviour of MMC [28, 29, 30, 31, 32]. The method most frequently employed to predict the evolution of residual stresses and mechanical properties has been the finite element method. Davis et al. [33] studied by means of FEM the residual stresses that arise after a temperature drop ΔT in a TiC particle reinforced Al (second order stresses) matrix using 3D simple cubic and face-centered cubic arrays. The results obtained for $\Delta T=256^\circ\text{C}$ are shown in Figure 2.4 a) and b) for a simple cubic array. The mean stress value calculated over one phase of the composite is of a hydrostatic nature, and is compressive for the particle and tensile for the matrix. Considerable plastic flow occurs during cool down. In Figure 2.4 b), the plastic zone surrounding the particle is shown. The yielding of the matrix substantially decreases the stress and strain in the particle. Davis et al. also showed that the mechanical properties were modified by the initial residual stresses, especially at the beginning of plastic deformation.

Similar results concerning the distribution of microstresses around a single SiC inclusion embedded in an Al matrix were reported by Roatta et al. [34]. In this case, the Eshelby's model [35] was used for the calculations. After cooling, a negative value of radial strain and positive tangential strain were found in the Al matrix close to the interface with SiC particles. These results are shown in Figure 2.5 a) and b). It was shown that even when the yield stress of the composite is not reached, plastic regions are formed in the matrix due to the initial residual stresses.

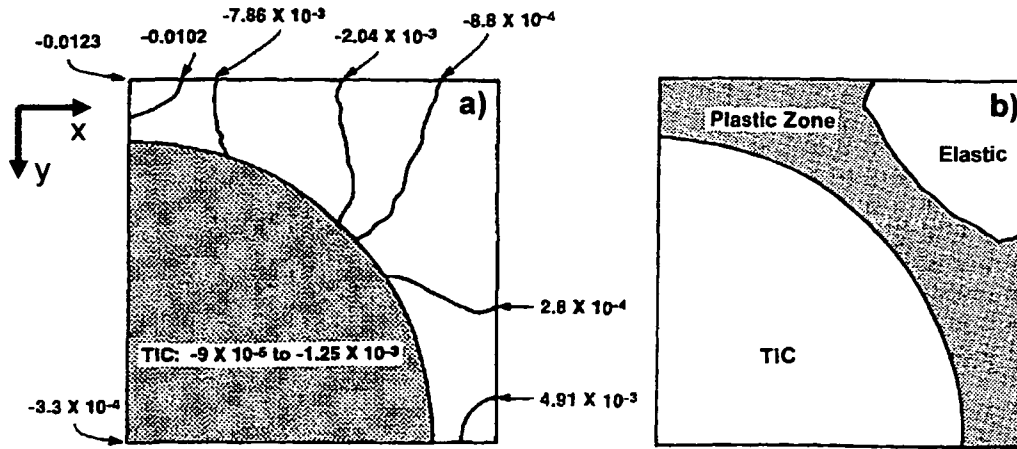


Figure 2.4.a) Calculated residual strain in y direction due to CTE mismatch in the xy plane of simple cubic array. $\Delta T = -256K$ from stress-free state assumed. b) Resulting region of plastic flow in the Al matrix surrounding the TiC particle due to cooling 256K. The matrix was assumed to be elastic/perfectly plastic with tensile yield stress $\sigma_y = 245MPa$. [33]

Levy-Tubiana et al. [36] applied a self-consistent model to estimate the internal stresses produced due to an external stress in an Al/SiC_p reinforced MMC and correlate these results with experimental results obtained using neutron diffraction measurements. They found experimentally that the mismatch stresses determined for both phases relax for tensile as well as compressive deformation but this process does not correspond with the results of the model. They argued that the operating micromechanisms are quite complex, with relaxation occurring equally in both tensile and compression modes, and equally in the three principal directions. Furthermore, the plastic flow in the matrix reduced the effect of thermal treatment of the material.

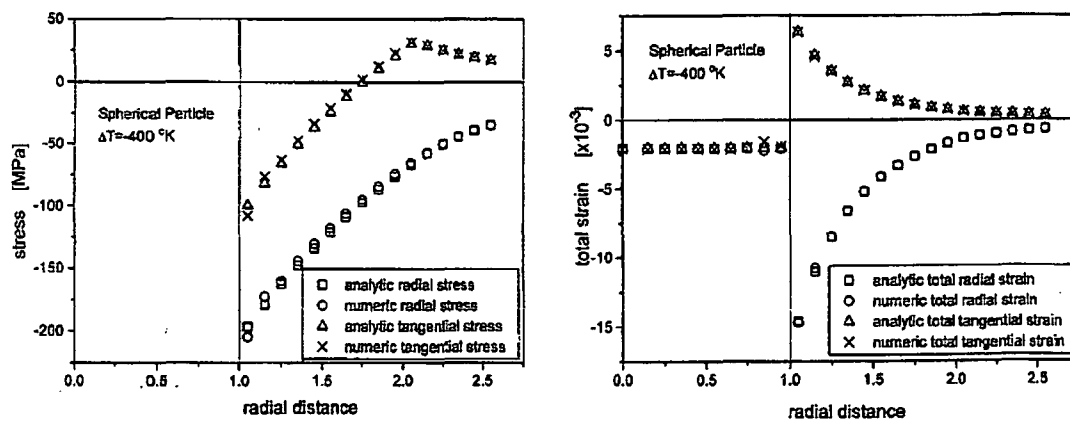


Figure 2.5. Radial and tangential stress (a)/strain (b) vs. radial distance (normalized by the particle radius) for $\Delta T = -400K$ for a spherical SiC embedded in an Al matrix [34].

Heinrich et al. [37] carried out large-angle convergent beam electron diffraction measurements in a AlSi12CuMgNi alloy reinforced with 20vol% Al₂O₃/SiO₂ short fibres in order to determine the strain fields due the thermal stresses produced by the thermal mismatch between matrix and reinforcement. They found that the strain field is not homogeneously distributed around the fibres. Surface reactions of spinel phases of an extent of several tens of

nanometers cause local stress concentrations. These internal stresses can lead to plastic deformation of the Al matrix, to cracking of the fibres and of Si segregations. According to them, these third order stresses, and not the second order stresses caused by the thermal mismatch, dominate at matrix-fibre interfaces.

X-rays and neutron diffraction investigations carried out during thermal cycling of an AlSi7Mg alloy reinforced with 70vol% of SiC particles by Göbel et al. [38] revealed that the larger second order stresses appear during slow cooling of the material from 150°C to 50°C. These internal stresses decrease with increasing temperature and disappear at around 200-250°C during the first cycle and they even result in reverse stresses during the following cycles. The third order stresses relax during the first thermal cycle indicating that the material may not be strongly changed during subsequent thermal cycles of moderate heating and cooling rates.

All the above explained represents a small depiction of the so far reported results regarding thermal stresses in discontinuously reinforced MMC but clearly shows its importance not only as an academic/scientific field of study but also regarding the consequences that internal stresses may have in engineering applications of MMC.

2.1.4 Isothermal Creep in discontinuously reinforced MMC

The following sections are a short description of the main features that have been reported regarding isothermal creep in discontinuously reinforced MMC. The topics are organized according to the structure followed in [39]. The theory of isothermal creep is well described in [40, 41].

2.1.4.1 Strengthening Mechanisms in MMC

During creep of MMC with aluminium matrix, it is usually assumed that the reinforcement phases are non-creeping, so the observed strain is due wholly to creep mechanisms occurring in the matrix. However, the creep behaviour for a MMC is not the same as that of the unreinforced matrix regarding not only to values of strain and strain rate but also to creep mechanisms. This is due to the load redistribution owing to the reinforcement and/or to a different microstructure of the matrix, i.e. defects density like increased grain boundaries to volume ratio.

We refer to direct strengthening when there is a load transfer from the matrix to the reinforcement. When the matrix creeps, there will be a misfit between the matrix and the reinforcement, resulting in the effective transfer of the applied load to the reinforcement. This results in a redistribution of stresses within the matrix, which is expected to reduce the driving

force for matrix creep. As the deformation proceeds, the degree of misfit between the two phases increases, and this will progressively transfer load to the reinforcement. This increasing degree of misfit between the matrix and the reinforcement will also produce a driving force for thermally activated stress relaxation to occur. These processes (which may constitute microstructural damage), which are driven by a reduction in the overall energy of the system, act to unload the reinforcement and reduce stress concentrations in the matrix surrounding the reinforcement. The overall creep response of the MMC will depend on the two competing effects of load transfer and stress relaxation. Direct strengthening is the type of strengthening normally observed in short and continuous fibre reinforced MMC. Dlouhy et al. [42] have developed a model that reproduces satisfactorily the creep curves obtained experimentally for aluminium based short fibre reinforced metal matrix composites. According to them, isothermal creep in SFRM is governed by the three following microstructural mechanisms: (i) loading of fibres by means of the formation of a work hardened zone around the fibres due to an increase of dislocation density. (ii) Unloading of fibres caused by the movement of dislocation loops to the end of the fibres where they annihilate. This recovery process results in flow of matter around the fibre ends. (iii) Breakage of fibres into subfibres after reaching a critical fibre stress. This has two important consequences: in the short term, the stress on the subfibres decreases and the mean stress in the matrix increases. However, subfibres are then further loaded due to the more intensive plastic deformation in the matrix and can break again. In the long term, the combination of fibre breakage and recovery (movement of dislocation loops towards fibre ends) causes the increase of the deformation rate in tertiary creep.

Indirect strengthening occurs when the presence of the reinforcement modifies the microstructure of the matrix. For example, the size and distribution of precipitates, the matrix grain size, subgrain size and dislocation substructure and density can all be affected by the reinforcement, and will consequently influence the mechanical response of the MMC. Strain hardening is normally the main strengthening mechanism involved in particle reinforced MMC and although it may effectively strengthen the composite at low temperatures, particles bigger than dispersoids may weaken PRM at elevated temperatures, particularly the creep resistance due to the increase of easy diffusion paths (such as dislocations and interfaces).

2.1.4.2 Creep Exponent and Activation Energy

Generally, the literature available for creep in discontinuously reinforced MMC reports values of creep exponent n and activations energy Q that are much higher than those found for the unreinforced matrix and that can be explained by the currently existing models

of creep [43, 44, 45, 46, 47]. Nardone and Streife [48] proposed to use an equation developed for precipitate and oxide dispersion strengthened alloys which is in fact a modification of the normally used Norton's law [40] since it introduces a threshold stress σ_{TH} :

$$\dot{\epsilon}_c = A \cdot \left(\frac{\sigma - \sigma_{TH}}{E} \right)^{n_0} \cdot \exp \left(- \frac{Q_{SD}}{R \cdot T} \right) \quad (2.1)$$

where $\dot{\epsilon}_c$ is the minimum creep rate, σ the applied stress, E the Young's modulus of the composite, Q_{SD} the activation energy for self diffusion of the matrix, R the universal gas constant, T the test temperature and n_0 a value of stress exponent in agreement with the available creep theories. This equation has shown to be in good conformity with experimental data for discontinuously reinforced MMC. Thus, the creep exponent n and the activation energy Q obtained experimentally are called apparent stress exponent n_{app} and apparent activation energy Q_{app} , respectively. In general, the parameter n_{app} decreases with increasing applied load at constant temperature (see for example Figure 2.6 b)), and/or with decreasing test temperature at constant stress. It has also been found to increase with decreasing reinforcement size and increasing inclusion aspect ratio, but does not change significantly with reinforcement volume fraction. In the case of the Q_{app} , it was found in many investigations that it increases with decreasing applied stress. Q_{app} was also found to decrease with increasing reinforcement size and decreasing reinforcement aspect ratio, for a given stress level. However, it must be emphasized that the threshold stress σ_{TH} is merely an approximation that permits a better description of experimental creep data and although many theoretical models have been developed attempting to achieve a physical interpretation [49, 50, 51, 52], no one of them has shown a good correlation with experimental data and it only seems reasonable to suggest that the mechanisms of load transfer, dislocation-reinforcement interaction and the presence of fine oxide dispersion particles all contribute to the high values observed for n_{app} and their temperature dependence on Q_{app} .

2.1.4.3 Importance of Reinforcement Parameters

The creep behaviour of a composite will be a result of the competing processes of load transfer and stress relaxation. The mechanisms of relaxation may (e.g. cavitation, reinforcement fracture, matrix micro-cracking, debonding, etc.) or may not (e.g. interfacial sliding, diffusion, matrix flow, dislocations climbing, etc.) constitute structural damage of the composite. If relaxation occurs, the reinforcement will be unloaded, reducing the load transfer from matrix to reinforcement, thus increasing the mean matrix stresses, and decreasing the load bearing capacity of the MMC. Experimental evidence shows that stress relaxation is

sensitive to microstructural parameters such as shape, size and distribution of the reinforcement and therefore their influence on promotion of stress relaxation has to be taken into account since it may result in lower creep resistance. However, stress relaxation mechanisms within the matrix can also lead to an improvement of the creep properties of the composite under certain conditions and this is one of the main results found during the development of this thesis for the SFRM and will be discussed in Chapter 7.

Reinforcement Size

During this work, the size range considered for reinforcement of MMC is beyond that producing dispersion strengthening. Reinforcement size can influence the creep resistance in several ways. First, if the size of the reinforcement is increased, but the volume fraction kept the same, there will be an increase in the interparticle spacing. At sufficiently high interparticle spacings, the subgrain size will revert from being interparticle spacing controlled to stress controlled, and hence there will be a corresponding change in the stress sensitivity.

The scale of the reinforcement has shown experimental evidence that it can be detrimental to the creep behaviour. Creep tests conducted on a powder metallurgy produced SiC particle reinforced Al composite by Winand et al. [53] and by Tjong et al. [44] show that there may exist a critical interparticle spacing (reinforcement size) below which the reinforcement can improve the high-temperature creep properties (see Figure 2.6 a) and b)). Winand et al. [53] argued that if interfacial diffusion were the dominant stress relaxation mechanism for their investigated PRM, then it would be expected that this would be more significant with the smaller 3 μm particles, because of the smaller diffusion distances involved. However, this was not the case. Furthermore, if diffusional relaxation were rate controlling then one would expect load transfer to be more significant at high strain rates, for which diffusional relaxation has less time to take place. However, it was found that the load transfer was poorer for the 20 μm particles, the faster the strain rate. This suggests that it is the microstructural damage which is acting to relax the internal stresses predominantly. It is important to remark that PM produced Al-MMC contain as well Al_2O_3 dispersoids which influence the creep behaviour significantly.

Whitehouse et. al. [54, 55] have shown that the size of a cavity that nucleates at the reinforcement-matrix interface is directly related to the size of the reinforcement. Also, the larger the cavity, the less stable it will be. Consequently, cavitation in composites with large reinforcement, will be less stable than for fine reinforcement, and hence more detrimental to the properties.

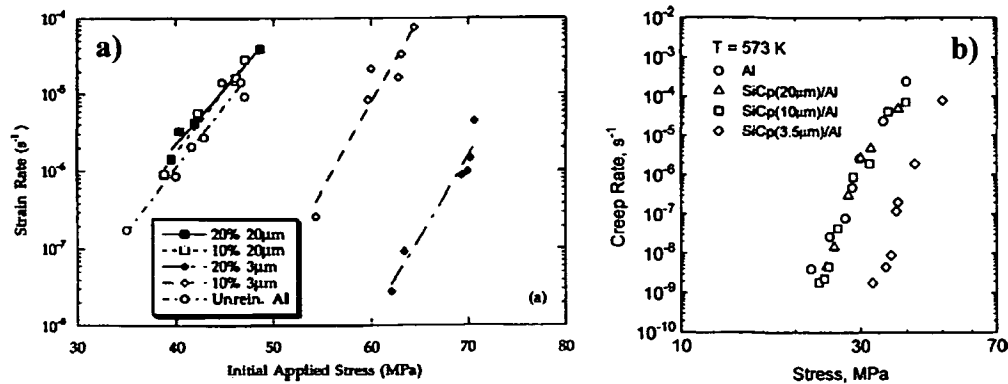


Figure 2.6. Measured variation of minimum creep rate with applied stress for unreinforced and reinforced Al: a) SiC particle reinforced Al at 270°C from [53] and b) for SiC particle reinforced Al tested at 300°C from [44].

Reinforcement Aspect Ratio

Generally, an increase in the aspect ratio of a creep resistant reinforcement will further enhance the creep resistance. Here, it is the load transfer to the reinforcement that dominates the creep response, so an increase in aspect ratio will result in a corresponding increase in the load transfer.

However, an increase in the aspect ratio of a reinforcement is not always beneficial to the creep response of the composite. Whitehouse et al. [56] reported that if the studied system is one in which the unreinforced matrix has superior creep behaviour to the “reinforced” material, there may be a reduction in the creep resistance with increasing “reinforcement” aspect ratio. Figure 2.7 a) and b) show some of the results obtained in [56] for commercially pure Al unreinforced and reinforced with spherical and angular Al_2O_3 particles, Al_2O_3 and carbon short fibres produced by powder-metallurgy tested at 270°C.

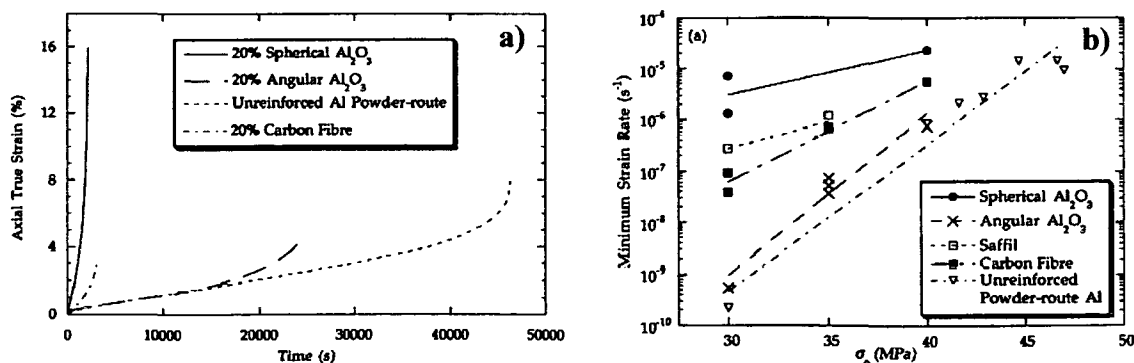


Figure 2.7. Results obtained in [56] for unreinforced commercially pure Al and reinforced with reinforcements of different aspect ratios tested at 270°C.

These data reveal that low aspect ratio angular particles show better creep resistance than the short fibres, while all the studied composites are inferior to the unreinforced Al matrix, contrary to the expectations of load transfer. The reason for this behaviour is

explained by the authors as related to the ease and stability of damage. Again, the matrix has to be considered as dispersion strengthened.

Reinforcement Shape

The local stress distribution around a reinforcement is highly sensitive to the shape of reinforcement [57, 58, 59]. It is found that reinforcement angularities produce the highest stress concentration within the surrounding matrix. Consequently, it would be expected that the angular particles would nucleate cavities more readily during creep than spherical particles. Microstructural observations on angular reinforced materials show that, as predicted by FEM simulations, voids tend to form at the reinforcement angularities along the line of the applied stress. These cavities are very small, and distributed uniformly at the interfaces throughout the specimen, suggesting that such damage is stable and can be accommodated without leading immediately to failure, which can be an advantage in comparison to spherical reinforced composites where the absence of angularities may lead to think that these materials would show a better creep resistance. However, as shown in Figure 2.7 a) and b), this is not the fact because cavitation near spherical particles occurs as large voids within the matrix which cause rapidly catastrophic failure by initiating the crack path. Such voids are localized near the specimen fracture surface.

Reinforcement Distribution

It has also been pointed out in [56], that composites with a uniform reinforcement distribution show consistently better creep resistance than those where the reinforcement is clustered. The reason for this is related to the damage stability. In regions where the reinforcement is clustered, there is a high degree of triaxial constraint in the matrix. This inhibits local plastic flow as a stress relaxation mechanism, and promotes damage in the form of cavitation instead. Such cavities tend to be large and unstable. This has been confirmed by microstructural observations that show that this type of cavitation is invariably localized in the region of fracture. Furthermore, during MMC production may occur that reinforcement clustering will result in porous zones since the matrix will not be infiltrated between the particles and/or fibres. This is obviously a disadvantage for the creep resistance of the composite since the reinforcement effect desired when a MMC is designed will not be achieved. Such porous zones can also act as crack formation sites that will promote early failure of the composite. One example of an uninfiltrated region in extruded particle reinforced Al alloys produced by stir casting is shown in Figure 2.8.

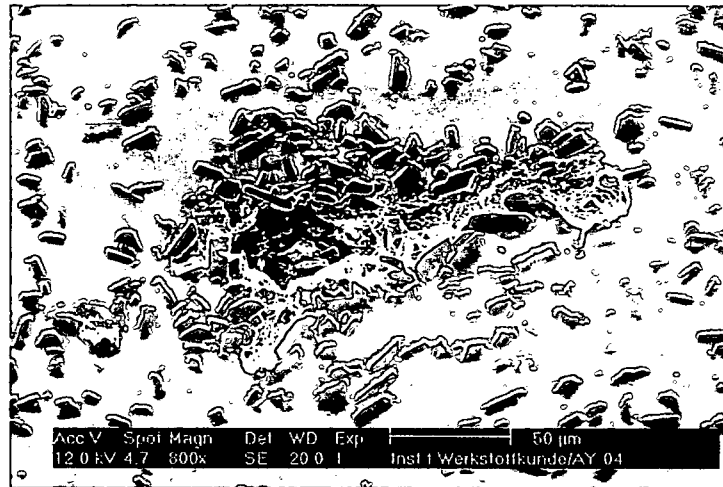


Figure 2.8. Non wetted zone in a particle clustering site in 6061/Al₂O₃/22p produced by stir casting and subsequently extruded [9].

3 Experimental

3.1 Particle Reinforced Materials

Two particle reinforced materials together with the unreinforced matrix were studied during the development of this work. The PRM consist of irregularly shaped (angular) α - Al_2O_3 particles embedded in a 6061 aluminium wrought alloy matrix. The PRM were fabricated by DURALCAN Ltd. [10] using a stir casting process (see Paragraph 2.1.2.1) and delivered in the form of extruded rods of 11mm and 12mm diameter for the unreinforced and reinforced materials, respectively. The deformation by extrusion amounted to $\phi = 3$ [60]. The chemical composition of the matrix is shown in Table 3.1.

6061 Alloy	Mg	Si	Cu	Cr	Fe	Zn	Mn	Ti
Limit Content [61]	0.8-1.2	0.4-0.8	0.15-0.4	0.04-0.35	<0.7	<0.25	<0.15	<0.15
6061 [62] Matrix	0.95	0.8	0.3	0.2	0.5	0.09	0.1	-

Table 3.1. Chemical composition of the matrix alloy.

The hot-extrusion process, carried out in order to homogenize the particles distribution and close the pores formed during the stir casting process, causes at the same time an alignment of the reinforcement in the direction of the extrusion axis. The particle dimension in longitudinal and transverse direction to the extrusion axis are shown in Table 3.2 for the two investigated PRM.

Material	Direction to extrusion axis	Average size [μm]
6061/ Al_2O_3 /10p	Transverse	5.7 ± 2.4
	Longitudinal	7.4 ± 3.6
6061/ Al_2O_3 /22p	Transverse	9.3 ± 4.5
	Longitudinal	10.4 ± 6.2

Table 3.2. Particle dimensions after the hot-extrusion process.

3.1.1 Reinforcement Distribution

Figure 3.1 a), b) and Figure 3.2 a), b) show optical micrographs for the two PRM in the directions longitudinal and transverse to the extrusion axis. It is possible to observe the already mentioned alignment of the particles in the direction of the extrusion but nevertheless a uniform distribution of the reinforcement throughout the material is achieved.

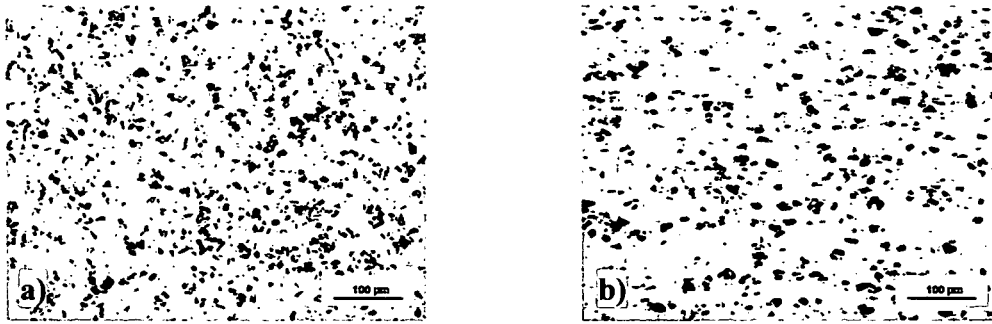


Figure 3.1. 6061/Al₂O₃/10p in direction transverse to extrusion direction (a) and in extrusion direction (horizontal axis) (b).

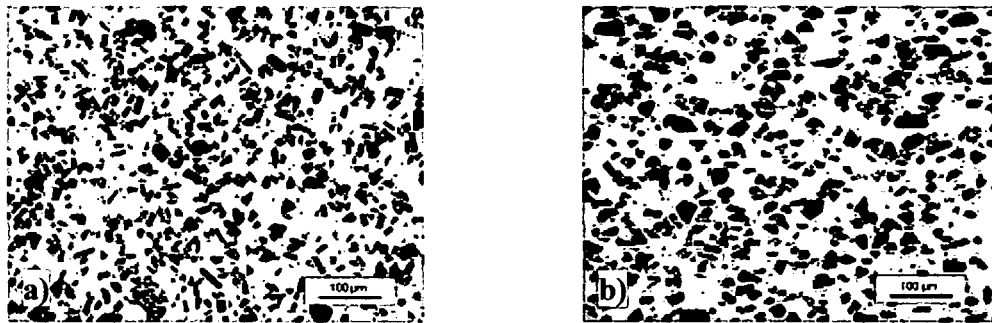


Figure 3.2. 6061/Al₂O₃/22p in direction transverse to extrusion direction (a) and in extrusion direction (horizontal axis) (b).

3.1.2 Thermal Treatment

The age hardening behaviour of the 6061 alloy results mainly in the growing of F.C.C. Mg₂Si precipitates, with a stoichiometric composition Mg:Si = 1.73:1 in weight [63], according to the following sequence [64]:

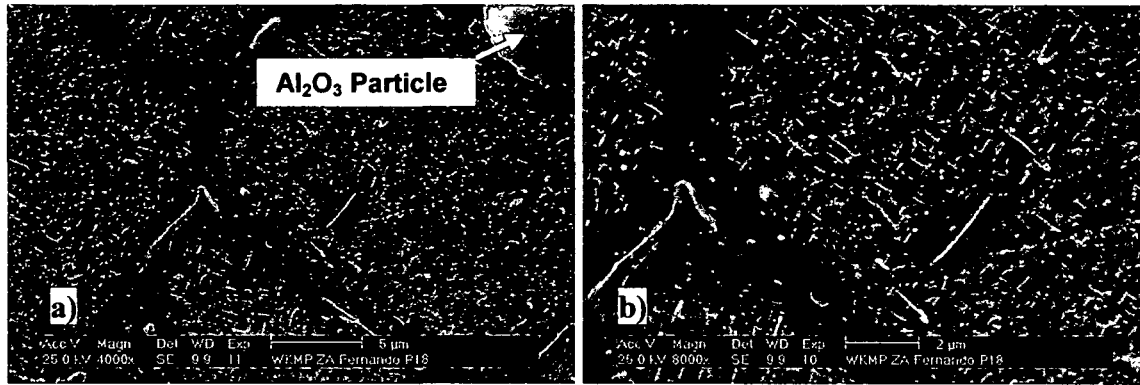


In the matrix, there is a surplus in Si (Mg:Si ~ 1.2:1 in weight) which causes to form Si clusters initially, if homogeneously nucleated. The presence of the reinforcement phase in the composite materials does not provoke any change in the precipitation sequence although it results in an acceleration of the precipitation kinetics due to an increase of the dislocation density caused during cooling from the solid solution treatment temperature by the difference in CTE between the matrix and the reinforcement [65]. Heterogeneous nucleation will prevail and the growth of the precipitates is accelerated owing to the higher diffusivity of Mg and Si along the dislocations paths.

Prior to test, the matrix and the two PRM were subjected to a T6 thermal treatment [63] and then overaged during 30 minutes (this thermal treatment will be designated as T6-S hereunder) as shown in Table 3.3. Figure 3.3 a) and b) show the overaged β Mg₂Si needles observed in a 10vol% particle reinforced sample after the T6-S treatment.

Material	Solution Treatment	Ageing	Overaging
6061	530°C/30'-Water quenched	160°C/24h	300°C/30'
6061/Al ₂ O ₃ /10p	560°C/30'-Water quenched	160°C/8h	300°C/30'
6061/Al ₂ O ₃ /22p			

Table 3.3. T6-S thermal treatment for the unreinforced and PRM 6061 alloys.

Figure 3.3 a) and b). Mg₂Si precipitates and precipitation free zones at grain boundaries and matrix-particle interface after T6-S heat treatment in a 10% PRM sample.

3.1.3 Interfacial Reactions

SEM investigations conducted for the two composite materials showed the presence of a layer of spinel crystals (MgAl₂O₄) between the Al₂O₃ particles and the matrix. Experiments conducted in the same composite by Berek et al. [66], showed that this spinel layer is formed during solution treatment in the temperature range between 525°C and 560°C which is coincident with the solution treatment temperature used in this study for the reinforced materials.

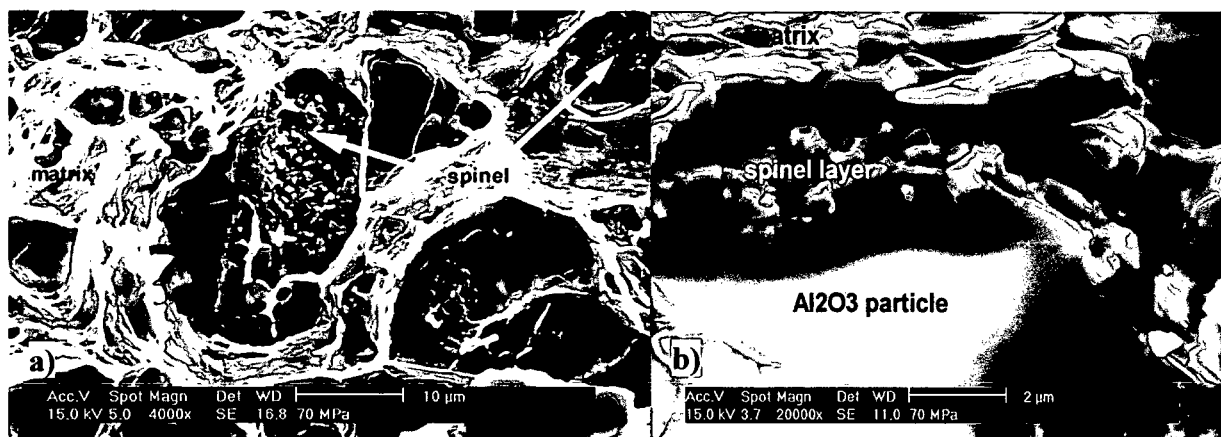
Figure 3.4. Spinel reaction layer on the surface of unbroken Al₂O₃ particles a), and surrounding a broken particle, b).

Figure 3.4 a) and b) show this reaction layer for two different cases. In Figure 3.4 a) an alumina particle coated by spinel crystals is shown in a fracture surface of a 70MPa creep test where no matrix is found in between the spinel crystals. Figure 3.4 b) shows how the spinel crystals grow along the interface of a broken Al₂O₃ particle surrounded by matrix.

The growing of this MgAl_2O_4 layer on the reinforcement surface influences the precipitation kinetics since the matrix will be depleted from Mg which could form Mg_2Si . Besides that, the already mentioned heterogeneous nucleation of clusters in the regions of high density of dislocations as well as precipitation free zones at grain boundaries and interfaces lead to non-uniform distribution of precipitates [67].

3.2 Short Fibre Reinforced Materials

An AlSi12CuMgNi alloy unreinforced and reinforced with Al_2O_3 short fibres was produced using a squeeze-casting process (see Paragraph 2.1.2.1). The chemical composition of this alloy is shown in Table 3.4 [68].

Preforms of randomly planar distributed Saffil® [69] short fibres with 10, 15 and 20vol% fibre content were used as reinforcement for the SFRM. The dimensions of the preforms were $130 \times 130 \times 20 \text{ mm}^3$. The short fibres consist of 96-97% $\delta\text{-Al}_2\text{O}_3$ and 3-4% SiO_2 . The trace components present in the fibres as well as their main physical and mechanical properties are summarized in Table 3.5 and Table 3.6 [70].

Element	Al	Si	Cu	Mg	Ni	Fe	Mn	Zn	Ti
Mass%	Matrix	11-13	0.8-1.3	0.8-1.3	1.3	0.7	0.3	0.3	0.2

Table 3.4. Chemical composition of AlSi12CuMgNi matrix alloy.

Trace Component	Fe	Cr	Ni	Na	Mg	Ca	Cl
ppm	400	60	140	875	130	525	80

Table 3.5. Trace components present in Saffil® short fibres.

Melting Point [°C]	Max. Use Temp. [°C]	Density [g/cm ³]	Mean Fibre Diameter [μm]	E [GPa]	Tensile Strength [MPa]
>2000	1600	3.3	3.0-3.5	300	2000

Table 3.6. Properties of Saffil® short fibres.

Figure 3.5 shows a SEM picture of a 20vol% preform looking on to the plane where the fibres are randomly distributed. We can see a homogeneous fibre distribution with fibre length dimensions ranging from approximately $10 \mu\text{m}$ to more than $200 \mu\text{m}$. The fibre diameters are between 1 to $10 \mu\text{m}$ and the mean aspect ratio of the fibres is 80.

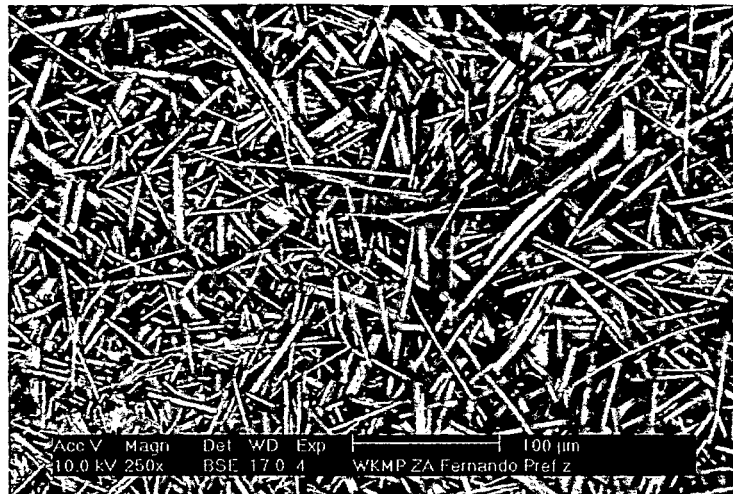


Figure 3.5. 20vol% fibres preform in the plane of random fibre orientation.

3.2.1 SFRM Production using the Squeeze Casting Process

The SFRM were produced using the facilities available at the Institute of Materials Science and Technology at the TU Clausthal [71].

The preforms were maintained at 1000°C during 12 hours prior to infiltration. Then, the hot preforms were inserted into the compression mould and the molten alloy was then poured in at 800°C. The pressure was applied in two steps to squeeze the melt into the preform: 1) 72 MPa during 15sec and 2) 144MPa during 90sec. The final product are plates of SFRM surrounded by matrix material with a diameter of 205mm and a height between 40 – 50mm as shown schematically in Figure 3.6.

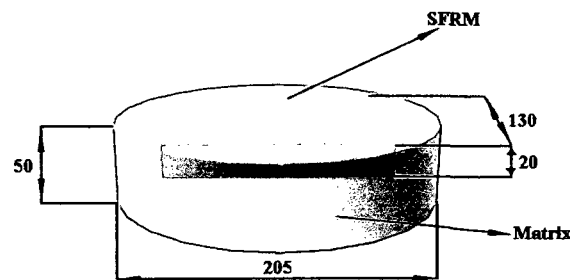


Figure 3.6. SFRM and Matrix plate after squeeze casting.

3.2.2 Reinforcement Distribution

SFRM samples were cut from the original plates, mechanically polished and then observed under the optical microscope in order to analyse the orientation and distribution of the reinforcement after squeeze casting. This was done for the three investigated volume fractions and Figure 3.7, Figure 3.8 and Figure 3.9 show that the composites present a uniform random planar distribution on the X-Y plane.

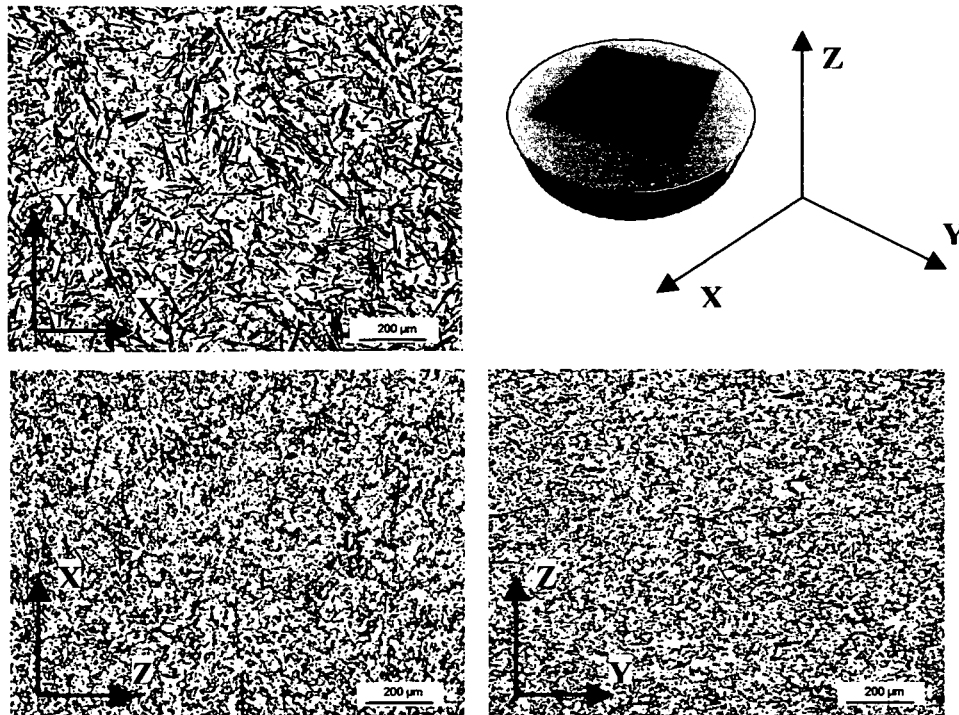


Figure 3.7. Fibres orientation and distribution for the AlSi12CuMgNi/Al₂O₃/20s material.

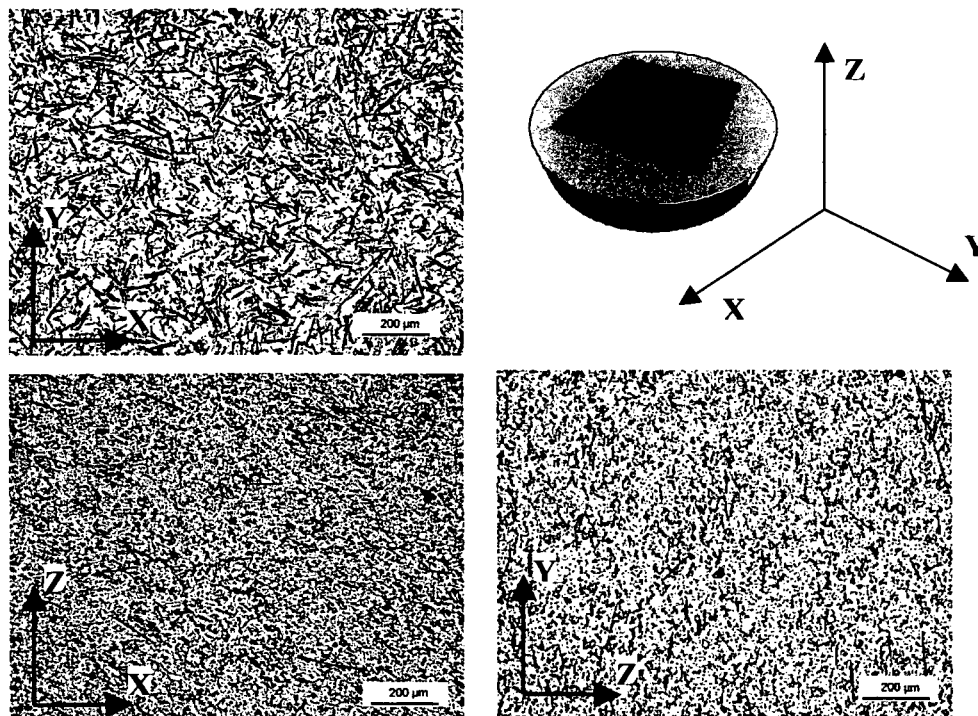


Figure 3.8. Fibres orientation and distribution for the AlSi12CuMgNi/Al₂O₃/15s material.

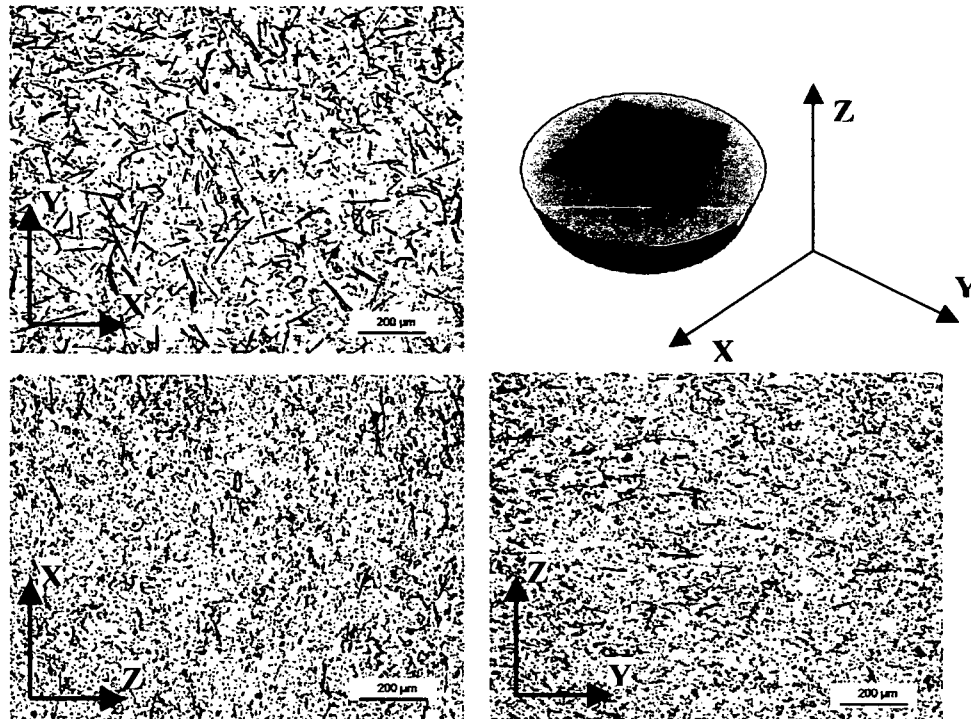


Figure 3.9. Fibres orientation and distribution for a AlSi12CuMgNi/Al₂O₃/10s material.

3.2.3 Thermal Treatment

Similarly to the PRM, the SFRM were subjected to a T6 thermal treatment [63] and then overaged during 30min at 300°C (T6-S) as shown in Table 3.7.

Material	Solution Treatment	Ageing	Overaging
AlSi12CuMgNi, AlSi12CuMgNi/Al ₂ O ₃ /10s, 15s, 20s	480°C/4h – Oil quenched	190°C/4h	300°C/3h

Table 3.7. T6-S thermal treatment for the unreinforced and reinforced AlSi12CuMgNi alloys.

3.2.4 Present Phases and Interfacial Reactions

After the thermal treatment, the three SFRM and the unreinforced alloy were subjected to EDX analysis in order to identify the present phases. The same phases were found for all the studied materials except obviously for the additional existence of the ceramic fibres in the SFRM. Figure 3.10 and Figure 3.11 a) and b) show the morphology of the identified phases in an AlSi12CuMgNi/Al₂O₃/20s sample under SEM and optical microscope, respectively. The points on these pictures correspond to EDX spot analysis and the obtained spectrums are depicted in Figure 3.12 to Figure 3.17.

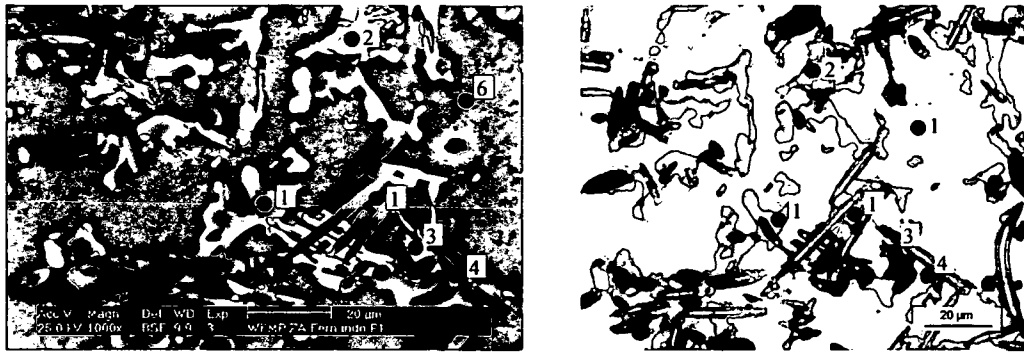


Figure 3.10. Morphology of the phases for an AlSi12CuMgNi/Al₂O₃/20s sample observed under SEM (a) and optical microscope (b).

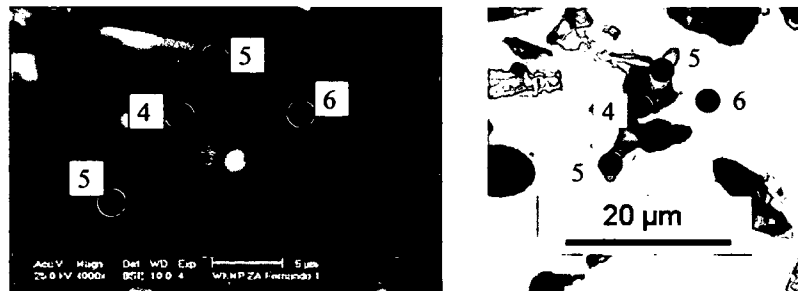


Figure 3.11. Morphology of the phases for an AlSi12CuMgNi/Al₂O₃/20s sample observed under SEM (a) and optical microscope (b).

A qualitative analysis of the obtained EDX analysis show that the points in Figure 3.10 and Figure 3.11 a) and b) correspond to:

- (1) **Si rich phase.** The AlSi12CuMgNi alloy has an eutectic composition of α -Al and Si. This phase is easily observable throughout the surface of the sample both under SEM and the optical microscope. At the studied condition (T6-S) it is usually found surrounding the Al₂O₃ fibres (see points 1).
- (2) **Fe rich phase.** Its orange colour makes it easy to distinguish under the optical microscope. Some appear rounded, some show a needle structure mainly at the borders of the round ones (point 2). It probably corresponds to the α -AlFeSi compound [63]
- (3) **Ni rich phase.** Dark brown phase under the optical microscope (see point 3). It was found surrounding the Al₂O₃ fibres. Ni is added to the AlSi12CuMgNi alloy to increase the elevated temperature strength and/or reduce the coefficient of thermal expansion. The elevated temperature properties improvement is achieved by the formation of an Al₆Cu₃Ni intermetallic phase that is stable at high temperatures [63].

- (4) **Al₂O₃ fibre** (see point 4). These fibres contain between 3-4% of SiO₂ as well as traces of Mg. This Mg may correspond to rests of MgO used for polishing of the sample or could also indicate an interface reaction between the matrix and the fibre. SEM pictures taken with higher resolutions did not show any appreciable interface reaction although TEM studies carried out by Wang et al. on a Saffil® fibre reinforced AlSi12CuMgNi alloy showed the presence of a spinel layer of a few tens of nanometers[72].
- (5) **Mg-Si rich phase**. Blue phase under the optical microscope (see points 5). Aluminium and the binary constituent Mg₂Si form a quasi binary system [73]. However, it was expected that during the solution treatment this Mg₂Si phase would dilute in the matrix. X-rays maps and EDX analysis carried out in overaged (T6-S) and solution treated (T4) samples, respectively confirmed the presence of Mg₂Si both in the unreinforced and reinforced material. Furthermore, EDX analysis carried out in an unreinforced and a reinforced sample solution treated at 540°C during two hours did not show any presence of Mg₂Si indicating that the solution temperature used in this work as described in 3.2.3 was not enough to achieve a complete solution of this phase.
- (6) **α-Al matrix**. Contains the non-resolvable (by SEM) precipitates of Cu-rich phases and Mg₂Si (see point 6).

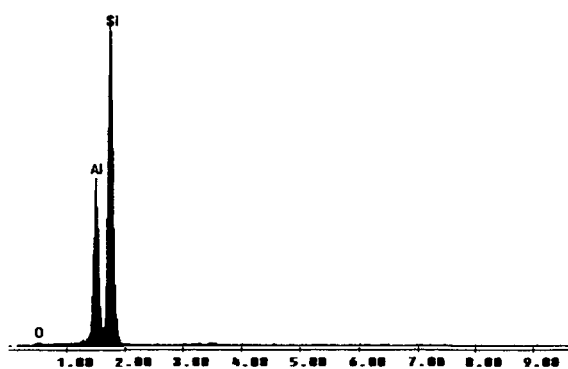


Figure 3.12. Si rich phase (1).

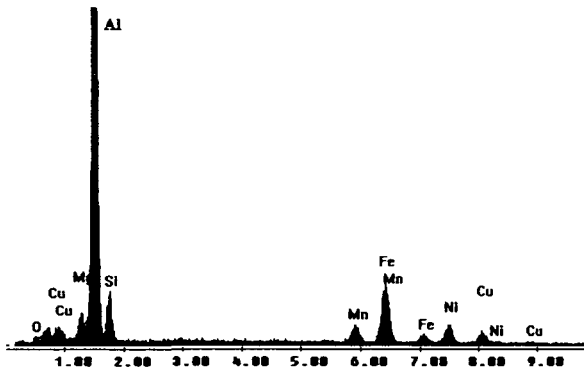


Figure 3.13. Fe rich phase (2).

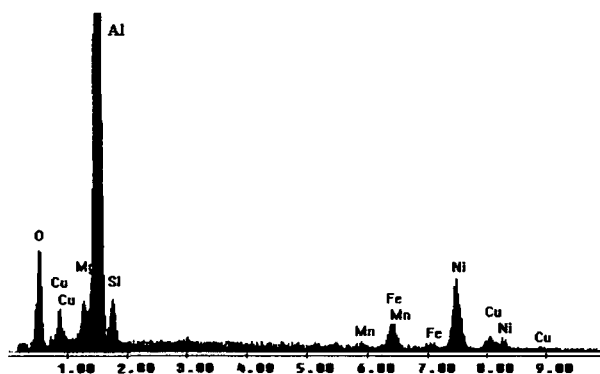


Figure 3.14. Ni rich phase (3).

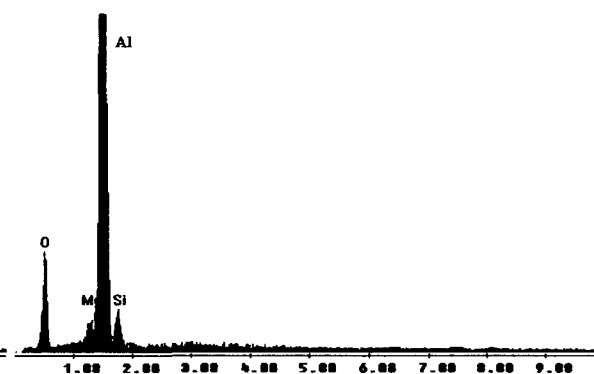
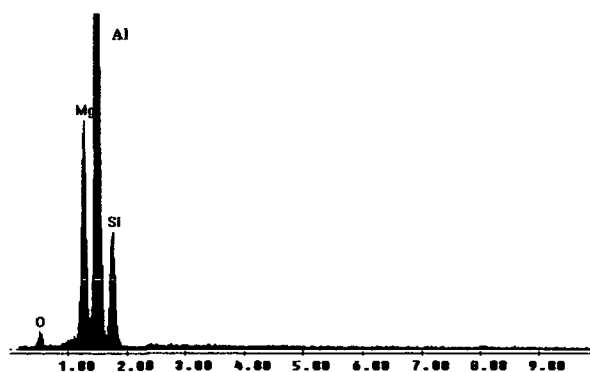
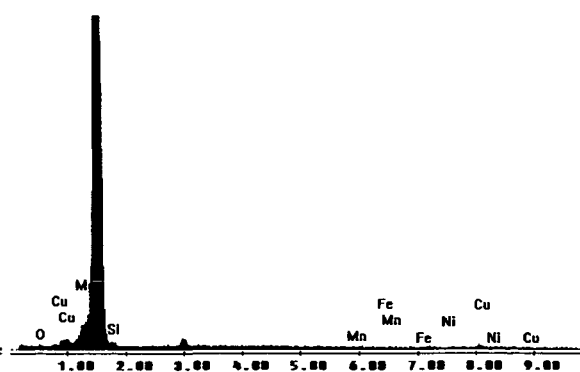
Figure 3.15. Al₂O₃ fibre (4).

Figure 3.16. Mg-Si rich phase (5).

Figure 3.17. α -Al matrix (6).

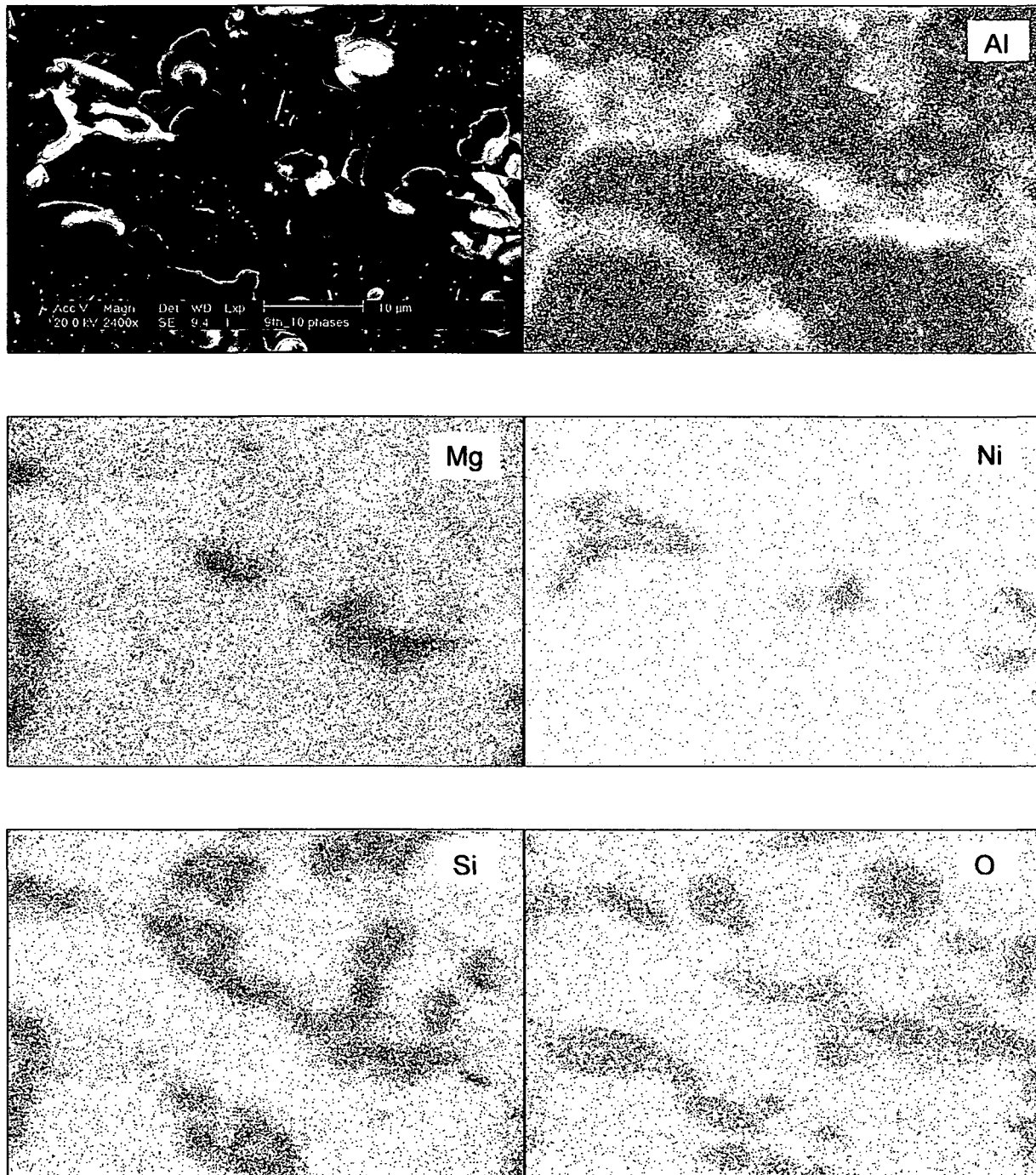


Figure 3.18. X-rays maps of an AlSi12CuMgNi/Al₂O₃/10s sample (512x400 pixels scanning matrix) after a T6-S thermal treatment and subsequent overaging at 300°C during 1000hr. The Mg-Si rich dark phase is present in this material due to a low solution temperature. The position of Al₂O₃ fibres is indicated by the O map and the eutectic Si by the high Si content zones without Mg. The brightest phase corresponds to a Ni based intermetallic phase (see Figure 3.14).

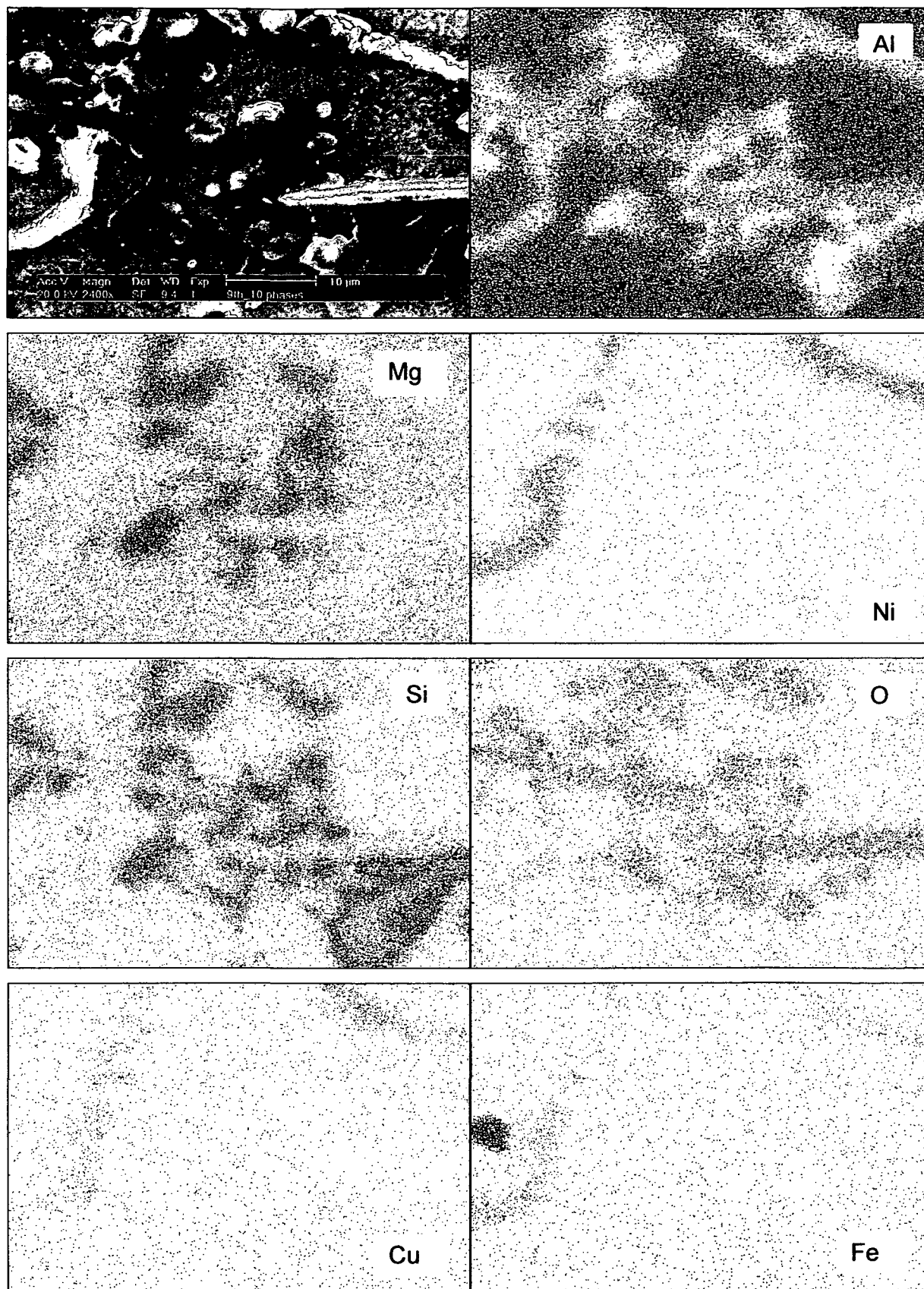


Figure 3.19. X-rays maps of an AlSi12CuMgNi/Al₂O₃/10s sample (512x400 pixels scanning matrix) after a T6-S thermal treatment and subsequent overaging at 300°C during 1000hr. The Mg-Si rich dark phase is present in this material due to a low solution temperature. The position of Al₂O₃ fibres is indicated by the O map and the eutectic Si by the high Si content zones without Mg. The presence of Ni, Cu and Fe based intermetallic phases is also observable.

Figure 3.20 shows a SEM picture of a section of an AlSi12CuMgNi/Al₂O₃/20s sample on the plane of the fibres prior to testing. It can be seen that a large amount of pores show up in the interface between adjacent fibres as well as between fibres and eutectic Si or intermetallic phases. These voids are formed during the squeeze casting process and were found in all the investigated SFRM materials but most in the 20 vol% reinforced composite and one possible reason for this may be the decrease in fibres-interspacing in comparison with the materials with lower reinforcement volume fraction [74]. Furthermore, as stated in [75], if parallel fibres touch, the pressure needed to infiltrate contact lines between fibres is calculated to be infinite, increasing thus the probability of pore formation for the AlSi12CuMgNi/Al₂O₃/20s composite. Also, the squeezing step during the casting process may not be able to fill all the shrinkage pores due to the higher compression resistance of the 20vol% preform.

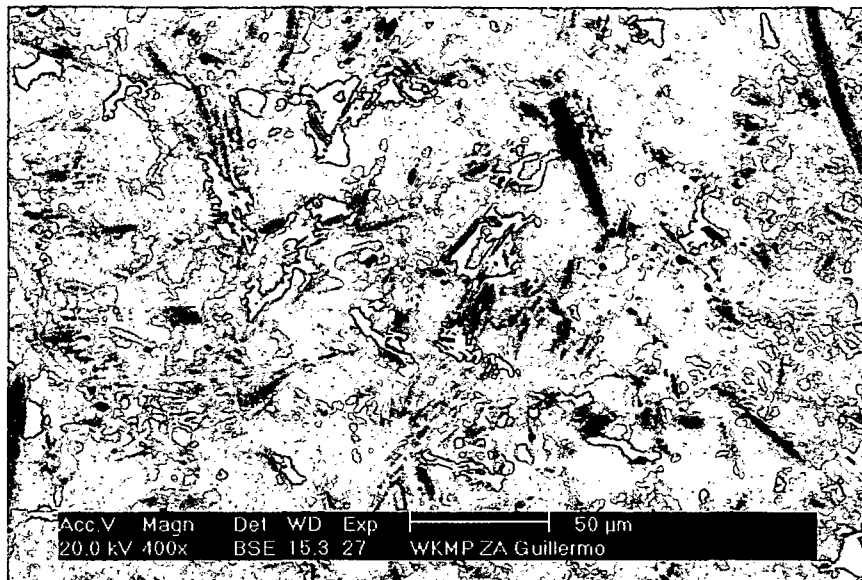


Figure 3.20. SEM micrograph of an AlSi12CuMgNi/Al₂O₃/20s showing the presence of pores in the interface between matrix and fibres and between adjacent fibres.

3.2.5 Interaction of Si Phase with Al₂O₃ Short Fibres

Samples of untested unreinforced and reinforced matrix in the T6-S condition were deep etched using a 50 vol% solution of HCl in order to investigate the interaction between the Si from the eutectic and the reinforcement fibres in the AlSi12CuMgNi/Al₂O₃/xxs composites. The samples were etched until no reaction bubbles were observable (approx. 3 hours for the matrix and 12 hours for the MMC). The etched samples were then observed under the SEM and the obtained micrographs are shown in Figure 3.21 and Figure 3.22 for the matrix and the MMC, respectively.

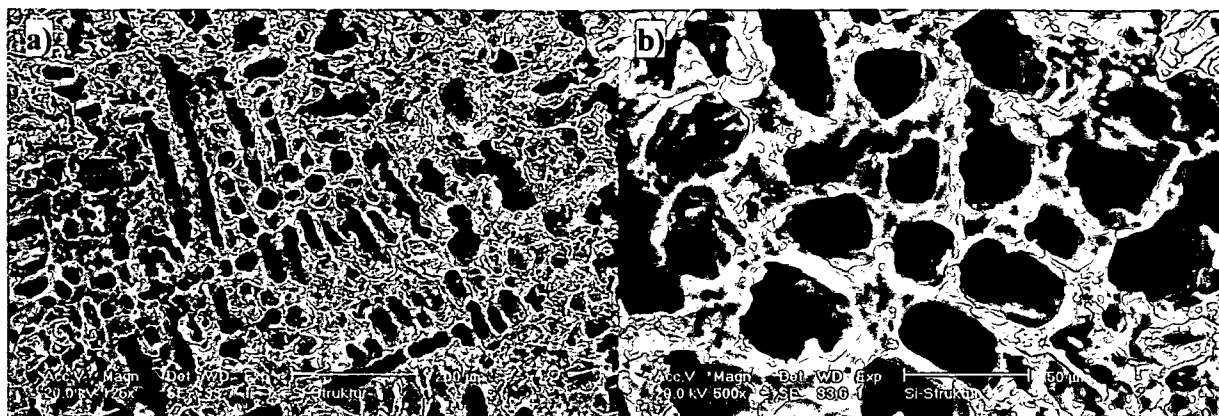


Figure 3.21. a), b) Si structure in a AlSi12CuMgNi T6-S sample after deep etching.

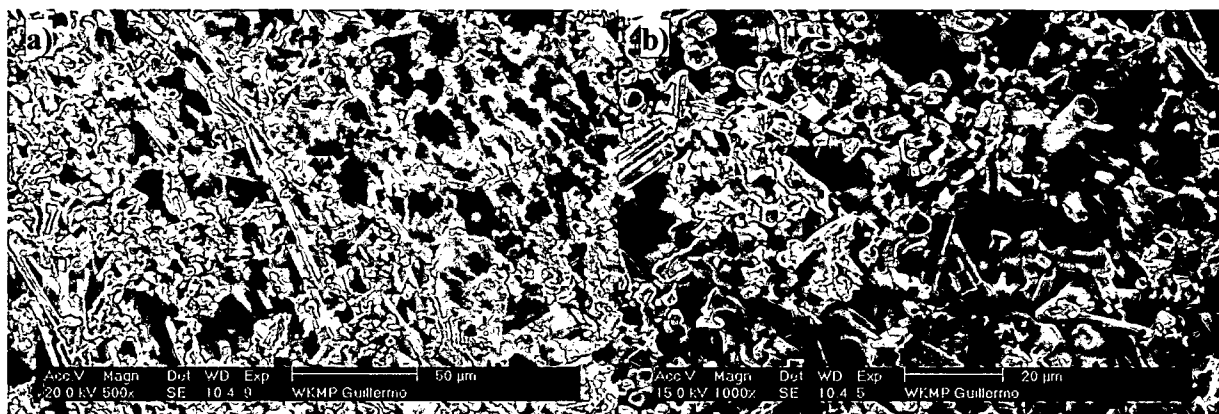


Figure 3.22. a), b) Si structure in a AlSi12CuMgNi/Al₂O₃/15s T6-S sample after deep etching.

Figure 3.21 a) and b) show the formation of an interconnected 3D Si network with holes that are a 3D negative image of the Al matrix. In the case of the MMC (Figure 3.22), the fibres show to be either surrounded or connected by the Si network resulting in a rigid 3D network consisting of reinforcement and eutectic Si confirming what has been already proposed in [76] and [77].

3.3 Creep Tests

3.3.1 Equipment Description

Tensile creep tests were carried out in order to study the creep behaviour of the described discontinuously reinforced aluminium alloys and the corresponding unreinforced matrices. For this purpose, an old creep test rig from the year 1957 was modified so that a new digital acquisition system, inductive displacement transducers and a digital temperature control system were integrated [78]. Figure 3.23 a) and b) show schematically the arrangement of the test equipment used during the development of this work and a picture of actual equipment set-up, respectively.

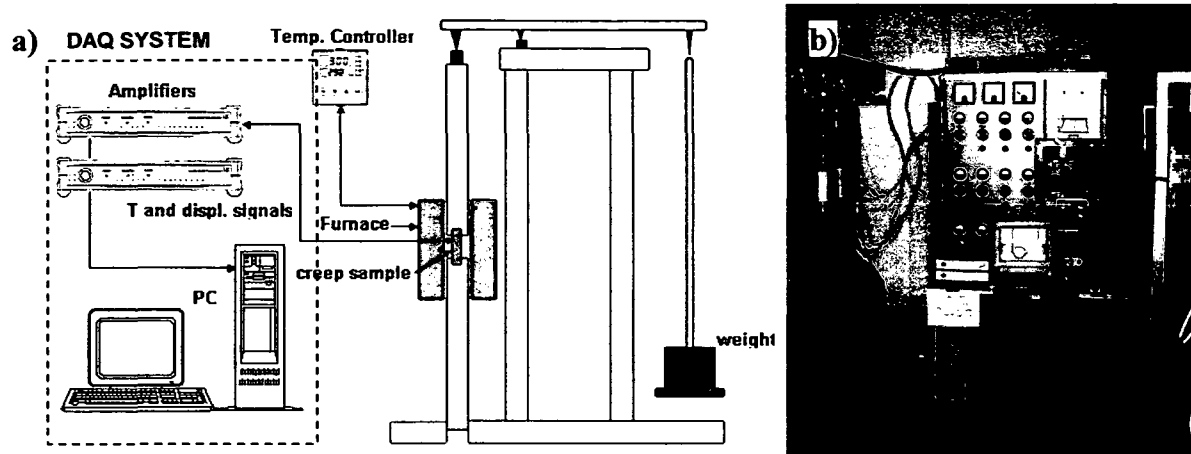


Figure 3.23. Creep test rig set-up: a) schematically, b) actual.

As shown in Figure 3.23 a) the load can be changed using weights. These weights are available in form of plates from 200g up to 5kg. The temperature of the sample was measured using three type K thermocouples at the bottom, centre and top of the sample, respectively but only the thermocouple at the bottom was used to control the temperature since it showed to be the most stable (smaller temperature oscillations). The creep tests were carried out in an air atmosphere at $300 \pm 3^\circ\text{C}$. The strain during the tests was measured using linear variable displacement transducers (LVDT) provided by Micro-Epsilon [79] with a sensitivity of 56mV/V and a resolution of $0.01\mu\text{m}$. The measured signals (temperature and strain) were then amplified and recorded using a data acquisition system made up of a PC and external amplifiers model Spider8 provided by Hottinger Baldwin Meßtechnik G.m.b.H. [80].

3.3.2 Sample Geometry

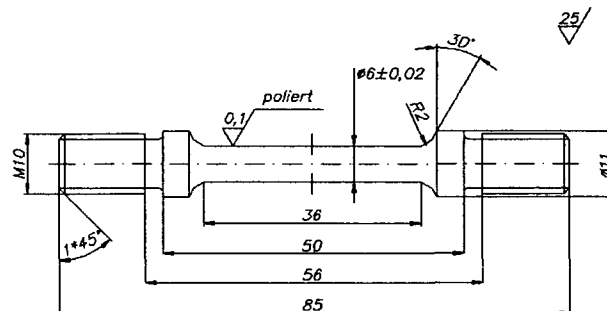


Figure 3.24. Sample Geometry.

Figure 3.24 shows the geometry of the samples used for the tensile creep tests. The design was done according to the requirements of the standard DIN EN 10291.

3.3.3 Creep Tests Procedure

In the case of the PRM and the unreinforced wrought alloy, the tests were carried out at constant load during the whole tests and they were continued until well advanced tertiary stage or fracture of the sample.

The creep tests for the SFRM were carried out so that the load was increased or decreased after reaching a minimum creep rate (see Figure 3.25). This was done in order to study the influence on the creep behaviour of periods at higher load before returning to the initial load (e.g. 30MPa \rightarrow 40MPa \rightarrow 30MPa).

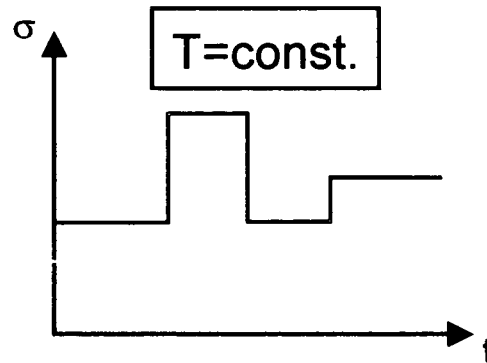


Figure 3.25. Scheme of the creep test procedure for SFRM.

3.4 In Situ Tensile Creep Tests

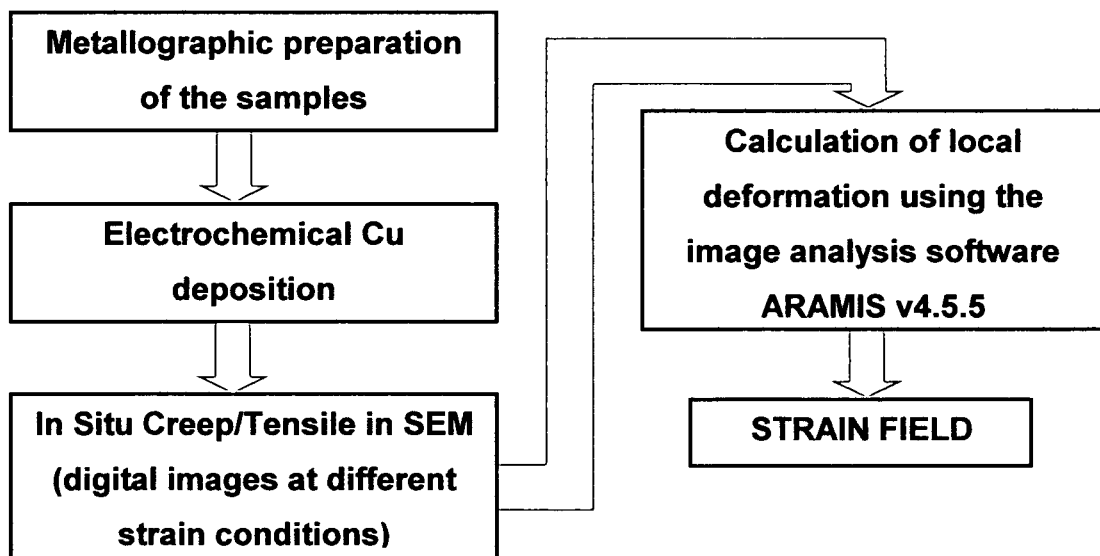


Figure 3.26. Flow diagram for strain field calculation procedure.

The measurement of strain and/or stress fields in MMCs under tensile and creep conditions has been object of intensive theoretical studies during the last years [81, 82, 83, 84]. Recently, a few new methods to visualize experimentally the strain fields in MMCs have been described [85, 86, 87, 88, 89]. During the development of this thesis, a procedure combining the use of In Situ creep tests in a SEM together with an image analysis system was used to visualize and analyse the strain fields developed in the investigated PRM and SFRM under tensile creep conditions. The motivation for our investigations was the possibility to compare the obtained results with FEM predictions as well as to observe experimentally the difference

in the deformation behaviour in comparison with previously obtained results for the same materials during room temperature tensile tests [90, 91].

The flow diagram in Figure 3.26 shows schematically the step by step procedure followed in order to obtain the strain fields developed during the tests.

3.4.1 Sample Geometry

The samples were machined according to the following geometry. The thickness of the samples ranged from 0.4 to 1.4mm.

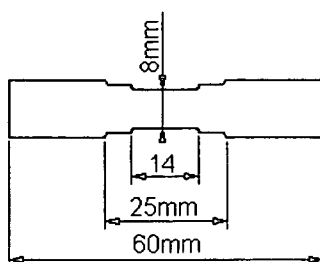


Figure 3.27. Sample geometry.

3.4.2 Metallographic Preparation of the Samples

The samples must be polished in order to obtain a surface suitable for observation under the SEM. For this purpose, the samples were embedded in an epoxy polymer and then polished by hand using wet SiC abrasive paper of sizes 120, 180, 320, 500, 800, 1200, 2400 and 4000, successively. The samples were then polished using diamond paste of sizes 6, 3 and 1 μ m on cloth plates. A final polishing was then carried out using MgO powder. Finally, the samples were unmounted from the epoxy polymer.

3.4.3 Electrochemical Copper Deposition

Copper “islands” were electrochemically deposited on the surface of the samples. This was done in order to obtain randomly distributed high contrast marks which are necessary for the calculation of the local strain (see Paragraph 3.4.5). An electrolytic cell like the one shown in Figure 3.28 was used for this purpose. A 1molar solution of CuNO_3 (copper nitrate) was used as electrolyte. A piece of commercially pure Al was used as anode and the sample was the cathode. A difference of potential $\Delta V=5\text{V}$ showed to be enough to reduce the copper on the sample. This ΔV was then applied during 5sec approximately. An optimal deposition time corresponds to that after which the distribution of copper marks is random throughout the surface of the sample. A time too short will give a good distribution of copper marks but with an insufficient amount of contrast points for processing of the pictures. Times too long will result in clustering of the copper marks. Figure 3.29 show the results of copper deposition for

a 6061/ Al_2O_3 /10p sample for the cases when the deposition time is too short, optimal and too long, respectively.

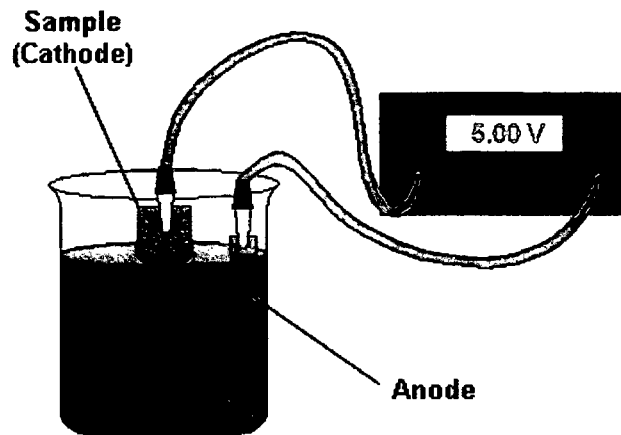


Figure 3.28. Electrolytic cell used for the deposition of copper on the samples.

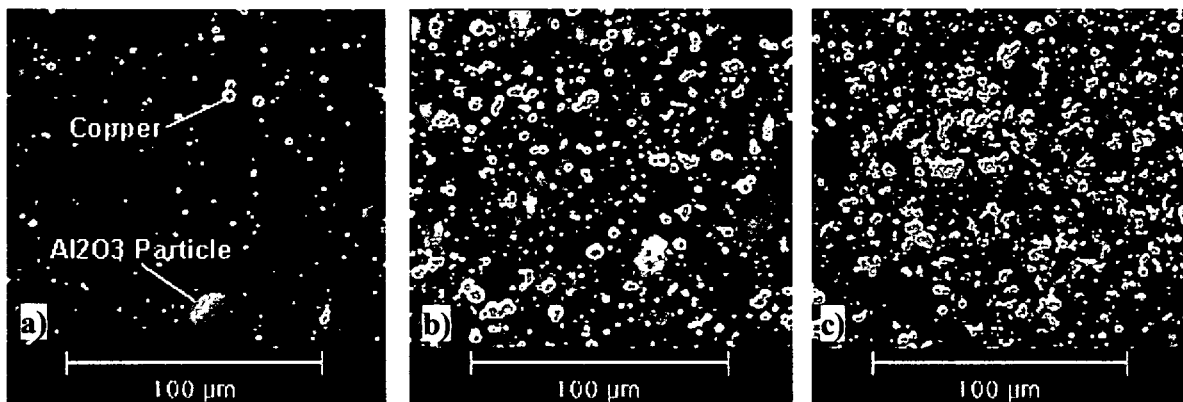


Figure 3.29. Influence of deposition time for a 6061/ Al_2O_3 /10p sample: a) too short (approx. 1s), b) optimal (between 3 and 5s) and c) too long (more than 5s).

It was possible to achieve an excellent copper deposition for the two PRM materials with copper “islands” with diameters from $1\mu\text{m}$ to $5\mu\text{m}$. On the other hand, for the SFRM resulted that the copper agglomerated around the ceramic fibres and on the intermetallic phases. Nevertheless, the presence of several phases with different grey levels in the SFRM materials (see Paragraph 3.2.4) provided also the contrasts points necessary for the investigations. The distribution of the copper islands for the 10vol% particle reinforced material and for the fibre reinforced material is depicted in Figures 3.30 a), b) and c).

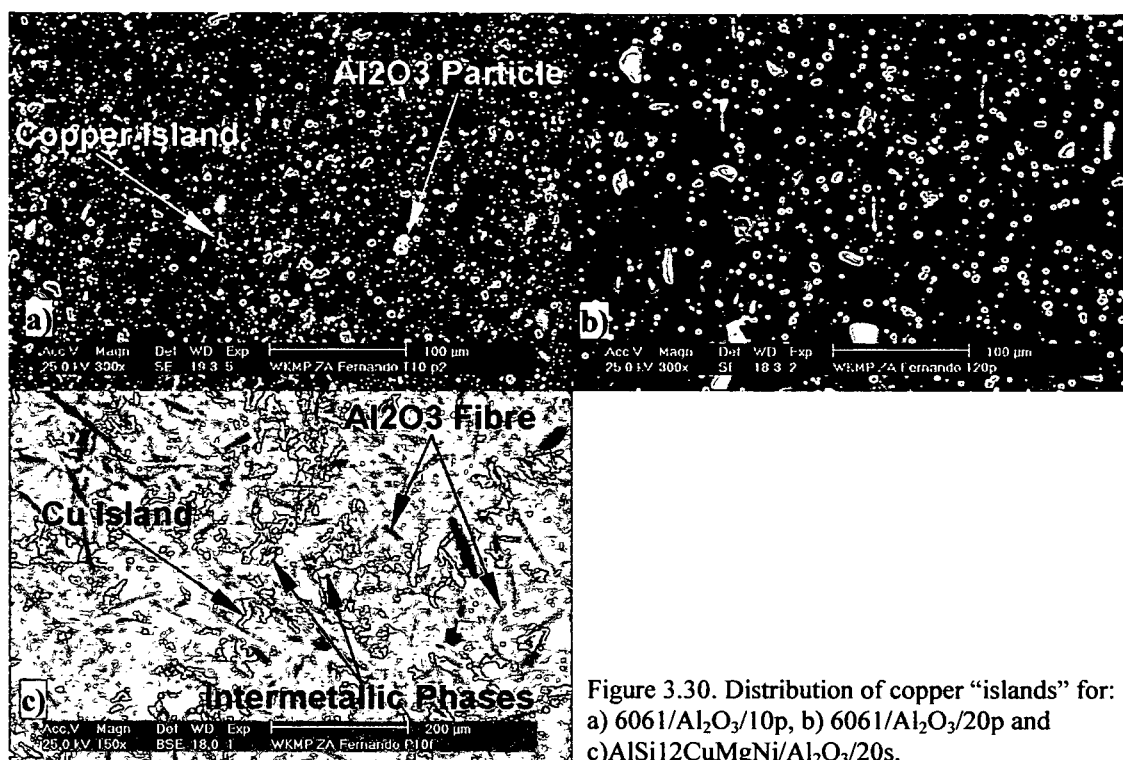


Figure 3.30. Distribution of copper “islands” for: a) 6061/Al₂O₃/10p, b) 6061/Al₂O₃/20p and c) AlSi12CuMgNi/Al₂O₃/20s.

3.4.4 In Situ Tensile/Creep Test inside a SEM

An In Situ stage model 5000N fabricated by Kammrath & Weiss [92] was used for carrying out the creep tests inside a Phillips XL 30 Scanning Electron Microscope. This In Situ stage allows to test samples under tensile and compression load up to 5000N and at temperatures up to 500°C.

Weight	2.4Kg
Maximal load (tensile /compression)	+/- 5000N
Maximal displacement	4mm symmetrical (8mm total)
Speed	0.2 – 25µm/sec
Max. Sample Thickness	5mm
Max. Sample Width	10mm
Max. Sample length	60mm
Motor	30W
Displ. Measurement	LVDT
Load Measurement	Load cell
Temp. Measurement	K thermocouple
Control	Load control Displ. Control Temp. control
Heating system	Electrical resistance

Table 3.8. Technical specifications of In Situ stage model 5000N.

Figure 3.31 a) and b) show the In Situ stage and the In Situ stage already mounted in the SEM, respectively. Table 3.8 gives the main technical specifications of this equipment.

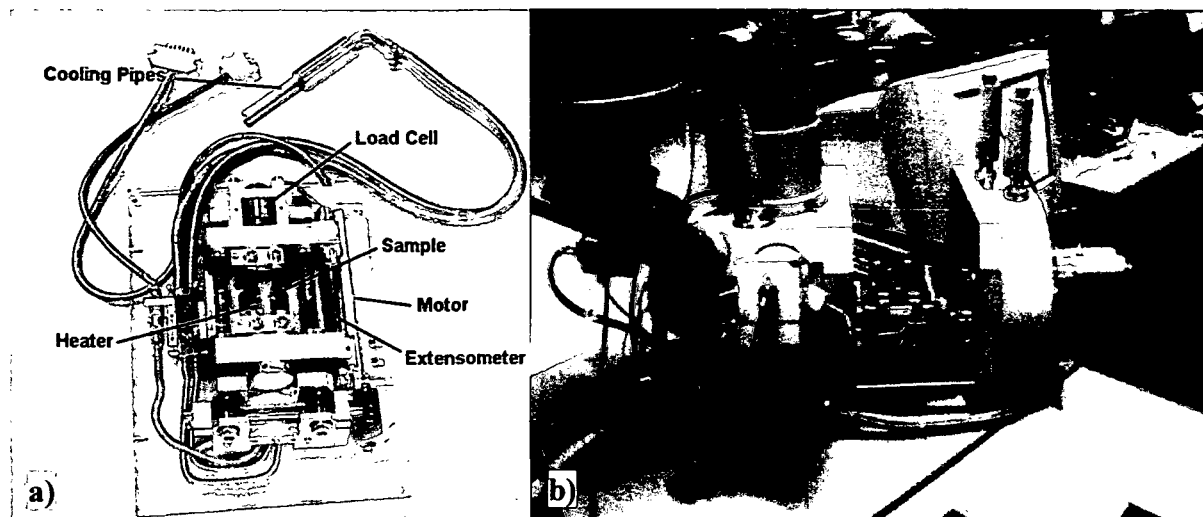


Figure 3.31. a) In Situ stage and components. b) In Situ stage in SEM.

The In Situ stage is digitally controlled using a PID controller connected to a PC. With this device, it is possible to control the temperature, load and displacement during a test.

The heat is transmitted to the sample by means of an electrical heater (Figure 3.32) located under the sample (see Figure 3.31 a)). The heater is constituted by a heating plate connected to the electrical source, a water channel which together with the cooling pipes and an external water pump form the refrigeration system of the stage and a threaded head which in contact with the sample serves as the physical medium to conduct the heat from the heating plate to the sample.

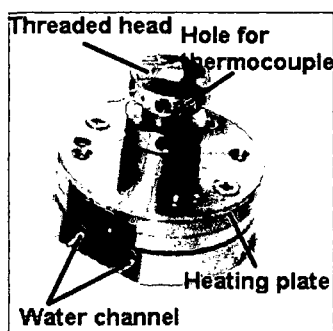


Figure 3.32. Electrical heater.

Two type K thermocouples are provided with the In Situ stage. One of them is used for controlling and the other one for monitoring the temperature. The control thermocouple was inserted in one of the holes shown in Figure 3.32. Thus, the temperature of the heater was controlled. The other thermocouple was welded on the surface of the sample immediately above the contact point between the threaded head and the sample in order to monitor the temperature of the specimen. The difference between these temperatures is depicted in Figure 3.33 a) as a function of time. We can see that at the testing temperature (300°C), there is a difference of 55°C between the temperatures measured by the two thermocouples. A test in order to determine the temperature gradient between the centre and the border of the sample

was carried out. Thus, the monitoring thermocouple was welded to one of the borders of the sample (at 15mm from the centre of the specimen) and the temperature was increased up to 350°C since this is the temperature at which 300°C (the test temperature) are reached at the centre of the specimen. The results are shown in Figure 3.33 b) and we see that there is a temperature gradient of 110°C between the centre and the border of the specimen. This means that the images taken during the creep test must be localized directly at the centre of the specimen in order to guarantee a test temperature of 300°C.

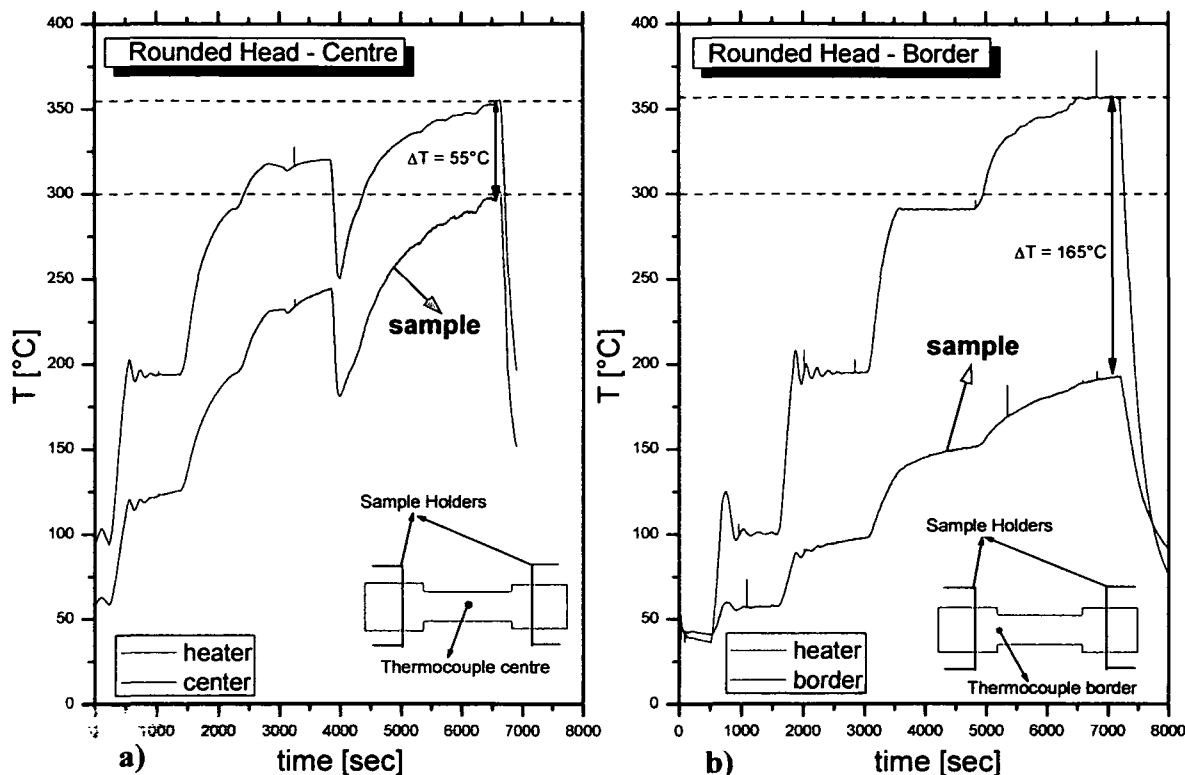


Figure 3.33. a) Difference of temperature between the heater and a thermocouple welded at the centre of the sample. b) Difference of temperature between the heater and a thermocouple welded at the border of the sample.

3.4.4.1 Creep Tests

Figure 3.34 shows schematically the procedure followed for carrying out the creep tests using the In Situ stage. The numbers in the figure represent the positions where pictures were taken for later calculation of the local deformation. After taking a picture in the initial position (1), a preload of 10MPa was applied before heating up the sample (position (2)). After reaching the test temperature (position (3)), the sample was held at this condition during one hour (position (4)). The testing load was applied after reaching this point (position (4')). The creep test was carried until reaching a global deformation of at least 1% (position (5)) and the sample was then cooled down to room temperature (position (6)).

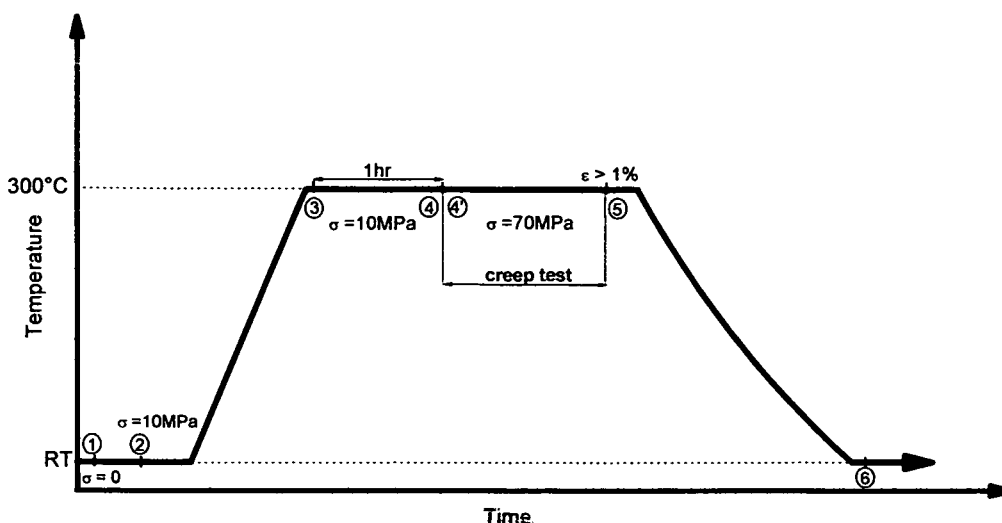


Figure 3.34. Scheme showing the procedure followed for carrying out a creep test using the In Situ stage.

3.4.5 Calculation of the Local Deformation

The software ARAMIS v.4.5.5 developed by G.O.M. G.m.b.H. [93] was used for performing the calculations of the strain fields. The working principle of this software is based on the hypothesis that the distribution of grey values in a squared shaped portion of a picture before deformation corresponds to the distribution of grey values of the same original portion after being subjected to deformation. Thus, to determine the local deformation, the software compares pictures taken in different deformation conditions. The Cu marks produce grey values distinct from those of the original picture, which shall be well distributed over the imaged areas. That is the reason why the deposition of copper islands on the investigated samples is necessary (see paragraph 3.4.3) to identify the previously mentioned squared shaped portions (facets).

The first thing to do performing the calculations is to define the two pictures which correspond to the two different deformation conditions to be compared. The first one will be used as the reference condition. The next step is to divide the reference picture in the desired amount of facets of a certain size in pixels. A grid is then generated on the picture and the central point of each facet (centre of gravity) is identified. This is shown as an example in Figure 3.35. In order to start with the calculations, the program needs a starting point. This means that the user has to find a point (pixel) of the picture in the deformed stage that corresponds to a point (pixel) of the reference picture. Thus, the software recognizes the initial deformed facet and continues recognizing the other ones together with their gravity centres using its internal algorithm. After this, the software is ready to calculate the displacement of the gravity centres between the two pictures and with this the local deformation of the tested sample.

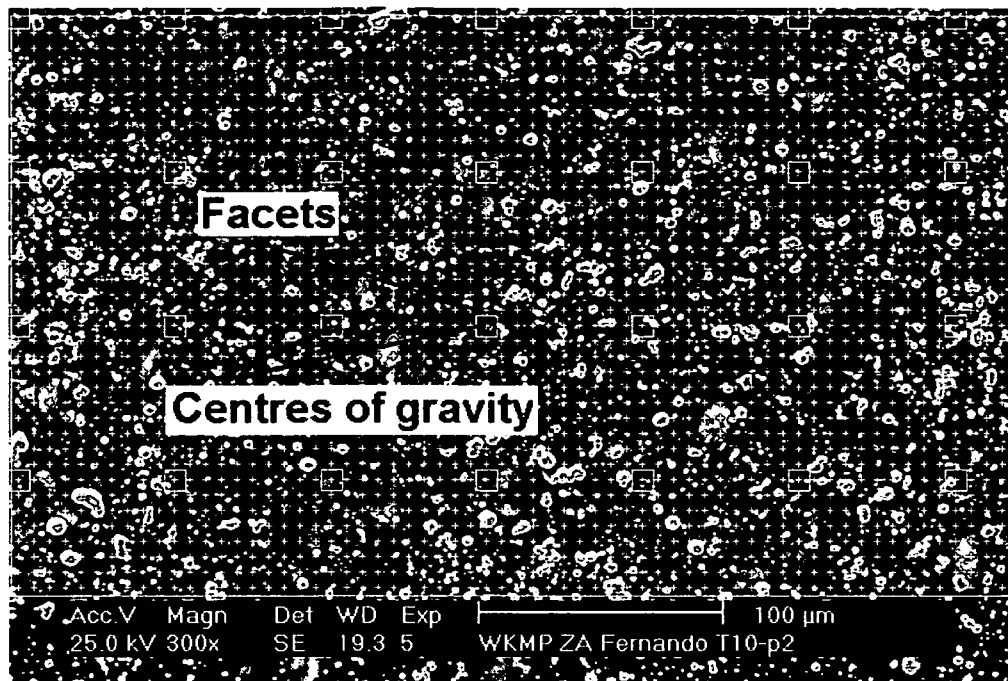


Figure 3.35. Facets and gravity centres generated in a reference picture.

3.5 Microscopy

The microstructure before and after testing as well as the damage analysis together with strain evolution (In Situ tests) was investigated using both a Phillips XL30 Scanning Electron Microscope and/or a Zeiss Axioplan light microscope with an integrated digital camera. The qualitative analysis of the elements present in the different phases contained in the investigated materials was performed using an Energy Dispersive X-Ray (EDX) analysis device provided by EDAX and attached to the SEM.

3.6 Young's Modulus Analysis

The determination of the Young's Modulus as well as its dependence on the temperature was performed using a Dynamic Mechanical Analysis (DMA) device developed by TA Instruments [94] model DMA 2980. The experiments were conducted using a 3 point bending configuration in a temperature range from 25 to 350°C. The frequency and the amplitude used during the tests was 1Hz and 50μm, respectively. The sample dimensions were 50x4x2mm³.

4 Modelling

4.1 The Eshelby's Method Applied to Strain Evolution in Thermal Cycling Creep (TCC)

The model developed by Eshelby in order to estimate different properties of discontinuously reinforced MMC [35, 95] will be used in the present section to study the nature of strain evolution during thermal cycling of the 6061/Al₂O₃/22p PRM. The experimental work was carried out during the PhD thesis of Peter Prader [2,3] at the Vienna University of Technology. A detailed description of the Eshelby's method can be found in [17] and has been partially transcribed in Appendix A. When using this approximation we must keep in mind that the Eshelby's model can only be applied if the behaviour of the material is fully elastic.

4.1.1 Brief Introduction to TCC

The only difference in the experimental conditions between isothermal and TCC tests is the applied temperature profile during the course of the experiment. As it is known, the temperature and the mechanical load are held constant during an isothermal creep test, while for TCC a temperature profile is applied to the sample and can present different shapes such as rectangular or, like in our case, triangular. The initial strain ϵ_0 due to constant external load is eliminated. The relative elongation of the sample is measured and contrarily to isothermal creep, the deformation can be due to 4 different effects: (1) thermal elongation produced due to the change of the temperature during test, (2) variation of elastic properties of the material since they change with temperature, (3) internal stresses due to mismatch in thermal expansion and (4) creep mechanisms.

Figure 4.1 shows the temperature and load profiles applied as well as the corresponding variation of total strain ϵ_{tot} and the plastic elongation ϵ_{tcc} during one of the tests carried out in [2]. The purpose of this figure is to show that during each thermal cycle an incremental amount of plastic strain ϵ_{tcc} is developed but superimposed to the thermal elongation ϵ_{th} , the elastic elongation produced by the variation of the elastic properties of the material $\epsilon_{\Delta E}$ and the elastic strain produced by the internal stresses $\epsilon_{\sigma i}$. Thus,

$$\epsilon_{tcc} = \epsilon_M - \epsilon_{th} - \epsilon_{\Delta E} - \epsilon_{\sigma i} \quad (4.1)$$

where ϵ_M is the strain measured during the test. Therefore, the values of the elastic strains must be calculated in order to obtain the effective elongation of the sample during the test. This does not present big difficulties for ϵ_{th} and $\epsilon_{\Delta E}$ if the values of CTE and Young's modulus (together with their variation with temperature) are available. On the other hand, the calculation of $\epsilon_{\sigma i}$ will require deeper analysis of the material properties since it will depend on the properties of the matrix and the reinforcement phase and the interaction between them while changing the temperature.

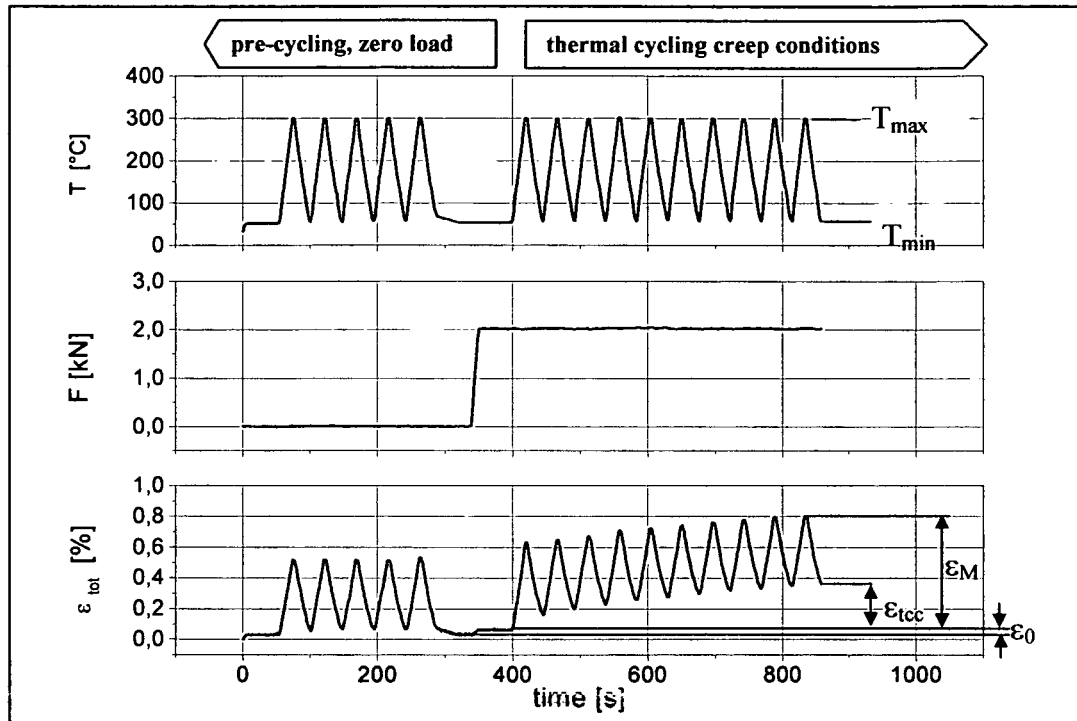


Figure 4.1. Example of TCC test showing the difference between the measured strain ϵ_M and the effective plastic strain ϵ_{tcc} .

4.1.2 Experimental Conditions and Results

The TCC tests were conducted on 6061/Al₂O₃/22p T6-S using a Gleeble 1500 apparatus developed by Dynamic Systems Incorporated (DSI), Poestenkill, USA [96] which combines full resistance heating thermal capabilities and hydraulic servomechanical testing performance in a single system. Specimens were subjected to triangular thermal cycles between 50°C and 300°C using a heating/cooling rate of 12.5K/s and a holding time of 3s (see Figure 4.1). Constant mechanical tensile load was applied corresponding to initial stresses of $\sigma_0 = 40$ and 80MPa, respectively.

Figure 4.2 and Figure 4.4 show the ϵ_M obtained during tests conducted at 40MPa and 80MPa, respectively. The analysis explained in Paragraph 4.1.1 has to be applied to these results in order to obtain the actual values of plastic strain ϵ_{tcc} . This was done for the whole

curves but three cycles at the beginning, $\frac{1}{4}$, $\frac{3}{4}$ and at the end of the test (see Figure 4.3 and Figure 4.5) were specially analysed in order to achieve not only a qualitative but also a quantitative comprehension of the concepts involved.

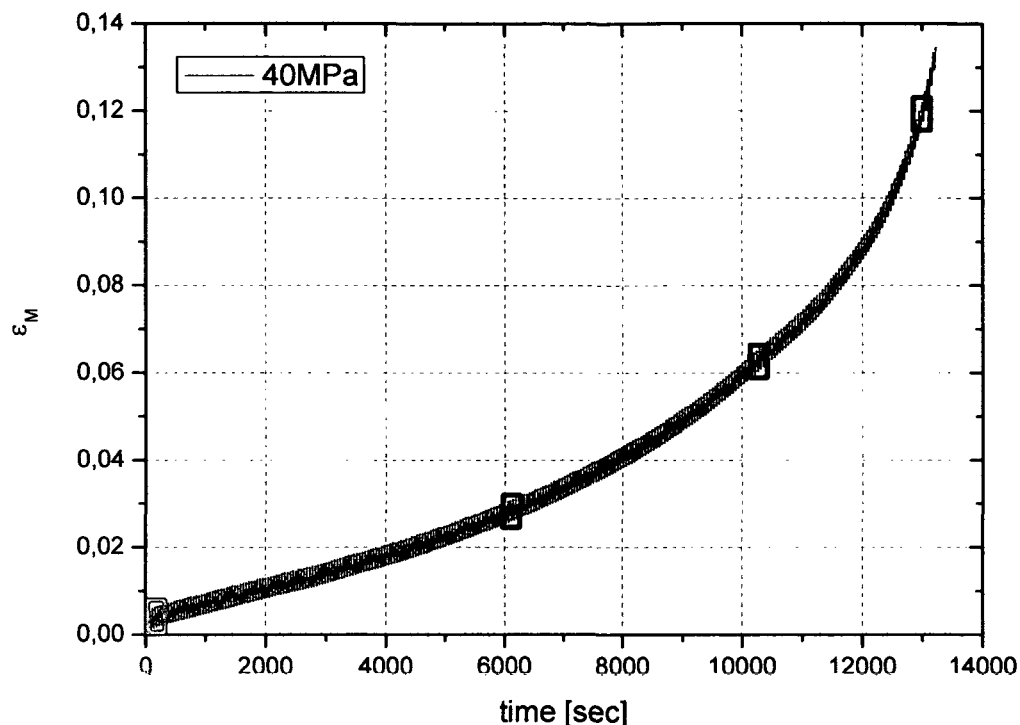


Figure 4.2. ε_M obtained during a TCC test carried out at 40MPa. The rectangles show the regions that were studied in detail (see Figure 4.3).

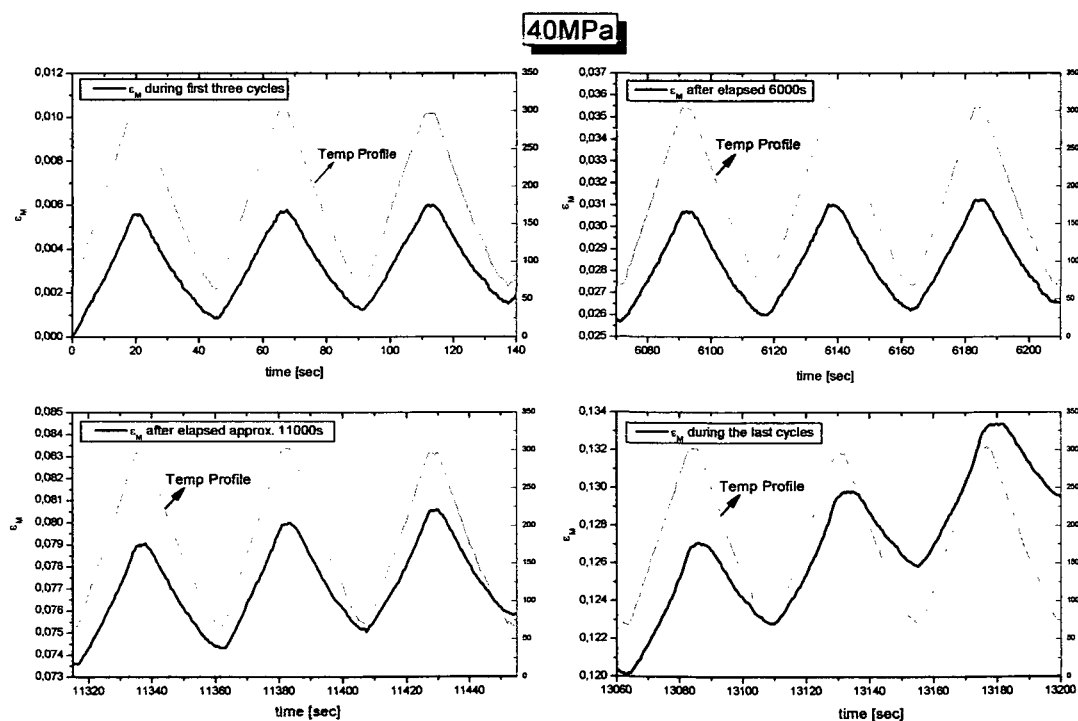


Figure 4.3. Detail of ε_M obtained during different stages of a TCC at 40MPa. The temperature profile is also shown.

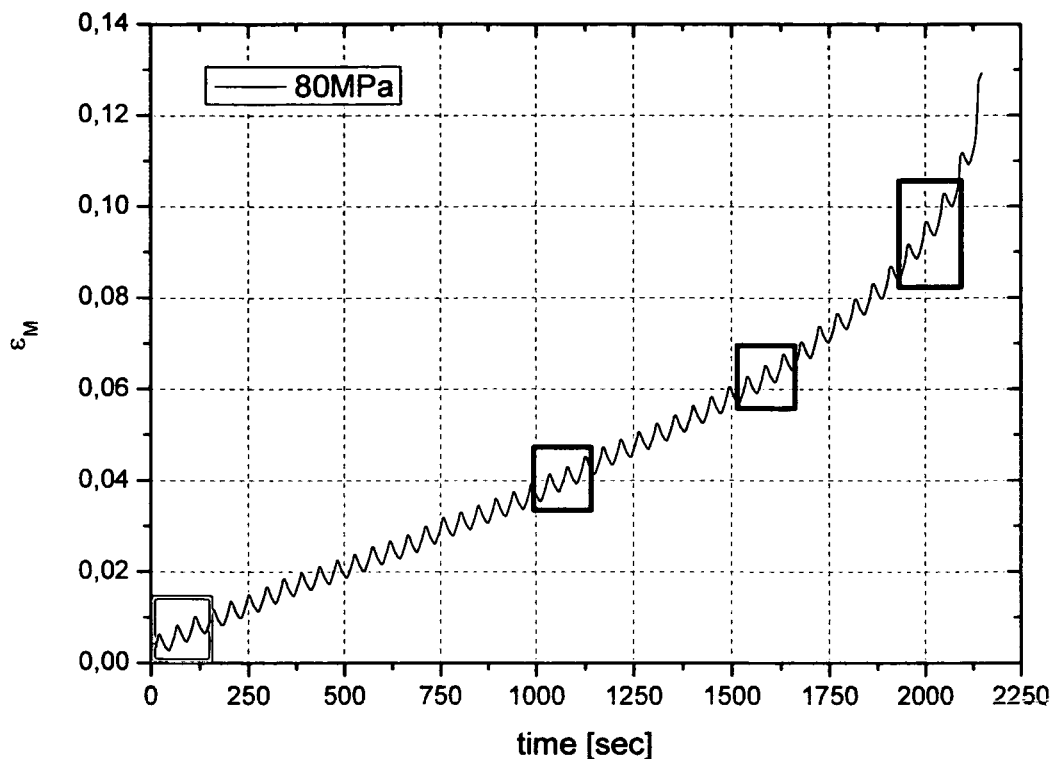


Figure 4.4. ε_M obtained during a TCC test carried out at 80MPa. The rectangles show the regions that were studied in detail (see Figure 4.5).

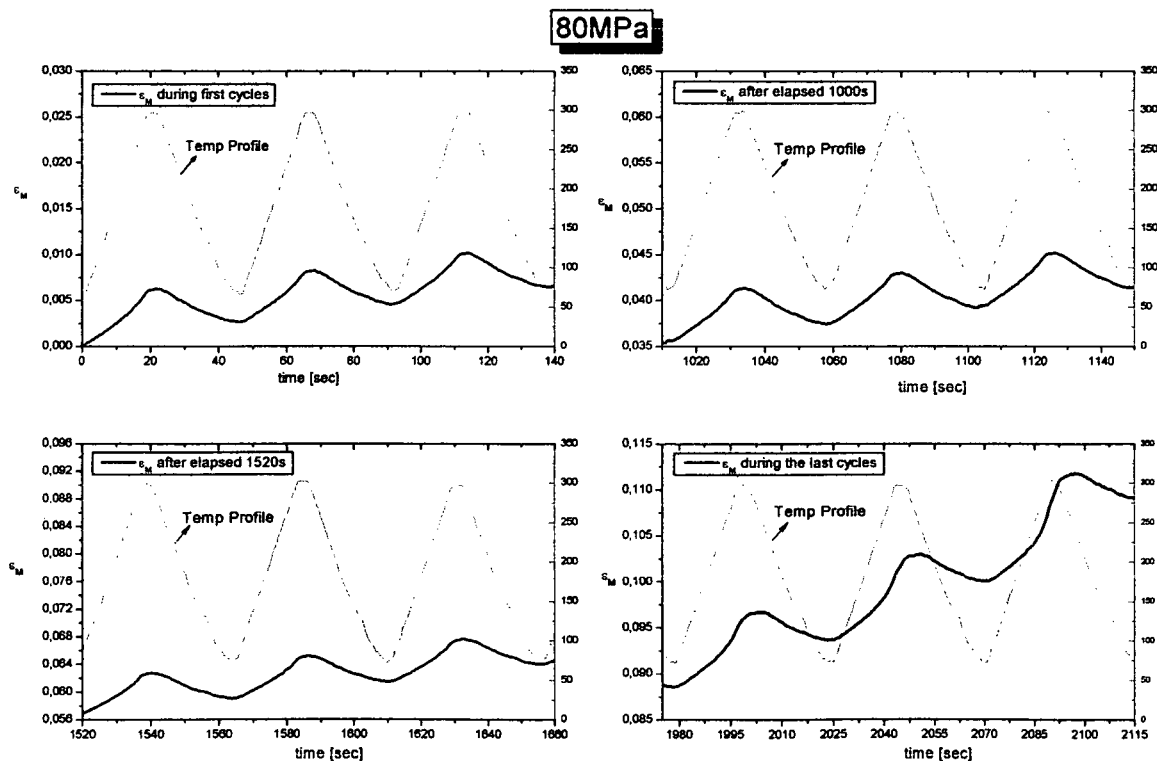


Figure 4.5. Detail of ε_M obtained during different stages of a TCC at 80MPa. The temperature profile is also shown.

4.1.3 Thermal elongation and contraction ε_{th}

The thermal elastic deformation produced due to the change of temperature along the temperature cycles was calculated using the instantaneous coefficient of thermal expansion of the material (CTE) according to the simple following relationship:

$$\varepsilon_{th} = \alpha_c \cdot \Delta T \quad (4.2)$$

where α_c is the instantaneous CTE of the composite and ΔT is the temperature change along the cycle. The experimental values of the instantaneous CTE were taken from [97] and are shown in Figure 4.6 in a temperature range between 20°C to 300°C.

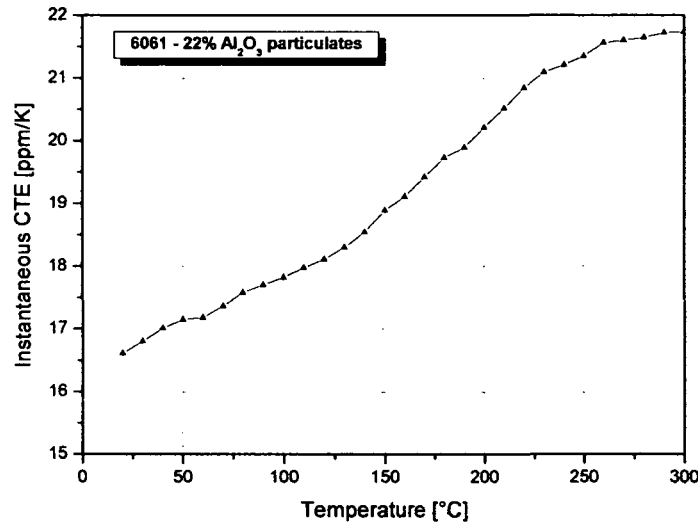


Figure 4.6. Instantaneous CTE for the PRM according to [97].

This curve was then fitted using a grade 3 polynomial resulting in the following equation:

$$\alpha_c(T) = 16.95519 - 0.00864 \cdot T + 2.11088 \cdot 10^{-4} \cdot T^2 - 4.28094 \cdot 10^{-7} \cdot T^3 \quad (4.3)$$

$$R^2 = 0.99629$$

4.1.4 Elastic Deformation due to Variation of Young's Modulus with Temperature $\varepsilon_{\Delta E}$

Due to the thermal cycles and the dependence of Young's modulus on temperature, the Hooke's law has to be modified according to the following equation:

$$\varepsilon_{\Delta E} = \sigma_A \cdot \left(\frac{1}{E_0} - \frac{1}{E(T)} \right) \quad (4.4)$$

where σ_A is the external stress, E_0 the Young's modulus of the composite at a reference temperature (in our case 25°C) and $E(T)$ is the Young's modulus as a function of the temperature.

The variation of the E modulus with temperature was considered to be linear throughout the investigated temperature range and was interpolated between room temperature and 300°C for the values obtained in [2] and shown in Table 4.1.

T [°C]	E [GPa]
25	94
300	69

Table 4.1. Young's modulus of the PRM at room temperature and at 300°C.

Thus, the linear equation used for the calculations was:

$$E_c(T) = -0.0909 \cdot T + 96.273 \quad (4.5)$$

4.1.5 Elastic Strain Produced by Internal Stresses ε_{ith}

The formation of internal stresses in a material depends not only on its constituents but also on its history (processing, thermal treatments, etc.). With the use of the Eshelby's model, it is possible to determine the internal stresses produced due to thermal effects and/or external forces within the elastic region of the composite.

One of the central points of the calculations using this method is the right choice of the Eshelby's tensor S (see Annex A). Its determination can be done taking into account the aspect ratio of the reinforcement and the Poisson's modulus of the matrix. The analytic solution of the S tensor is only possible for simple shapes of the reinforcement phases [17]. In our case, the reinforcement presents an alignment in the direction of the extrusion axis which coincides with the load direction (see Figure 3.2 b) and although the particles have an irregular shape, but elongated in the load direction, they were considered as ellipsoids in the calculation. For this case, the S tensor is:

$$S = \frac{4 \cdot Q}{3} + R \cdot I_3 + 2 \cdot s^2 \cdot T \quad (4.6)$$

where,

$$Q = \frac{3}{8 \cdot (1 - \nu)}, R = \frac{1 - 2 \cdot \nu}{8 \cdot (1 - \nu)}, T = Q \cdot \frac{4 - 3 \cdot I_1}{3 \cdot (s^2 - 1)}, I_3 = 4 - 2 \cdot I_1, \\ I_1 = \frac{2 \cdot s}{(1 - s)^{\frac{2}{3}}} \cdot (s \cdot (s^2 - 1)^{\frac{1}{2}} - \cosh^{-1} s) \quad (4.7)$$

in which s is the aspect ratio of the reinforcement and ν the Poisson's modulus of the matrix.

According to the cutting and welding exercise introduced by Eshelby (See Figure A.1), we can consider a differential thermal contraction or expansion misfit produced by a temperature change dT in the composite as a shape change ε^{T*} . Thus,

$$d\varepsilon^r = (\alpha_l(T) - \alpha_m(T)) \cdot dT \quad (4.8)$$

where α_l is the CTE of the inclusion and α_m the CTE of the matrix both as a function of the temperature. From Equation A.6 (we write it here again for a better clarity of the procedure), the deformation of the ghost inclusion $\varepsilon_{\Delta T}^T$ for a differential temperature drop can now be estimated as

$$\varepsilon_{\Delta T}^T = -\left\{(\mathbf{C}_M - \mathbf{C}_I) \cdot [\mathbf{S} - \mathbf{f} \cdot (\mathbf{S} - \mathbf{I}) - \mathbf{C}_M]\right\}^{-1} \cdot \mathbf{C}_I \cdot \varepsilon^T \quad (\text{A.6})$$

$$d\varepsilon_{\Delta T}^T = -\left\{(\mathbf{E}_M(T) - \mathbf{E}_I(T)) \cdot [\mathbf{S} - \mathbf{f} \cdot (\mathbf{S} - \mathbf{I})] - \mathbf{E}_M(T)\right\}^{-1} \cdot \mathbf{E}_I(T) \cdot (\alpha_I(T) - \alpha_M(T)) \cdot dT \quad (4.9)$$

where

$E_M(T)$ = Young's modulus of the matrix as a function of temperature

$E_I(T)$ = Young's modulus of the inclusion as a function of temperature

\mathbf{I} = identity matrix

f = reinforcement volume fraction

Combining the equations for the mean stress in the matrix and the reinforcement with Equation (4.9) and integrating between $T_0 = 50^\circ\text{C}$ and $T_f = 300^\circ\text{C}$ we obtain that:

$$\langle \sigma \rangle_M = -\mathbf{f} \cdot \mathbf{C}_M (\mathbf{S} - \mathbf{I}) \cdot \varepsilon^T \quad (\text{A.17})$$

$$\langle \sigma \rangle_I = (\mathbf{1} - \mathbf{f}) \cdot \mathbf{C}_M \cdot (\mathbf{S} - \mathbf{I}) \cdot \varepsilon^T \quad (\text{A.18})$$

$$\langle \sigma \rangle_{Mith}(T) = \int_{T_0}^{T_f} \mathbf{f} \cdot \mathbf{E}_M(T) \cdot (\mathbf{S} - \mathbf{I}) \cdot \left\{(\mathbf{E}_M(T) - \mathbf{E}_I(T)) \cdot [\mathbf{S} - \mathbf{f} \cdot (\mathbf{S} - \mathbf{I})] - \mathbf{E}_M(T)\right\}^{-1} \cdot \mathbf{E}_I(T) \cdot (\alpha_I(T) - \alpha_M(T)) \cdot dT \quad (4.10)$$

$$\langle \sigma \rangle_{lith}(T) = -\int_{T_0}^{T_f} (\mathbf{1} - \mathbf{f}) \cdot \mathbf{E}_M(T) \cdot (\mathbf{S} - \mathbf{I}) \cdot \left\{(\mathbf{E}_M(T) - \mathbf{E}_I(T)) \cdot [\mathbf{S} - \mathbf{f} \cdot (\mathbf{S} - \mathbf{I})] - \mathbf{E}_M(T)\right\}^{-1} \cdot \mathbf{E}_I(T) \cdot (\alpha_I(T) - \alpha_M(T)) \cdot dT \quad (4.11)$$

We still have to consider the effects on the internal stresses produced by the external load. According to (A.16):

$$d\varepsilon_{\sigma A}^T = -\left\{(\mathbf{E}_M(T) - \mathbf{E}_I(T)) [\mathbf{S} - \mathbf{f} \cdot (\mathbf{S} - \mathbf{I})] - \mathbf{E}_M(T)\right\}^{-1} \cdot (\mathbf{E}_M(T) - \mathbf{E}_I(T)) \cdot \frac{\sigma^A}{\mathbf{E}_M(T)} \quad (4.12)$$

where σ^A is the applied load. Then, integrating between T_0 and T_f , as we did above, yields

$$\langle \sigma \rangle_{M\sigma A}(T) = \int_{T_0}^{T_f} \mathbf{f} \cdot \mathbf{E}_M(T) \cdot (\mathbf{S} - \mathbf{I}) \cdot \left\{(\mathbf{E}_M(T) - \mathbf{E}_I(T)) \cdot [\mathbf{S} - \mathbf{f} \cdot (\mathbf{S} - \mathbf{I})] - \mathbf{E}_M(T)\right\}^{-1} \cdot (\mathbf{E}_M(T) - \mathbf{E}_I(T)) \cdot \frac{\sigma^A}{\mathbf{E}_M(T)} \cdot dT \quad (4.13)$$

$$\langle \sigma \rangle_{I\sigma A}(T) = -\int_{T_0}^{T_f} (\mathbf{1} - \mathbf{f}) \cdot \mathbf{E}_M(T) \cdot (\mathbf{S} - \mathbf{I}) \cdot \left\{(\mathbf{E}_M(T) - \mathbf{E}_I(T)) \cdot [\mathbf{S} - \mathbf{f} \cdot (\mathbf{S} - \mathbf{I})] - \mathbf{E}_M(T)\right\}^{-1} \cdot (\mathbf{E}_M(T) - \mathbf{E}_I(T)) \cdot \frac{\sigma^A}{\mathbf{E}_M(T)} \cdot dT \quad (4.14)$$

Finally, we can approximate the deformation due to internal stresses using the rule of mixtures as

$$\varepsilon_{\sigma I} = (\mathbf{1} - \mathbf{f}) \cdot \frac{\langle \sigma \rangle_M}{\mathbf{E}_M(T)} + \mathbf{f} \cdot \frac{\langle \sigma \rangle_I}{\mathbf{E}_I(T)} \quad (4.15)$$

where

$$\langle \sigma \rangle_M = \langle \sigma \rangle_{Mith} + \langle \sigma \rangle_{M\sigma A} \quad (4.16)$$

$$\langle \sigma \rangle_i = \langle \sigma \rangle_{lith} + \langle \sigma \rangle_{logA} \quad (4.17)$$

The Table 4.2 shows the values of CTE and Young's modulus for the matrix at different temperatures according to [98] and these values were then fitted using a quadratic and a linear equation for the Young's modulus and the CTE, respectively, in order to use them in our calculations resulting in

$$E_m(T) = -2 \cdot 10^{-4} \cdot T^2 + 0.0197 \cdot T + 70.83 \quad (4.18)$$

$$R^2 = 0.9999$$

$$\alpha_m(T) = 0.0185 \cdot T + 19.81 \quad (4.19)$$

$$R^2 = 0.9929$$

T [°C]	E [GPa]	C.T.E. [$10^{-6}K^{-1}$]
50	71.38	20.51
100	71.05	21.66
150	69.83	22.72
200	67.74	23.69
250	64.77	24.57
300	60.92	25.36
350	56.18	26.06
400	50.57	26.66
450	44.08	27.18
500	36.75	27.61

Table 4.2. Young's Modulus and CTE for different Temperature values for the 6061 matrix alloy according to [98].

The values of CTE and Young's modulus for the reinforcement were considered constant in the studied temperature range using values extracted from [2]

$$\alpha_l = 8.5 \text{ ppm/K}$$

$$E_l = 430 \text{ GPa}$$

4.1.6 Determination of the Plastic Deformation during TCC tests

The evolution of plastic deformation during the TCC tests shown in Figure 4.2 and Figure 4.4 was then calculated using Equations (4.1), (4.2), (4.4) and (4.15) and the results are shown in Figure 4.7 to Figure 4.14 for the regions depicted in Figure 4.3 and in Figure 4.5. The regions of the cycles where the temperature is above approximately 240°C produce the

largest amount of thermal and athermal plastic deformation for both loads. This means that the calculations carried out using the Eshelby's method can not be applied for these zones but during the rest of the test they may reflect the actual strain evolution. Actually, for Al alloys the temperature at which the creep effects are observable is approximately 100°C but it seems that the heating/cooling rate during the thermal cycles is too high to allow deformation by creep mechanisms. We see that the subtraction of an elastic strain due to internal stresses reduced in more than 50%, for the worst case (beginning of the 40MPa), the negative creep observed in [2, 3]. A more realistic calculation of the elastic deformation introduced by internal stresses (e.g. taking into account the real reinforcement shape, reinforcement distribution, etc.) would eliminate this periods of reverse creep.

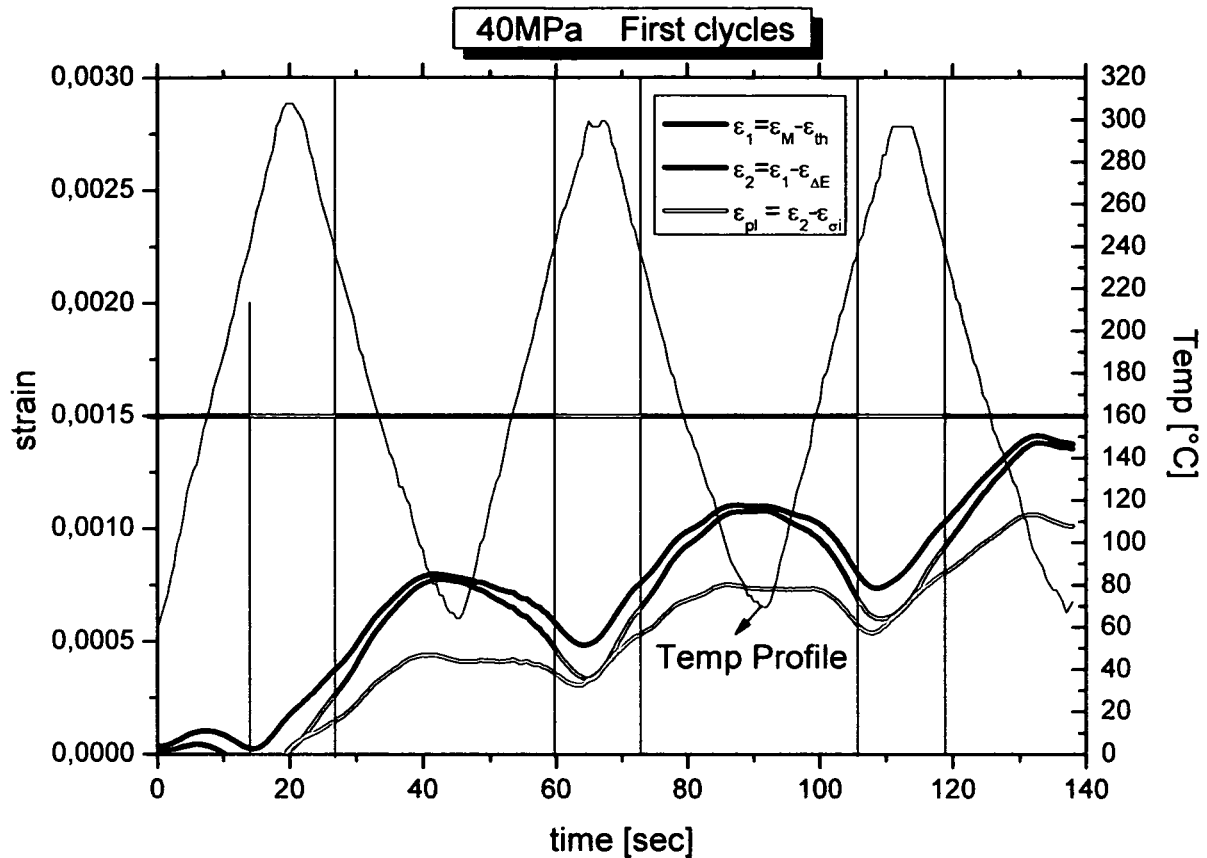


Figure 4.7. ϵ_{pl} evolution during the first cycles of a TCC test with $\sigma_A = 40\text{MPa}$.

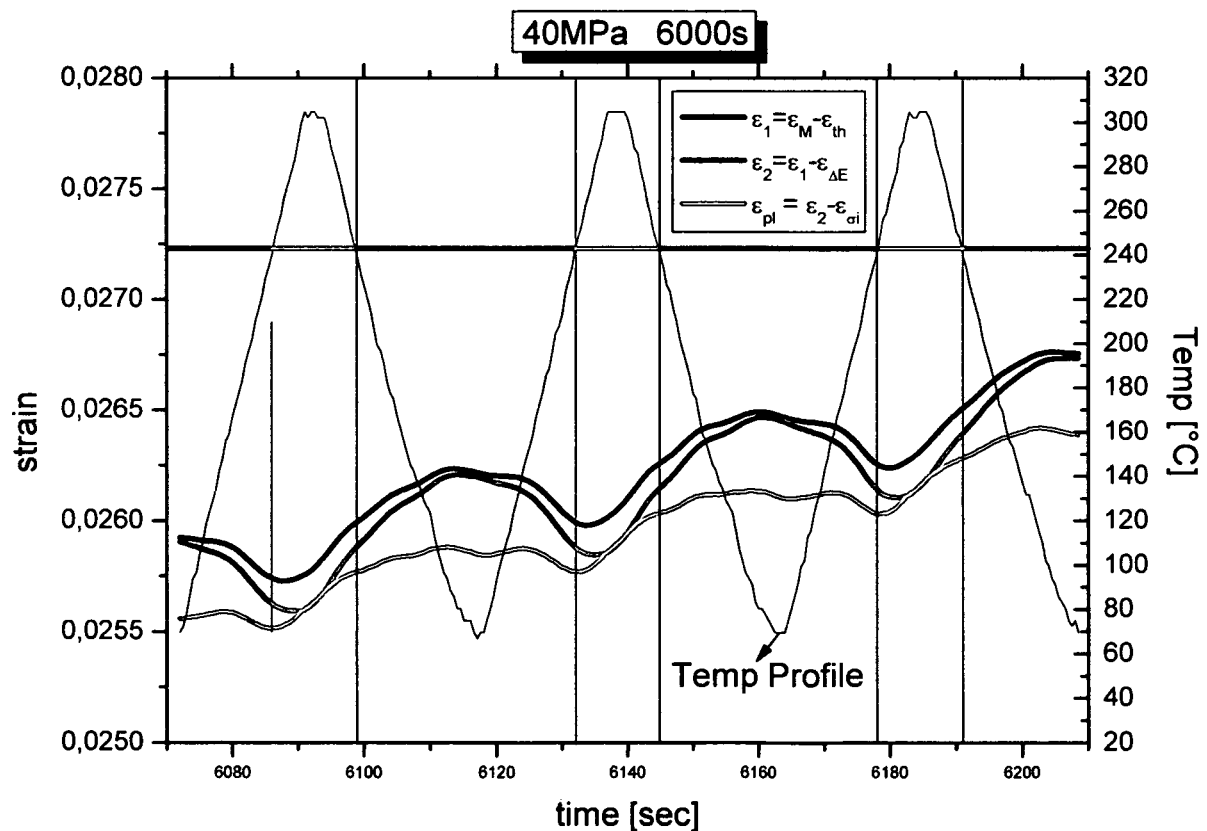


Figure 4.8. ϵ_{pl} evolution after 6000s of a TCC test with $\sigma_A = 40\text{MPa}$.

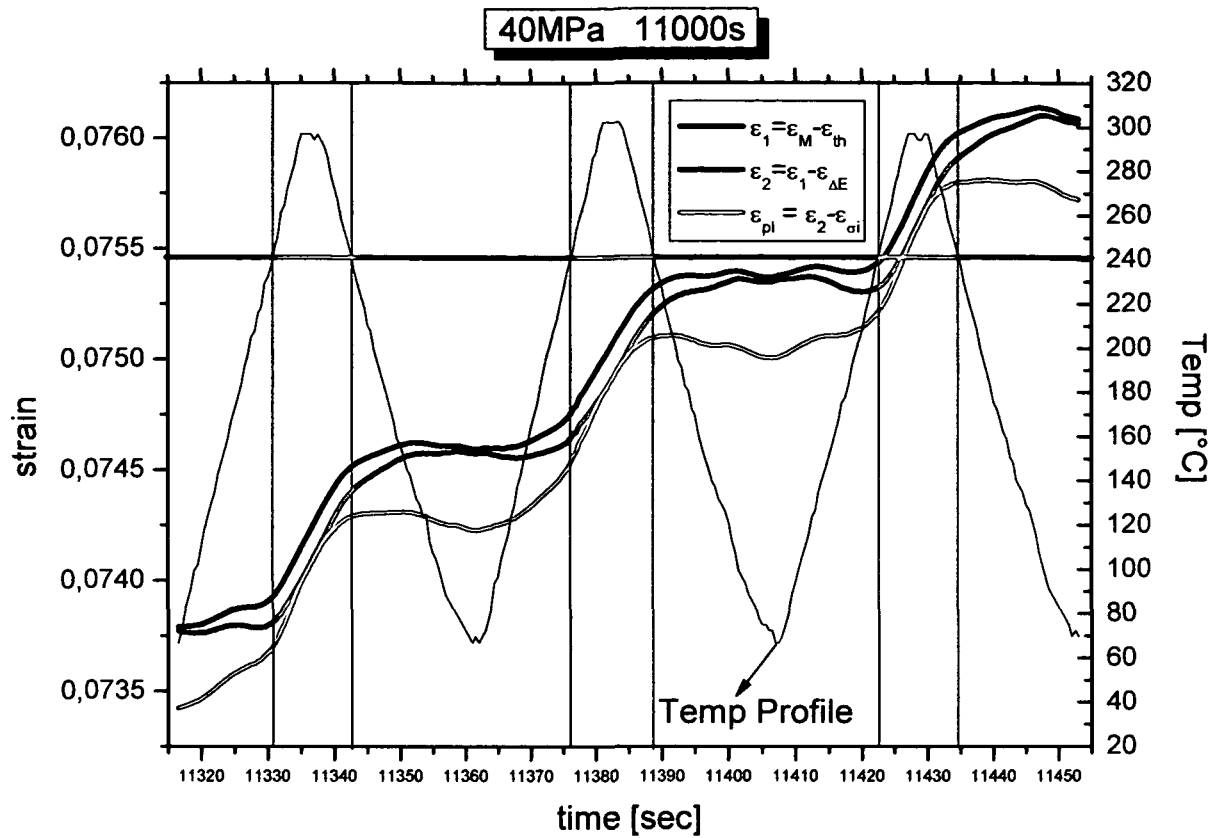


Figure 4.9. ε_{pl} evolution after 11000s of a TCC test with $\sigma_A = 40\text{MPa}$.

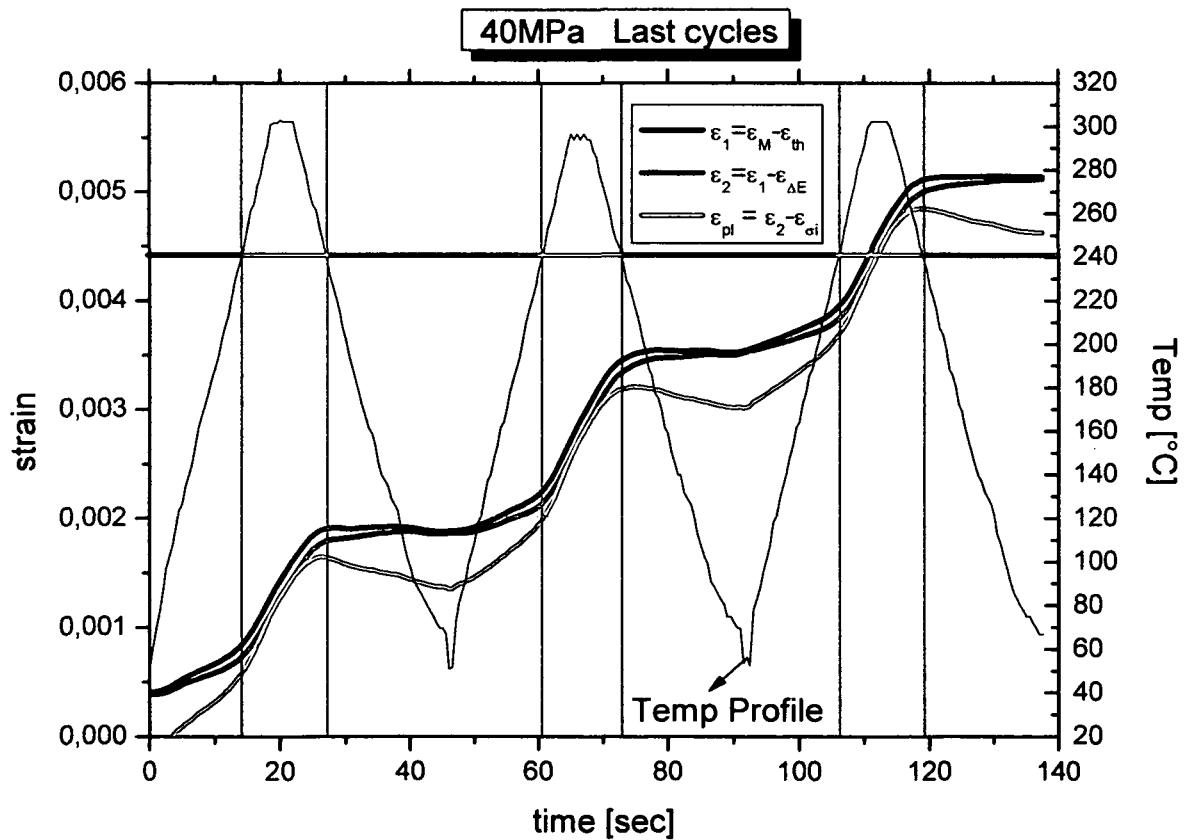


Figure 4.10. ε_{pl} evolution during the last cycles of a TCC test with $\sigma_A = 40\text{MPa}$.

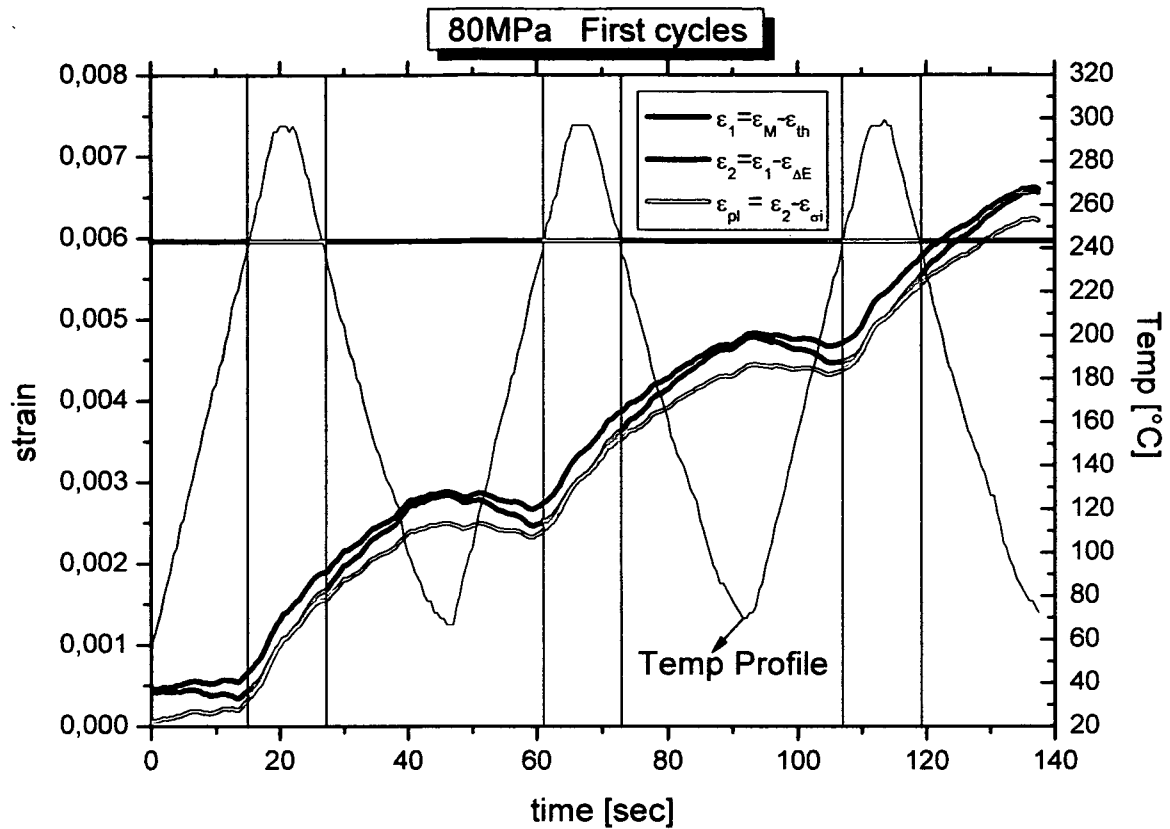


Figure 4.11. ε_{pl} evolution during the first cycles of a TCC test with $\sigma_A = 80\text{MPa}$.

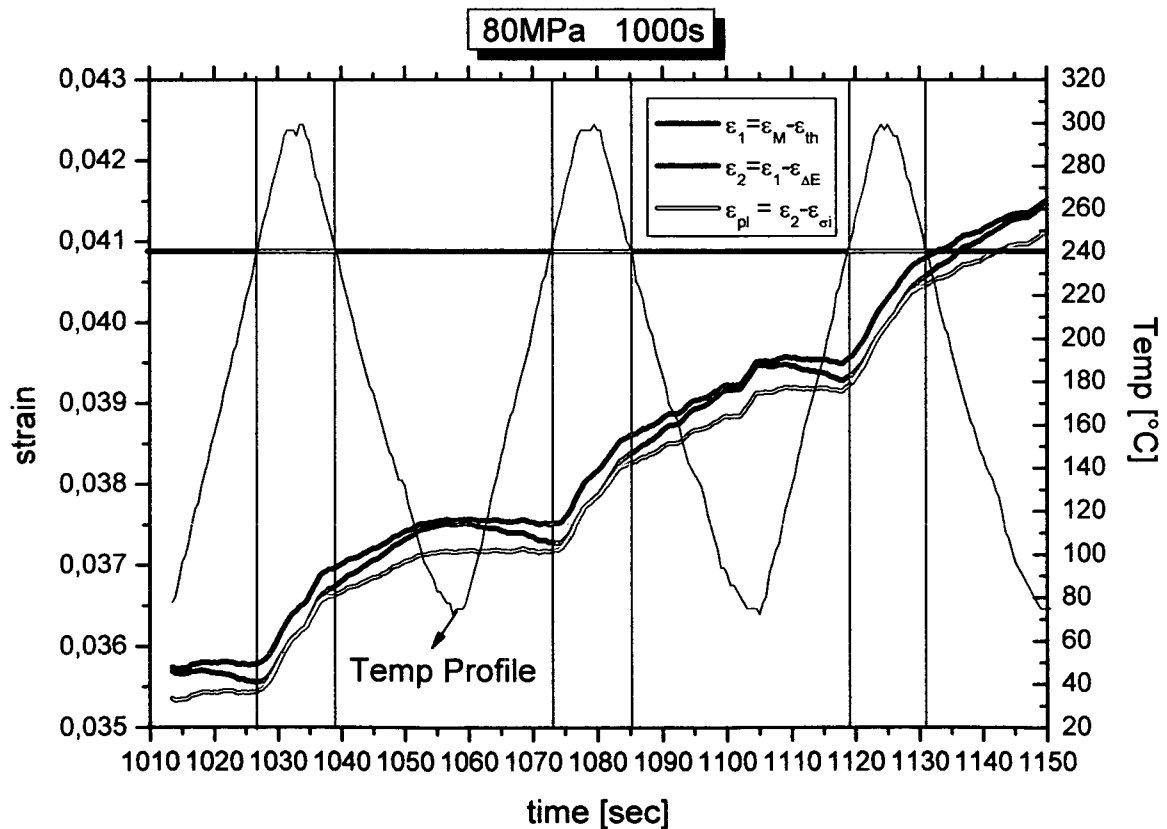


Figure 4.12. ε_{pl} evolution after 1000s of a TCC test with $\sigma_A = 80\text{MPa}$.

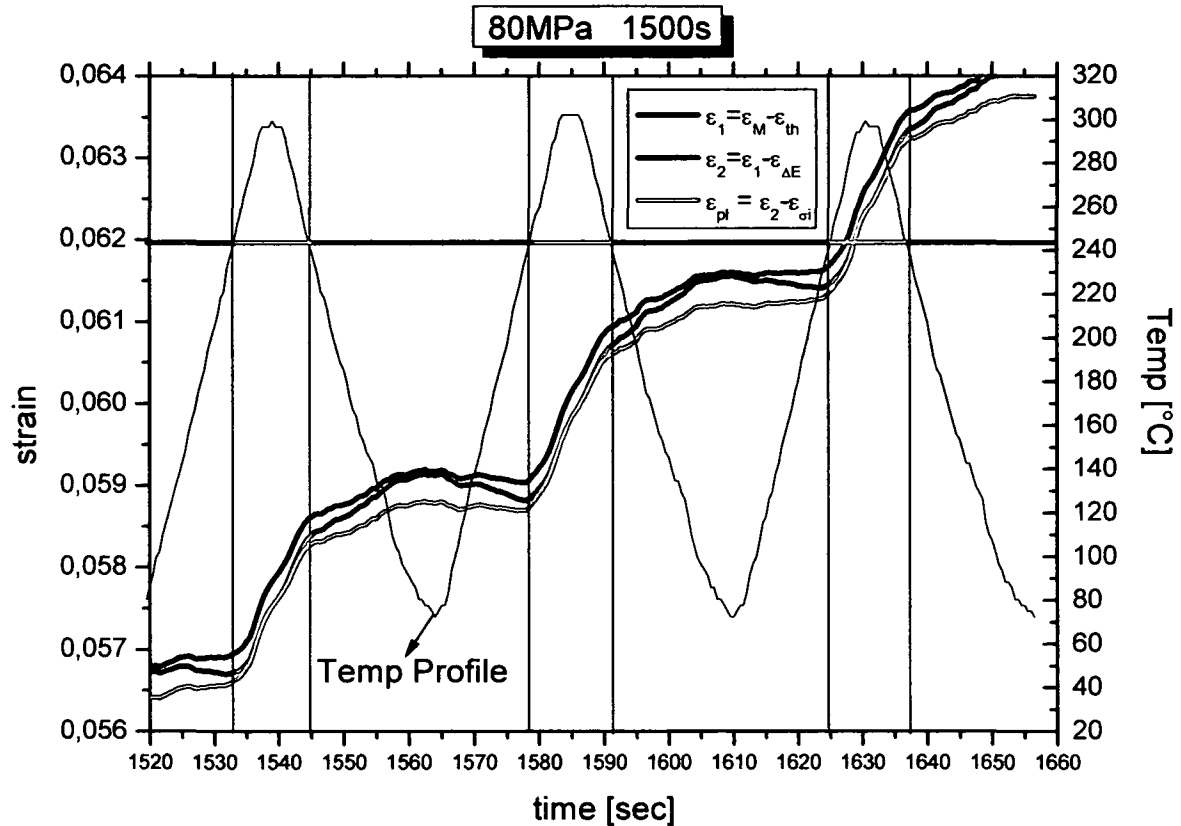


Figure 4.13. ε_{pl} evolution after 1500s of a TCC test with $\sigma_A = 80\text{MPa}$.

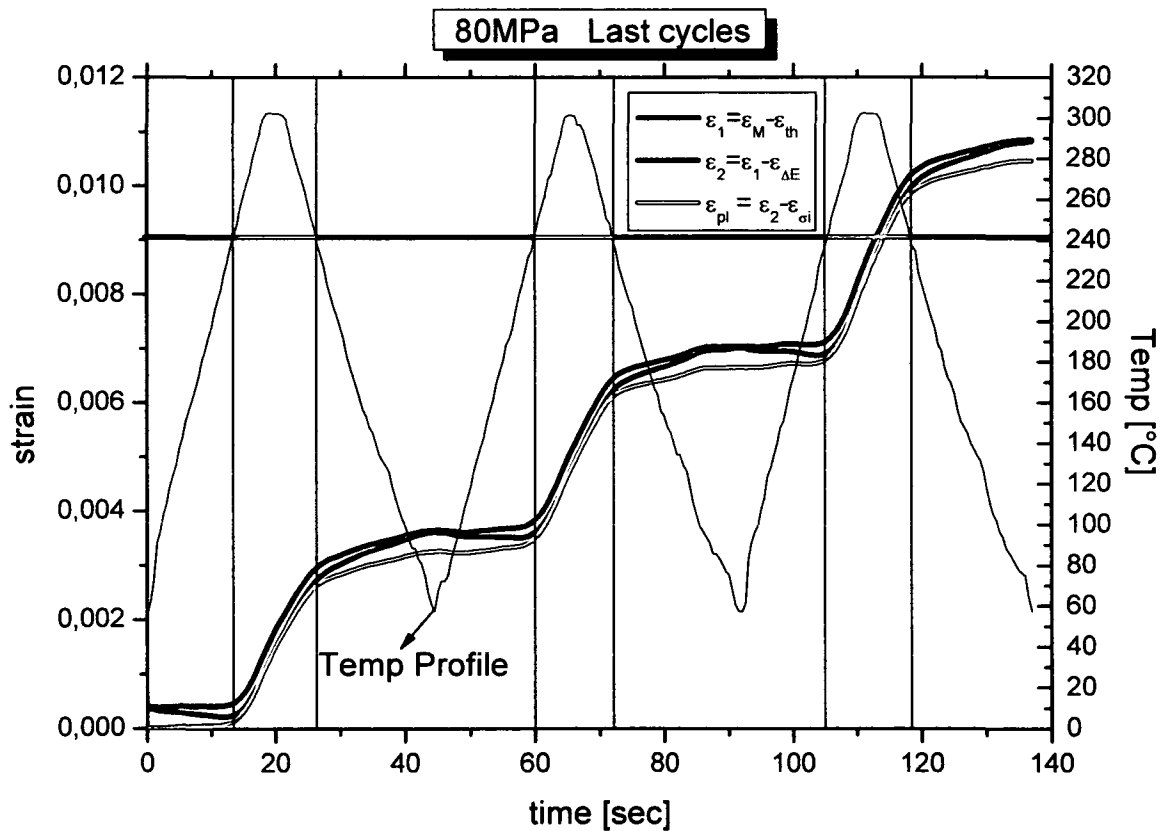


Figure 4.14. ε_{pl} evolution during the last cycles of a TCC test with $\sigma_A = 80\text{MPa}$.

5 Results

5.1 Isothermal Creep

The following sections contain the results obtained for all the investigated materials during the isothermal creep tests described in Paragraph 3.3. These are depicted in form of creep strain ϵ vs exposure time t and strain rate $\dot{\epsilon}$ vs t diagrams.

5.1.1 6061 and 6061/Al₂O₃/22p

The tests were carried at initial stress values of 15, 20, 25, 30, 40, 50, 60 and 70MPa. Figure 5.1 a) to p) and Figure 5.2 a) to q) show the results obtained for the unreinforced 6061 alloy and the 6061/Al₂O₃/20p particle reinforced material, respectively. They exhibit a typical three-stage behaviour with a hardly observable short primary stage and a secondary stage characterised by a minimum creep rate, which then slowly increases until an accelerated increase is reached which is assigned to tertiary creep. The $\dot{\epsilon}$ vs t diagrams show that the shape of the creep curves for both materials is independent of the test load. The reinforced alloy exhibits a less pronounced primary and tertiary creep stage and a higher strain rate than the unreinforced matrix from the beginning of the experiment. The two materials show that after the minimum creep rate has been passed there is a steady increase in the strain rate for all the samples until approximately 50 to 80% of the total lifetime of the specimen has passed. After this, there is a significant acceleration of the strain rate leading to fracture of the specimen. In the case of the unreinforced alloy and stresses smaller than 40MPa (Figure 5.1 a) to h)), about 30-50% of the lifetime is characterised by a more or less constant creep rate. On the other hand, the PRM shows for all the tested stresses that after a minimum creep rate is reached, sudden acceleration in the deformation rate occurs during the last part of the tests (at approx. 80% of the lifetime).

The main characteristic values obtained during the creep tests are summarised in Table 5.1.

Sample	$\dot{\epsilon}_{\min}$ [1/s]	$t_{0.2\%}$ [hr]	$t_{1\%}$ [hr]	ϵ_{rupt} [%]	t_{rupt} [hr]	$t_{2/3}$ [hr]	$\epsilon_{2/3}$ [%]
6061matrix							
0-15-1	1E-9	328	515	40	715	300	0.14
0-15-2	1.1E-9	379	-	-	-	-	
0-20-1	2E-9	173	392.5	-	-	-	
0-20-2	3.2E-9	111.2	339	14.8	397	300	0.4
0-25-1	3E-9	147	306	-	-	250	0.5
0-25-2	2.7E-9	185	282	-	-	230	0.5
0-30-1	5.5E-9	83.5	240	-	-	170	0.5
0-30-2	5.5E-9	100	200	10.2	230	160	0.5
0-40-1	1.1E-13	27.5	157.5	-	-	180	1.5
0-40-2	8.1E-9	51	147	12.3	182	170	2
0-50-1	2.7E-8	16	53.6	-	-	50	1
0-50-3	1.4E-8	28.5	83.5	-	-	110	2.5
0-60-1	5.5E-8	3.4	22	10.7	34	27	1.7
0-60-2	8E-8	5	19	5.6	27.1	21	1.3
0-70-1	1.6E-4	3.2	6.3	5.1	8.5	7.5	1.8
0-70-2	2.5E-7	2.1	6.2	5.7	9.8	8	1.8
6061/Al₂O₃/22p							
22-15-1	5.8E-9	190	570	23.8	2341	1700	3
22-20-1	2.7E-8	16	92.5	-	-	125	1.5
22-20-2	1.9E-8	20.5	125	-	-	150	2.1
22-25-1	3E-8	8	67.4	-	-	110	2
22-25-2	3E-8	19.5	73	-	-	80	1.2
22-30-1	6E-8	8.3	36.4	-	-	-	
22-30-2	5E-8	3	41.4	-	-	-	
22-40-1	1.2E-7	2.1	17.7	-	-	40	4
22-40-3	1.5E-7	3	14	9.5	34.2	23	2.3
22-50-1	3E-7	1.5	7.5	9	18.6	12	2
22-50-2	3E-7	1.5	6	6.1	12	8	2
22-60-1	6.6E-7	0.6	3.2	6	5.1	4	1.3
22-60-2	5.6E-7	0.8	3.6	6.6	6.6	5	1.7
22-70-1	1.6E-6	0.2	1	7.6	1.9	1.4	2

Table 5.1. Characteristic values obtained during isothermal creep tests for the unreinforced 6061 and the particle reinforced 6061/Al₂O₃/22p alloys. The first number in the sample name corresponds to the reinforcement volume fraction, the second one to the applied load and the third to specimen number.

5.1.2 *AlSi12CuMgNi*, *AlSi12CuMgNi/Al₂O₃/10s*, *AlSi12CuMgNi/Al₂O₃/15s* and *AlSi12CuMgNi/Al₂O₃/20s*

Figure 5.3 a) to p), Figure 5.4 a) to t), Figure 5.5 a) to r) and Figure 5.6 a) to h) show the results obtained for the unreinforced and short fibre reinforced cast alloys during the isothermal creep tests with changes of load. The stress during each period is indicated in the diagrams. All the materials show a primary creep stage at the beginning of the test. This stage finishes when a minimum creep rate is reached. At this point the load was changed and it was maintained until a new minimum creep rate at the new load was reached. Figure 5.5 a) and b)

show an ageing period which belongs in fact to periods at 10MPa tensile test where no deformation by creep was observable.

The most remarkable point here is that in the case of the SFRM and for all reinforcement volume fractions, the minimum creep rate achieved after a transient increase of load (e.g. 30MPa \rightarrow 40MPa \rightarrow 30MPa) will be smaller than during the first loading. This effect takes place not only during uninterrupted tests, in which the decrease of load results generally in inverse primary creep, but also after long periods of ageing at the test temperature where classical primary creep is observed.

5.2 Microscopic Analysis

The results obtained by means of scanning electron microscopy of samples after being subjected to isothermal creep for both unreinforced and reinforced wrought and cast alloys are presented in this section. Special attention will be paid to the preferential zones of structural damage initiation such as pores' formation, reinforcement's fracture, interface debonding and damage of the different phases present in these materials.

5.2.1 6061 and 6061/Al₂O₃/22p

Figure 5.7 a) shows a low magnification fracture surface of an unreinforced sample tested at 40MPa. The specimen shows a typical cup and cone fracture with an important necking which is an indication of a ductile failure of this material. Figure 5.7 b) shows the same fracture surface but at higher magnification. It can be seen that it is composed mostly of a fine dimple structure resulting from void growth and coalescence while no cleaved matrix is observable, supporting the previous affirmation of a ductile fracture. Furthermore, the presence of deep large honeycomb structures surrounded by much finer of such structures as found in Figure 5.7 b) is representative of a transgranular fracture [67]. All the described features are observable in all the fractured samples of the unreinforced wrought alloy.

In Figure 5.8 a) and Figure 5.9 a) we can see two fracture surfaces at low magnification of the 6061/Al₂O₃/22p material tested at 15 and 70MPa, respectively. It can be seen that the composite fails in a more brittle manner than the unreinforced alloy as evidenced by the smaller necking effect for the PRM. However, the particle reinforced samples tested at lower stresses show a higher necking than those tested at higher loads.

The fracture surfaces depicted in Figure 5.8 b) and Figure 5.9 b) show the presence of unbroken alumina particles inside the dimples. Broken particles in the fracture surface were hardly observable for all the investigated loads. This suggests that the composite fails by decohesion of the interface between the particles and the matrix and the almost complete

absence of matrix in between the spinel crystals, as shown in Figure 3.4 a), supports this conclusion. The fracture surfaces in the PRM are composed mostly of dimples resulting from void growth and coalescence while cleaved matrix was not observable, indicating thus a ductile failure type. Another remarkable fact observable in Figure 5.8 b) and Figure 5.9 b) is the difference in the size of the dimples between smaller and higher stresses. The dimples in the 15MPa sample appear bigger than the dimples in the 70MPa sample.

Figure 5.10 a) and b) show two longitudinal sections of a 15MPa and a 70MPa PRM specimen, respectively. The vertical axis corresponds to the tensile axis. For the 15MPa sample, cracks connecting more than one particle were generally observed. Individual voids formed around the particles were hardly observable and no cracks were found at a distance larger than about 500 μ m from the fracture surface. Higher stressed samples presented less strain localisation by necking. In the case of the 70MPa sample, the crack initiators were identified as voids which formed at the sharp edges of the alumina particles. A high concentration of individual voids can be observed around the particles up to distances of around 1mm from the fracture surface.

Figure 5.11, Figure 5.12 and Figure 5.13 a) and b) show longitudinal sections of unreinforced samples tested at 70, 40 and 15MPa, respectively. These samples were etched using a KOH solution in order to reveal the presence of Mg_2Si precipitates. It can be observed that the sample subjected to a exposure time of 8.5hr (70MPa) presents a much higher amount of precipitates in comparison with the sample tested at lower loads (exposure time = 210 and 715hr). Furthermore, the size of the precipitates in the sample tested at 70MPa reaches a maximum length of approximately 1 μ m, while the maximum precipitate's length for the sample tested at 40MPa is approximately 2-3 μ m and finally, the sample tested at 15MPa shows coarser Mg_2Si precipitates with a maximum length of approximately 5 μ m which are also much thicker than for shorter exposure times. No precipitates could be observed using the SEM for the case of the unreinforced material prior to testing (T6-S condition). A similar study was conducted on the PRM alloy and the results are shown in Figure 5.14 and Figure 5.15 for samples tested at 60 and 15MPa, respectively. It is observable that the material tested at 60MPa (exposure time = 5.1hr) presents Mg_2Si precipitates of approximately the same size as the matrix tested at 70MPa but the amount of precipitates is markedly larger for the composite. Figure 5.14 a) shows also a precipitates free zone along a grain boundary, effect that could not be observed for the unreinforced matrix. On the other hand, the composite tested at 15MPa (exposure time = 2341hr) shows, similarly to the unreinforced alloy, that the precipitates have grown during the test resulting in coarse particles but, on the contrary to the

matrix material, not only needle shape precipitates were found but also large (approx. 3 μm diameter) rounded precipitates can be observed (see Figure 5.15 b). The precipitates' morphology prior to testing was already shown in Figure 3.3 for the case of the PRM.

5.2.2 *AlSi12CuMgNi*, *AlSi12CuMgNi/Al₂O₃/10s*, *AlSi12CuMgNi/Al₂O₃/15s* and *AlSi12CuMgNi/Al₂O₃/20s*

Figure 5.16 a) and b) show characteristic profiles of fracture surfaces for the unreinforced and fibre reinforced cast alloys. The matrix shows a fracture perpendicular to the load direction with necking. On the other hand, the SFRM shows a fracture with an inclination angle of approximately 45° which is representative for fracture by shear. Results reported by Milicka et al. [99] for compression tests carried out in a short fibre reinforced magnesium alloy using different orientations of the fibres' plane show that the lowest creep resistance for this SFRM corresponds to an orientation angle of 45° respect to the load axis. This may suggest that 45° shear stresses are produced in this kind of composites and the fibres will be able to carry a smaller fraction of these shear stresses if they are oriented parallel to this plane than for other fibres' plane orientation. No necking was observable in the composite material for all the investigated volume fractions. Figure 5.18 to Figure 5.22 show micrographs of the cross section A-A sketched in Figure 5.17. It is observable that the fibres' plane presents an inclination angle between 0-45° considered respect to the horizontal axis of section A-A.

Figure 5.23 a) and b) show the fracture surface of a matrix sample fractured at 40MPa (see Figure 5.3 g) and h)). It is characterised by a fine dimpled microstructure resulting from void growth and coalescence revealing a ductile nature of fracture. Matrix cleavage was hardly observable throughout the investigated samples. Generally, intermetallic particles can be found inside the dimples and in most of the cases these correspond to the Mg_2Si phase (see Paragraph 3.2.4). The platelet-like shape of these particles make them prone to decohesion if they are oriented perpendicularly to the tensile axis. This is an indication that one of the failure mechanisms in the unreinforced material is the debonding between this phase and the matrix. An example of a dimple with a Mg_2Si particle inside of it is shown in Figure 5.24 b). A phase containing Cu was found in most of the cases on the Mg_2Si platelets (bright particles in Figure 5.24 b)).

Figure 5.25 a) and b) show two different regions of a fracture surface for the matrix material where dimples can be observed. The white crosses belong to dimples of eutectic Si while the black ones correspond to Ni and Fe rich intermetallic phases (see Paragraph 3.2.4).

Figure 5.26 a) shows a picture of a longitudinal section of an unreinforced sample near the fracture surface. The vertical axis corresponds to the tensile axis. Cracks going through the Si phase are observable as well as the formation of pores in the interface between the Si or the intermetallic phases and the matrix. The same sample was then deep etched in order to reveal the condition of the eutectic Si structure (see Paragraph 3.2.5). The results are shown in Figure 5.26 b) and we see that many cracks oriented perpendicularly to the tensile axis are present.

The fracture features for the SFRM are depicted in Figure 5.27 and in Figure 5.28 for the case of 10% and 15% short fibre reinforced samples, respectively. The vertical axis corresponds to the tensile axis. These four pictures are representative for the behaviour observed in all fractured samples for all studied volume fractions. Ceramic fibres were hardly observable throughout the fracture surface since most of them were embedded in the matrix even in the case of broken fibres suggesting that the matrix continued elongating after the fibres broke resulting in the sleeve-like structure of the fracture surface. A similar fracture morphology was found for a AlSi5Cu3/Al₂O₃/20s SFRM in [100]. Figure 5.29 a) and b) show higher magnification SEM pictures with broken fibres inside the dimples. Decohesion of fibres was only observable for the case in which they were aligned perpendicularly to the load direction as shown in Figure 5.30 a) and b). This does not mean this is the only possibility of fibre decohesion since such a phenomenon is not easy to distinguish if it occurs at the end of the fibres aligned parallel to the tensile axis. Fibre pull out was not observable in the investigated samples.

Longitudinal sections of fractured samples after creep tests are shown in Figure 5.31 and Figure 5.32 for 15vol% and 10vol% SFRM samples, respectively. In contrast to the unreinforced cast alloys, the SFRM materials show a smaller amount of cracks in the intermetallic phases and eutectic Si but many broken ceramic fibres with the fracture oriented perpendicularly to the tensile direction (vertical axis). In some regions the crack on the fibres continues along the intermetallic phases and/or eutectic Si as it can be seen in Figure 5.32 a). Decohesion between the reinforcement and the matrix was found both at the end of fibres aligned in the tensile direction as well as around fibres aligned perpendicularly to the tensile axis.

Fracture of the ceramic fibres or Si and intermetallic phases was not observable during investigations of longitudinal sections of interrupted creep tests samples suggesting that the damage of these components begins only after the secondary creep stage and for $\epsilon > 1\%$.

Figure 5.33 shows a region in a 20vol% fibre reinforced sample in which a pre cracked fibre preform was found. The presence of this kind of structural damage in the material can be detrimental for the creep resistance since the properties in the interface between the unreinforced and reinforced regions are even worse than those for the unreinforced alloy [101].

5.3 Young's Modulus

The Young's moduli of the fibre reinforced and the unreinforced cast alloys were studied by means of DMA measurements. The results obtained in a range of temperature between 30 and 350°C are shown in Figure 5.34 for all the four materials. In this figure, the experimental values are compared with theoretical values obtained by means of the Eshelby's method [35, 95] (see Paragraph 4 and Annex A) using the results for the matrix. Thus, the theoretical values of Young's modulus for the composites were calculated using the formula:

$$E_c = \frac{\sigma^A}{\epsilon^A + f_{eff} \cdot \epsilon^T} \quad (5.1)$$

where σ^A is the applied stress, ϵ^A the elastic deformation of the matrix calculated as σ^A/E_M , f_{eff} is the *effective* reinforcement volume fraction and ϵ^T is given by Equation A.16 in Annex A. The effective reinforcement volume fraction refers to the amount of fibres that actually play a role contributing to strengthening of the metal matrix composite. As explained by Dlouhy et al. [42], only fibres with axis not too far away from parallel to the direction of load (all the directions contained in the plane of the fibres for our case) provide a significant reinforcement to the matrix. Thus, the stress carried by one fibre depends on the angle between the fibre axis and using this concept, Klipfel et al. [102] and Dlouhy et al. [42] applied the Eshelby's approach to estimate this effective volume fraction f_{eff} resulting for random planar distributed fibres:

$$f_{eff} \approx \frac{2}{5} \cdot f \quad (5.2)$$

The values of f_{eff} obtained for the fibre reinforced materials investigated in the present work are summarised in Table 5.2:

f [%]	f_{eff} [%]
10	4
15	6
20	8

Table 5.2. Values of f_{eff} for the three SFRM.

The experimental results show a very good agreement with the applied model principally for the 15vol% fibre reinforced material, where the difference between the

experiment and the calculations is between 0 - 2%, while for the 10vol% this disagreement is between 2 and 4%. The slight kink in the curves at about 250-300°C is an experimental artefact. The 20vol% SFRM gives the less accurate agreement between experimental results and the theoretical model with differences ranging from 2 to 5%. This may suggest that for both the 10 and 20vol% SRFM, the calculated f_{eff} overestimate the actual effective volume fraction that governs the composite response. However, the experimental results for the 20vol% material show that the Young's modulus in the investigated range of temperatures falls practically on the curve for the 15% material. This is not consistent with the expected results since it is of general agreement (both theoretical and experimental) that the bigger the reinforcement volume fraction the higher the Young's modulus. Furthermore, metallographic results have shown that the 20vol% SFRM has a higher amount of porosity after production in comparison to the other fibre reinforced composites and this may also contribute to the lower values found for the elastic modulus.

5.4 In Situ Tensile Creep Tests

5.4.1 6061/Al₂O₃/10p and 6061/Al₂O₃/22p

The strain fields obtained for the 6061/Al₂O₃/10p and the 6061/Al₂O₃/22p composites at the end of the In Situ creep tests (point 5 in Figure 3.34) are shown in Figure 5.35 and Figure 5.36, respectively. The strain fields were calculated using facets of 15x15 pixels (overlapped every 11pixels) which results in regions of approximately 15.5x15.5µm² and 13x13µm² for the 10vol% and the 22vol% composites, respectively. The “white holes” correspond to regions where the calculation of the local strain was not feasible due to a large difference between the grey values of the facets from the compared micrographs. This arises due to a poorer quality of the copper deposition process and/or a high difference in contrast when the pictures were taken. The strain corresponds to the deformation in the vertical direction which is also the load direction. In Figure 5.37 a) and b) and Figure 5.38 a) and b) the initial (prior to deformation) and final (after creep deformation) micrographs used for the determination of the strain field in the 10vol% and 22vol% PRM composites are depicted, respectively. The regions marked with rectangles in both the strain fields and the SEM pictures show deformation zones that can be identified by eye and that result in good correlation with the obtained results. Thus, for the 6061/Al₂O₃/10p alloy these regions show:

- 1) A high deformation zone in the matrix between a relatively large particle and a smaller particle aligned in the load direction. This is part of a

deformation band that starts in this zone and goes through the matrix making its path at the end of adjacent particles (region 2).

- 2) High deformation zone in the matrix that connects the deformation zone explained in 1) by means of a deformation band.
- 3) Similar to 1): a deformation band starts at the end of two adjacent particles aligned in the load direction.
- 4) A high local deformation that goes from one end of an elongated particle through the matrix passing through the broken end of an unusually large particle.

Similarly, for the 22vol% PRM, a “just by eye” analysis shows:

- 1, 2 and 3) A large broken particle with a crack going into the matrix what results in a localised high deformation zone.
- 4) A short deformation band going from an aligned broken particle to the ends of two unbroken aligned particles.

The good correlation obtained by these simple observations are an indication of the good results that can be obtained by means of these In Situ creep tests.

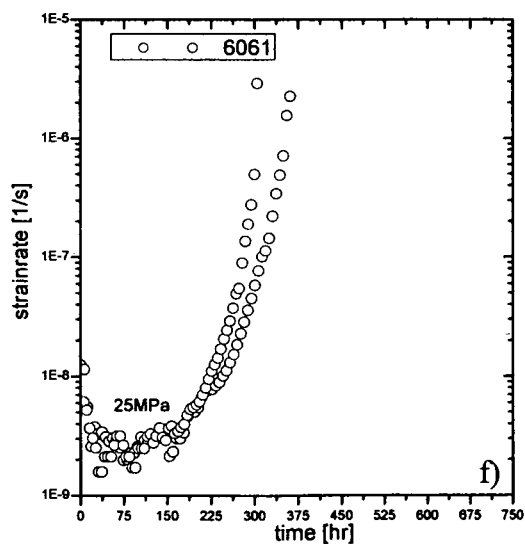
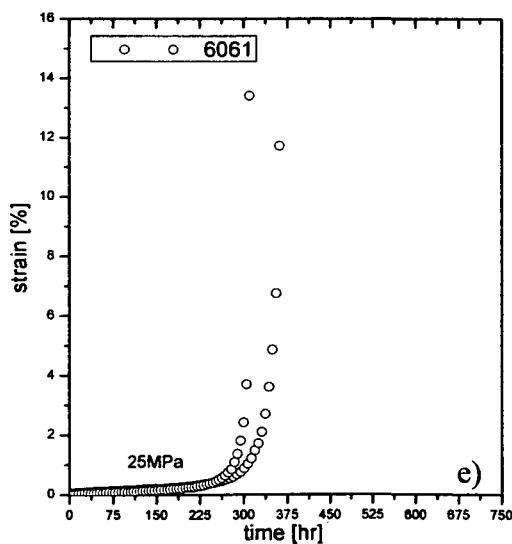
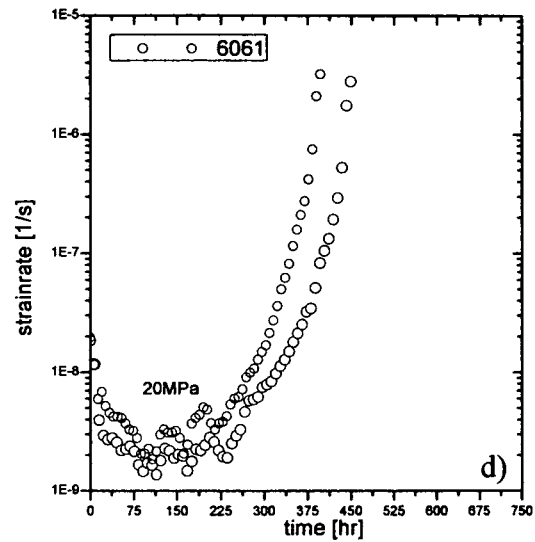
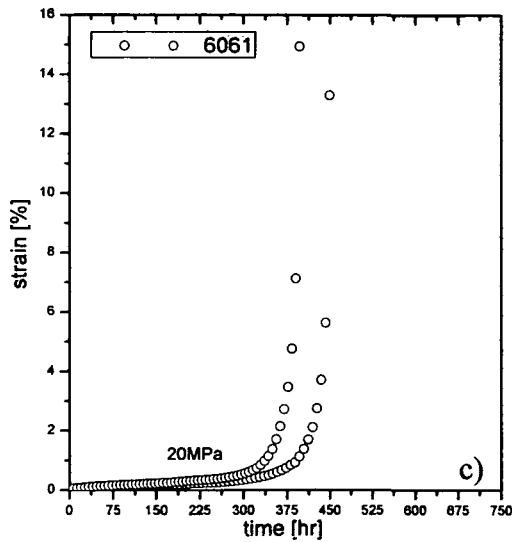
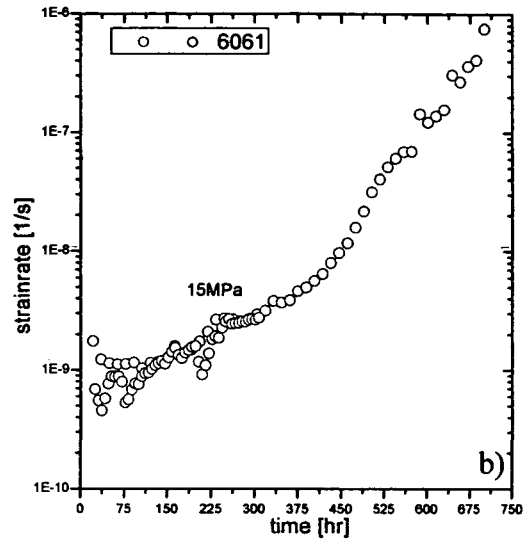
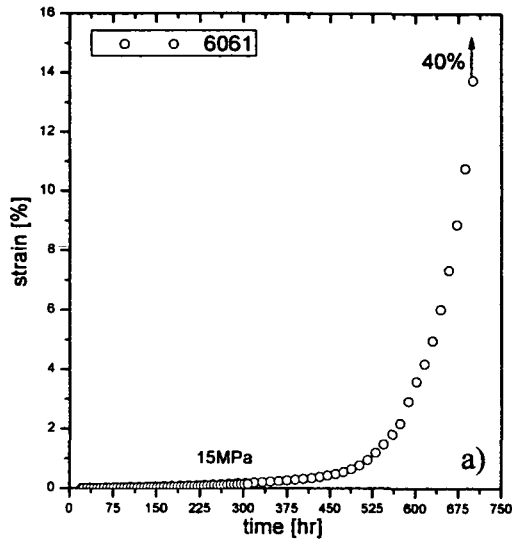
5.4.2 *AlSi12CuMgNi and AlSi12CuMgNi/Al₂O₃/20s*

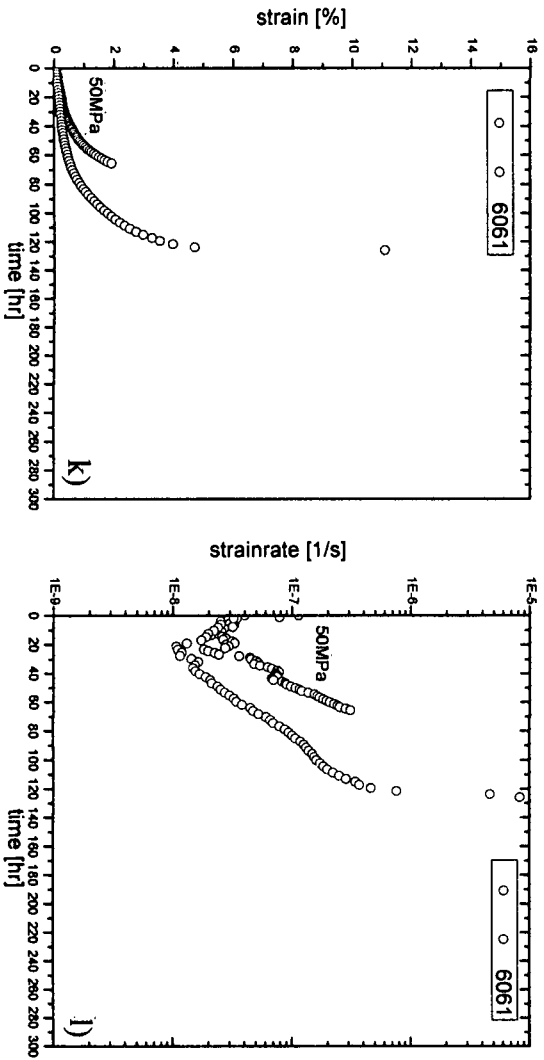
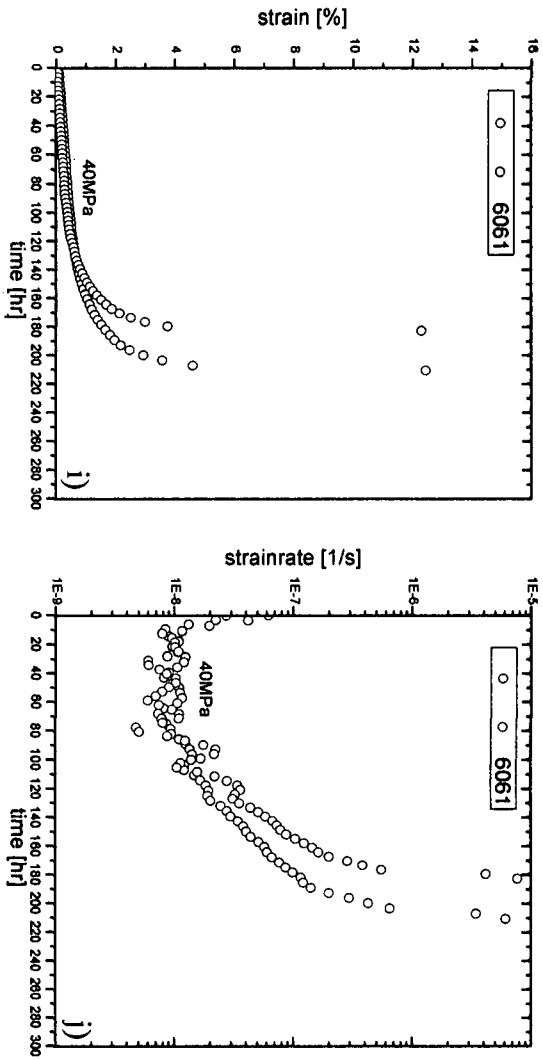
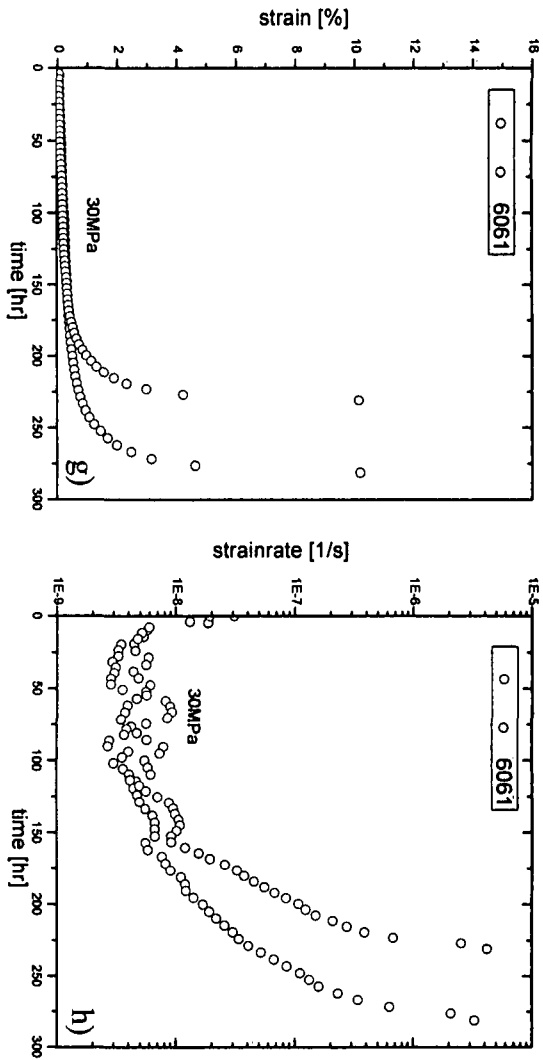
Figure 5.39 shows the strain field obtained after a regional global strain of 1.7% for an unreinforced AlSi12CuMgNi sample under creep conditions. The dark regions in this Figure correspond to the Si-eutectic phase while the white ones correspond to the intermetallic phases. As already explained for the PRM alloys, the “white holes” correspond to facets that could not be identified by the software and used for the calculations. The strain fields were calculated using facets of 17x17 pixels (overlapped every 11pixels) which results in regions of approximately 19.2x19.2µm². It is clearly observable that the regions with a more dense amount of Si as well as the intermetallic particles present the smallest local deformation.

Figure 5.40 shows the strain field obtained after a regional global strain of 0.78% for a 20vol% short fibre reinforced sample. The strain fields were calculated using the same

conditions as for the unreinforced AlSi12CuMgNi alloy. Although the areas selected for the determination of the strain fields showed a very good copper distribution that is not easy to achieve in this material, the copper islands “hide” the fibres present on the surface of the matrix and this turns the analysis of characteristic deformation regions very difficult. Figure 5.41 shows a SEM micrograph of the region studied, while Figure 5.42 is an overlapping of this image with the obtained strain field. The few fibres observable are drawn on these two pictures and a rough estimation seems to allow to argue that fibres with a certain degree of alignment with the tensile axis (vertical axis) show a high level of deformation at their ends, while fibres oriented perpendicularly to this axis show a high level of deformation along their length.

The copper islands were removed from the sample surface by means of a fine polishing in order to visualize the damage behaviour of the 20% SFRM. The results are shown in Figure 5.43 a) and b) and it is observable that the composite shows a similar behaviour to the composite tested under creep conditions using conventional equipment (see Paragraph 5.2.2): broken fibres with the fracture/s oriented perpendicularly to the tensile direction with some presence of cracks that go through the Si and intermetallic phases also oriented perpendicularly to the tensile axis. These damage mechanisms were only observable at distances smaller than 100 μ m from the fracture surface. No damage was observed in the composite at distances larger than 100 μ m from the fracture surface





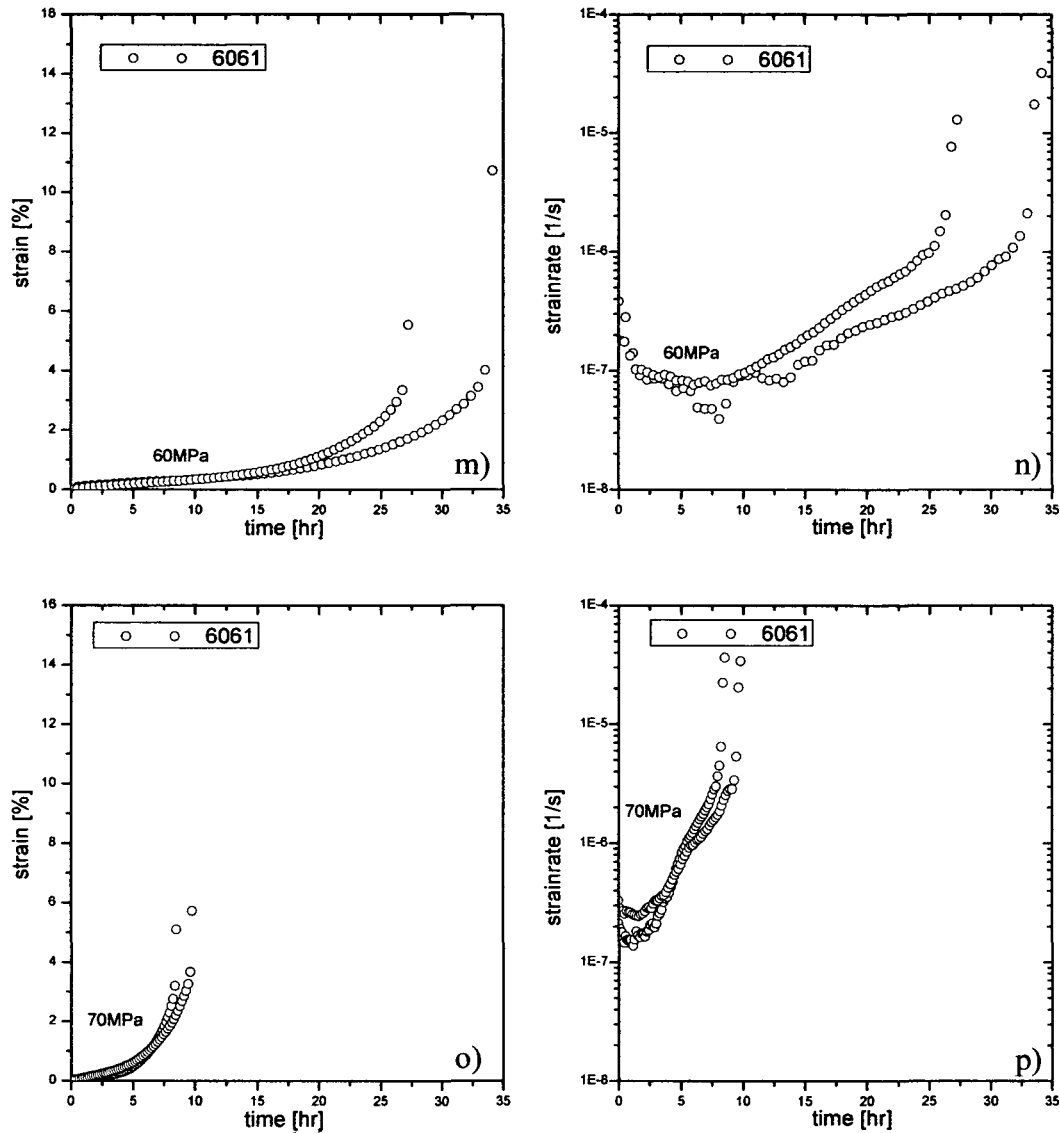
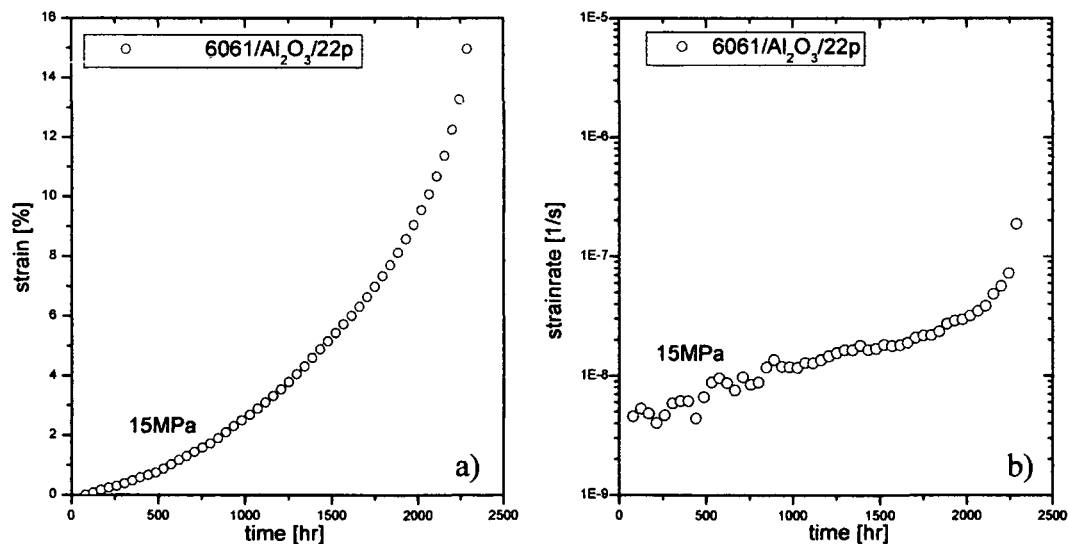
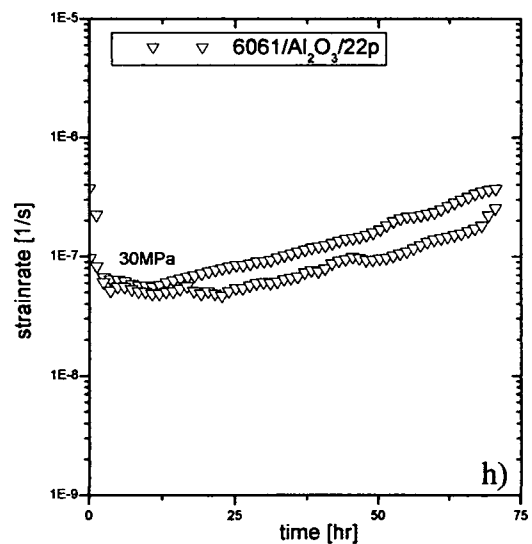
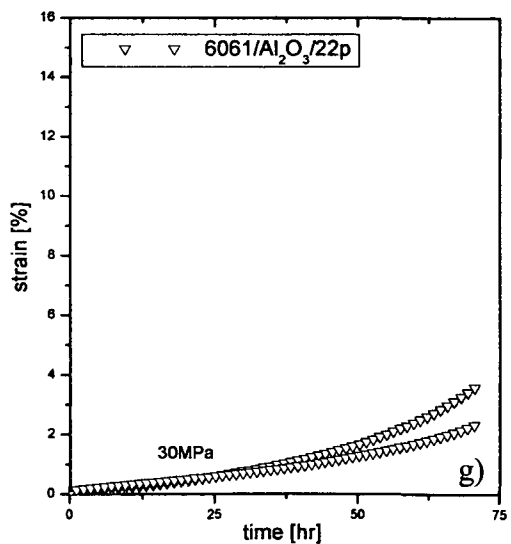
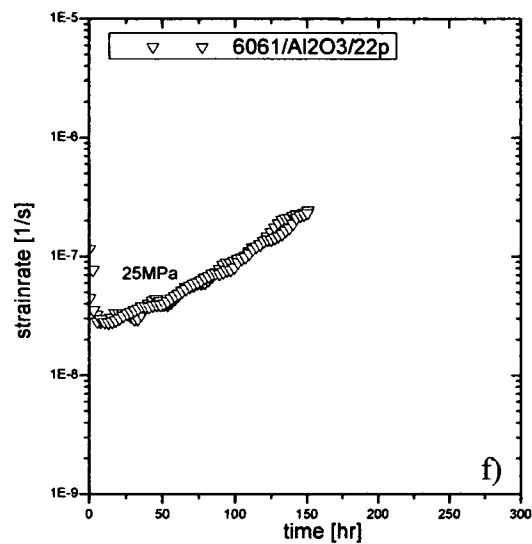
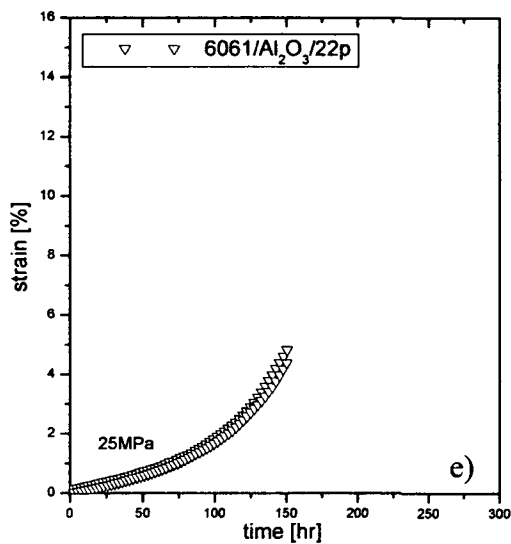
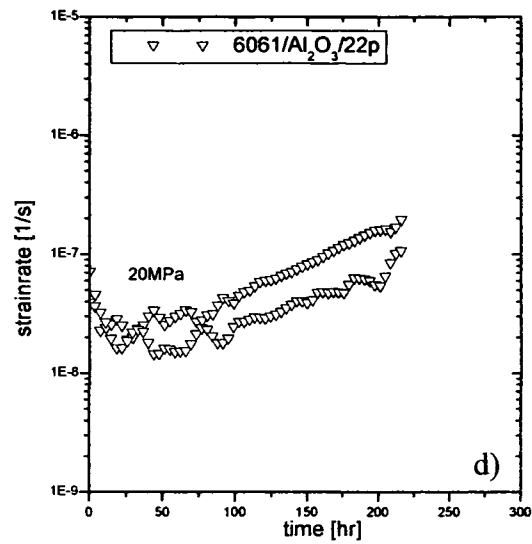
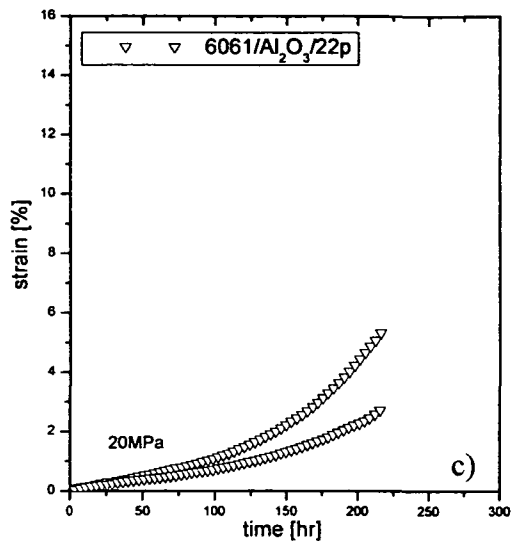
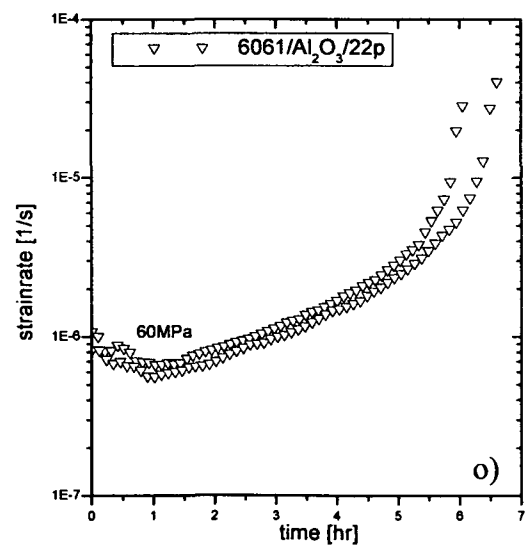
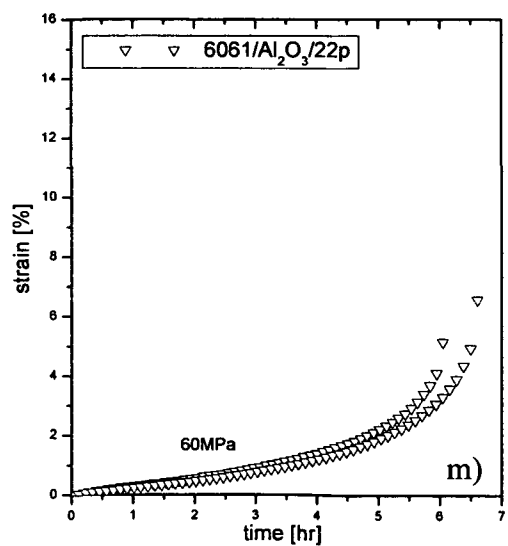
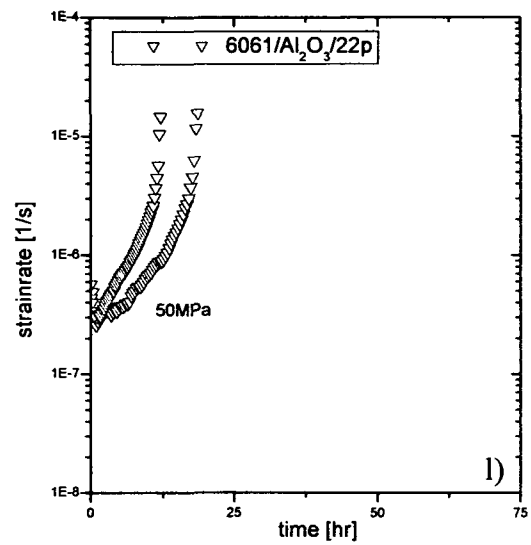
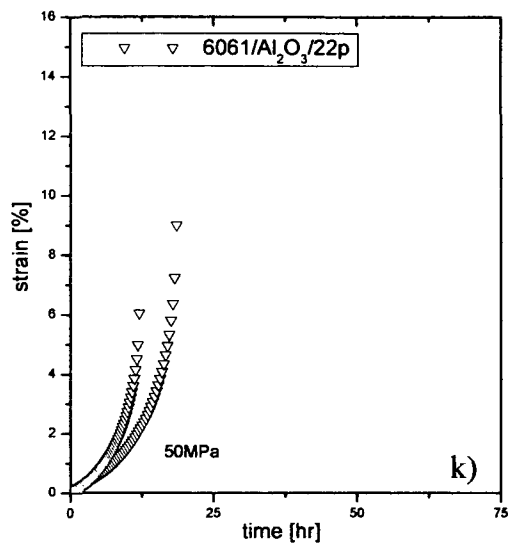
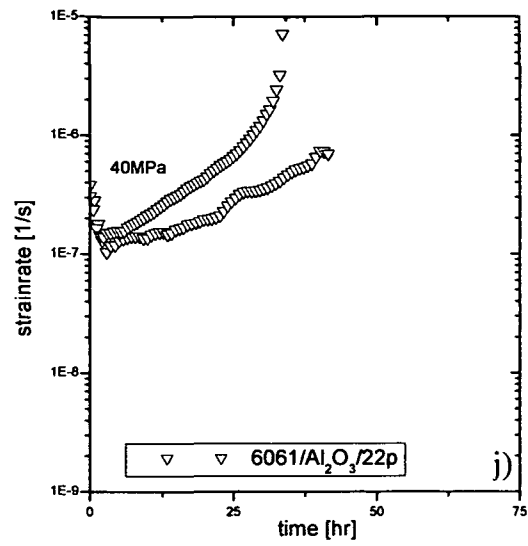
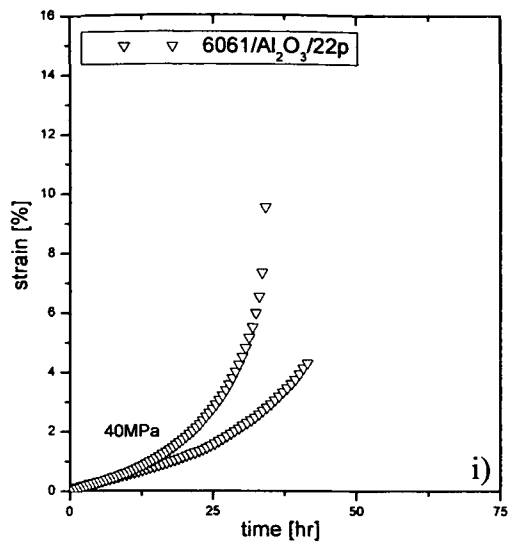


Figure 5.1a) to p) ϵ vs t and $\dot{\epsilon}$ vs t curves for the unreinforced 6061 alloy and applied stresses between 15 and 70 MPa.







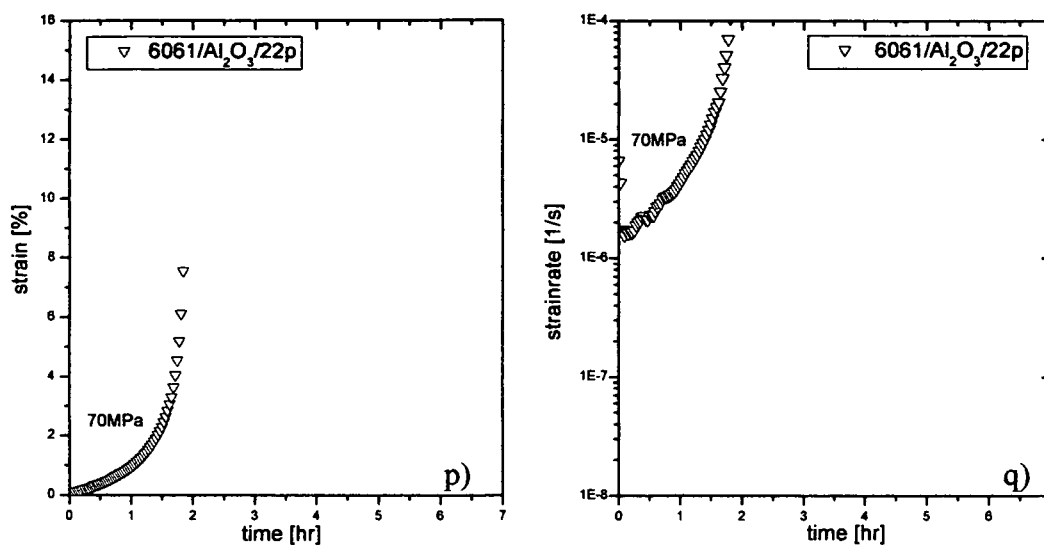
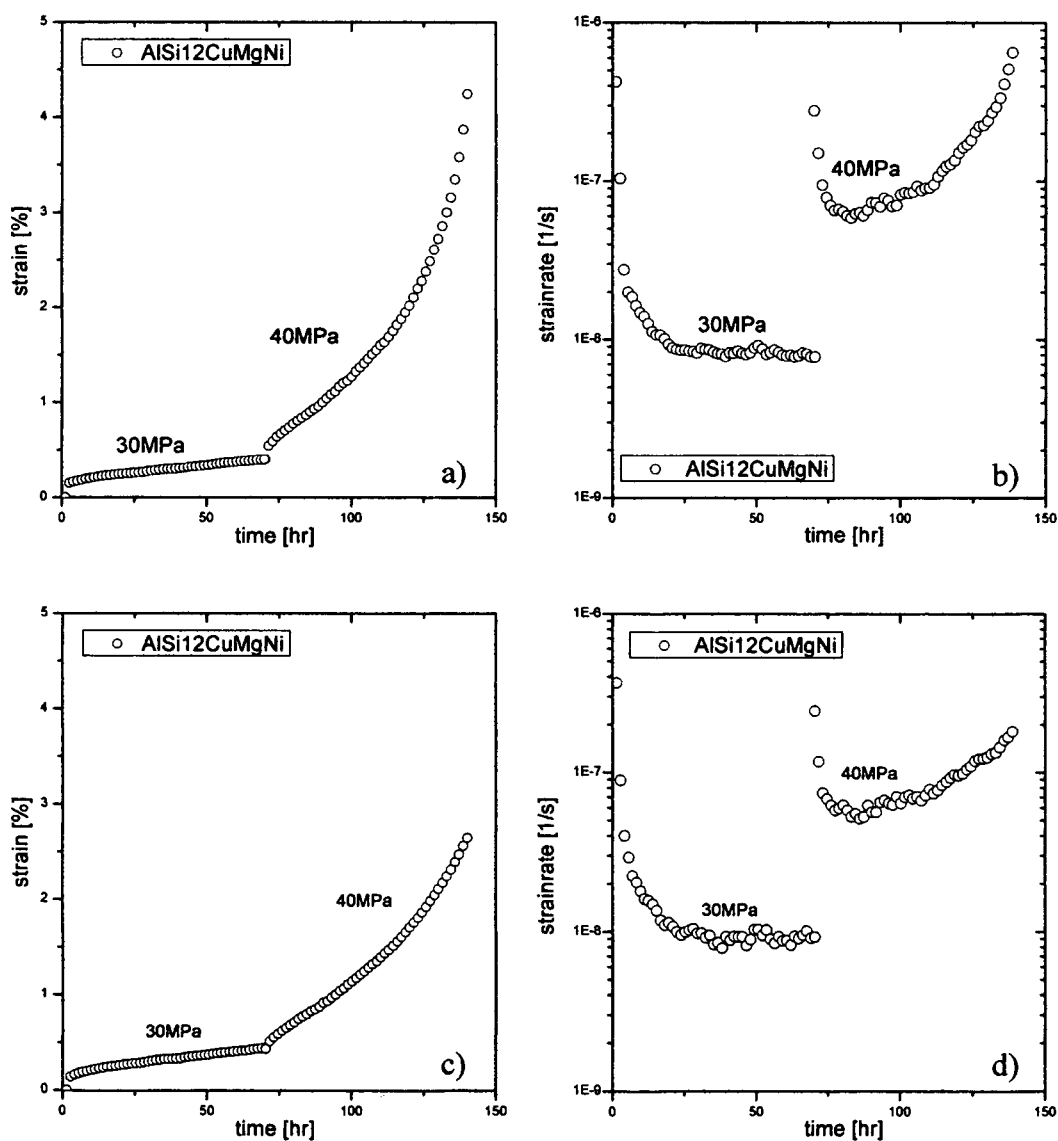
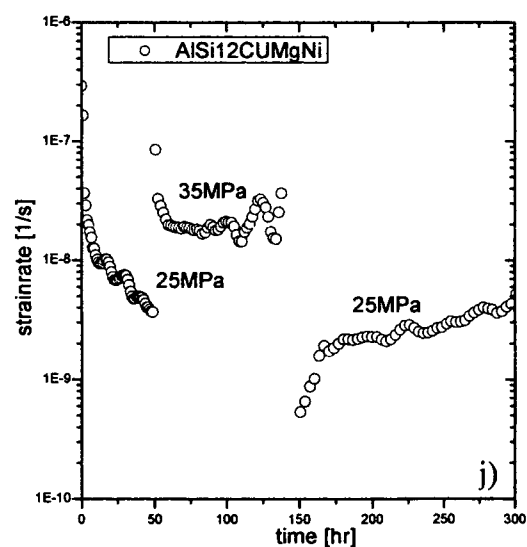
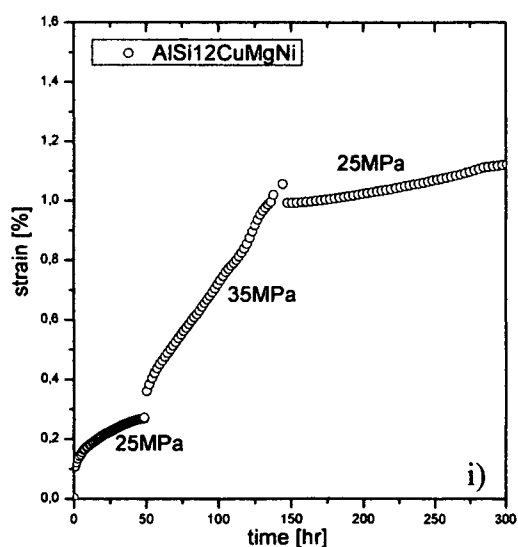
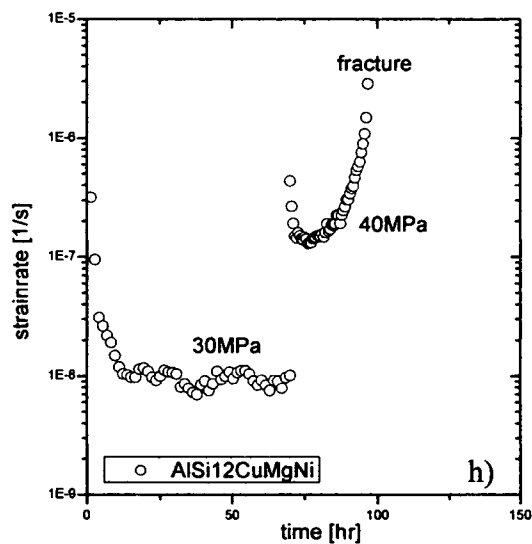
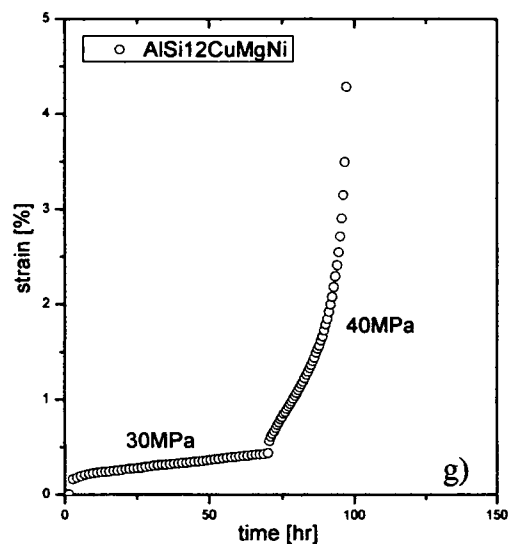
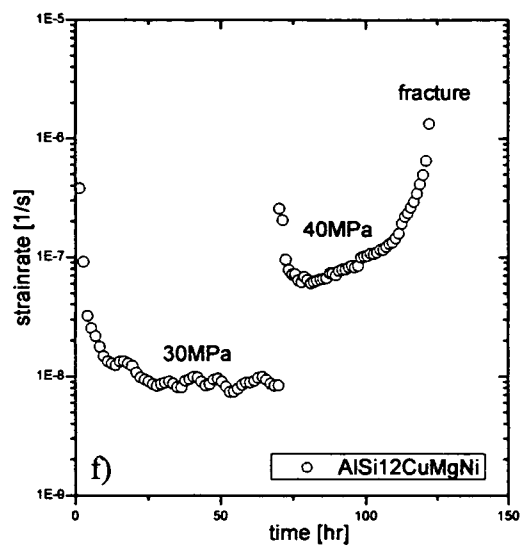
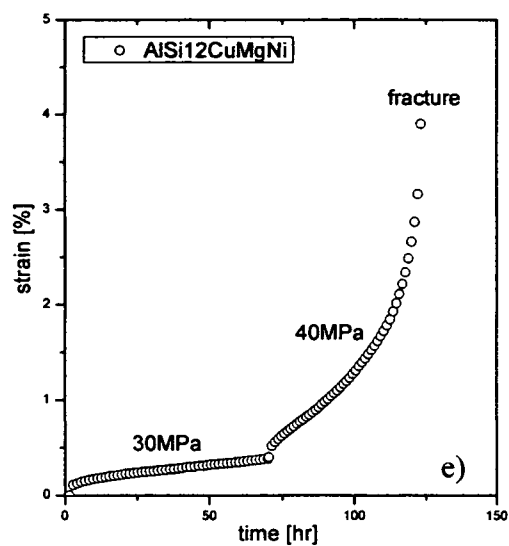


Figure 5.2 a) to q). ϵ vs t and $\dot{\epsilon}$ vs t curves for the PRM 6061/Al₂O₃/22p alloy and applied stresses between 15 and 70 MPa.





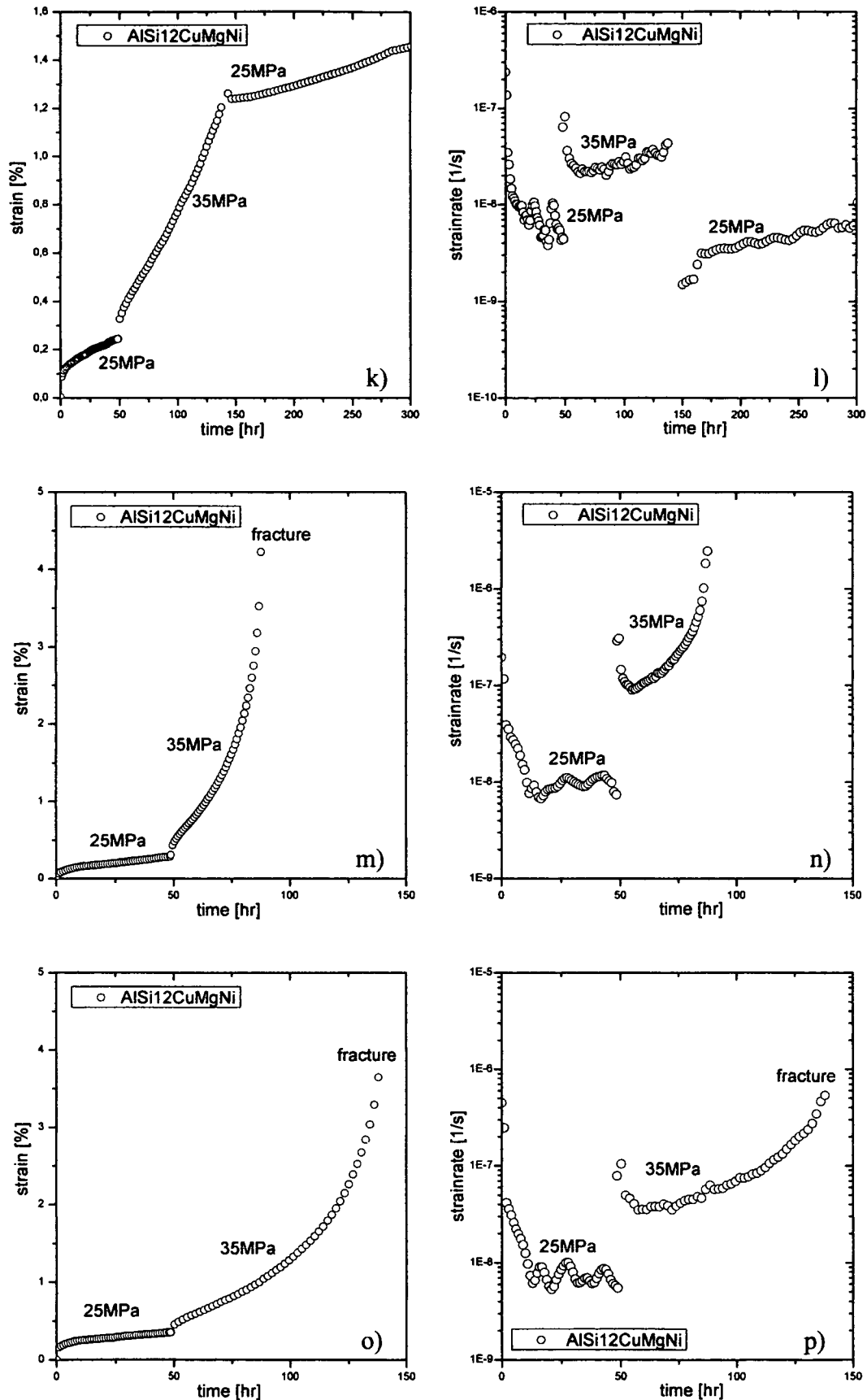
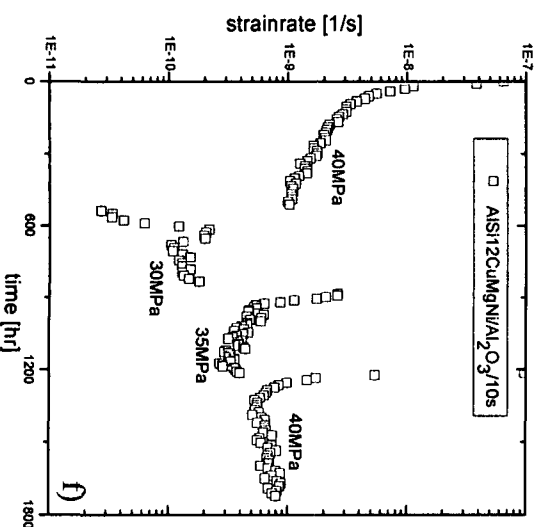
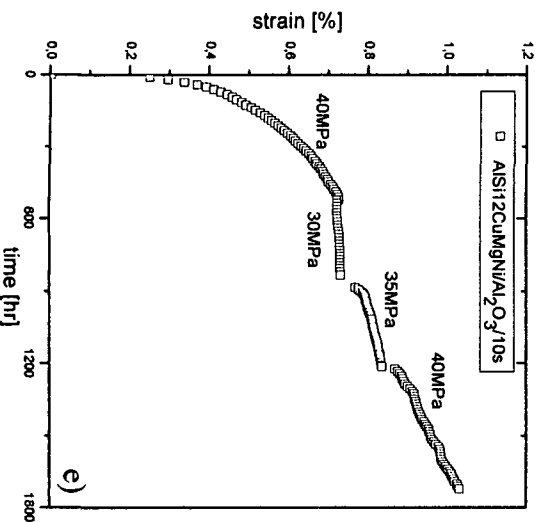
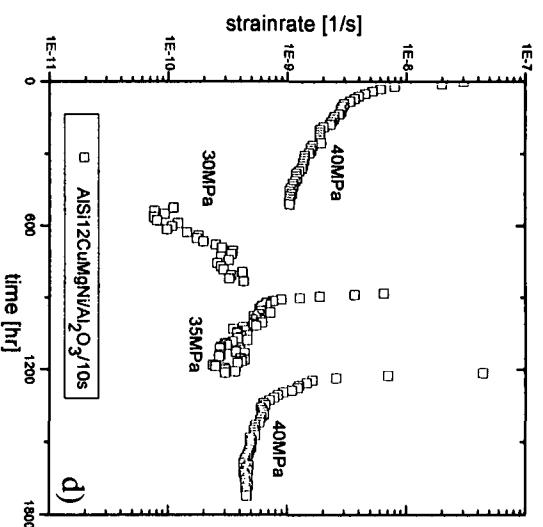
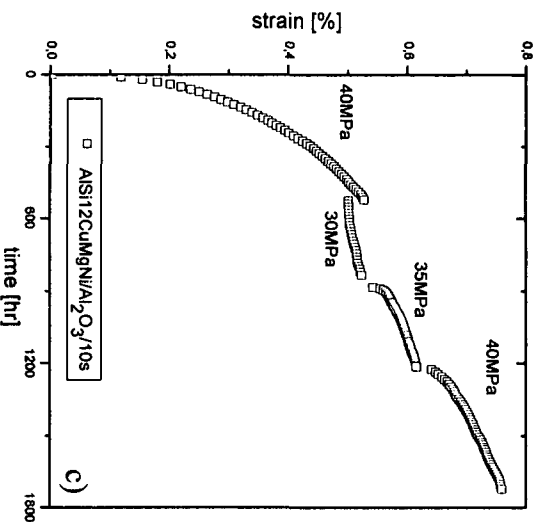
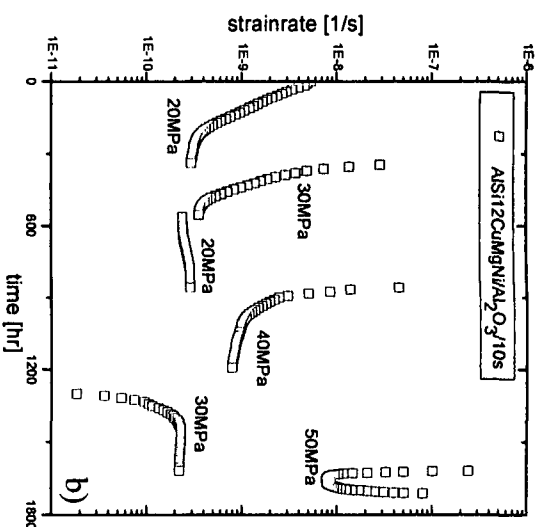
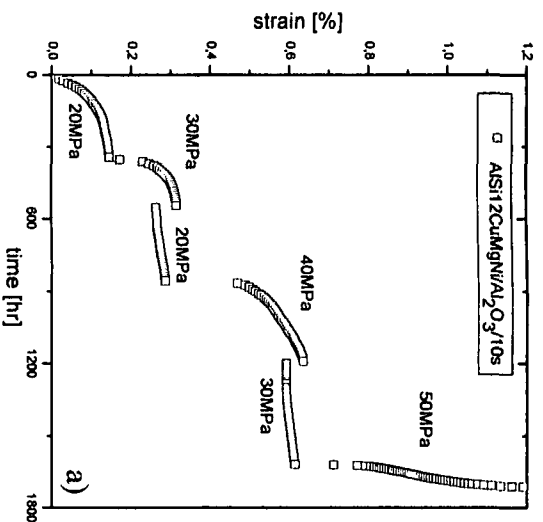
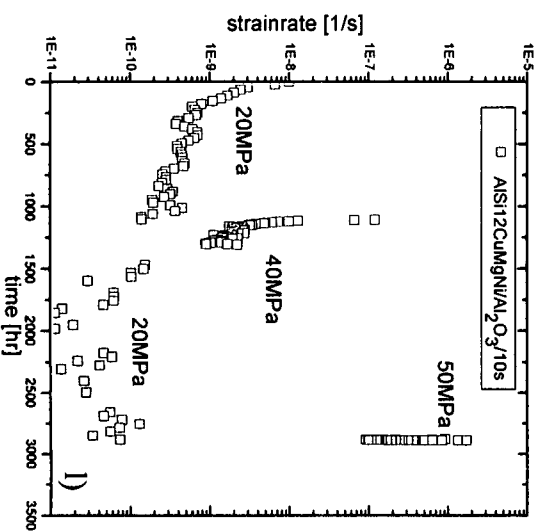
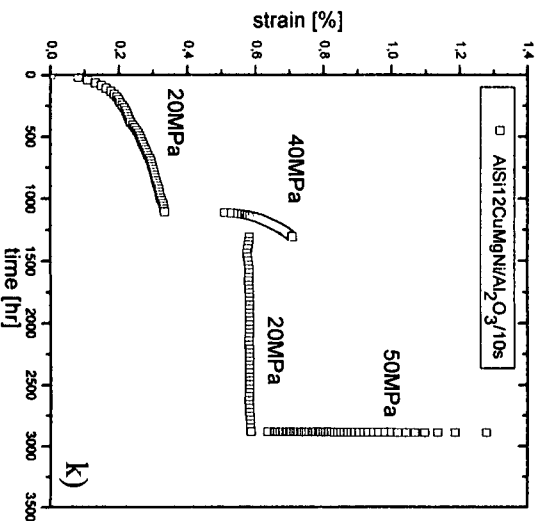
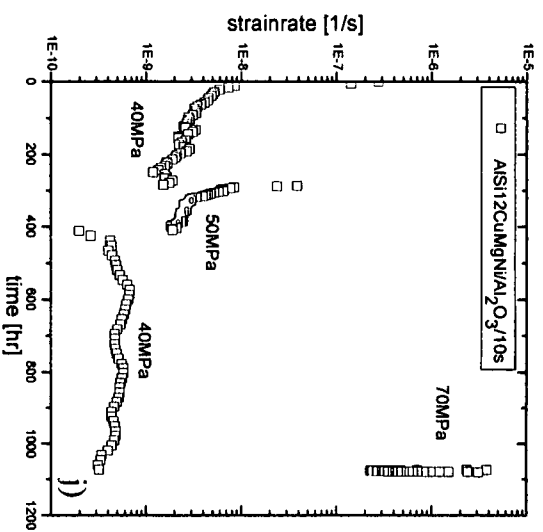
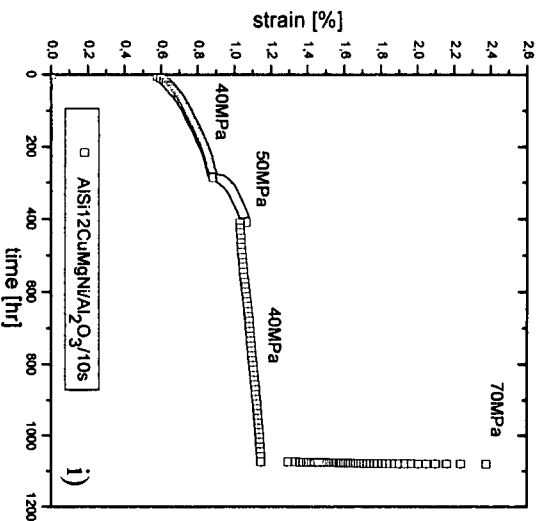
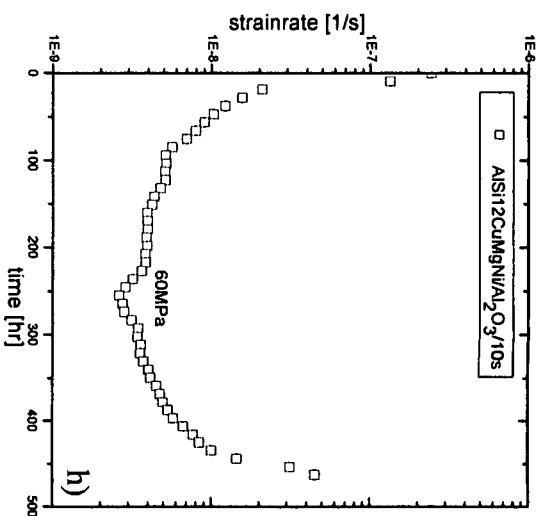
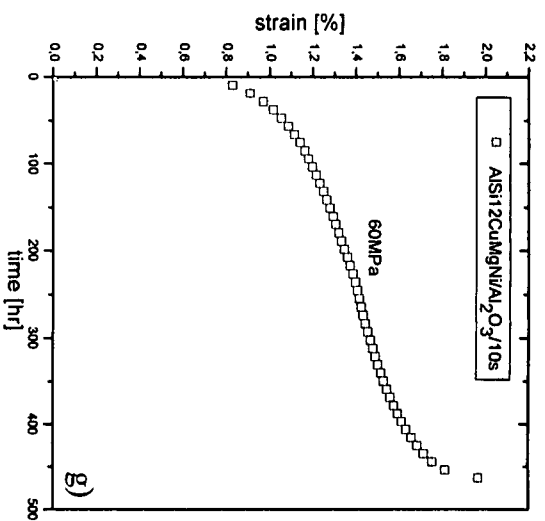
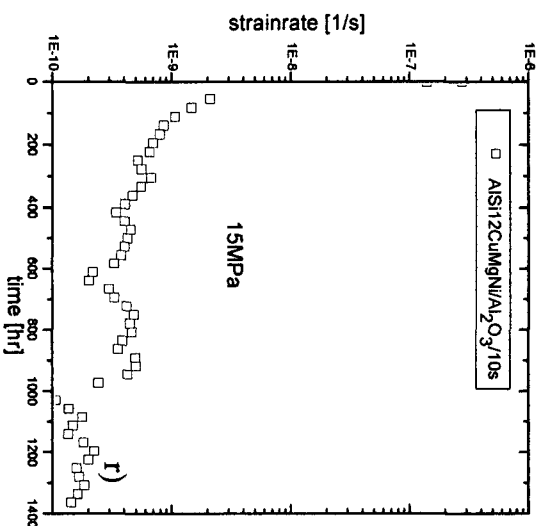
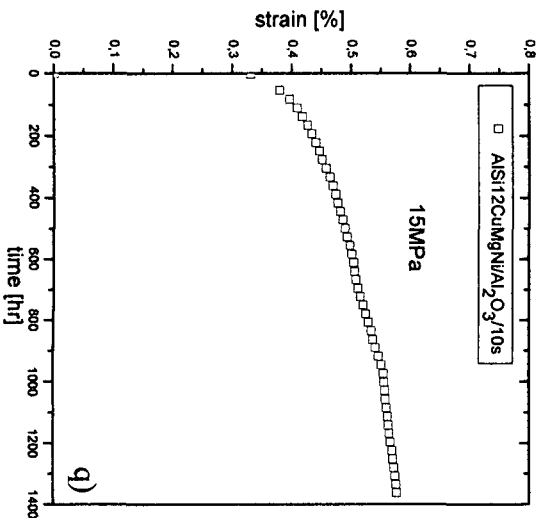
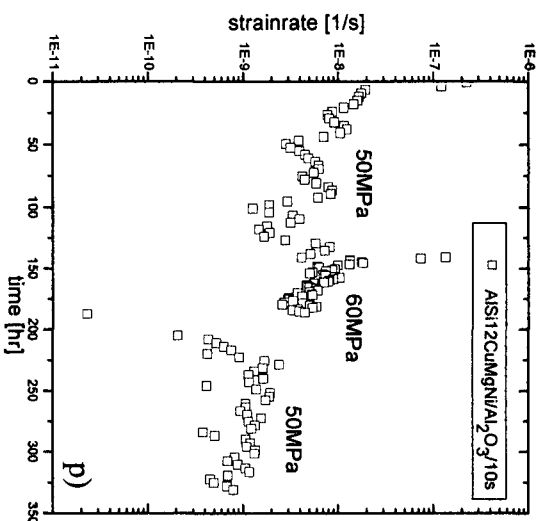
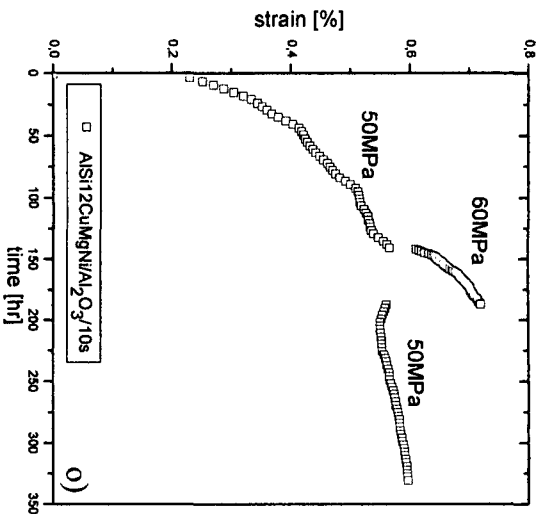
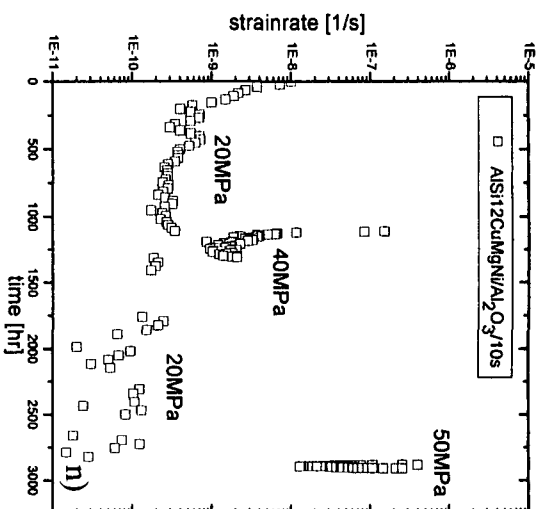
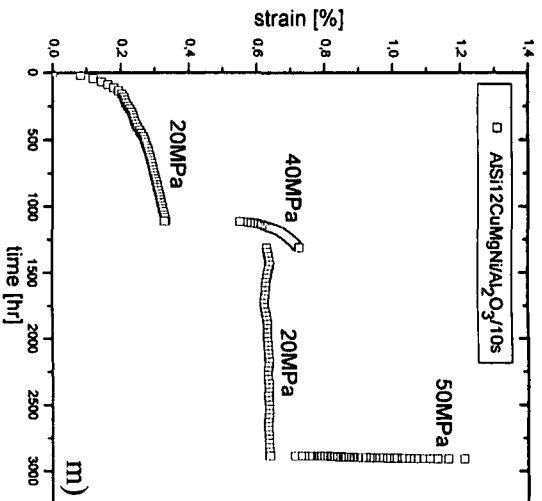


Figure 5.3 a) to p). ϵ vs t and $\dot{\epsilon}$ vs t curves for the unreinforced AlSi12CuMgNi.







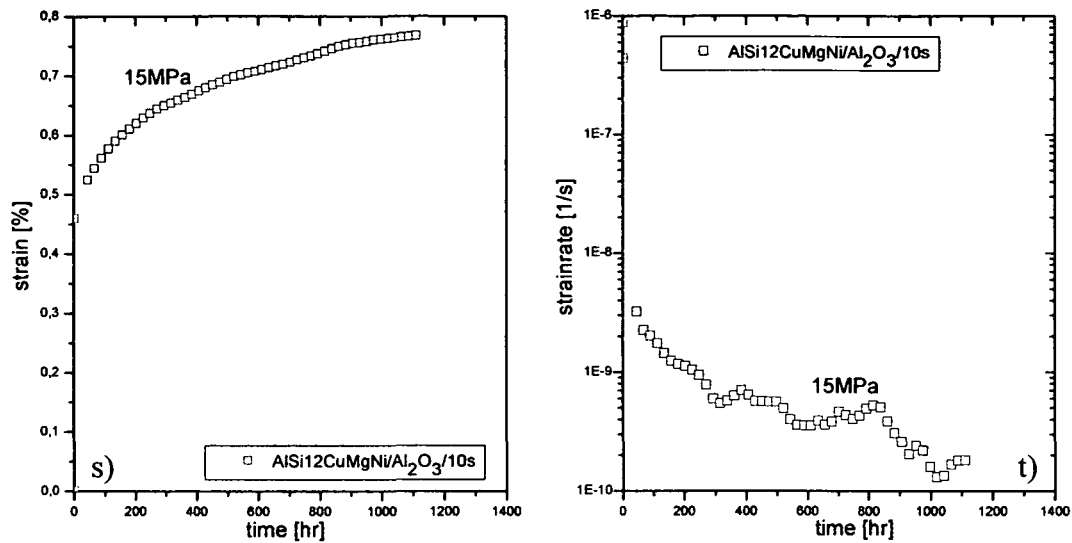
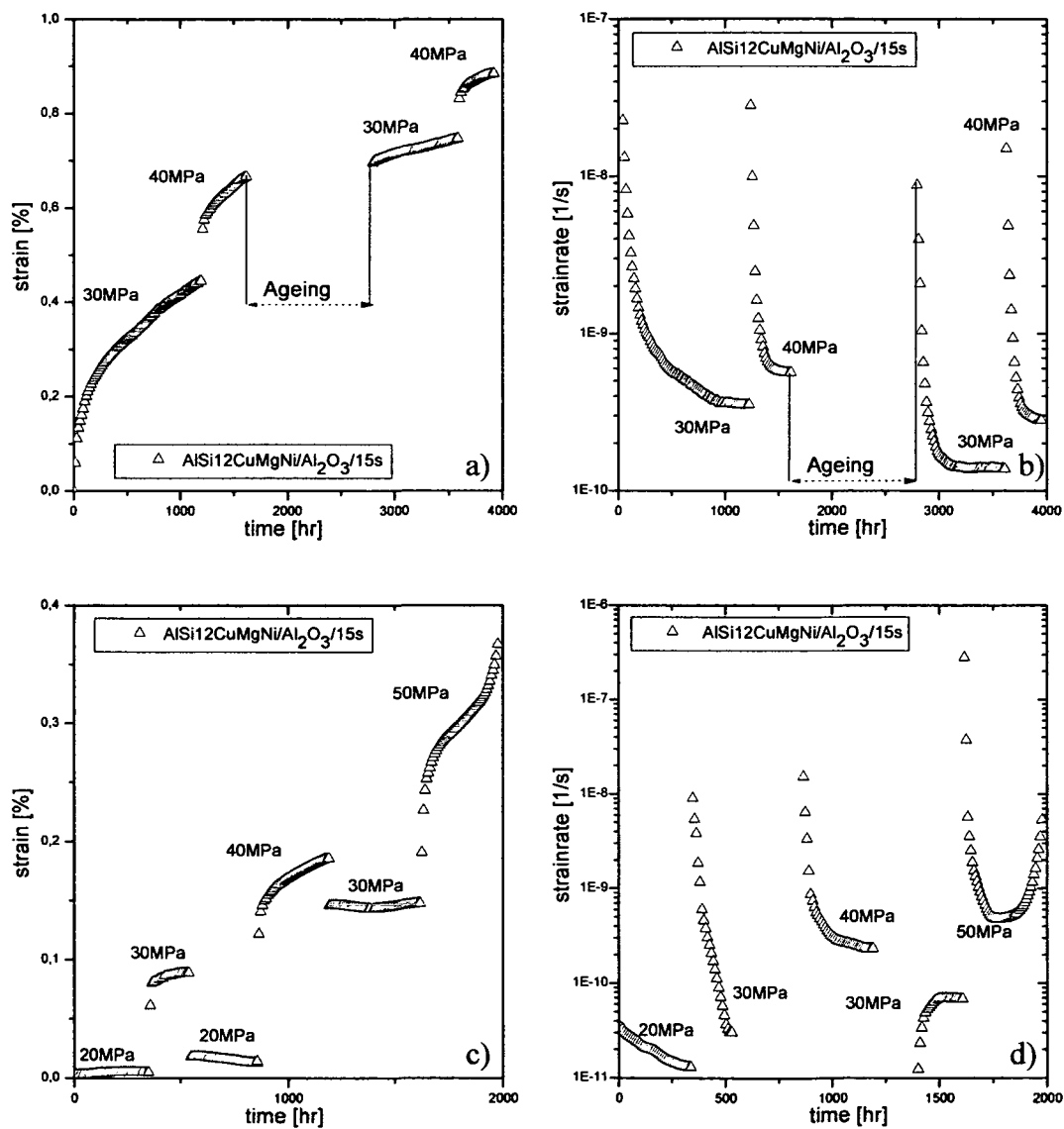
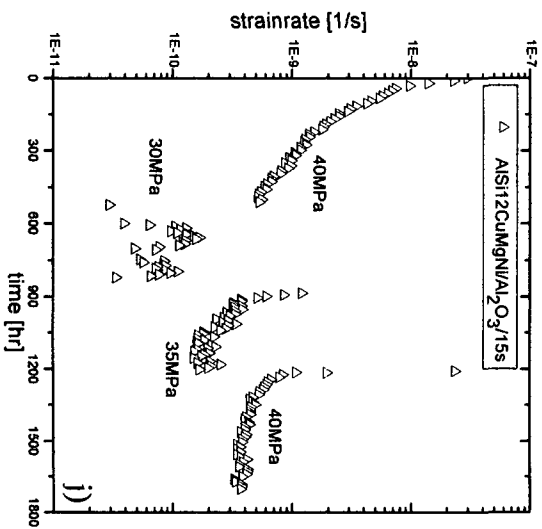
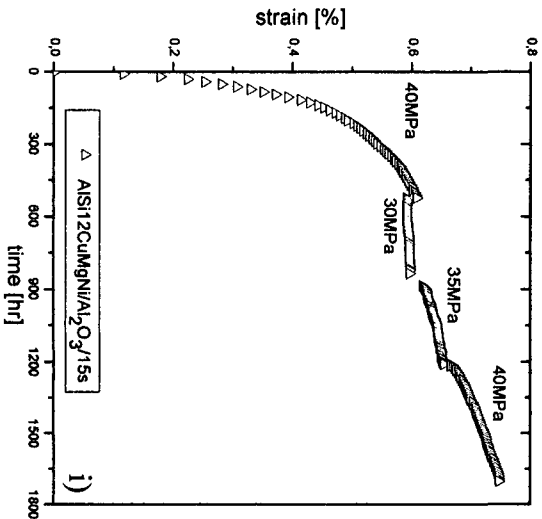
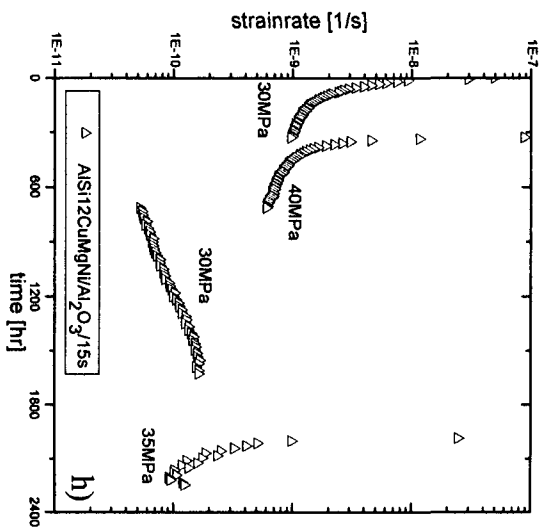
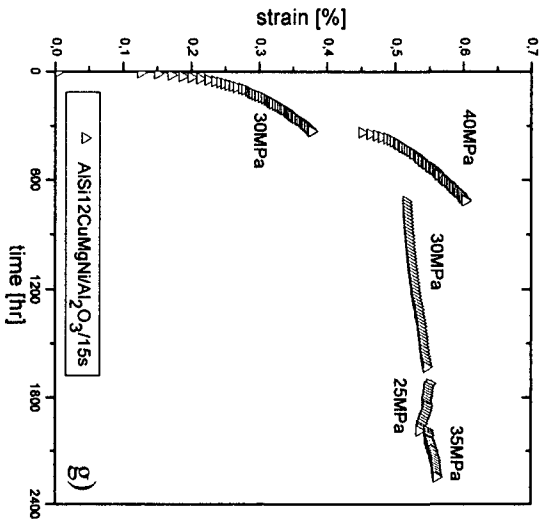
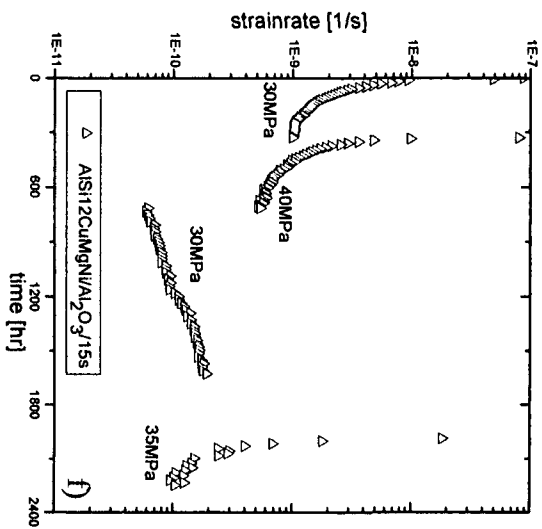
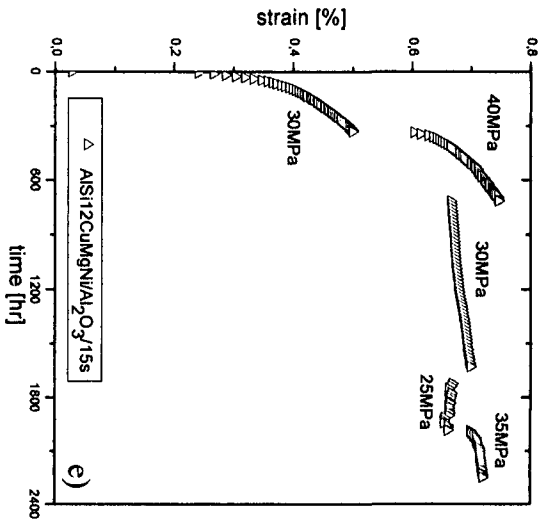
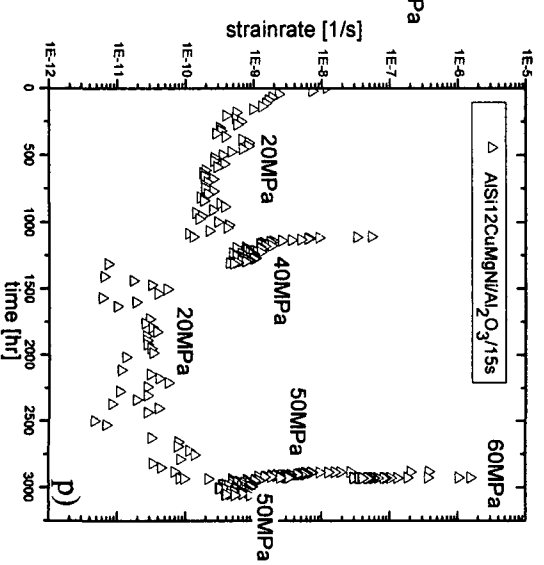
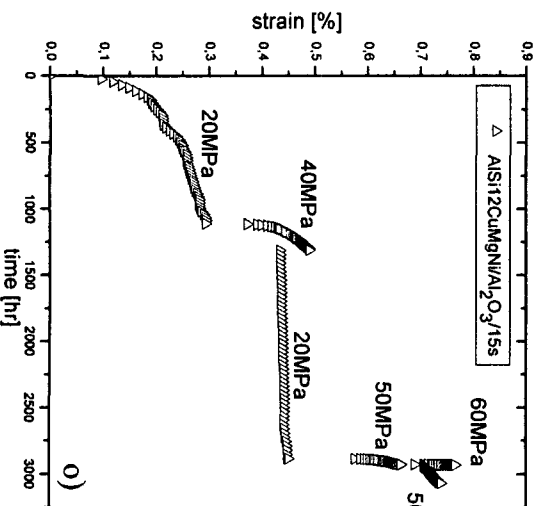
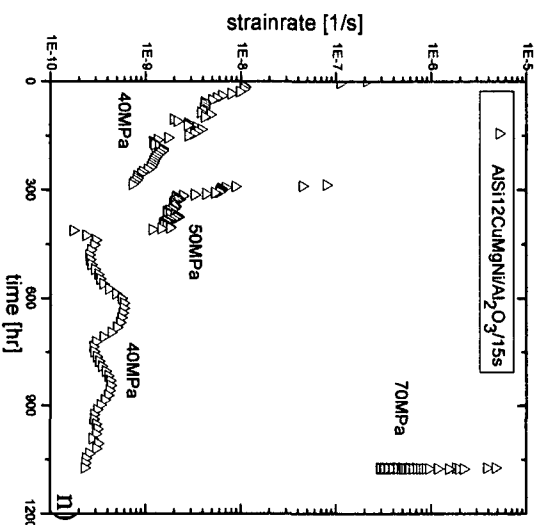
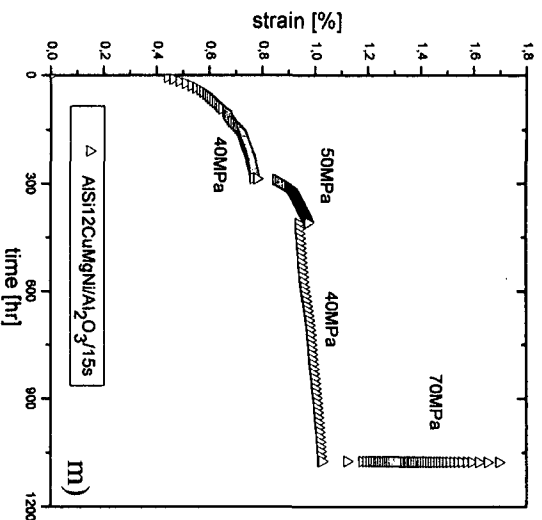
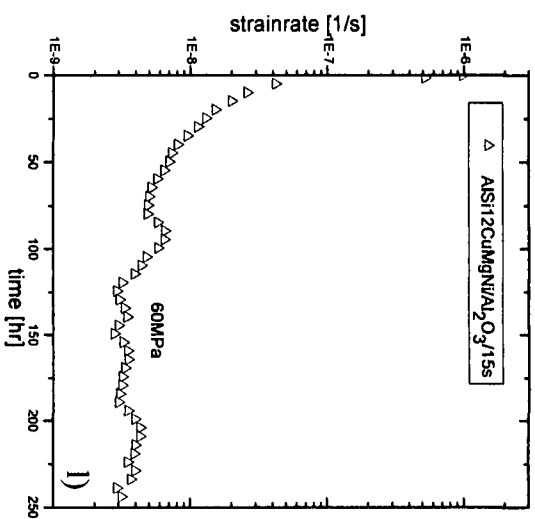
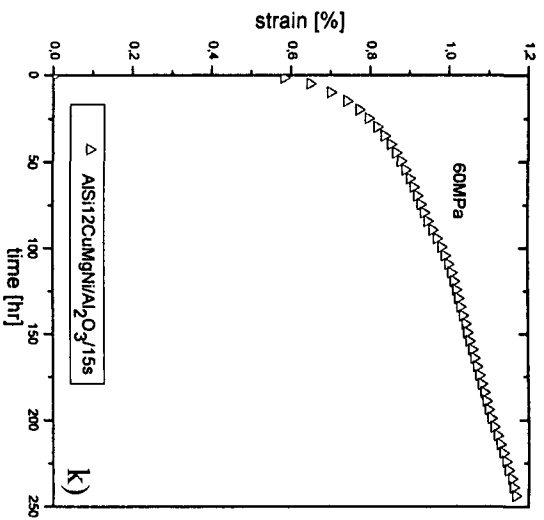


Figure 5.4 a) to t). ϵ vs t and $\dot{\epsilon}$ vs t curves for the AlSi12CuMgNi/Al₂O₃/10s SFRM.







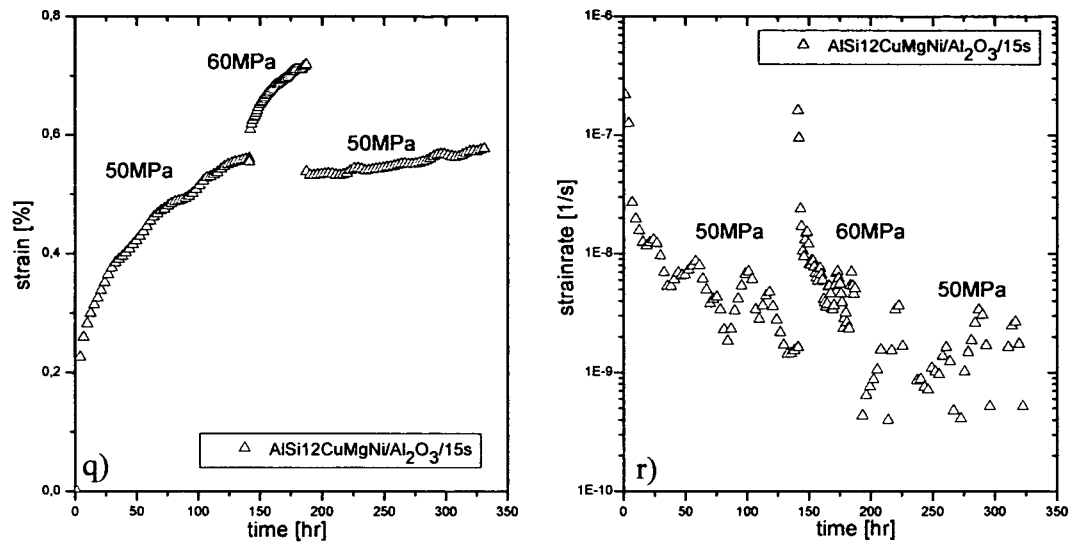
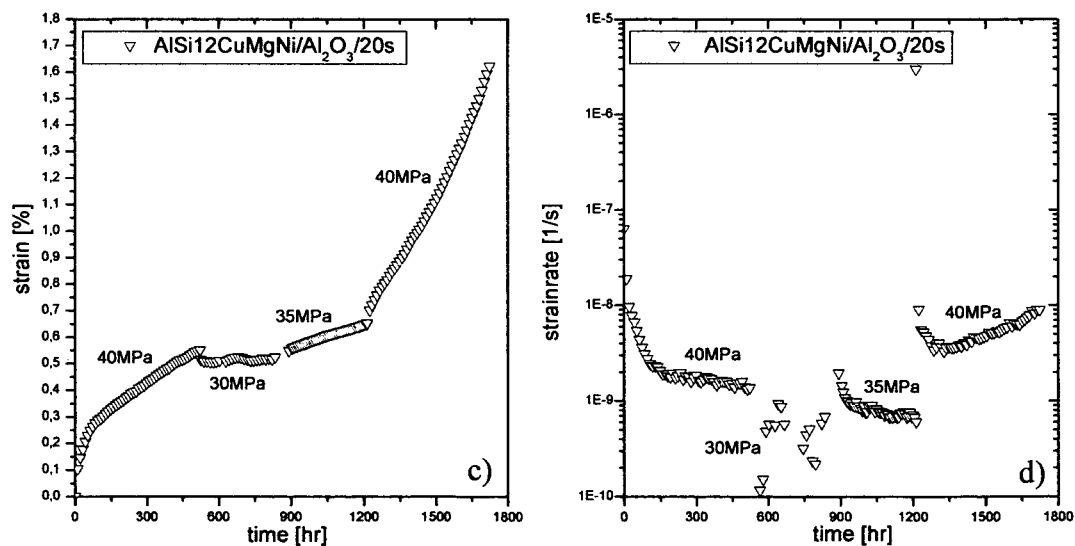
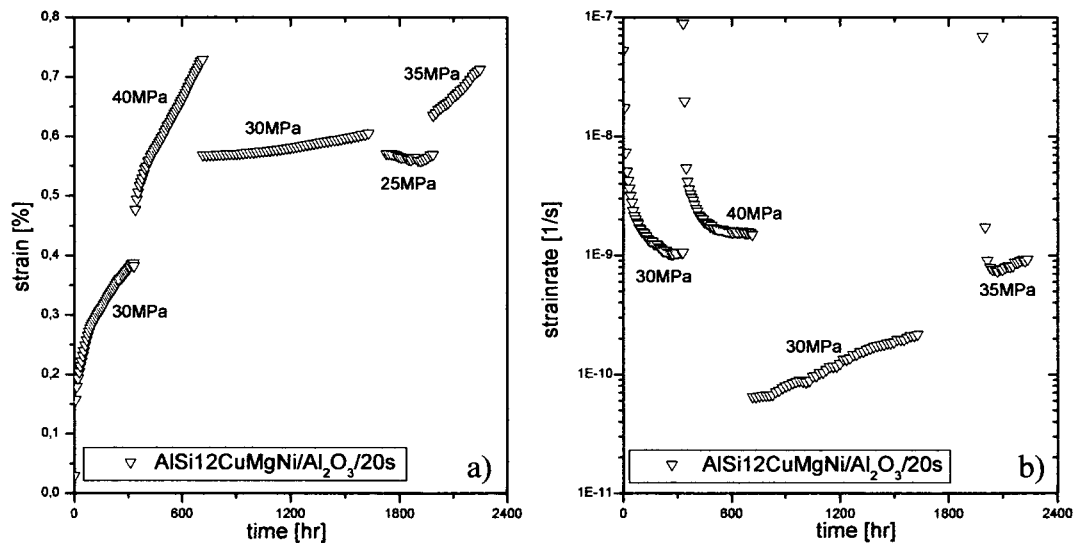


Figure 5.5 a) to r). ϵ vs t and $\dot{\epsilon}$ vs t curves for the AlSi12CuMgNi/Al₂O₃/15s SFRM.



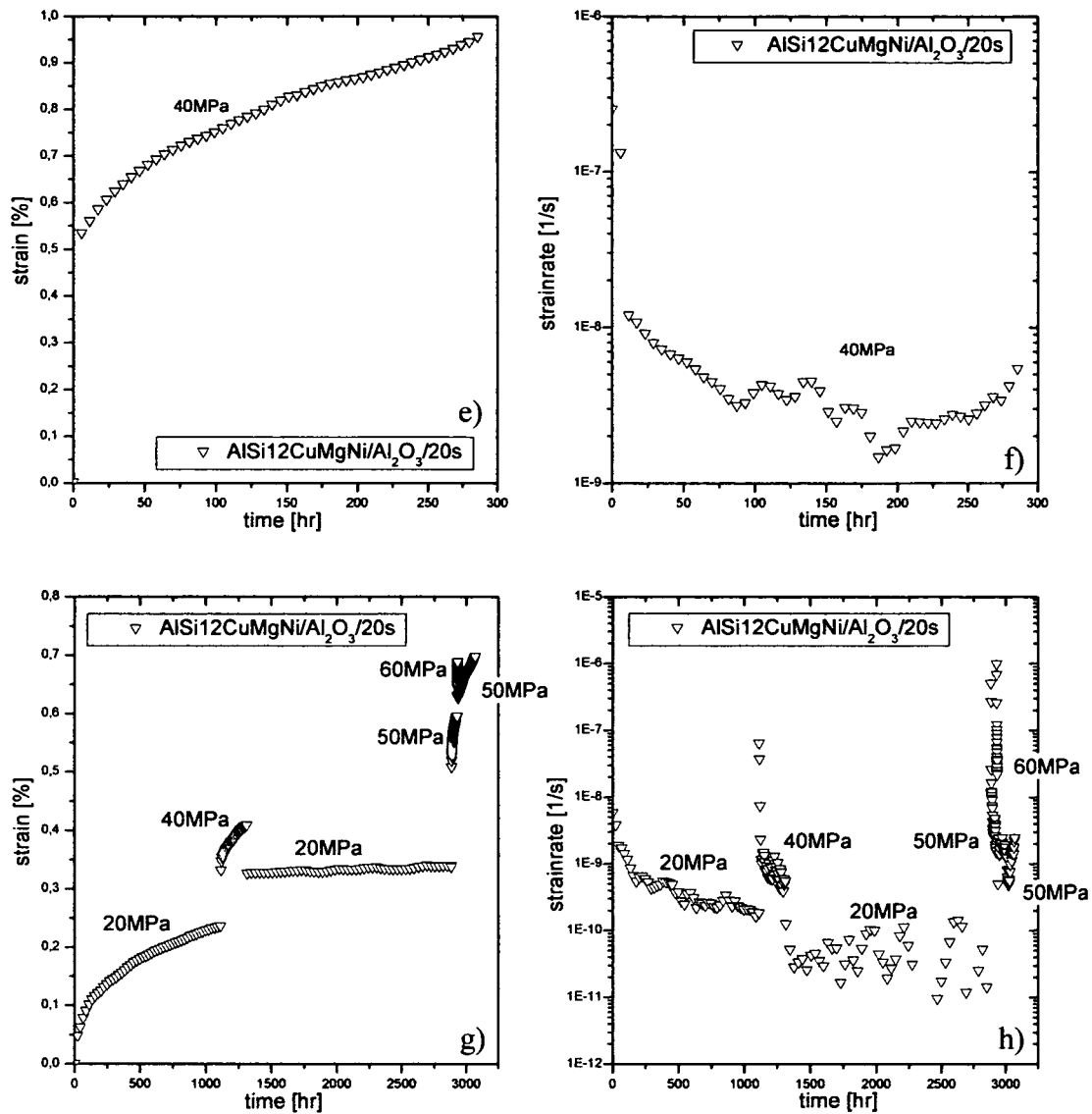


Figure 5.6 a) to h). ϵ vs t and $\dot{\epsilon}$ vs t curves for the AISi12CuMgNi/Al₂O₃/20s SFRM.

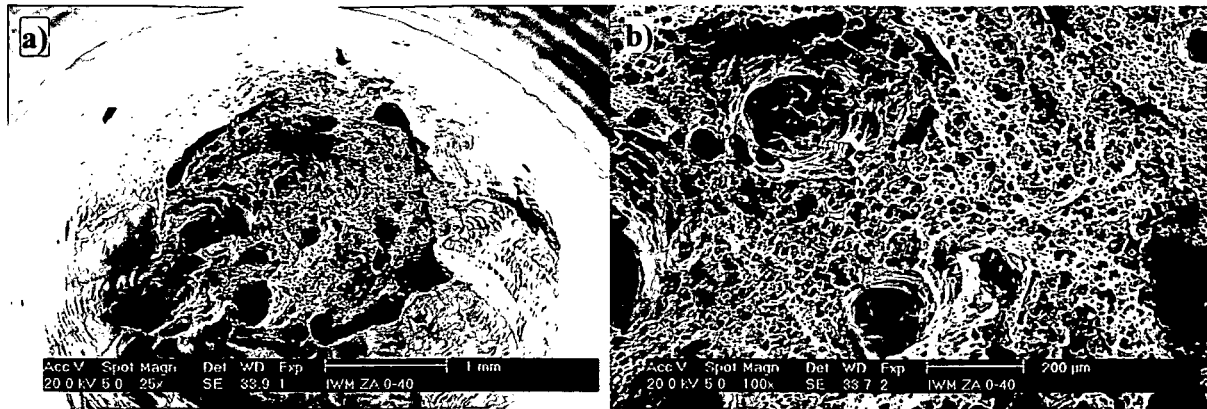


Figure 5.7 a) and b). Fracture surface of a 6061 sample tested at 40MPa ($t_{rupt} = 12.3hr$).

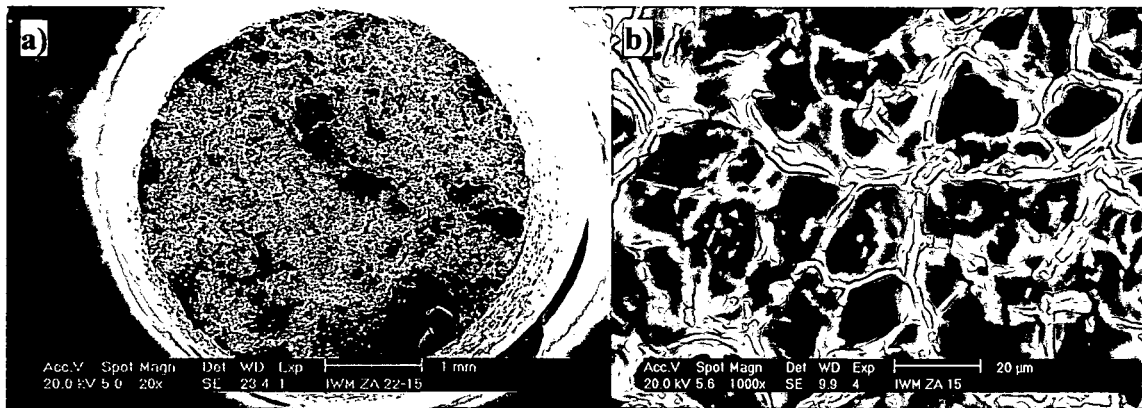


Figure 5.8 a) and b). Fracture surface of a 6061/ Al_2O_3 /22p sample tested at 15MPa.

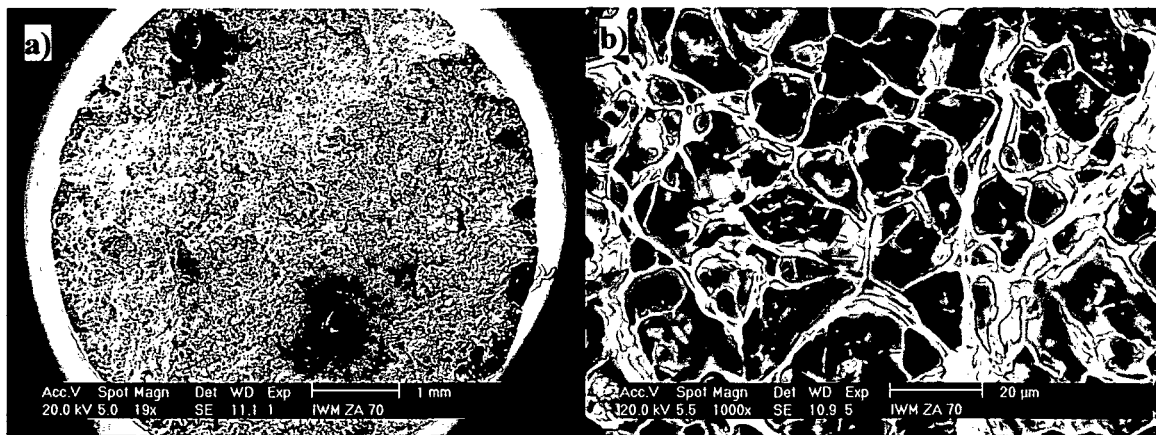


Figure 5.9 a) and b). Fracture surface of a 6061/ Al_2O_3 /22p sample tested at 70MPa.

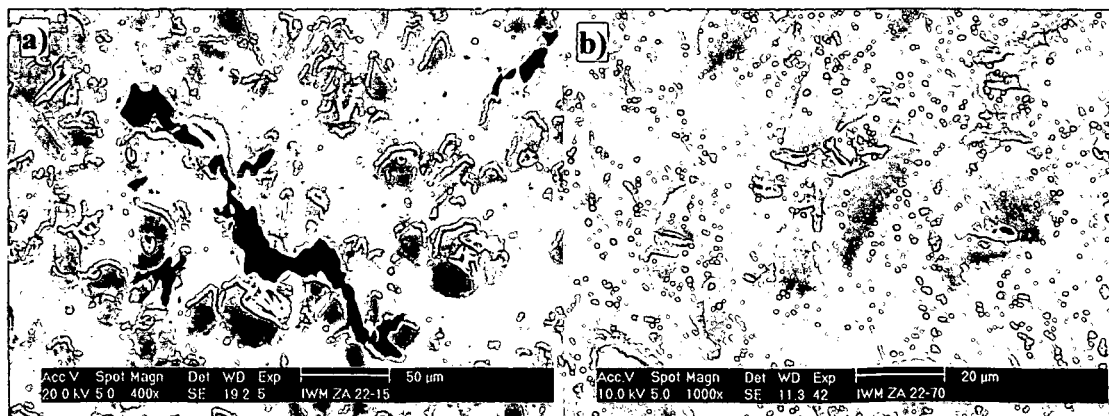


Figure 5.10. Longitudinal sections of 6061/ Al_2O_3 /22p tested at 15MPa a) and 70MPa b).

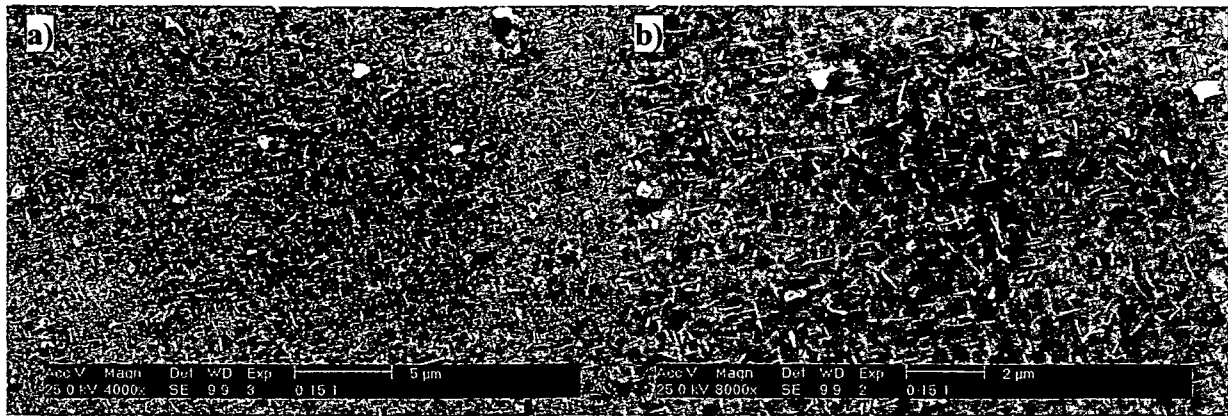


Figure 5.11 a) and b). Mg_2Si precipitates in a 6061 unreinforced sample tested at 70MPa (exposure time=8.5hr).

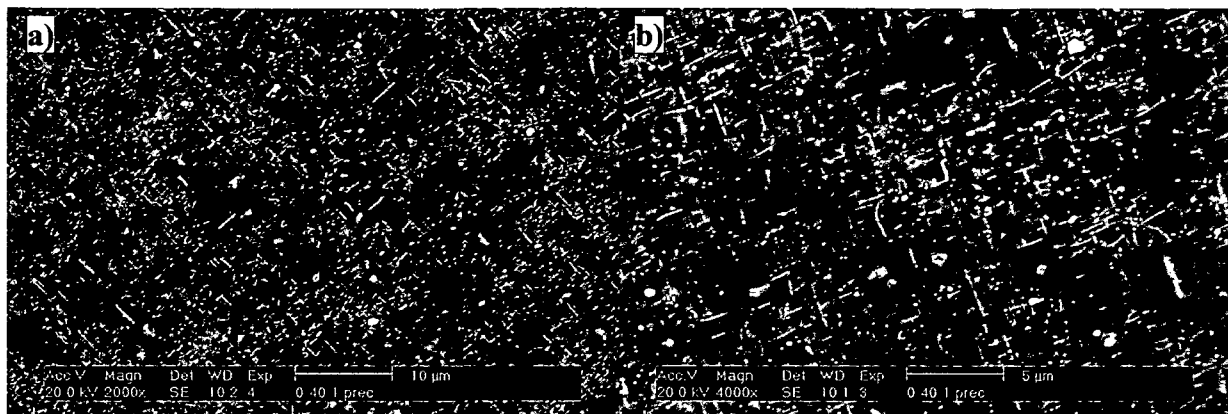


Figure 5.12 a) and b). Mg_2Si precipitates in a 6061 unreinforced sample tested at 40MPa (exposure time=210hr).

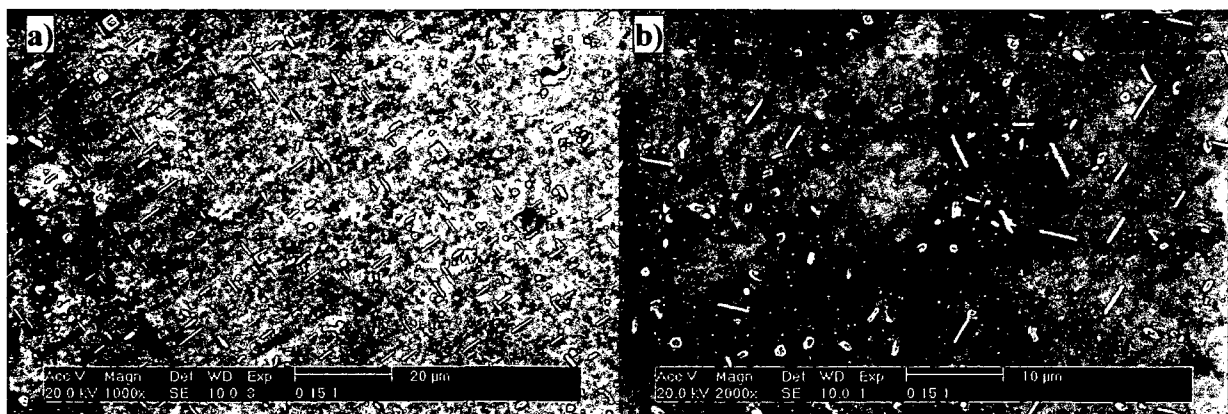


Figure 5.13 a) and b). Mg_2Si precipitates in a 6061 unreinforced sample tested at 15MPa (exposure time=715hr).

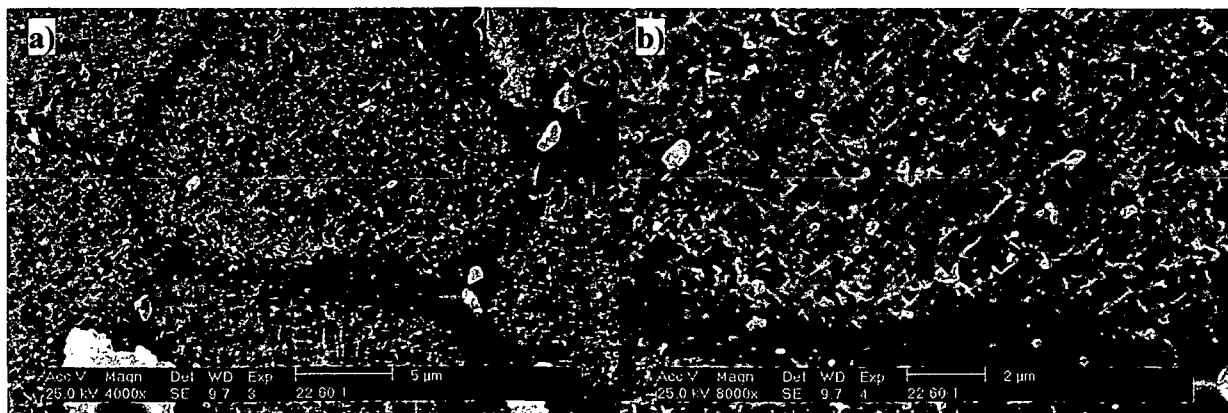


Figure 5.14 a) and b). Mg_2Si precipitates in a 6061/ Al_2O_3 /22p sample tested at 60MPa (exposure time= 5.1hr).

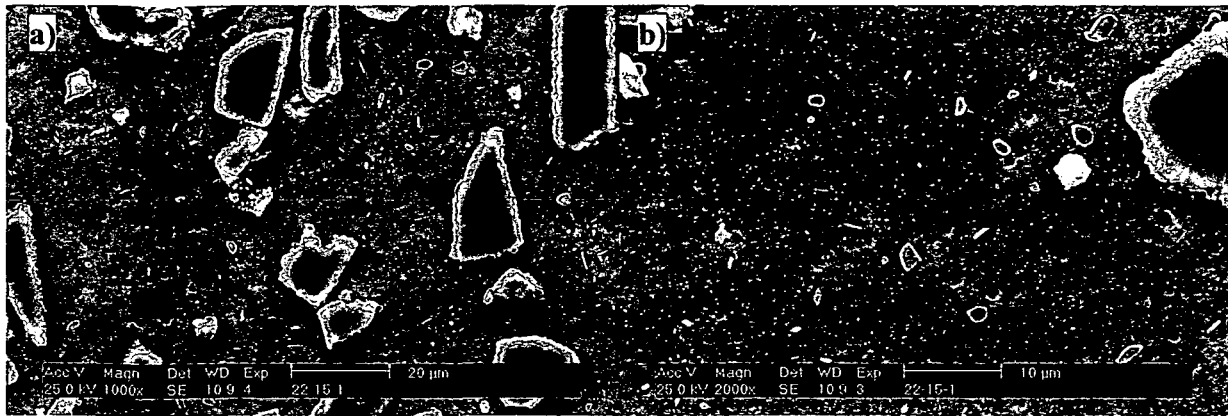


Figure 5.15 a) and b). Mg_2Si precipitates in a 6061/ Al_2O_3 /22p sample tested at 15MPa (exposure time=2341hr).

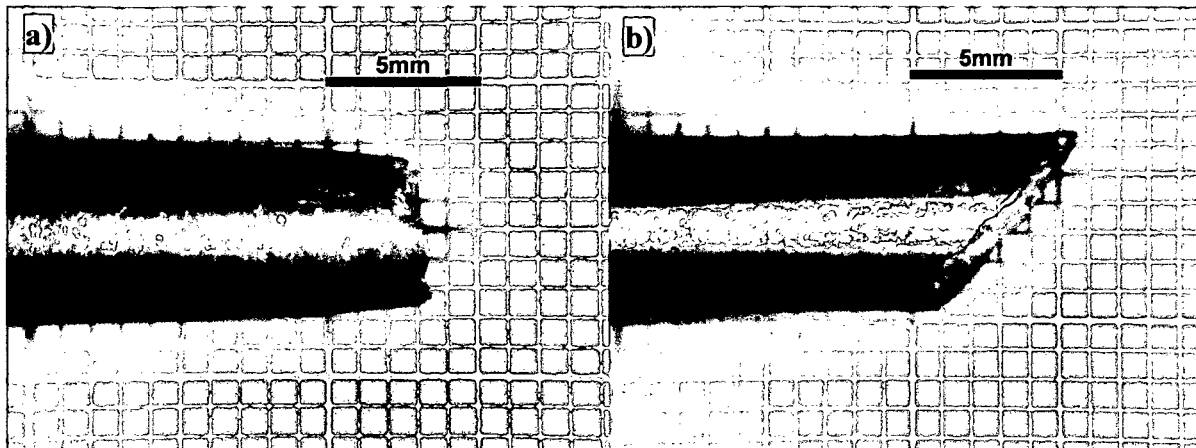


Figure 5.16. Profile of fracture surfaces after creep rupture for AlSi12CuMgNi a) and AlSi12CuMgNi/ Al_2O_3 /15s b).

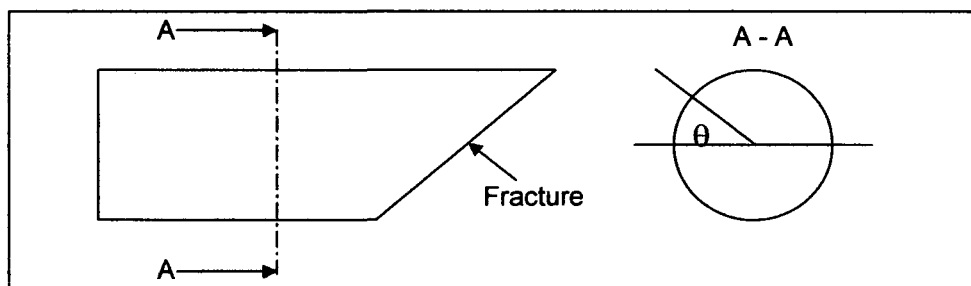


Figure 5.17. Scheme of the cross section A-A investigated in Figure 5.18 to Figure 5.22 in order to determine the orientation of the plane of the fibres respect to the fracture surface of the SFRM composites. θ represents the orientation angle of the plane of the fibres.

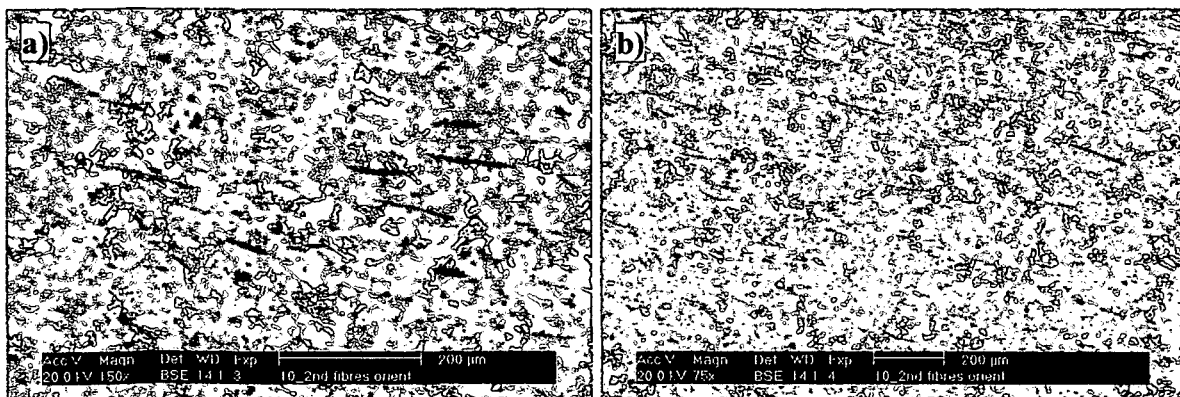


Figure 5.18 a) and b). Cross section A-A of a 10vol% fibre reinforced sample (creep test corresponding to Figure 5.4 a) and b)). θ is approximately 10° .

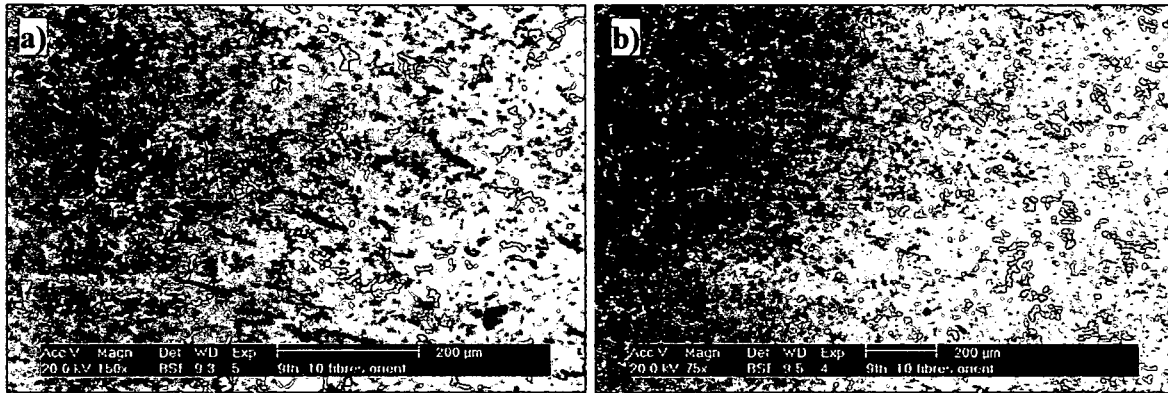


Figure 5.19 a) and b). Cross section A-A of a 10vol% fibre reinforced sample (creep test corresponding to Figure 5.4 i) and j)). θ is 0-15°.

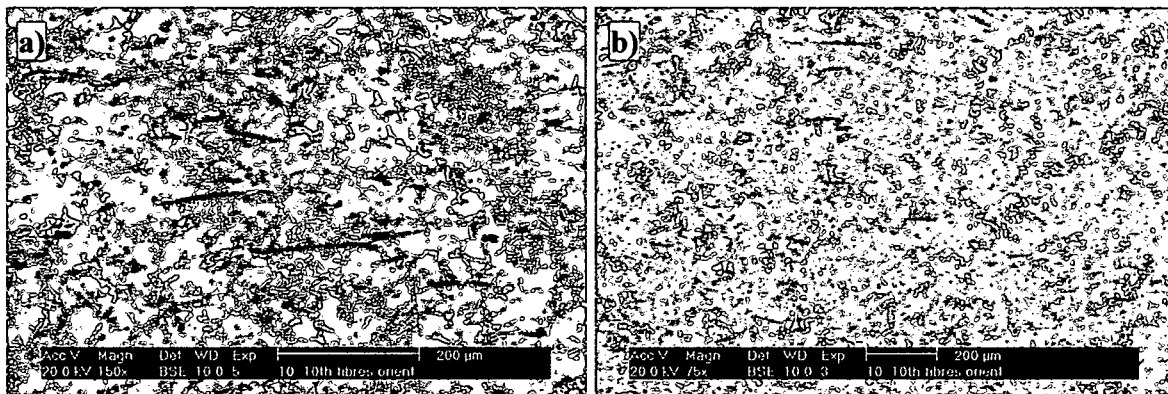


Figure 5.20 a) and b). Cross section A-A of a 10vol% fibre reinforced sample (creep test corresponding to Figure 5.4 m) and n)). θ is approximately 0°.

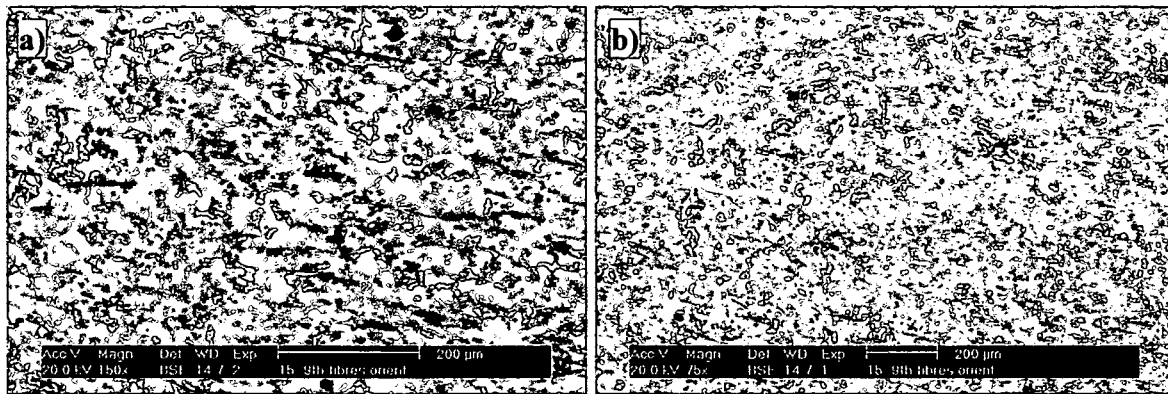


Figure 5.21 a) and b). Cross section A-A of a 15vol% fibre reinforced sample (creep test corresponding to Figure 5.5 m) and n)). θ is approximately 0°.

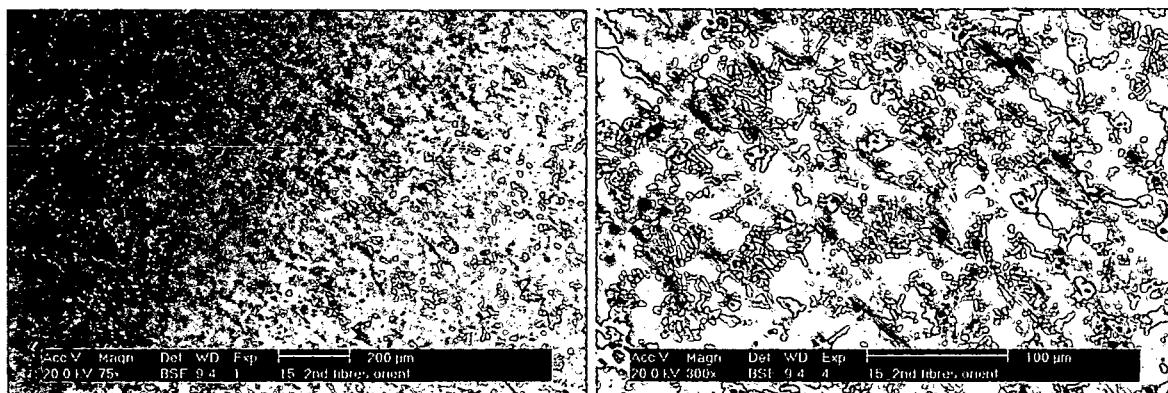


Figure 5.22 a) and b). Cross section A-A of a 15vol% fibre reinforced sample (creep test corresponding to Figure 5.5 c) and d)). θ is approximately 45°.

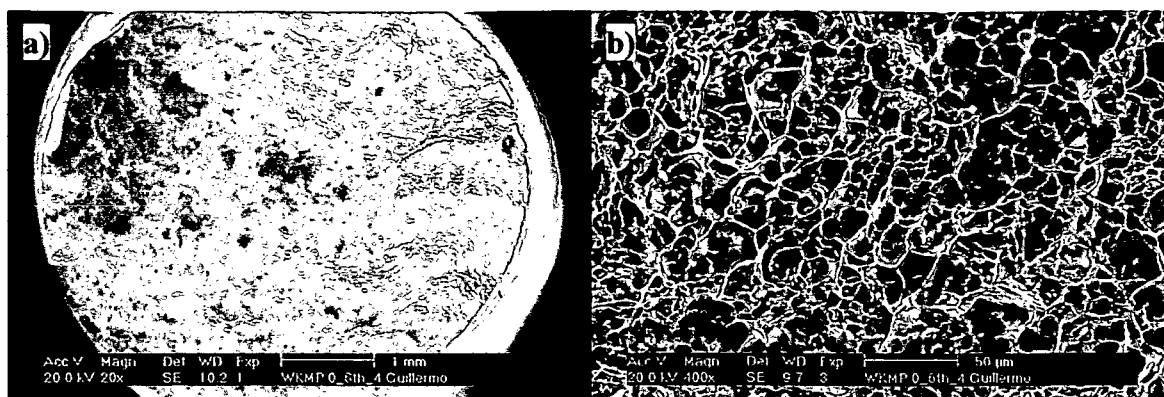


Figure 5.23 a) and b). Surface of an AlSi12CuMgNi sample fractured at 40MPa.

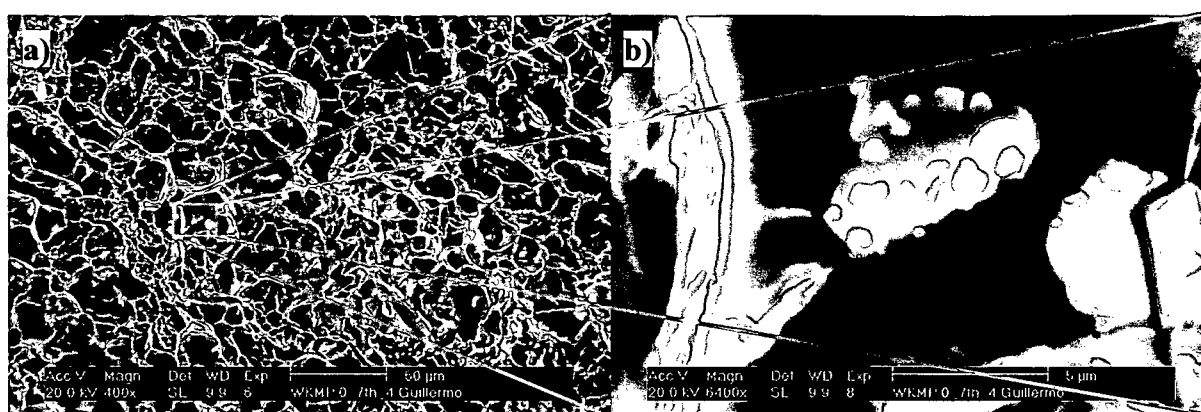


Figure 5.24. Mg_2Si particle inside a dimple. Note the presence of particles containing Cu on the Mg_2Si platelet.

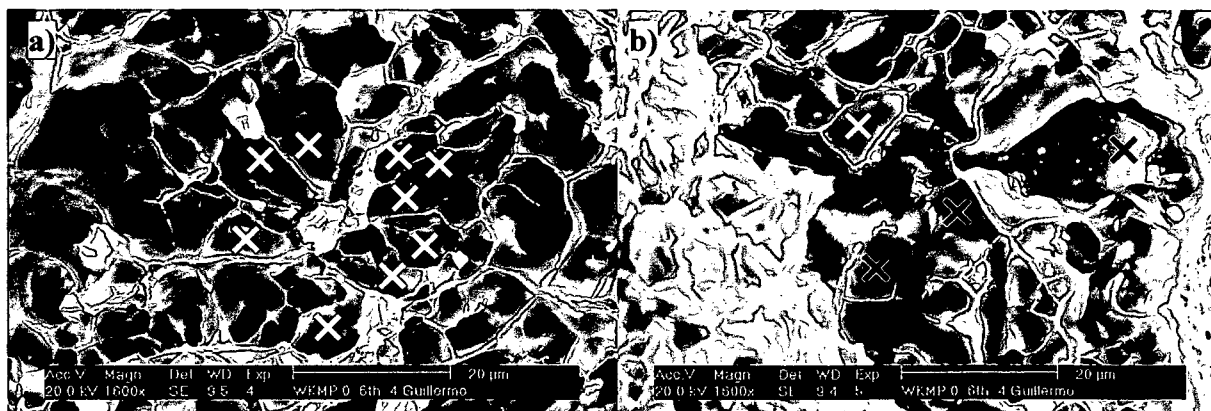


Figure 5.25. Dimple like structure on the fracture surface of an AlSi12CuMgNi sample. The white crosses correspond to eutectic Si dimples while the black ones correspond to intermetallic phases containing Fe and Ni.

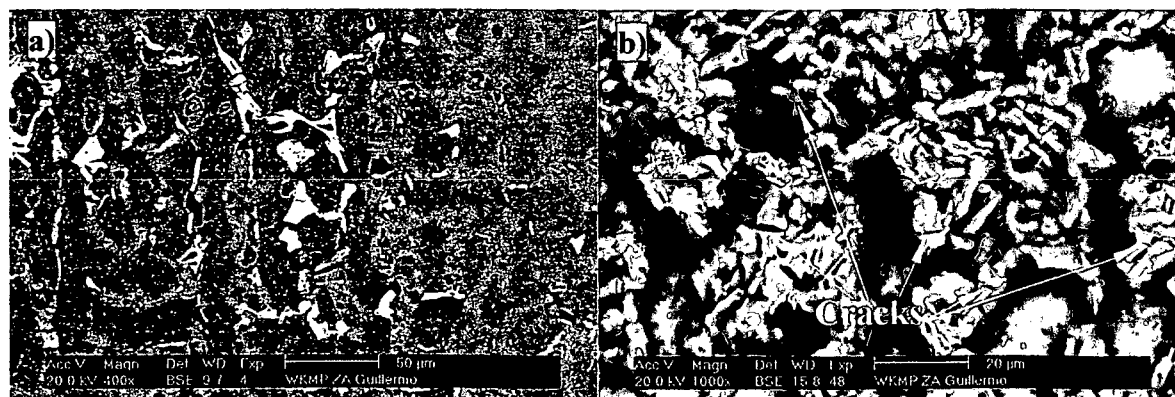


Figure 5.26. AlSi12CuMgNi near the fracture zone: a) Longitudinal section showing intermetallic phases (white) and eutectic Si (light grey). b) Deep etched sample showing cracks in the Si structure.

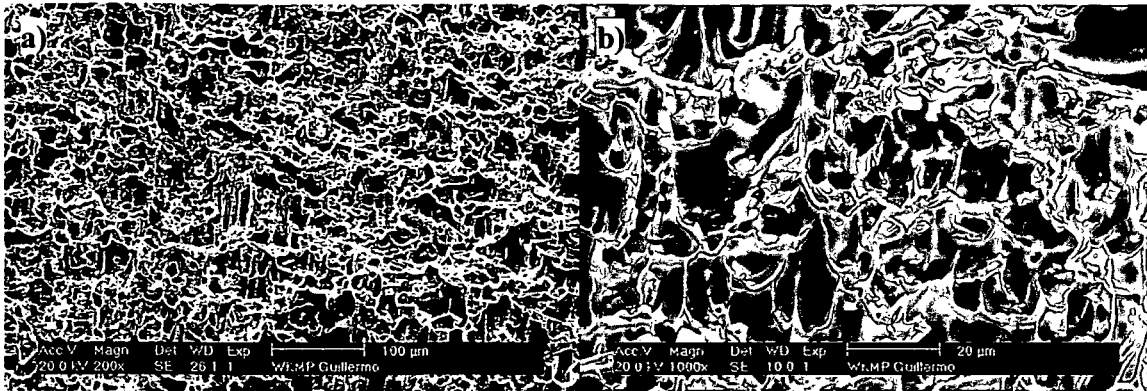


Figure 5.27 a) and b). Fracture surface of an AlSi12CuMgNi/Al₂O₃/10s sample at different magnifications (test Figure 5.4 c) and d)).

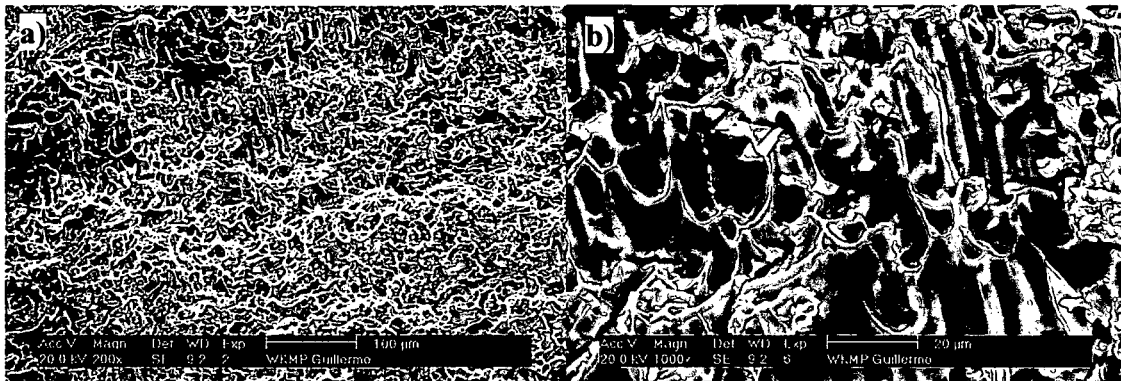


Figure 5.28 a) and b). Fracture surface of an AlSi12CuMgNi/Al₂O₃/15s sample at different magnifications (test Figure 5.5 c) and d)).

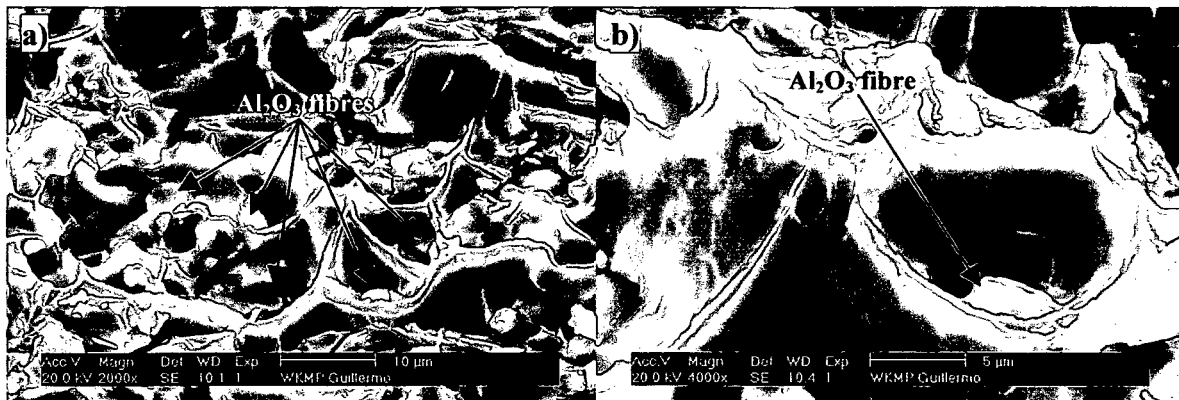


Figure 5.29 a) and b). Broken fibres inside of dimples for a 10% SFRM sample.



Figure 5.30. Decohesion of fibres aligned perpendicularly to the tensile direction (vertical axis) for: a) AlSi12CuMgNi/Al₂O₃/10s and b) AlSi12CuMgNi/Al₂O₃/15s.

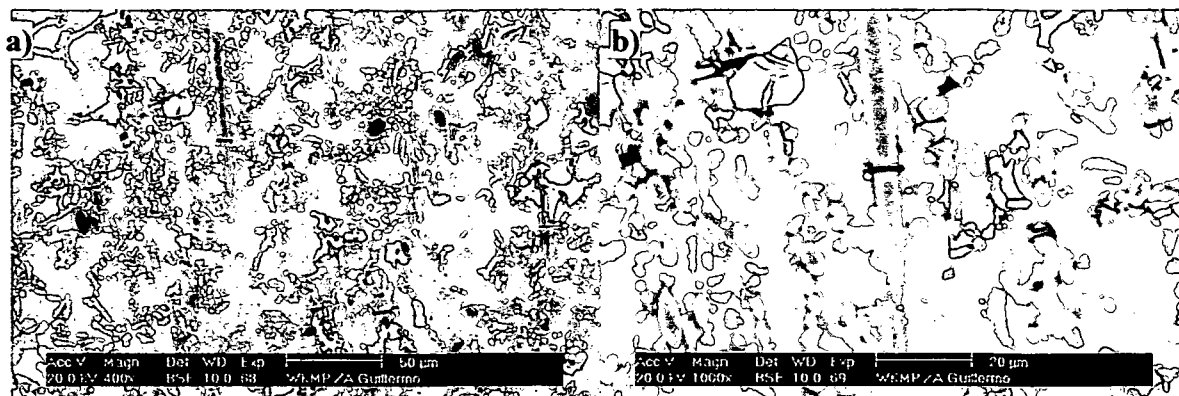


Figure 5.31 a) and b). Longitudinal section of a fractured AlSi12CuMgNi/Al₂O₃/15s sample after creep. (The vertical axis corresponds to the tensile axis).



Figure 5.32 a) and b). Longitudinal sections of a fractured AlSi12CuMgNi/Al₂O₃/10s sample after creep. (The vertical axis corresponds to the tensile axis).

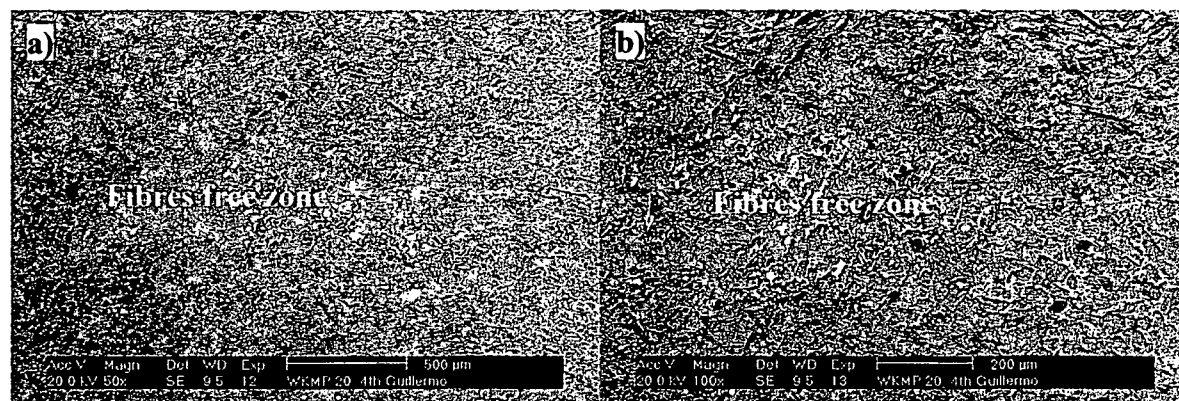


Figure 5.33 a) and b). Different magnifications of a fracture in the fibre preform for a AlSi12CuMgNi/Al₂O₃/20s sample tested during approximately 2200hr (see Figure 5.6 a) and b)) (horizontal axis is the tensile axis).

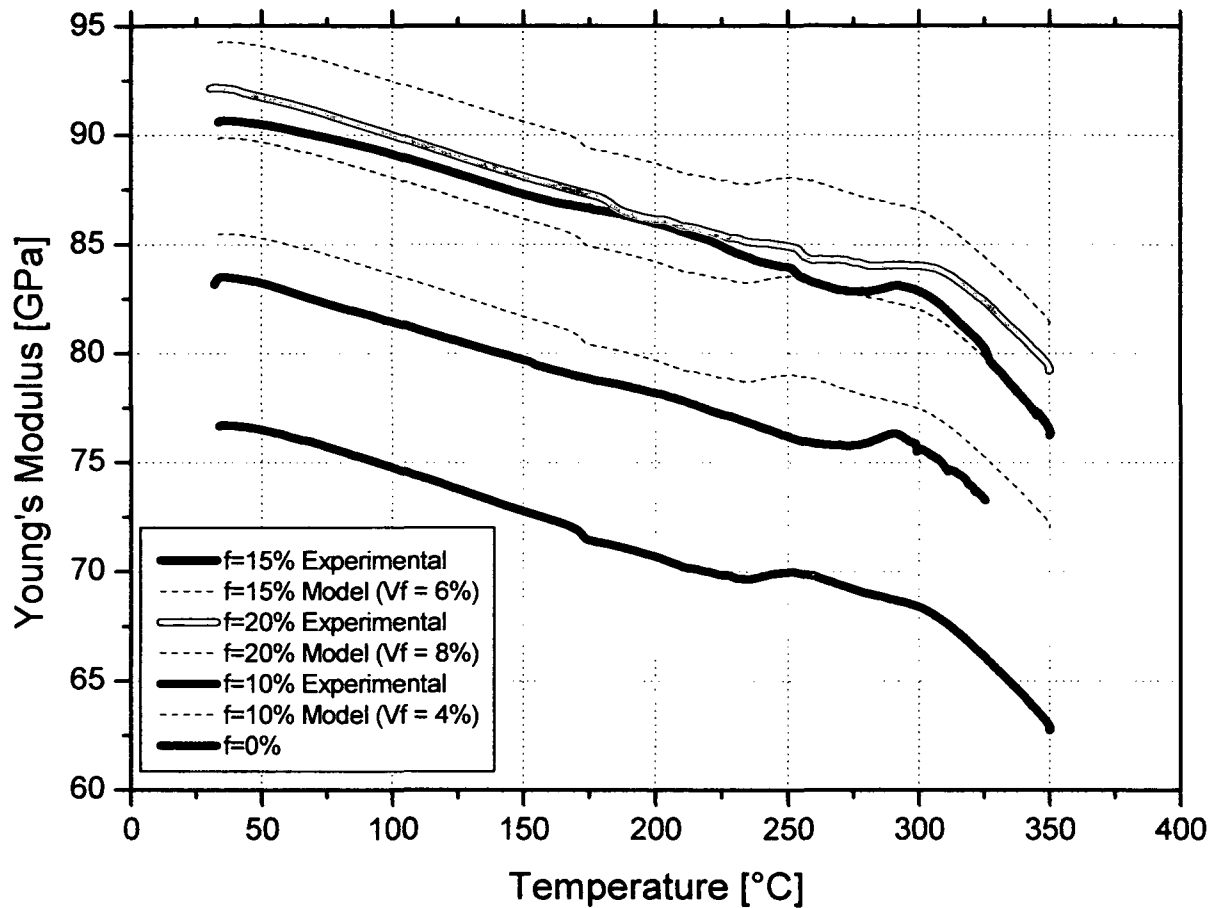


Figure 5.34. Values of Young's modulus as a function of temperature for the three reinforced and the unreinforced cast alloys showing experimental results obtained by DMA measurements as well as modelled results obtained by means of the Eshelby's method based on the results of the matrix.

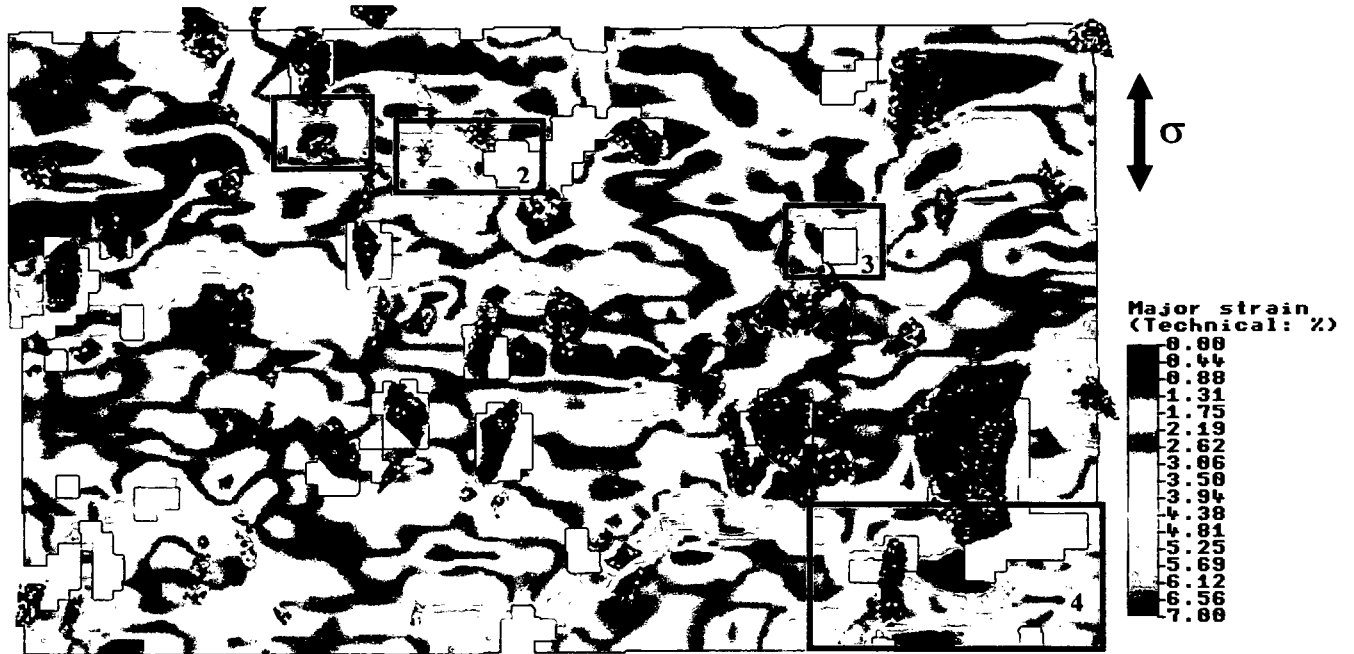


Figure 5.35. Strain field obtained for a 6061/ Al_2O_3 /10p sample after a creep test at 300°C. The global elongation of the region where the picture was taken amounts to 2.5%.

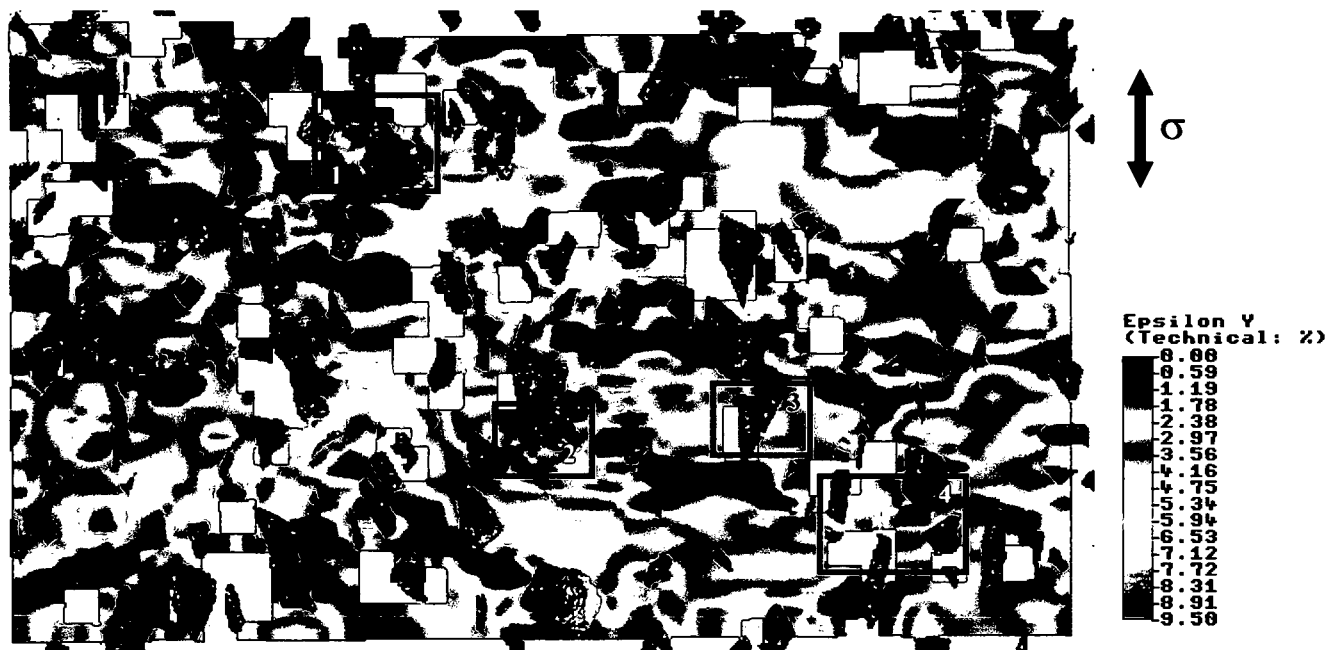


Figure 5.36. Strain field obtained for a 6061/ Al_2O_3 /22p sample after a creep test at 300°C. The global elongation of the region where the picture was taken corresponds to 2.9%.

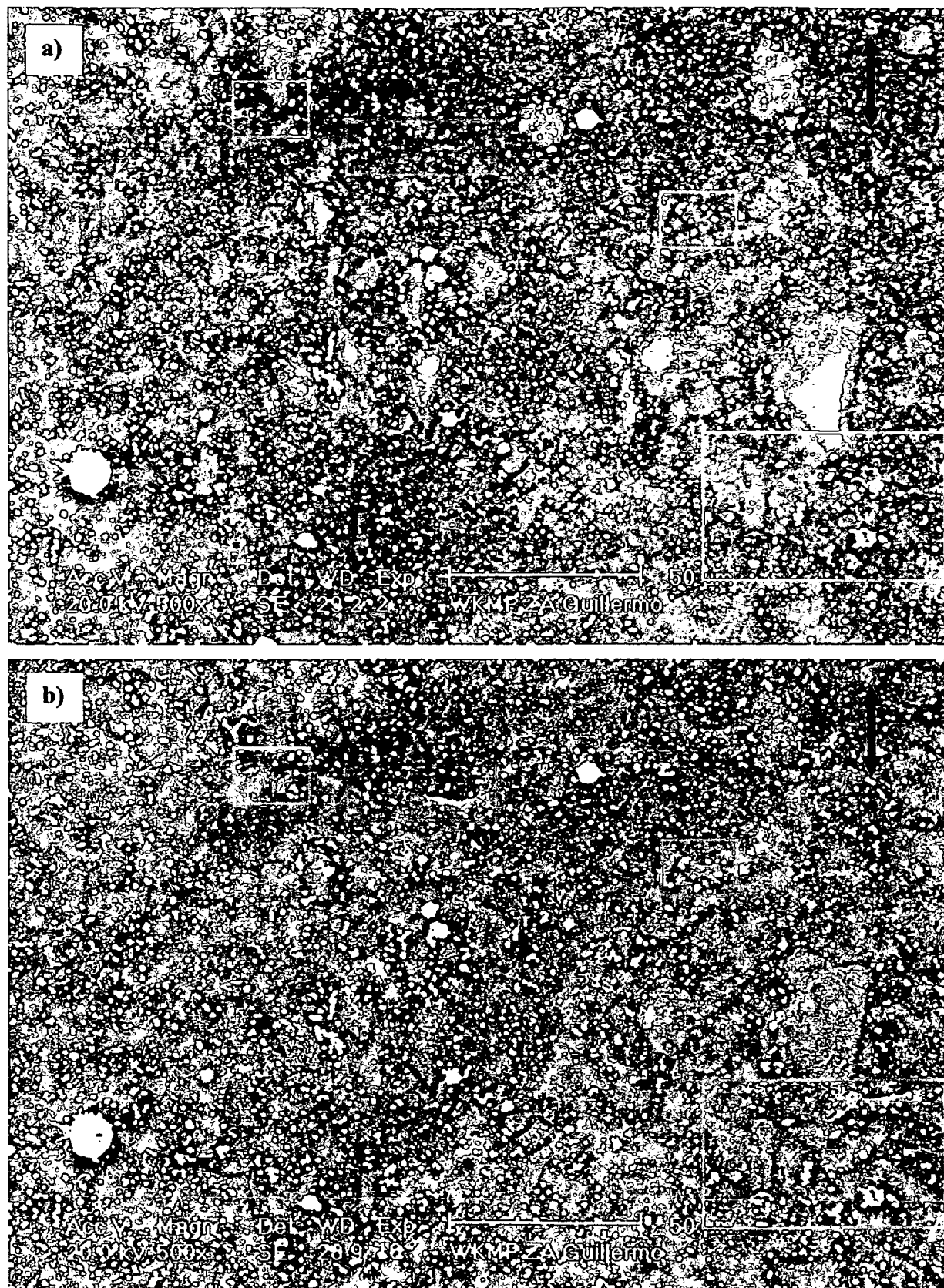


Figure 5.37. SEM pictures of the region for which the strain field shown in Figure 5.35 (6061/Al₂O₃/10p composite) was calculated: a) prior to deformation and b) after creep deformation. The rectangles show zones where high deformation is observable just by eye which is confirmed by the results of the strain field.

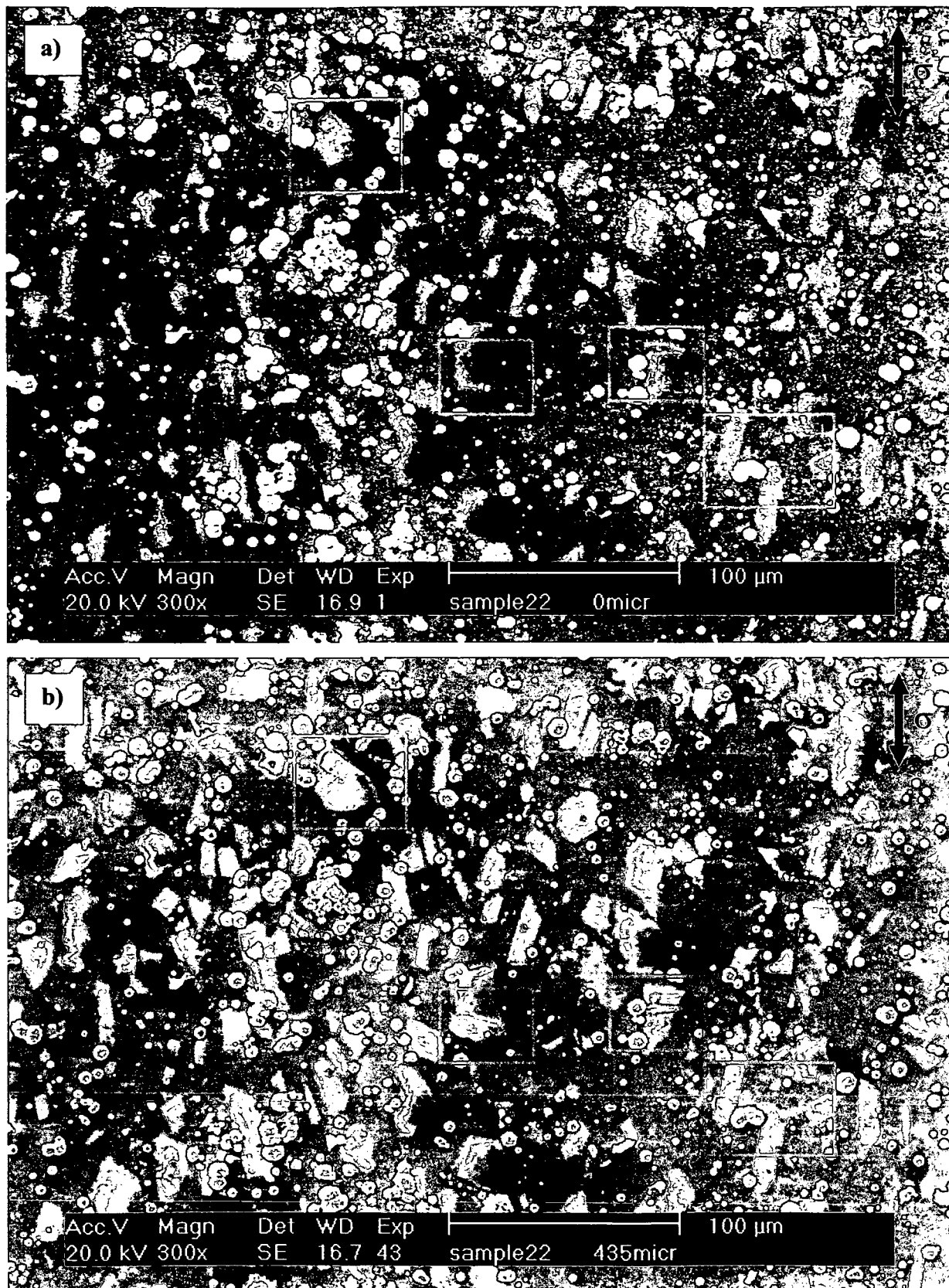


Figure 5.38. SEM pictures of the region for which the strain field shown in Figure 5.36 (6061/Al₂O₃/22p composite) was calculated: a) prior to deformation and b) after creep deformation. The rectangles show zones where high deformation is observable just by eye which is confirmed by the results of the strain field.

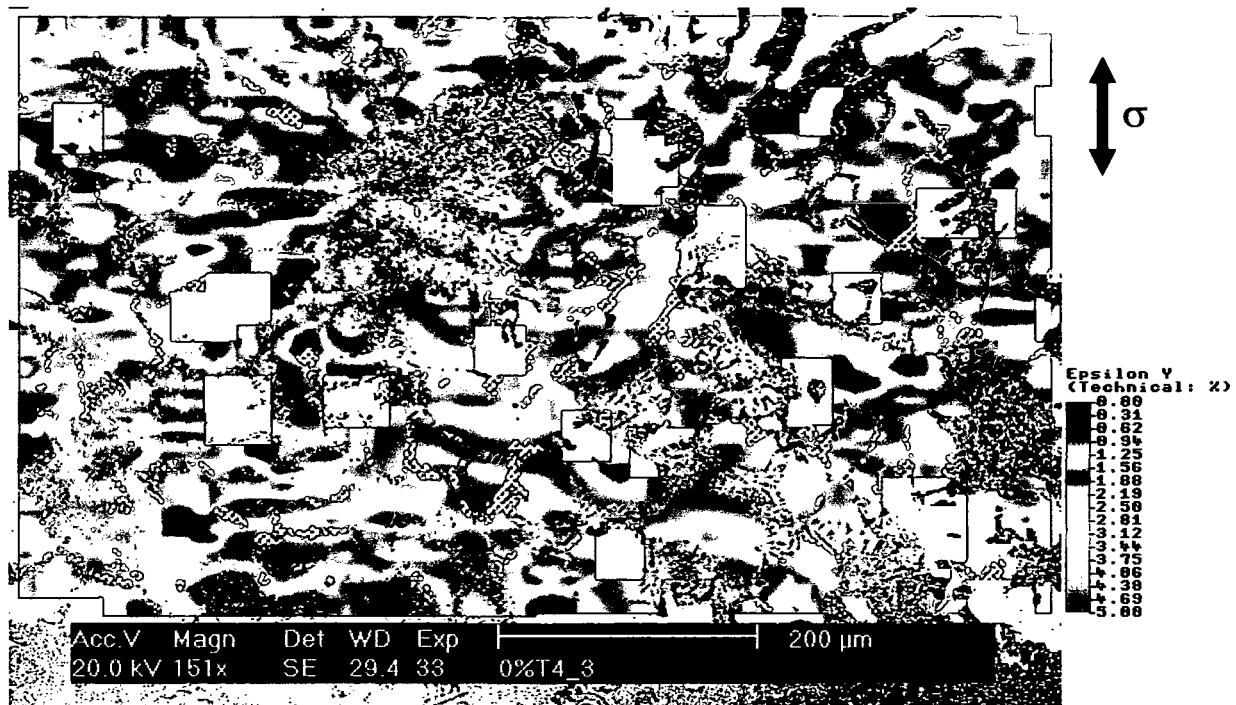


Figure 5.39. Strain field obtained for an unreinforced AlSi12CuMgNi sample after a creep test at 300°C. The global elongation of the region where the picture was taken corresponds to 1.7% strain. The dark regions correspond to the Si-eutectic phase while the white ones correspond to the intermetallic phases.

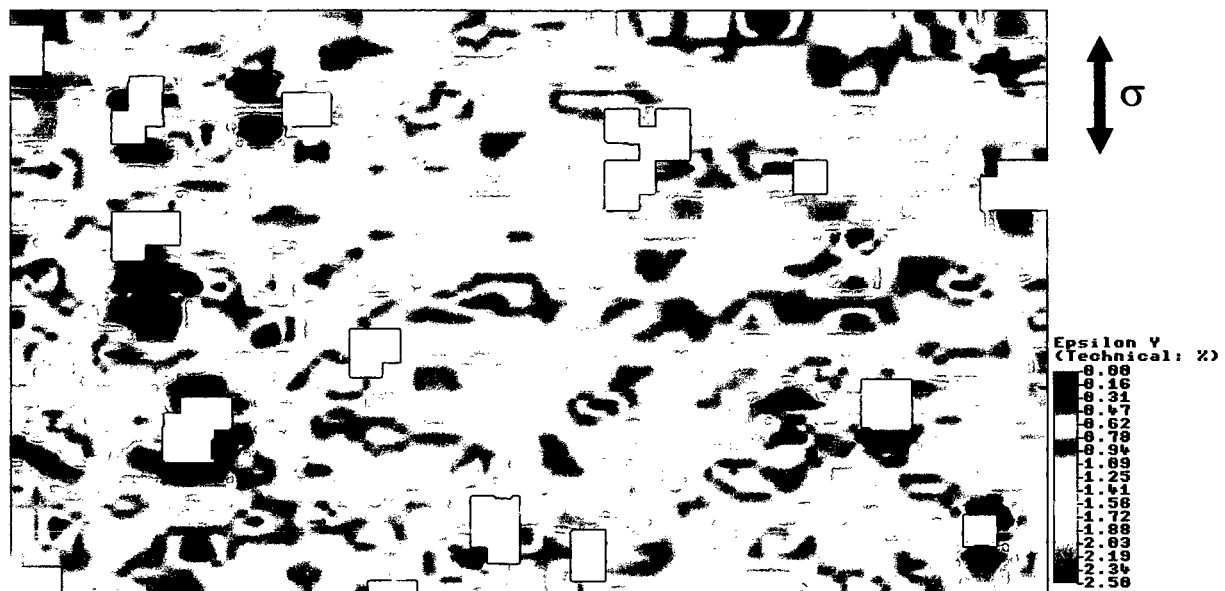


Figure 5.40. Strain field obtained for a AlSi12CuMgNi/Al₂O₃/20s sample after a creep test at 300°C. The global elongation of the region where the picture was taken corresponds to 0.78% strain.

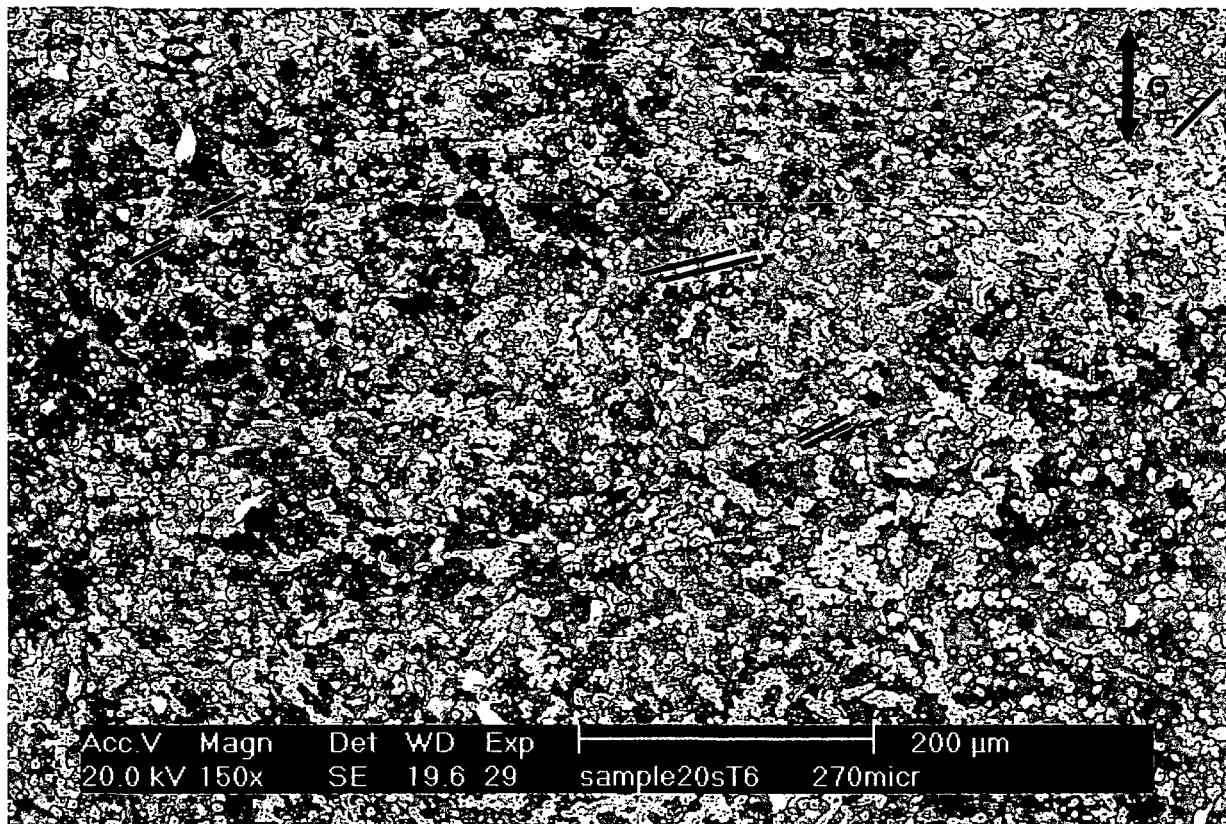


Figure 5.41. SEM pictures of the region for which the strain field shown in Figure 5.40 was calculated (AlSi12CuMgNi/Al₂O₃/20s).

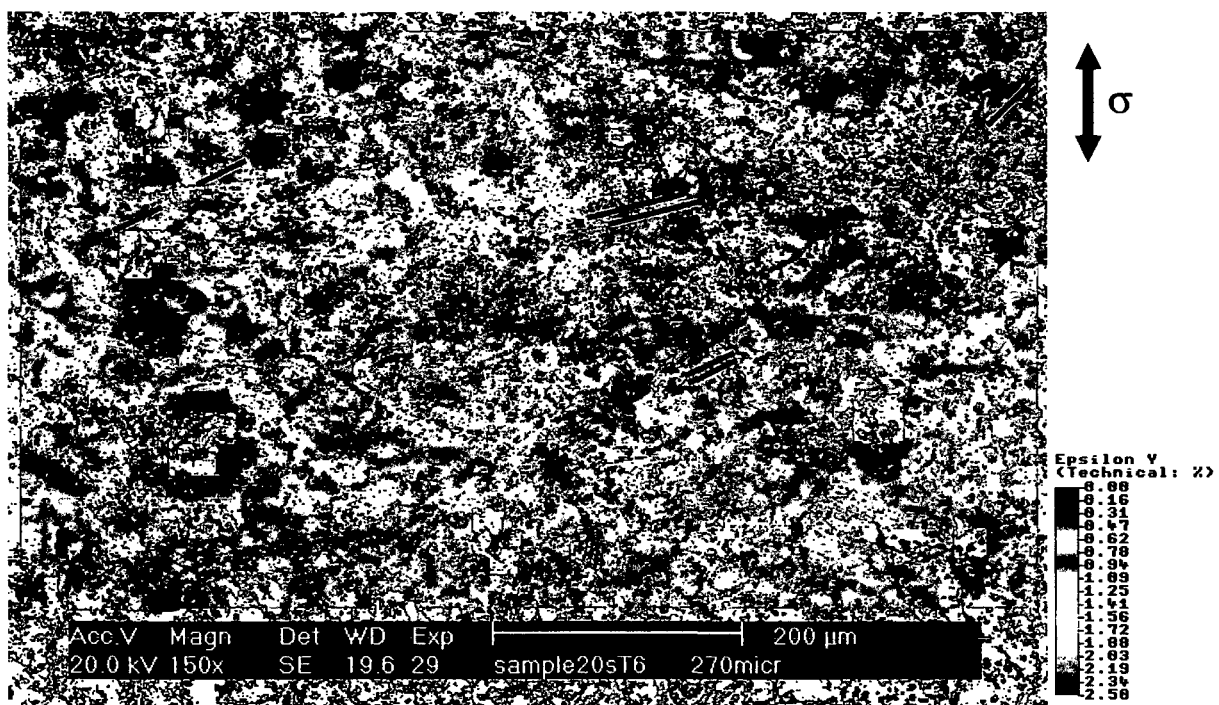


Figure 5.42. Overlapping of the strain field obtained for an AlSi12CuMgNi/Al₂O₃/20s sample after a global strain of 0.78% (Figure 5.40) and the SEM picture of the analysed region (Figure 5.41) (some fibre positions are marked).

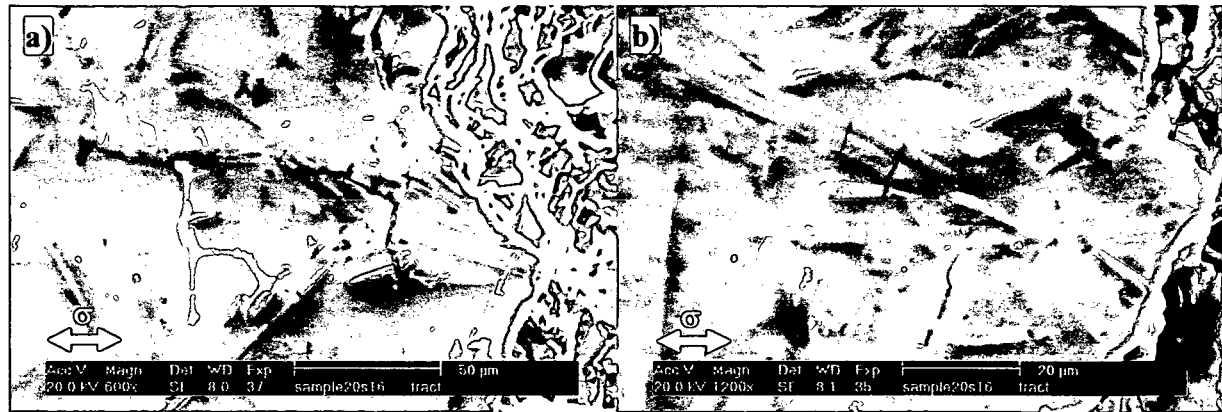


Figure 5.43 a) and b). Longitudinal section of a fractured sample tested under creep conditions using the In Situ stage.

6 Interpretation of Results

This chapter contains the interpretation and correlation of the results shown in Chapter 5 in order to achieve a better understanding of the behaviour of materials under diverse experimental conditions which are the basis for the discussion carried out in Chapter 7.

6.1 Isothermal Creep

6.1.1 6061 and 6061/Al₂O₃/22p

6.1.1.1 Creep Law (σ vs $\dot{\epsilon}_{\min}$)

The values of minimum creep rate vs. stress for each experiment and for both materials are plotted logarithmically in Figure 6.1 in order to investigate the dependence of the minimum creep rate on stress. With the help of this figure, the possible creep mechanisms were identified by means of the stress exponent n . The values of n obtained for different ranges of load are shown in Table 6.1 for the unreinforced material and for the metal matrix composite, respectively. These values of n show that it is not necessary to incorporate a threshold stress in the analysis of the creep behaviour for stresses up to 50MPa as it is usually done for PRM [103, 104, 105]. For stresses higher than 50MPa, the stress exponent increases according to power law breakdown [106].

σ_A	15-50MPa	50-70MPa
6061	2.2	7.0
6061/Al ₂ O ₃ /22p	3.1	5.4

Table 6.1. Stress exponent n for 6061 and 6061/Al₂O₃/22p.

The stress exponent obtained for the PRM clearly indicates that the mechanism governing creep deformation corresponds to viscous glide of dislocations. On the other hand, for the unreinforced matrix the obtained value of $n = 2.2$ does not correspond to a creep mechanism explained by the currently available theoretical models. To understand this behaviour, it is necessary to consider that the microstructure of the investigated matrix alloy does not remain constant during the tests as can be observed in Figure 5.11, Figure 5.12 and Figure 5.13 where the coarsening of Mg₂Si precipitates due to an overaging effect of the matrix takes place during the experiment. This results in a softening of the matrix that provokes that at smaller stresses (longer exposure times) the material creeps at a higher creep rate than it may result if the microstructure remained constant during the test. Thus, there exist

a time dependent threshold stress σ_{th} due to the effect of the precipitates which decreases with increasing exposure times (decreasing the applied load) and an experimental creep exponent n_{app} which will be larger than three for higher stresses and will decrease with decreasing the applied load. For the case in which the size of the precipitates will not produce a σ_{th} then, the creep exponent will have a value of three. Summarizing, the creep law governing the behaviour of the unreinforced matrix will be:

$$\dot{\epsilon}_{min} \propto (\sigma_A - \sigma_{th}(t))^n \quad (6.1)$$

where σ_A is the applied load and $\sigma_{th}(t)$ is the time dependent threshold stress due to the presence of “active” precipitates (precipitates contributing to the strengthening of the matrix). However, this equation results in a different n_{app} (different slope) for every tested load and does not represent the curve with slope $n = 2.2$ obtained from Figure 6.1. The shadowed region in this Figure illustrates this “detachment” of the creep exponent from the theoretical values due to the overaging effect. The PRM alloy suffers also coarsening of the precipitates (see Figure 5.14 and Figure 5.15) but as already stated, this effect is much faster in the composite than in the unreinforced alloy resulting in a smaller hardening effect of the matrix due to the presence of Mg_2Si precipitates. Furthermore, Figure 6.1 also shows that the minimum creep rate for the matrix is considerably lower than that for the reinforced material and therefore a load transfer from the matrix to the particles is improbable. This kind of behaviour has been found in other investigations conducted in similar PRM [67, 53, 54]. On the other hand, the rate of formation and annihilation of the dislocations subjected to thermally activated mobility is higher in the PRM than in the unreinforced matrix [107, 108]. This difference corresponds to an apparent tensile stress of about 25MPa in the matrix of the composite, enhancing creep in addition to the external load in the range of 25 to 50MPa. At smaller stresses, the stress difference for the same strain rate decreases.

6.1.1.2 Time – Strain – Stress relationship

Figure 6.2 a) and b) show the dependence of stress on the time to reach 0.2 and 1% strain as well as fracture for all the investigated stresses. A marked linear tendency is seen in the stress – creep time curve for values of time to 1% strain up to strain at fracture for both the unreinforced and the particle reinforced wrought alloy but with a remarkable difference: the matrix shows a change in the slope at a stress between 40 and 50MPa (above 100h exposure time), while the composite maintains the same slope for a wider range of loads tested (20-60MPa). The change in the $\sigma_{\%}(t)$ slope (i.e. acceleration of creep) is attributed to the overaging becoming significant above 100h of exposure.

The same data as in Figure 6.2 are replotted in Figure 6.3 for the values of $t_{1\%}$ and time to rupture to facilitate comparison between the reinforced and unreinforced materials. It can be seen that the values of $t_{1\%}$ for the composite are below the curves of the matrix down to stresses of about 15MPa where the points approach each other due to the change in slope. This indicates that for a determined condition of stress and temperature the creep deformation of the unreinforced material will always be smaller than the deformation of the composite after the same time elapsed. Only for small stresses (<15MPa), i.e. for long term exposures the PRM exhibits a longer service life time than the matrix.

6.1.1.3 Elongation at rupture

Figure 6.4 shows the correlation of the elongation at rupture to the time to fracture for the matrix and the composite. The observed behaviour shows a marked difference between the two materials. While the matrix shows a significant increase of the elongation at rupture above 400h of time to failure, which corresponds to approximately less than 20MPa where an increase in the deformation and of the tertiary creep rate takes place, the composite shows an approximately constant increase through all the logarithmic failure time scale. Although the ductility of the PRM increases significantly owing to creep deformation, the final strain in the composite is usually smaller than those in the matrix. The tertiary damage rate by coalescence of pores (see Figure 6.5 a) and b) where the creep curves for the matrix and the PRM at 15MPa are replotted in the same graph to facilitate the comparison) is much smaller for the PRM than for the matrix.

6.1.2 *AlSi12CuMgNi*, *AlSi12CuMgNi/Al₂O₃/10s*, *AlSi12CuMgNi/Al₂O₃/15s* and *AlSi12CuMgNi/Al₂O₃/20s*

6.1.2.1 σ vs $\dot{\epsilon}_{\min}$

The dependence of minimum creep rate on stress is depicted in Figure 6.6 to Figure 6.9 for both the unreinforced and short fibre reinforced cast alloy together with the values obtained for the creep exponent n . Figure 6.7 a), Figure 6.8 a) and Figure 6.9 a) show the results during the first loading stage, while Figure 6.7 b) Figure 6.8 b) and Figure 6.9 b) illustrate the results after a temporary increase of the load. Note the values of $n=3$ for the first loading, as it is usually expressed using a Norton's law. After a temporary load increase, n_2 increases with the volume fraction of reinforcement in the case of the composites. Such a situation does not take place for the unreinforced alloy where no difference can be found between first loading and reduction of load. A possible reason for this behaviour will be discussed in Paragraph 7.1.2.

A creep exponent of $n = 3 \pm 1$ fits for the matrix below 35MPa. At higher stresses, n approaches the value of $n = 6.3$ obtained in [109] for an AlSi7Cu3Mg alloy. A 15vol% short fibre reinforced composite was also theoretically investigated in [42] in similar load conditions and the value of $n=2.4$ obtained defers slightly from the value found in our investigations during the first loading for loads up to 40MPa.

The 3 SFRM exhibit significant higher creep resistance than the unreinforced matrix for the investigated loads. The 15vol% fibre reinforced composite shows the highest creep resistance. The 20vol% SFRM, as may have been suspected owing to the defects described in Paragraph 3.2.4, shows a lower creep resistance than the 15vol% SFRM and very similar to the 10vol% SFRM during the first loading but lower after a temporary increase of load.

6.2 In Situ Tensile Creep Tests

6.2.1 6061/Al₂O₃/10p and 6061/Al₂O₃/22p

The main characteristics of the strain fields determined for both PRM and depicted in Figure 5.35 and in Figure 5.36 are:

- a) Deformation bands build up in the matrix of both materials during tensile creep conditions. Such behaviour was also previously observed during room temperature tensile tests [90-91] and is predicted by tensile creep FEM calculations [81].
- b) Particles aligned in the direction of load tend to show high localised deformation at their ends and this is usually the main path of deformation bands.
- c) Particle fracture is observed in larger particles for both materials but more often for the 22vol% composite. This causes regions of high deformation in the matrix.
- d) Particle free zones are always regions of high strains except in the case where broken particles are found close to these regions. Here, the deformation is displaced to the surrounding of the broken particle.

- e) The role played by the clustering of particles is not so clear as in the case of RT tensile tests. The latter showed that particles clusters result in zones with the lowest level of deformation. However, the strain fields obtained in this work show that in some cases, the clustering of particles can produce areas with a considerable amount of deformation.

Figure 6.10 and Figure 6.12 show the evolution of the local strain during an In Situ creep test presented as frequency histograms for the 10vol% and 22vol% PRM. The global strain is considered only in the frame in which the SEM pictures were taken. The shape of the histograms are similar for both particle reinforced materials and indicate that during elongation not only the maximum is displaced to higher deformations but also the histogram is extended to higher values of strain and with a lower frequency value around this global strain.

Figure 6.11 shows a comparison between the local strain frequency of a RT tensile test and a creep test for similar deformation conditions (similar global strain) for a 6061/Al₂O₃/10p sample. There is a marked difference in the shape of these curves. While the sample subjected to RT deformation shows a practically symmetrical distribution of the local strain, the material under creep conditions shows, as already stated above, a trend to be affected by deformations of higher values of local strain. On the other hand, a similar analysis carried out for 6061/Al₂O₃/22p (see Figure 6.13) showed a similar distribution of the local deformations for these two different load conditions.

6.2.2 *AlSi12CuMgNi and AlSi12CuMgNi/Al₂O₃/20s*

Figure 6.14 shows the evolution of the local strain during an In Situ creep test presented as frequency histograms for the AlSi12CuMgNi matrix. Similarly to the PRM alloys, this material shows that the distribution of local deformation is displaced to higher values along the test and is increasing in width values for higher global strain conditions. At 3.45% creep strain, the strain distribution appears significantly wider showing again a tail at the higher end. This creep stage corresponds to the tertiary, where damage becomes significant (see Figure 5.26 a)).

Figure 6.15 shows the evolution of the local strain during an In Situ creep test presented as frequency histograms for the AlSi12CuMgNi/Al₂O₃/20s SFRM. There is a marked difference in comparison to the two PRM. While the latter showed a spreading towards higher local strain values as the In Situ creep test progresses, the short fibre composite shows a narrowing of the local strain distribution with an increase of the frequency

for values around the global strain of the sample. This may be an important result since it is an indication of the markedly different kinds of deformation behaviour presented by these two types of material and found during conventional tensile creep tests (see Paragraph 7.1.3).

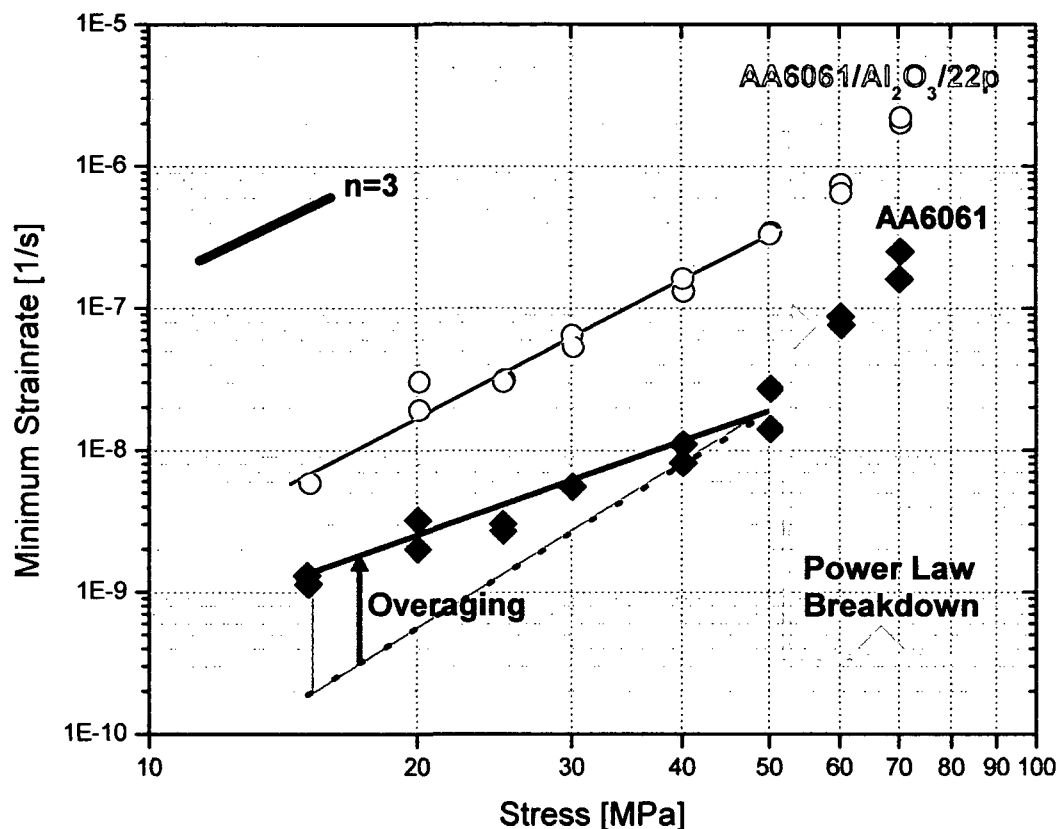


Figure 6.1. $\dot{\epsilon}_{\min}$ vs. σ curves for both unreinforced and reinforced wrought alloys showing slopes for stress exponent $n=1$ and stress exponent $n=3$. The shadowed region shows the effect of the overaging due to the exposure time.

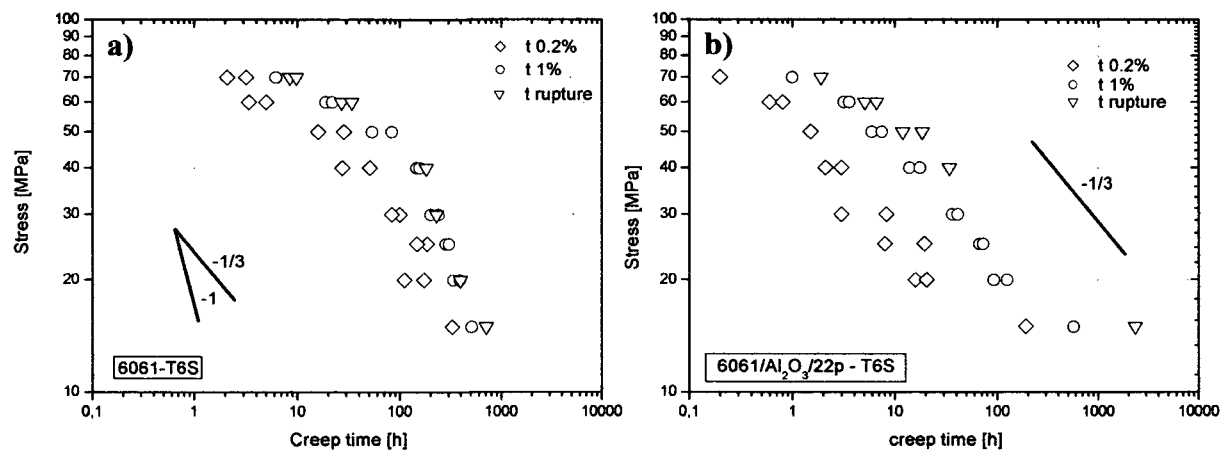


Figure 6.2. Dependence of stress on time for different values of strain for: a) 6061 and b) 6061/Al₂O₃/22p.

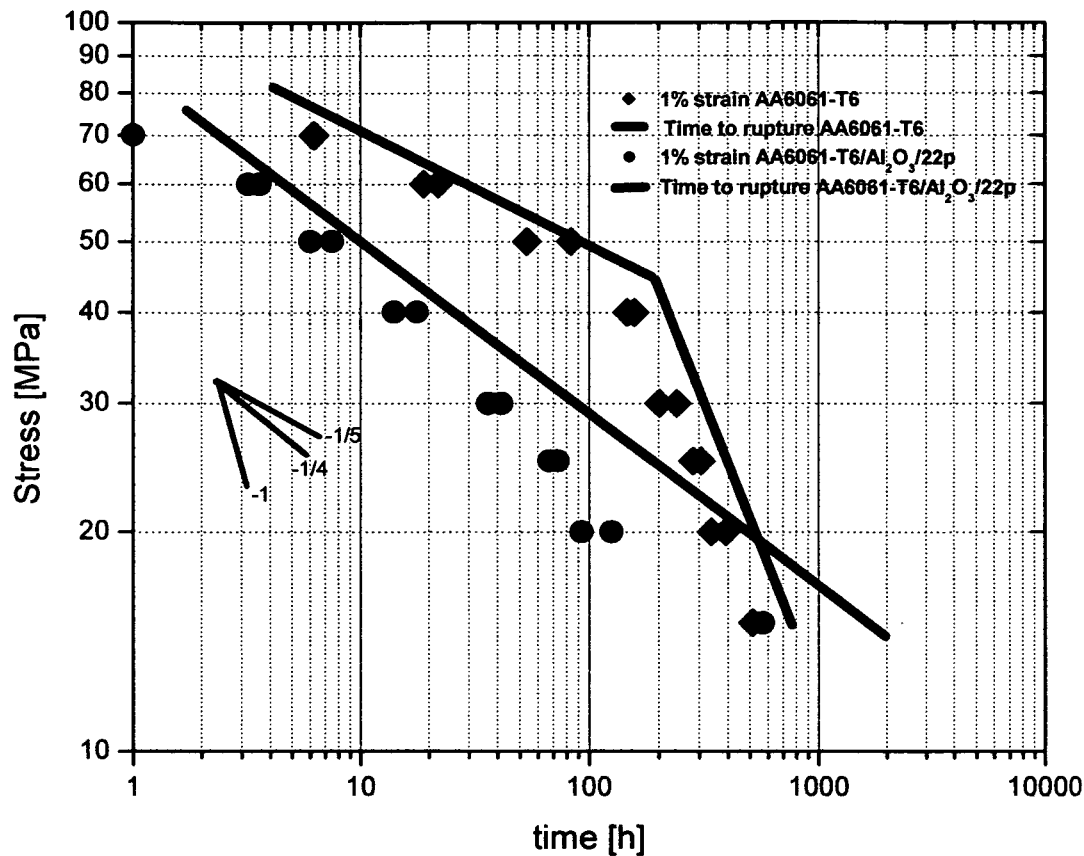


Figure 6.3. Stress vs. $t_{1\%}$ and rupture time for the two investigated materials.

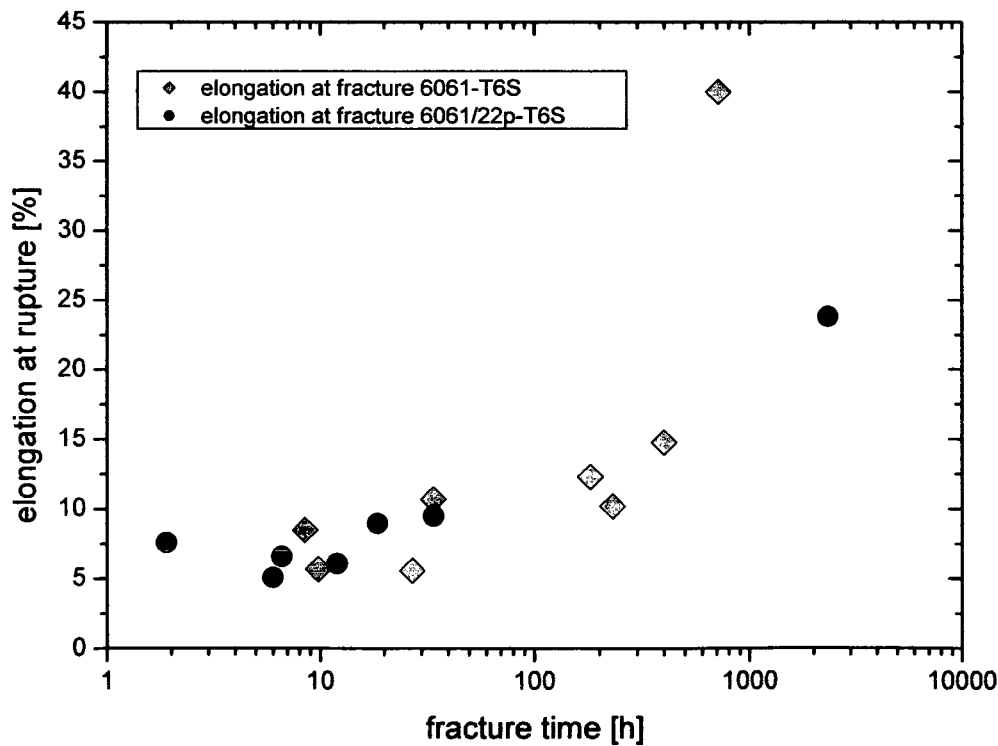


Figure 6.4. Correlation of time to failure to elongation at rupture for both the reinforced and the unreinforced wrought alloy.

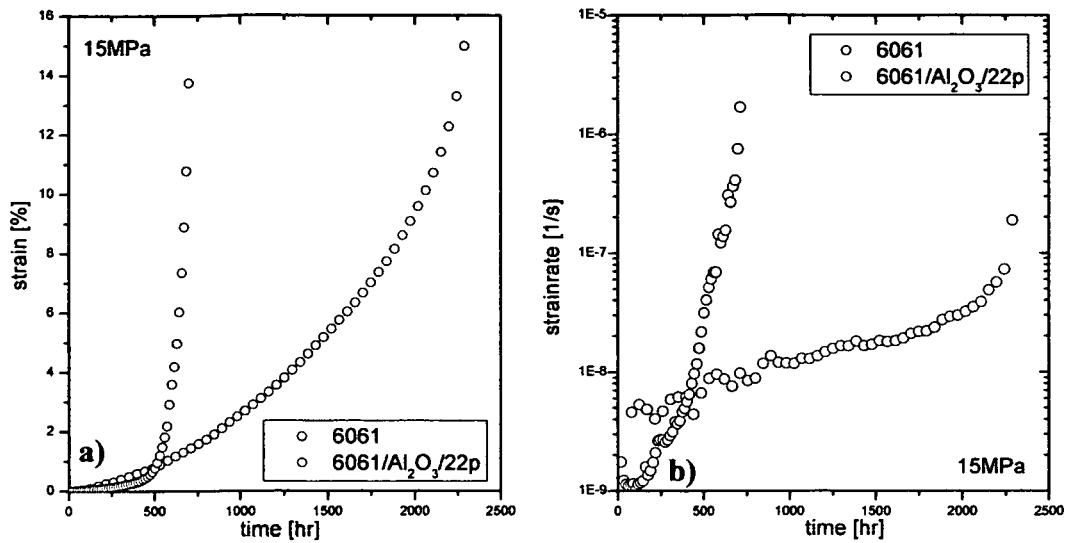


Figure 6.5. ϵ vs. t a) and $\dot{\epsilon}$ vs. t b) curves for tests carried out at 15MPa for the unreinforced and the particle reinforced wrought alloy showing that the damage rate (creep rate acceleration) for the PRM is much smaller than for the matrix.

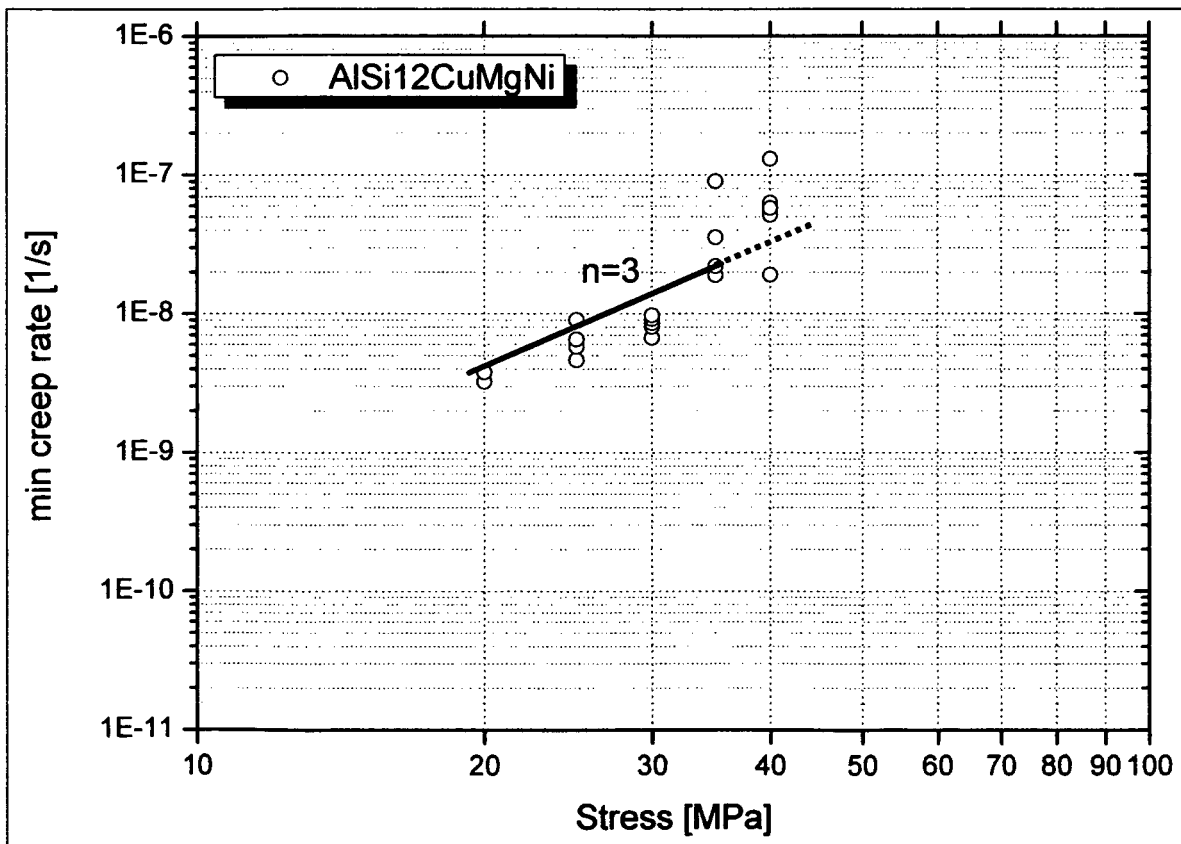


Figure 6.6. $\dot{\epsilon}_{\min}$ vs. σ dependence obtained for the unreinforced cast alloy.

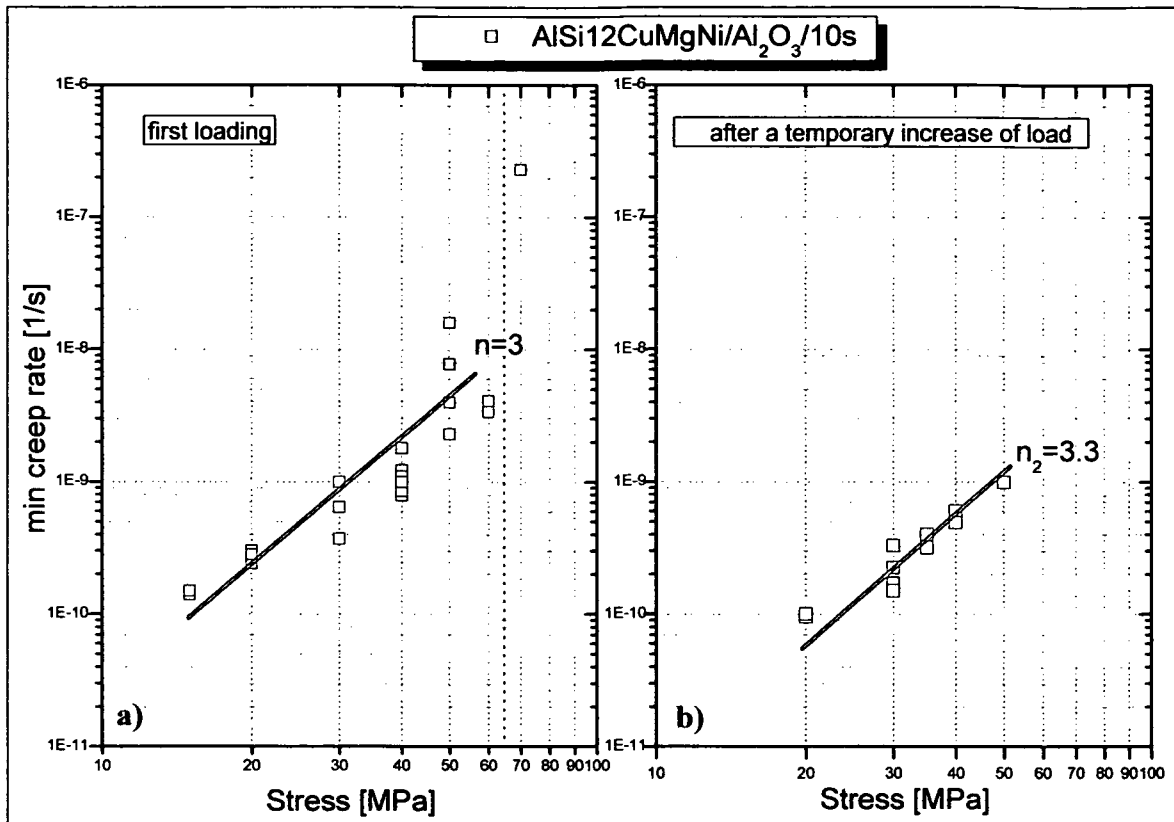


Figure 6.7. $\dot{\epsilon}_{\min}$ vs. σ dependence obtained for the AISi12CuMgNi/Al₂O₃/10s cast alloy: a) results for the first loading and b) after a temporary increase of load.

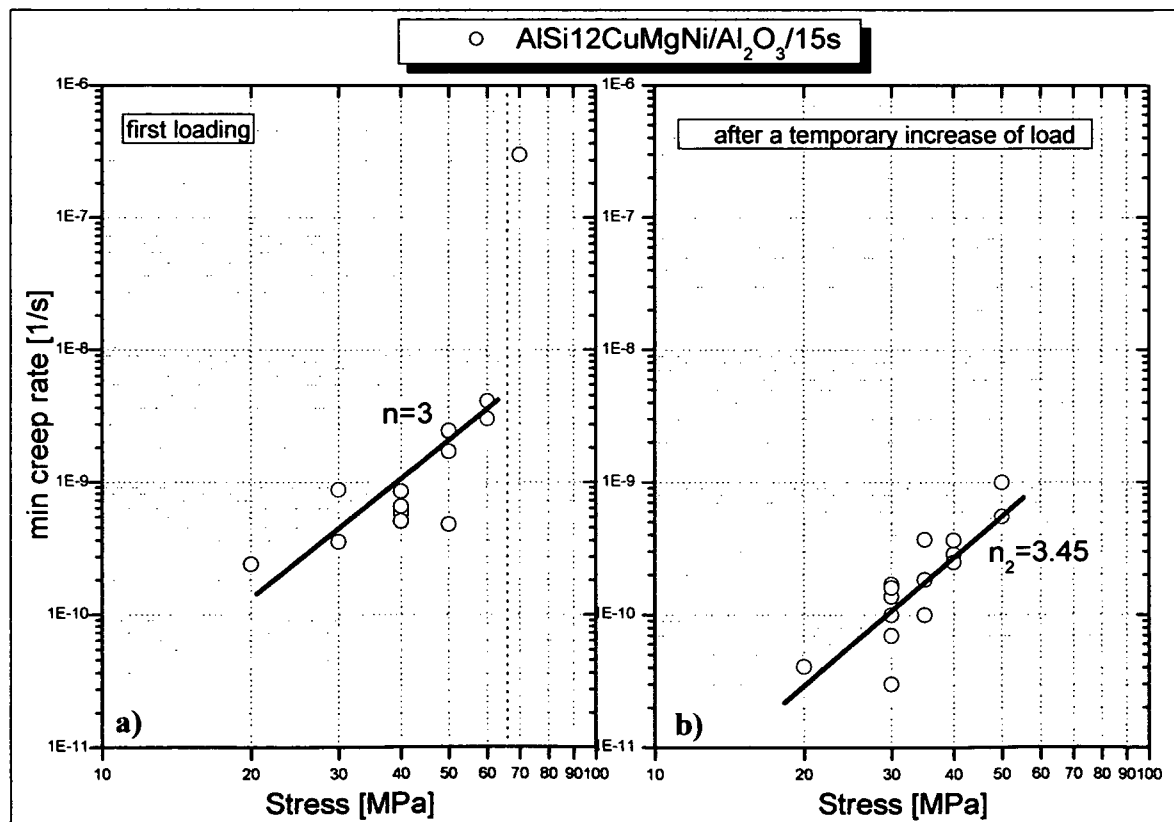


Figure 6.8. $\dot{\epsilon}_{\min}$ vs. σ dependence obtained for the AISi12CuMgNi/Al₂O₃/15s cast alloy: a) results for the first loading and b) after a temporary increase of load.

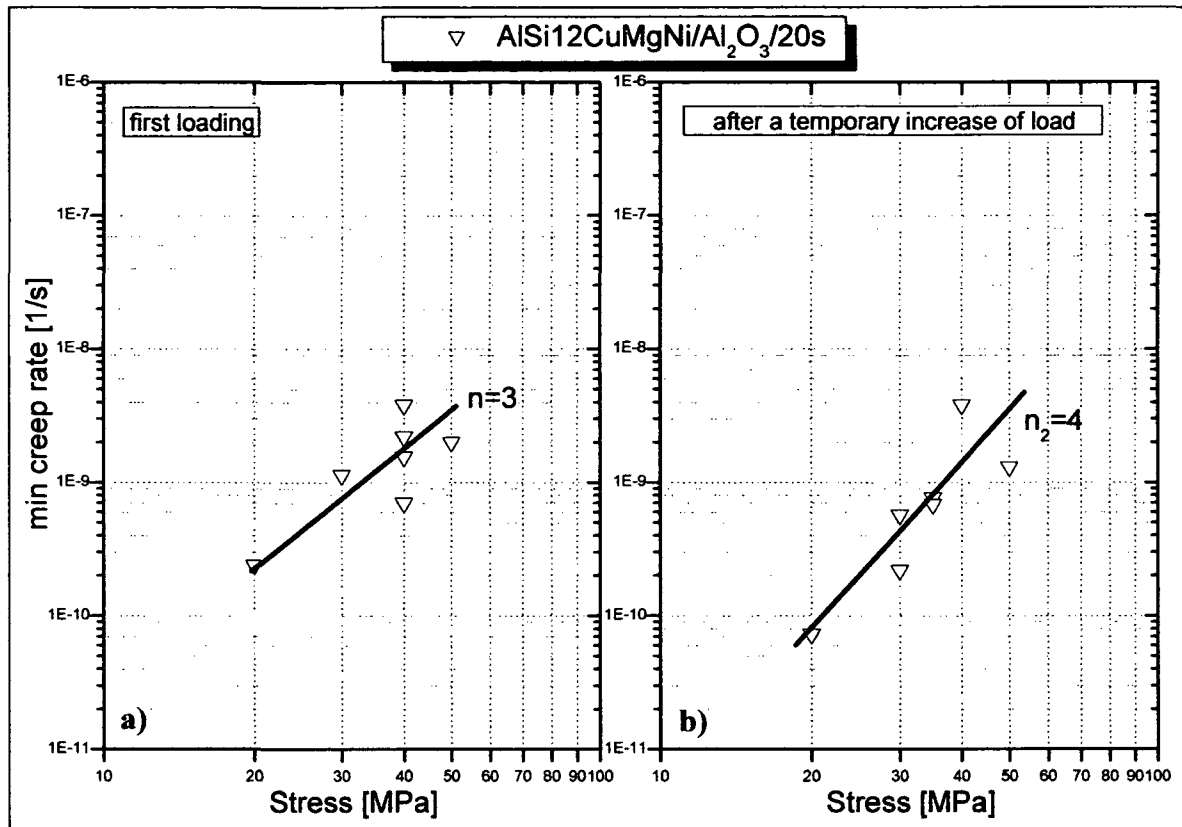


Figure 6.9. $\dot{\epsilon}_{\min}$ vs. σ dependence obtained for the AlSi12CuMgNi/Al₂O₃/20s cast alloy: a) results for the first loading and b) after a temporary increase of load.

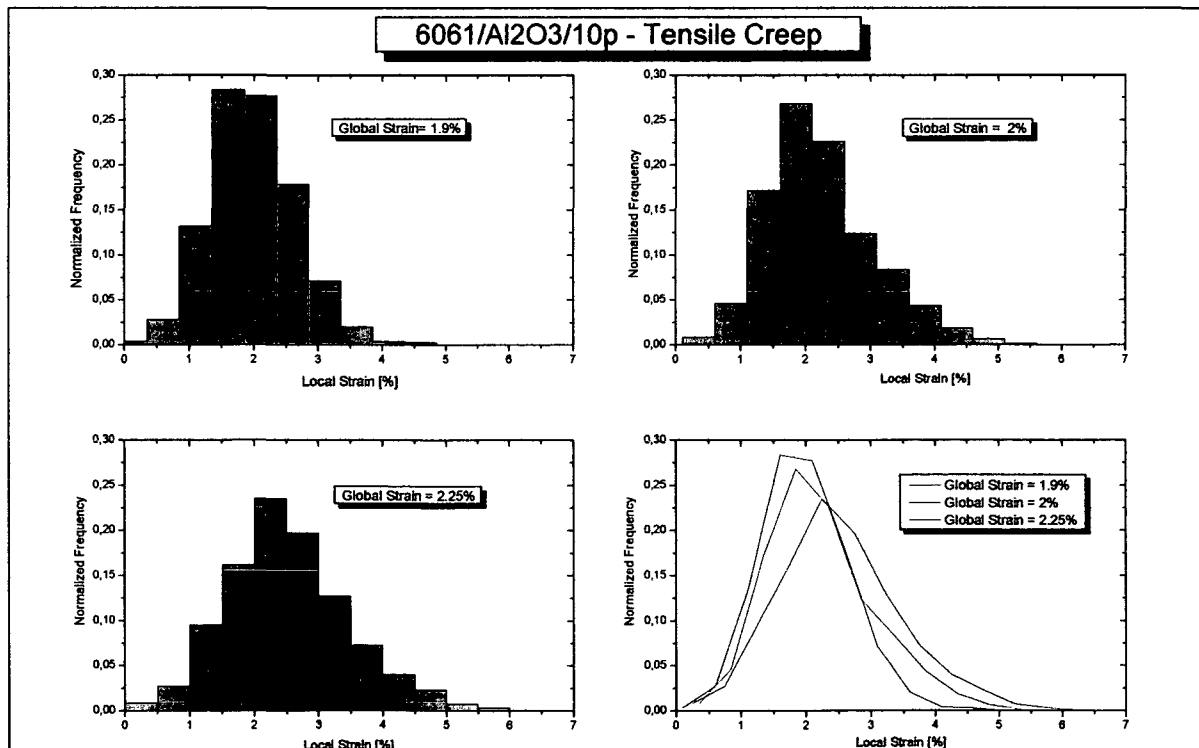


Figure 6.10. Local strain evolution during an In Situ tensile creep test at 300°C for a 6061/Al₂O₃/10p sample.

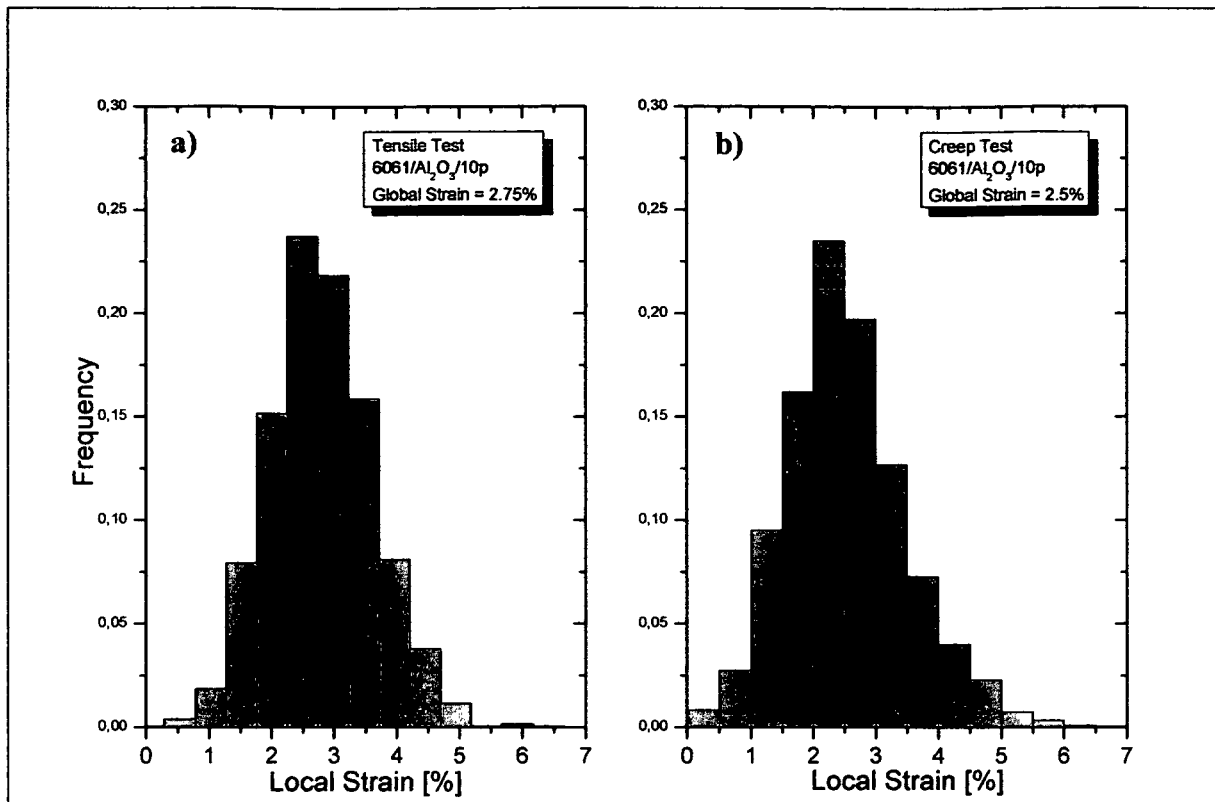


Figure 6.11. Comparison between local strains obtained for a 6061/Al₂O₃/10p composite subjected to a RT tensile test a) and to a creep test at 300°C b) with similar global strains.

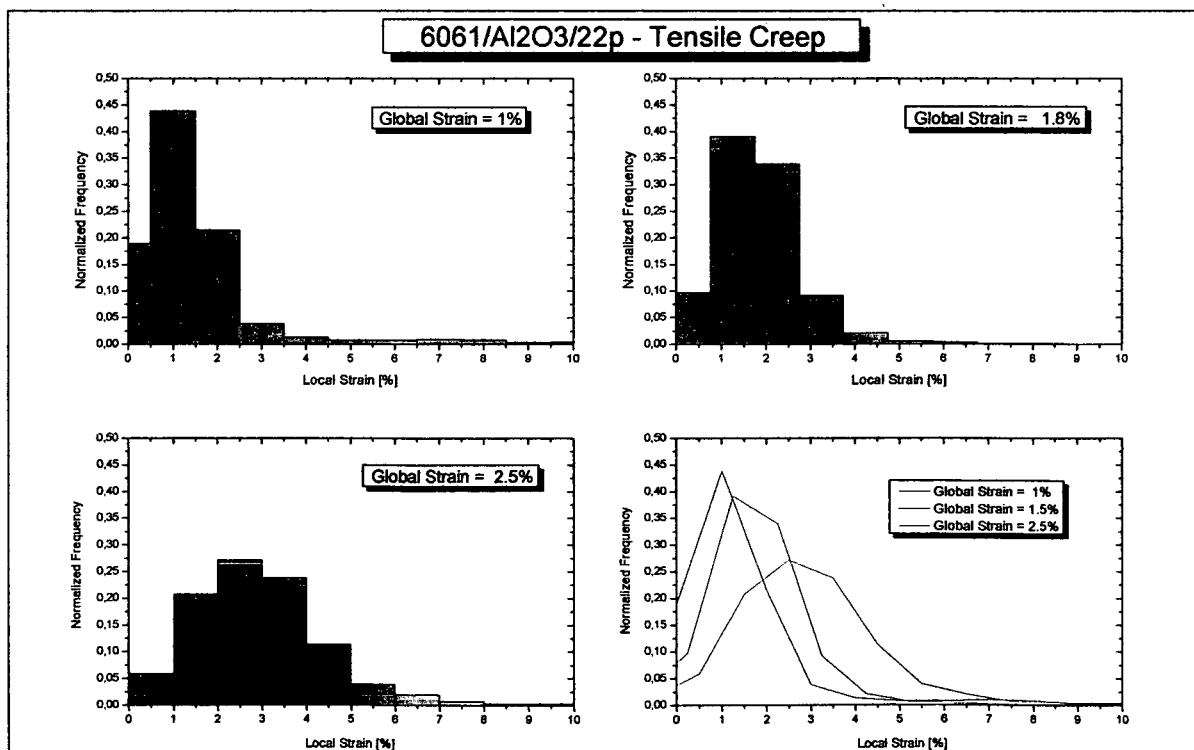


Figure 6.12. Local strain evolution during an In Situ tensile creep test at 300°C for a 6061/Al₂O₃/22p sample.

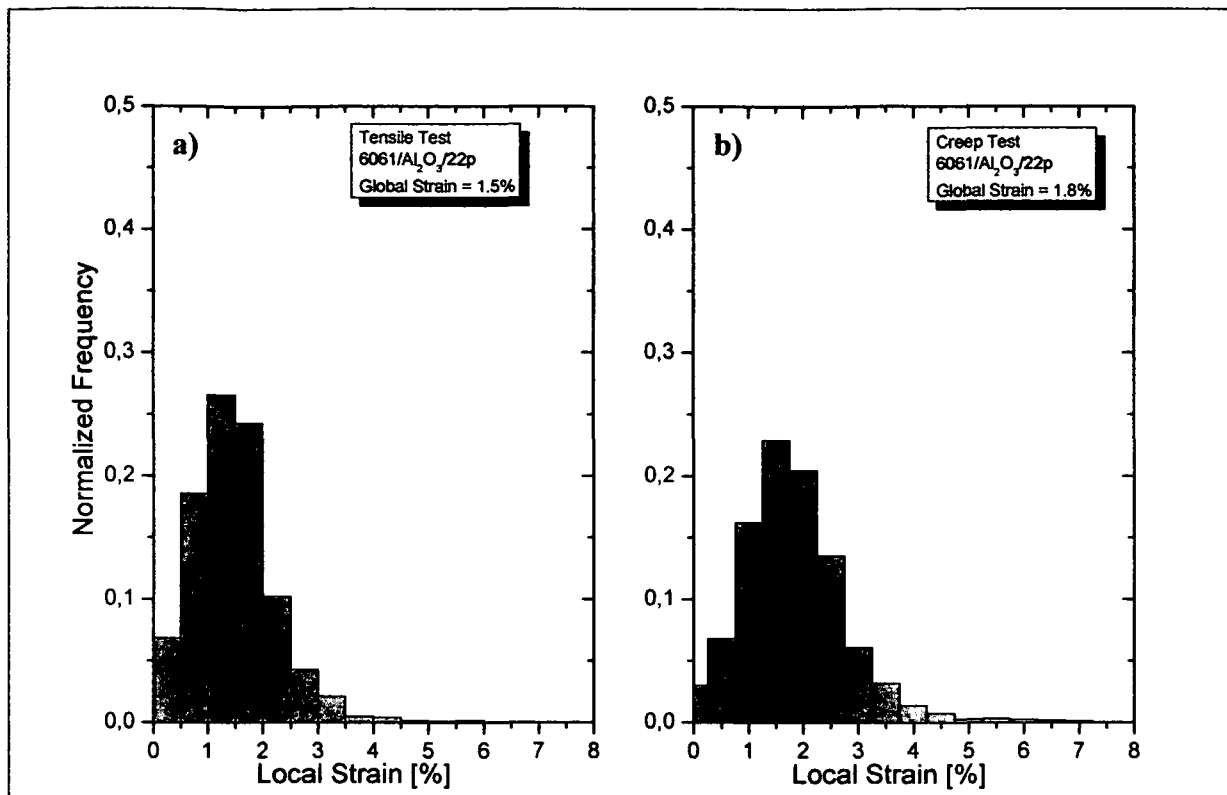


Figure 6.13. Comparison between local strains obtained for a 6061/Al₂O₃/22p composite subjected to a RT tensile test a) and to a creep test at 300°C b) with similar global strains.

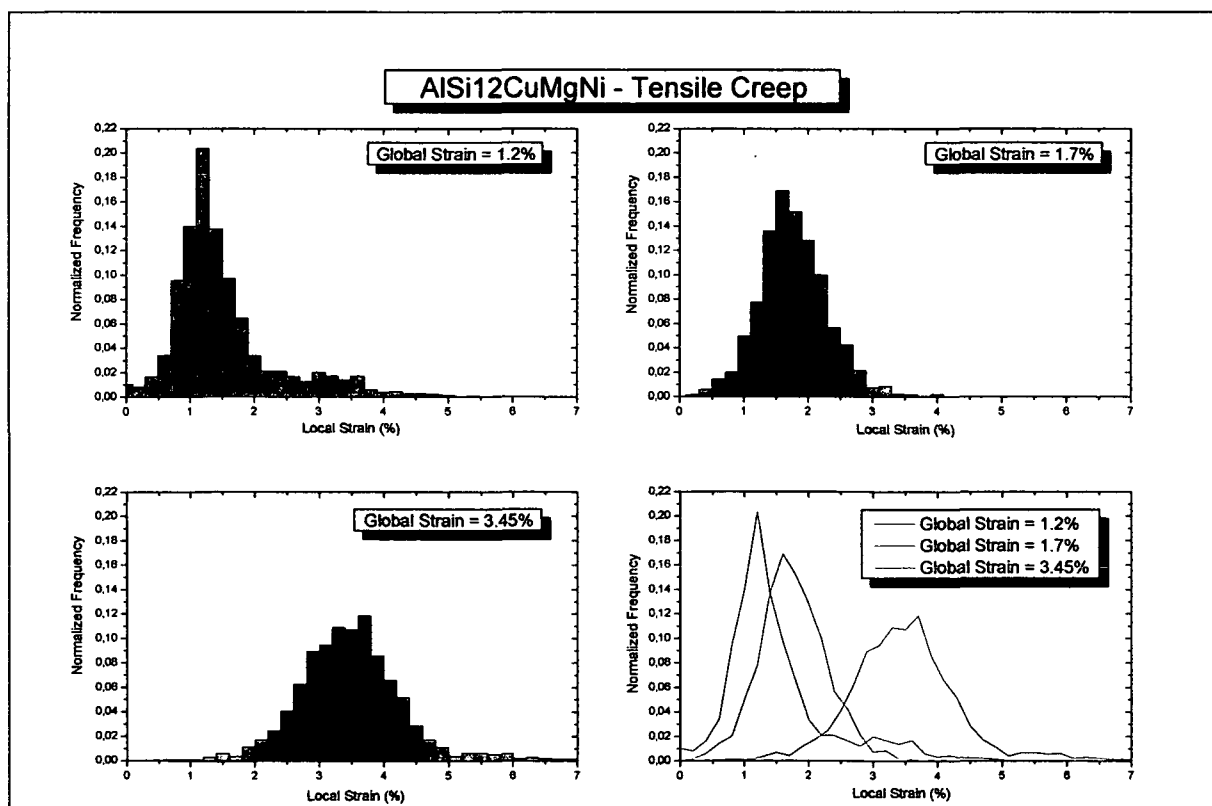


Figure 6.14. Local strain evolution during an In Situ tensile creep test at 300°C for an unreinforced AlSi12CuMgNi sample.

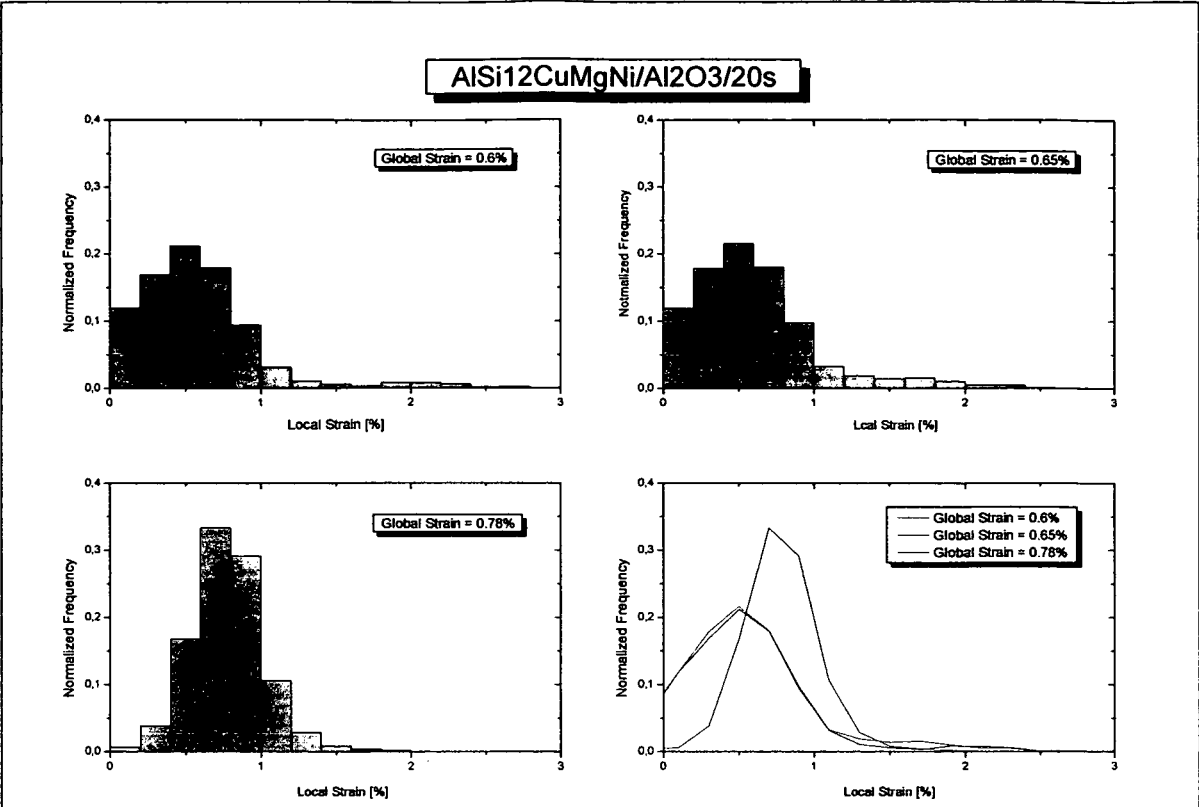


Figure 6.15. Local strain evolution during an In Situ tensile creep test at 300°C for an AlSi12CuMgNi/Al₂O₃/20s sample.

7 Discussion

7.1 Isothermal Creep Mechanisms

7.1.1 6061 and 6061/Al₂O₃/22p

7.1.1.1 Creep resistance in PRM compared to the unreinforced matrix

The larger dislocation density produced by the difference in CTE between the reinforcement and the matrix [107, 108] results in an increased work hardening of the PRM at RT which can lead to an improvement of the mechanical properties of these materials at low temperatures. By increasing the temperature from RT to 300°C, the elastic mismatch strains vanish. The internal stresses in the matrix are governed by the external load and the relatively high dislocation density will be adapted to the stress condition by thermal activation. Furthermore, the ceramic particles will act as dislocation sources at high temperatures. The sharp corners of the spinel crystals on the surface of the particles (see Figure 3.4) may act as Frank-Read sources. The necessary shear stress τ to expand a dislocation in this kind of sources is given by [110]

$$\tau = \frac{\mathbf{G} \cdot \mathbf{b}}{L} \quad (7.1)$$

where G is the shear modulus of the matrix, b the Burger's vector of the matrix and L the interspace between the anchors of the dislocation. In our case, G at 300°C is 18.8GPa, b is 2.5×10^{-10} m and L is approximately 0.5 μ m or less. Thus, τ results 9.4MPa, suggesting that for the studied applied loads the interface spinel crystals may act as Frank-Read sources, enhancing the increase of dislocation density during creep. Besides this mechanism of dislocation formation, the particles themselves may act as dislocation sources provided that a minimum mismatch strain is present in the interface between particle and matrix. Xin et al. [111] calculated using energy considerations that a mismatch strain of only 0.01% is necessary to emit dislocation from the interface of particles of approximately 10 μ m (same size as in this work) under an applied stress of 10MPa for an Al-SiC particle reinforced composite. The stress needed to produce a mismatch strain $\Delta\epsilon = 0.01\%$ for the PRM here studied is given by:

$$\sigma = \frac{\Delta\epsilon}{\left(\frac{1}{E_M} - \frac{1}{E_P} \right)} \quad (7.2)$$

which results in $\sigma = 5.7\text{MPa}$. These values of load are smaller than the applied loads used during our tests. The possibility of having the particles acting as dislocation sources by a mechanism of loop punching seems probable.

On the other hand, at high temperatures, the high dislocation density in the PRM provokes an increase of the apparent diffusion coefficient D in comparison to the unreinforced matrix [65]. Furthermore, the larger amount of dislocations around the particles produce an acceleration of the precipitation kinetics in the composite [64, 65] that accelerates the overaging effect observed for the unreinforced matrix. In the case of the PRM, precipitation strengthening becomes ineffective owing to the presence of the particles, which increase the strain rate by more than one order of magnitude compared with the matrix. The overaging of the matrix increases the strain rate by some 10^{-10}s^{-1} (see Figure 6.1), which becomes unobservable at higher strain rate levels. These effects are responsible for the observed decrease in the creep resistance of the PRM compared to the unreinforced matrix. All the reported works available in the literature in which PRM have a better creep resistance than the unreinforced matrix correspond to materials processed via powder metallurgy for which dispersion strengthening by the oxides from the skin of the Al powder is the responsible mechanism for the higher creep resistance of the composite.

Although the unreinforced wrought alloy studied in this work was tested in an overaged state, the stabilization time and soaking time prior to testing are not sufficient to achieve a stabilized microstructure [67, 112], therefore the effect of the precipitation kinetics on the microstructure of the matrix cannot be neglected.

7.1.1.2 Failure modes at low and high stresses

Tensile creep tests carried out in [53] for two PRM with different reinforcement sizes show that the composite with smaller reinforcement size ($3\mu\text{m}$) has a better creep resistance than the composite with larger reinforcement size ($20\mu\text{m}$). The authors state that if interfacial diffusion were the dominant relaxation mechanism, then it would be expected to be more significant with the smaller particles, because of the smaller diffusion distances involved and proposed that microstructural damage (easier for the $20\mu\text{m}$ particle) is the dominating relaxation process.

As stated in Paragraph 5.2.1, the SEM fractographs show a difference in dimple size between smaller and higher stresses. The dimples in Figure 5.8 b) (15MPa) are bigger than those in Figure 5.9 b) (70MPa). Furthermore, big cracks were found to be connecting the pores of more than one particle along cross sections of samples fractured at 15MPa in contrast to higher stressed samples where voids were normally found at the sharp edges of single

ceramic particles (see Figure 5.10 a) and b)). These differences may arise due to the crack formation process: at higher stresses, the development of voids at the edge of a particle leads to the formation of a dimple and fracture would occur as a result of growth of the voids formed at individual particles followed by failure of the matrix in between by high plastic deformation. On the other hand, for small stresses, bigger dimples and the presence of more than one particle per dimple suggest that the crack initiation and consequent fracture is due to the formation and coalescence of voids generated at two or more adjacent particles. The surrounding matrix fails by localised plastic deformation only after the void is big enough to produce a certain intensity factor K_I . Thus, comparing between high and low stresses:

$$K_I = 15\text{MPa} \cdot \sqrt{\pi \cdot a_1} = 70\text{MPa} \cdot \sqrt{\pi \cdot a_2}$$

$$225 \cdot a_1 = 4900 \cdot a_2$$

$$\frac{a_1}{a_2} = 21.8$$

which means that for 15MPa it is necessary a crack approximately 22 times longer (some 11 particles if a = particle length) than for 70MPa to produce the same stress intensity at the crack tip.

7.1.2 *AlSi12CuMgNi, AlSi12CuMgNi/Al₂O₃/10s, AlSi12CuMgNi/Al₂O₃/15s and AlSi12CuMgNi/Al₂O₃/20s*

As already stated in Paragraph 6.1.2.1, there is a difference in the minimum strain rate depending on the loading sequence during the tests for the three studied SFRM. This effect can be explained taking into account the redistribution of internal stresses around the ceramic fibres due to the external load. Figure 7.2 shows a graphic that indicates in a simplified way the processes involved during a creep test with stepwise loading. When the composite is subjected to an external load σ_1 , the stress is distributed between the fibre and the matrix following the concept of load transfer. According to the considerations taken into account in Paragraph 5.3, the stress ratio between fibres and matrix is given by

$$\frac{\sigma_f}{\sigma_m} = \frac{f_{\text{eff}} \cdot \frac{E_f}{E_c}}{(1 - f_{\text{eff}}) \cdot \frac{E_m}{E_c}} \quad (7.3)$$

where f_{eff} is the effective reinforcement volume fraction and E_f , E_m and E_c are the Young's modulus of the fibres, matrix and composite at 300°C, respectively. This results in a load transfer ratio of 0.18, 0.27 and 0.38 for the 10vol%, 15vol% and 20vol% SFRM, respectively. However, these values of load transfer ratio are only applicable at the beginning of the test,

since they will be lower as creep deformation takes place [113]. Thus, the mean stress seen by the matrix will be lower than the applied stress as indicated by σ_1^m in Figure 7.2. It is observed experimentally and for the first loading sequence that for the case of the 10vol% and 15vol% SFRM, there is a load transfer factor of approximately 0.55 and 0.65, respectively, (see Figure 7.10) resulting in:

$$\dot{\epsilon}_{\min 10\%} = A \cdot (\eta \cdot \sigma_A)^n \approx A \cdot (0.45 \cdot \sigma_A)^n \quad (7.4)$$

$$\dot{\epsilon}_{\min 15\%} = A \cdot (\eta \cdot \sigma_A)^n \approx A \cdot (0.35 \cdot \sigma_A)^n \quad (7.5)$$

where η is the percentage of external stress in the elastic regime acting on the thermally activated matrix. These values of the load transfer factor found experimentally differ from those calculated using Equation (7.3) which yields to 0.82 and 0.73 for the quoted volume fractions. This may indicate that the Eshelby's approximation used for estimating the values of f_{eff} is not applicable for the case of the studied composites subjected to creep conditions.

There is in fact an internal stress distribution $\sigma_i\{1\}$ in the composite due to the orientation of the fibres yielding values of stress higher than the applied external stress [114] as qualitatively sketched in Figure 7.1 a). Thus, the driving force for creep deformation will not only be the stress of the applied load but also the higher stresses present in the internal stress distribution $\sigma_i\{1\}$. This situation is depicted in Figure 7.2 for σ_1 resulting in minimum creep rates shown by the upper line. During creep exposure, the high end of the internal stress distribution will relax yielding a narrower strain distribution (see Paragraph 6.2.2). If the stress on the matrix is increased by $\Delta\sigma$ to an external stress σ_2 on the composite, the internal stresses distribution $\sigma_i\{2\}$ is obtained. In zones where the σ_{yield} of the matrix would be surpassed, there will be a plastic flow in these matrix regions in the SFRM. The sum of the initial internal stress $\sigma_i\{1\}$ and the increase of external stress due to $\Delta\sigma$ are limited by σ_y of the matrix increasing the portion of matrix elastically strained by the yield stress (see Figure 7.1 b)). If the external load is decreased for the following step for example to $\sigma_4 = \sigma_1$ in Figure 7.2, the new internal stresses distribution $\sigma_i\{4\}$ will not only be different from but also smaller than the former $\sigma_i\{1\}$ as high stress regions had been plastified (this situation is shown in Figure 7.1 for a loading sequence $\sigma_1 \rightarrow (\sigma_1 + \Delta\sigma) \rightarrow \sigma_1$). The higher stresses of the internal stress distribution in the matrix surrounding the fibre ends that cause the faster deformation by creep are reduced, which means that the new minimum creep rate after this temporary increase of load will result to be smaller than before the increase of load (lower line in Figure 7.2). The evolution of the internal stress distribution due to the applied load along the test is schematically represented in Figure 7.3.

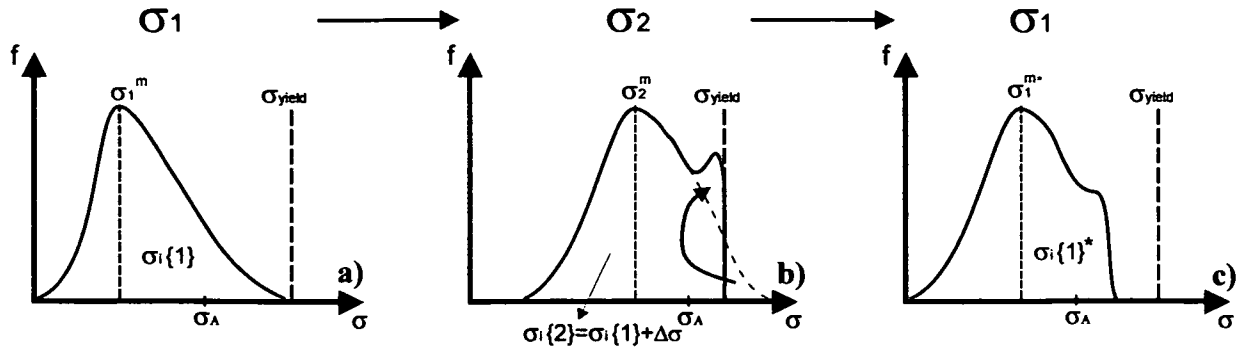


Figure 7.1. Evolution of the internal stress distribution during a loading sequence $\sigma_1 \rightarrow (\sigma_1 + \Delta\sigma) \rightarrow \sigma_1$. When the applied load σ_1 (a) is increased by $\Delta\sigma$ (b), the portion of the internal stresses which would surpass the yield stress of the matrix is “moved” to values near the elastic limit provoking a cutting in the distribution of internal stresses which remains when the load is decreased to σ_1 (c).

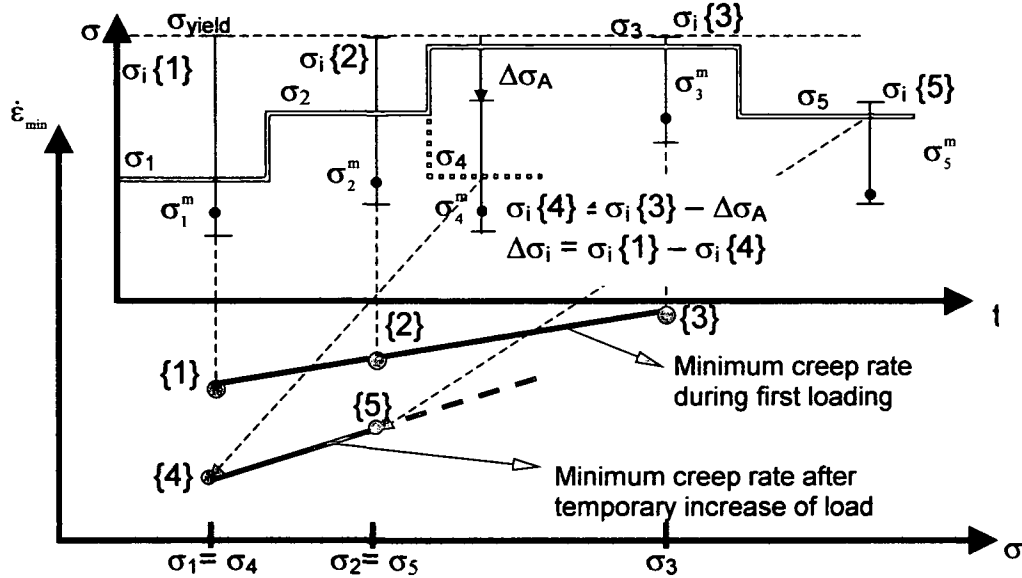


Figure 7.2. Description of the internal processes involved during the evolution of a creep test for the SFRM with changes of external load at creep temperature.

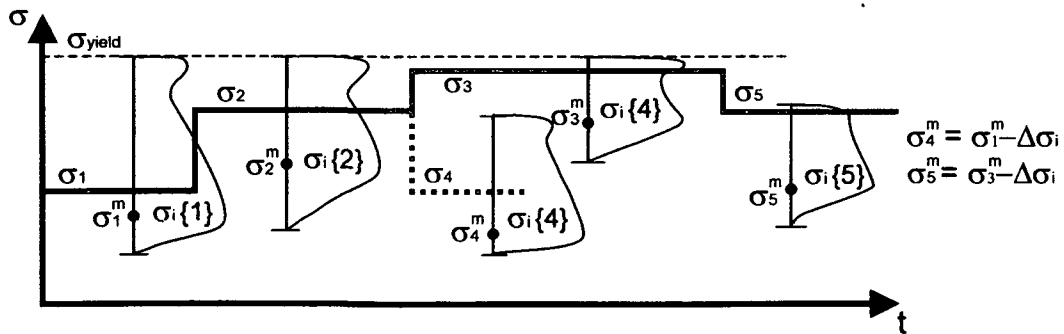


Figure 7.3. Schematic representation of the evolution of the volumetric distribution of stress in the SFRM for the test sequence shown in Figure 7.2.

According to this explanation, the creep exponents shown in Figure 6.7 b), Figure 6.8 b) and Figure 6.9 b) are only apparent and actually a reduction of the internal stress distribution $\Delta\sigma_i = \sigma_i\{1\} - \sigma_i\{4\}$ where $\sigma_i\{1\}$ and $\sigma_i\{4\}$ are the internal stresses distribution before and after the temporary increase of load is responsible for this behaviour. Thus, the equations describing the creep behaviour of these materials will be [40]:

$$\dot{\epsilon}_{min} = A \cdot \sigma_A^n \quad (7.6)$$

for the unreinforced matrix,

$$\dot{\epsilon}_{min} = A \cdot (\eta \cdot \sigma_A)^n \quad (7.7)$$

for the SFRM before an increase of load, and

$$\dot{\epsilon}_{min} = A \cdot (\eta \cdot \sigma_A - \Delta\sigma_i^*)^n \quad (7.8)$$

for the SFRM after a temporary increase of load. In this equation, σ_A is the applied stress and $\Delta\sigma_i^*$ corresponds to an average decrease in the load “seen” by the matrix as soon as the internal stress reaches the yield stress.

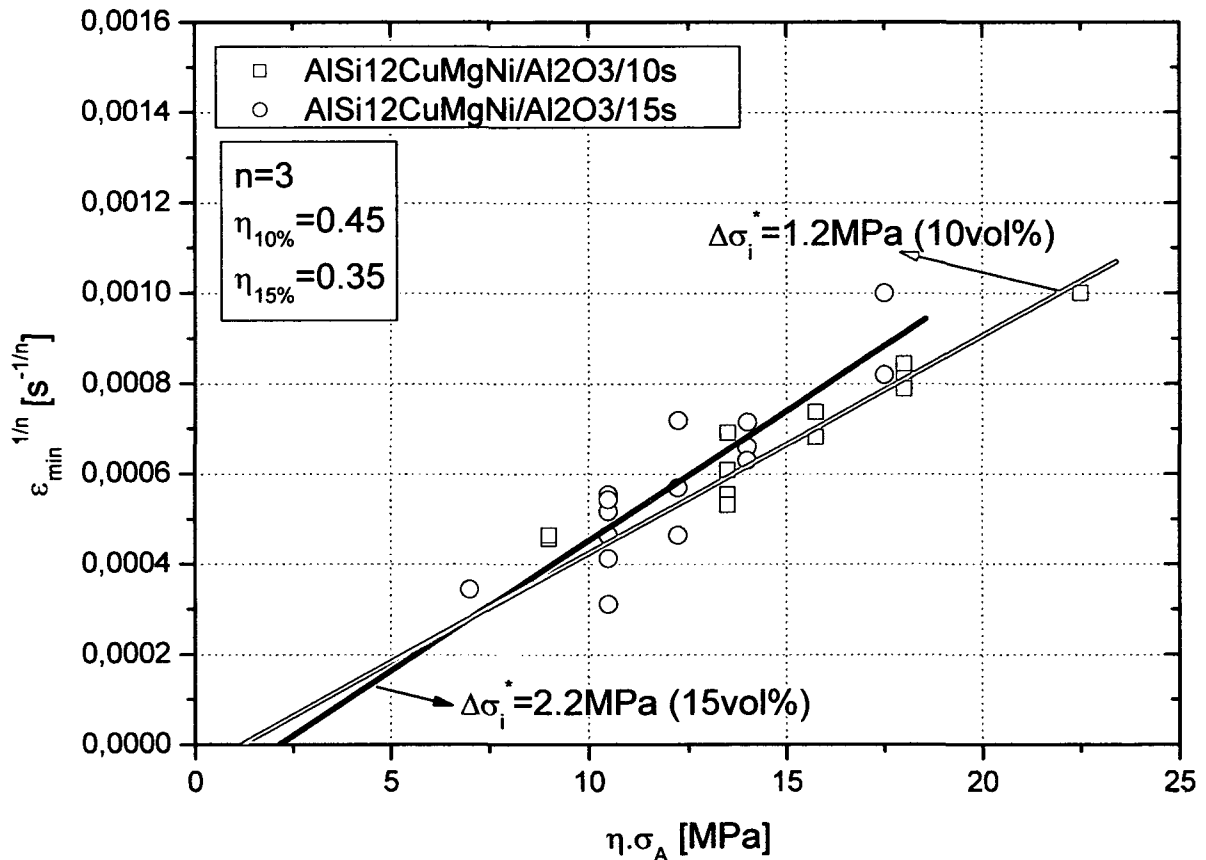


Figure 7.4. $\dot{\epsilon}_{min}^{1/n}$ vs. $\eta \cdot \sigma_A$ plot for the 10vol% and 15vol% SFRM using a creep exponent $n = 3$. A linear extrapolation of the $\dot{\epsilon}_{min}^{1/n}$ values to intersect the σ_A axis results in the values of $\Delta\sigma_i^*$.

Figure 7.4 shows a $\eta \cdot \sigma_A$ vs. $\dot{\epsilon}_{min}^{1/n}$ plot after a temporary increase of load and using a creep exponent $n=3$ which corresponds to the creep exponent obtained before the transitory overload and $\eta=0.45$ and 0.35 for the 10vol% and 15vol% SFRM, respectively. The intersection of a linear extrapolation with the $\eta \cdot \sigma_A$ axis will give the values of effective stress reduction $\Delta\sigma_i^*$ for the composites. From this Figure, we see that $\Delta\sigma_i^*$ is equivalent to 1 to 2MPa for the investigated composites. It has to be taken into account that these values of

$\Delta\sigma_i^*$ are averaged for the increases of load used in this work, which range between 5 and 20MPa.

Summarising, the prior discussion states that there is no change in the creep mechanism for the SFRM before and after a temporary increase of load as could be inferred from Figure 6.7 to Figure 6.9 where an apparent change in the creep exponent is observed. The real situation is suggested to be a balance of the maximum stresses within the internal stress distribution provoked by a localised flow of matter in zones where the yield stress of the matrix surrounding the fibres would be surpassed. The evolution of the local strain during In Situ tensile creep tests shown in Figure 6.15 also supports this conclusions since it indicates that after elapsed a certain time, the local strain peaks disappear (by means of a non damaging relaxation mechanism) concentrating the local deformation around the value of global strain of the sample.

As already explained for PRM, the fibres may also act as dislocation sources at their ends increasing thus the dislocation density during creep. Furthermore, and also similarly to the PRM, the creep rate of SFRM does not show any effect due to age hardening or overaging, but owing to the opposite mechanism, where the creep resistance is provided by the load carrying fibres.

7.1.2.1 Correlation with Dlouhy's Model

As already mentioned in Paragraph 2.1.4.1, Dlouhy et al. [42] have developed a micromechanical model for creep in short fibre reinforced aluminium alloys based on the following three microstructural mechanisms: (i) loading of fibres by means of the formation of a work hardened zone around the fibres due to an increase of dislocation density, (ii) unloading of fibres due to the movement of dislocation loops to the end of the fibres where they annihilate and (iii) breakage of fibres into subfibres after reaching a critical fibre stress. In this section, Dlouhy's model will be applied for the investigated SFRM with 15vol% in order to correlate the results to those obtained experimentally. The simulations carried out in [42] take into account the process of fibre breakage only for applied stresses larger than 40MPa in an AlSi7Cu3Mg alloy. Furthermore, fibre breakage was not observed in our samples before reaching tertiary state. Based on these two observations, damage processes will not be introduced in our numerical simulations.

The parameters used for the simulations are summarized in Table 7.1. The sources where these parameters were obtained from are also indicated but special considerations must be taken for the activation energy for a diffusion controlled recovery process Q and the effective volume fraction of fibres f_{eff} . Dlouhy et al. have used a value of $Q = 189 \text{ kJmol}^{-1}$

since it showed the best match between the experimental results and the simulations. In our case, the value of Q which best matched the calculation was $Q = 165 \text{ kJ mol}^{-1}$. A similar situation arises for the value of $f_{\text{eff}} = 0.025$ used in [42] but in this case, this value of effective volume fraction of reinforcement presented also the best match during our calculations, even better than the experimental value of $f_{\text{eff}} = 12\%$ obtained from Figure 7.10 and the theoretical value of $f_{\text{eff}} = 6\%$ calculated as explained in Paragraph 5.3.

Parameter	Value	Description	Source
b	$2.5 \times 10^{-10} \text{ m}$	Burgers vector	-
$B_{300^\circ\text{C}}$	$2.059 \times 10^{-13} \text{ MPa}^{-3} \text{ s}^{-1}$	Matrix Norton's law parameter	Figure 6.6
E_f	300 GPa	Young's modulus of the fibres	[70]
E_m	68.5 GPa	Young's modulus of the matrix	Figure 5.34
L_0	120×10^{-6}	Initial length of the fibres	[42]
n	3	Stress exponent in matrix	Figure 6.6
Q	$165 - 189 \text{ kJmol}^{-1}$	Activation energy for diffusion controlled recovery process	Present work - [42]
T	300°C	Test temperature	Present work
f_{eff}	$12 - 6 - 2.5\%$	Effective reinforcement volume fraction	Present work - [42]
ν_m	0.3	Matrix Poisson's ratio	-
σ_A	$10 - 40 \text{ MPa}$	Applied Stress	Present work

Table 7.1. Input parameters used for the simulations.

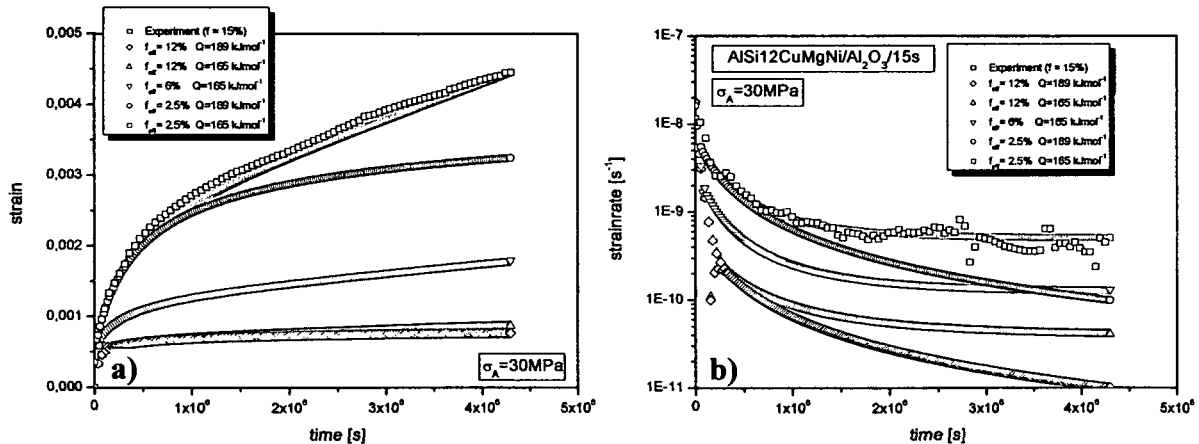


Figure 7.5. Results of the computer simulations using different values of f_{eff} and Q for a test started at 30 MPa for an $\text{AlSi12CuMgNi/Al}_2\text{O}_3/15\text{s}$ sample (see Figure 5.5 a) and b)).

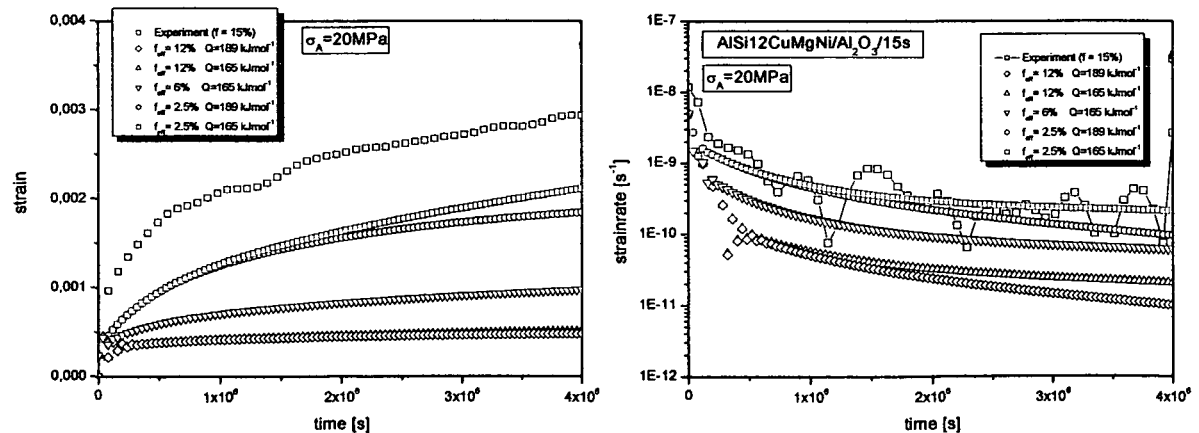


Figure 7.6. Results of the computer simulations using different values of f_{eff} and Q for a test started at 20 MPa for an $\text{AlSi12CuMgNi/Al}_2\text{O}_3/15\text{s}$ sample (see Figure 5.5 o) and p)).

Figure 7.5 and Figure 7.6 a) and b) depict the results obtained during the first loading at 30MPa and 20MPa for the test shown in Figure 5.5 a), b) and o), p), respectively, using different values of f_{eff} and Q . As previously mentioned, the best match is obtained using $f_{eff} = 2.5\%$ and $Q = 165\text{kJmol}^{-1}$. This value of f_{eff} indicates that according to the model, the fibres have a higher reinforcement effect than it may be implied from simple load transfer considerations.

The effect of the load changes carried out during the creep tests was also modelled for the tests shown in Figure 5.5 a) and b), g) and h) and o) and p) and the results are presented in Figure 7.7 to Figure 7.9. $f_{eff} = 2.5\%$ and $Q = 165\text{kJmol}^{-1}$ were used for the calculations. The experimental results show some scattering for the initial creep strain that can be observed comparing the curves during the first loading at 30MPa of Figure 7.7 a) and Figure 7.8 a) that can not always be correlated using the model. However, the strainrate curves show a much better correspondence between experiments and simulations and the results obtained before a temporary increase of load result in an excellent correlation. However, the model does not take into account the previously explained effect due to the balance of peaks in the internal stress distribution (see Paragraph 7.1.2) and therefore the calculated values of strainrate after the overloading periods are higher than the experimental ones. A coefficient has been introduced in the simulations in order to decrease the mean matrix stress after a temporary increase of load. The best match with the experiments has been obtained using 50% of the mean matrix stress for changes of load of 10MPa and 30% for changes of 20MPa.

The Dlouhy's model has reproduced satisfactorily the results obtained in this work during the first loading of AlSi12CuMgNi/Al₂O₃/15s creep tests. This means that the microstructural scenario proposed in [42] may represent the actual picture governing creep deformation in this material. For the case of creep tests after a period of overloading, a modification of the model is necessary in order to take into account the flow of matrix in regions where the yield stress of the matrix has been reached. The results obtained using an empirical coefficient in order to reduce the mean matrix stress suggest that there is a dependence of the obtained minimum creep rate values with the magnitude of the change of load.

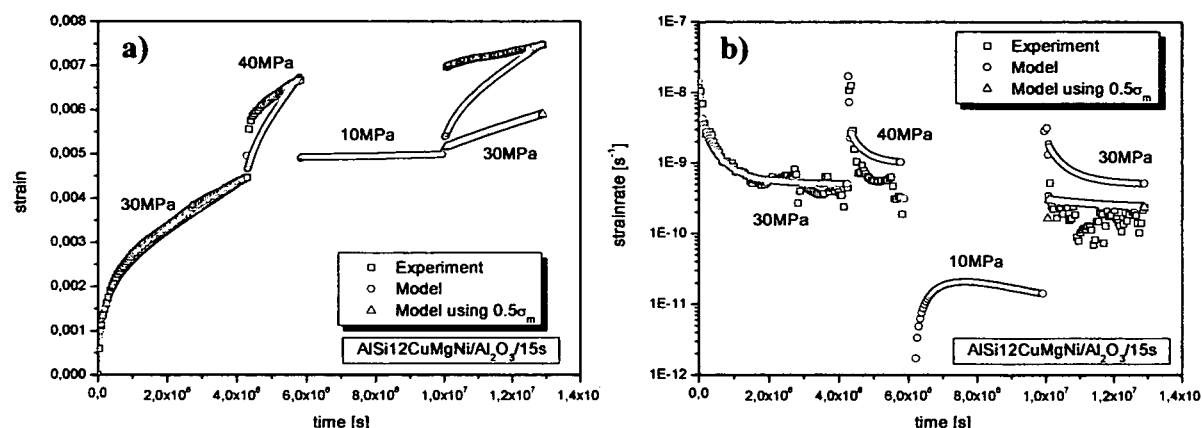


Figure 7.7. Results of the simulations with changes of load for the test shown in Figure 5.5 a) and b).

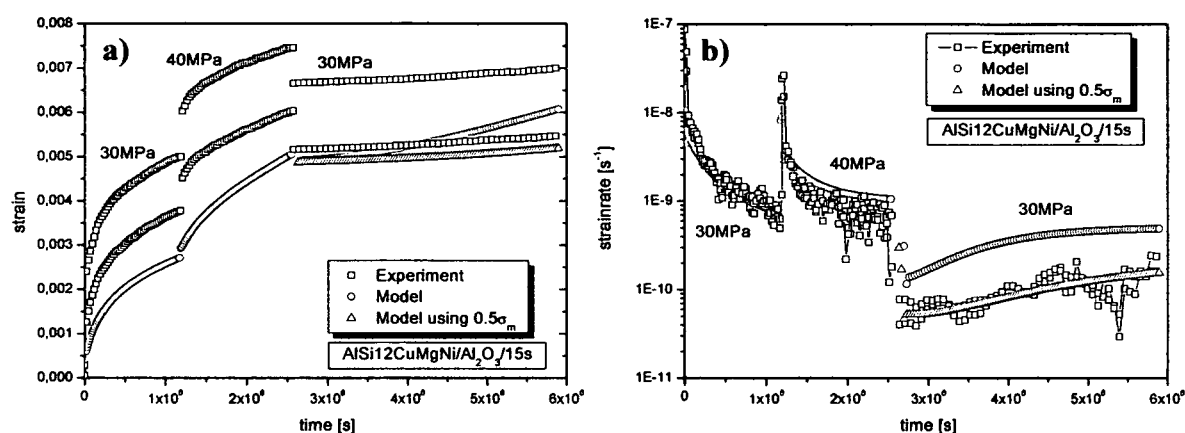


Figure 7.8. Results of the simulations with changes of load for the test shown in Figure 5.5 g) and h).

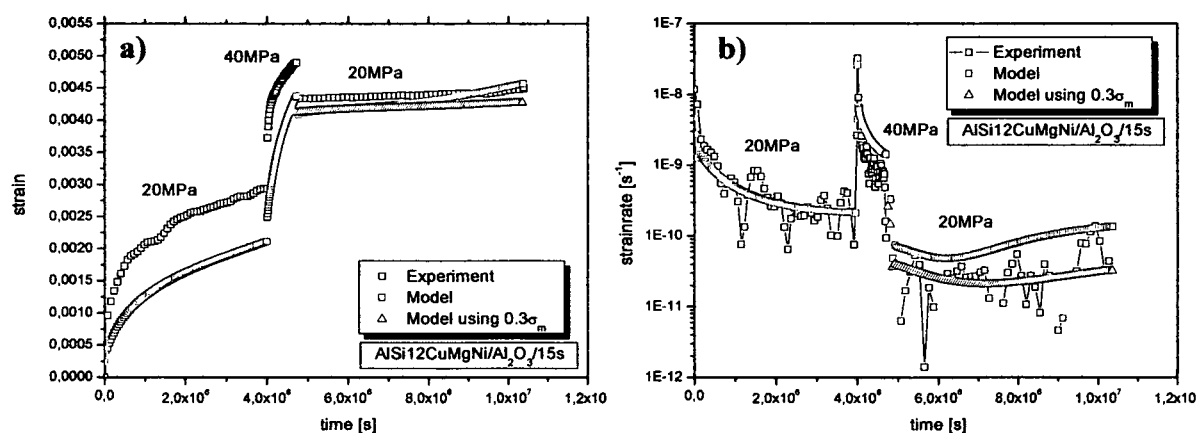


Figure 7.9. Results of the simulations with changes of load for the test shown in Figure 5.5 o) and p).

7.1.3 Isothermal Creep vs. Thermal Cycling Creep

In this section, the results obtained in this work for isothermal creep for the unreinforced and reinforced wrought and cast alloys are compared with previous results reported in [2, 3] for the PRM and in [101] for the unreinforced cast alloy and 20vol% SFRM under TCC conditions. In order to do this, it is necessary to change the representation of the minimum creep rate presented in these two previous works since the deformation rate was calculated as a mean value dividing the plastic elongation per cycle (see Chapter 4) by the

cycle time. This is an acceptable method when TCC tests under the same tests conditions are compared, but it does not reflect the actual deformation rate of these materials since it varies together with the temperature of the cycle as inferred from Figure 4.9 to Figure 4.14. Therefore, to accomplish a suitable comparison between TCC and isothermal creep, the maximum deformation rate per cycle is taken at a stage where the deformation of the material is stable, which corresponds to the region where the mean deformation rate is constant through a number of cycles. This “maximum creep rate per cycle” in TCC is found in the investigated materials during approximately 20% of the total cycle time and at temperatures above 240°C. These short time periods (approx. 10s) are attributed to a quasi primary creep behaviour that restarts in every cycle along the test. In each cooling phase the thermal mismatch creates local strain hardening. The corresponding dislocation structure develops each time again before creep becomes observable between 240°C and 300°C during heating and cooling.

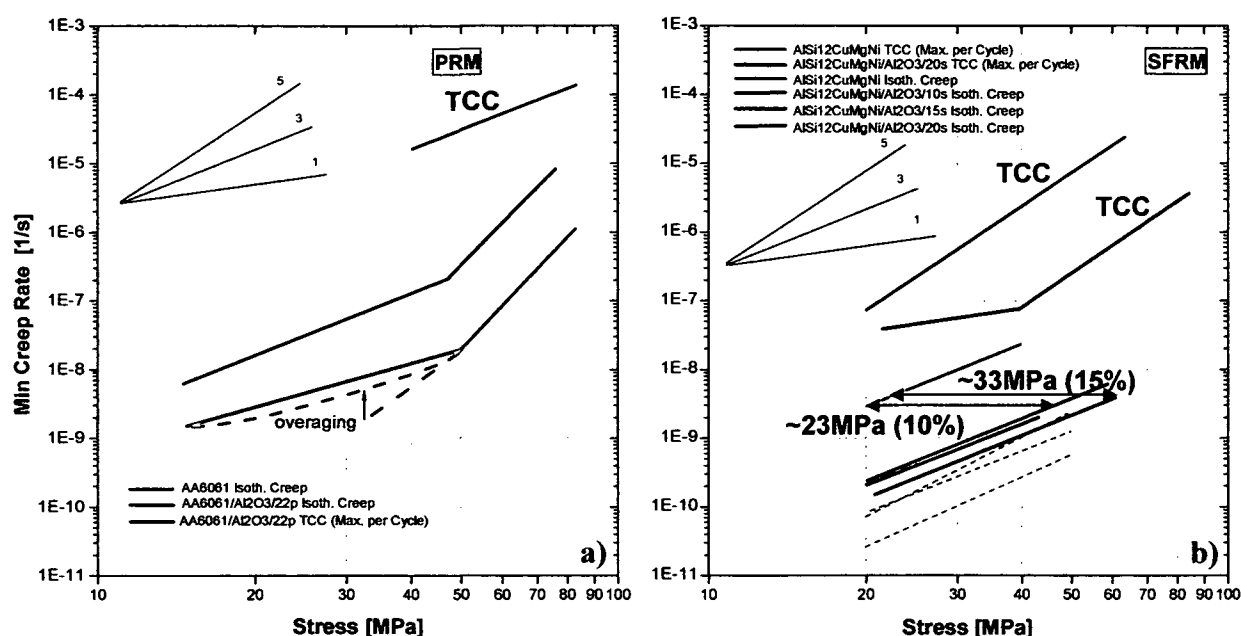


Figure 7.10. Dependence of applied stress on minimum creep rate and maximum creep rate per cycle for the unreinforced and reinforced wrought (a) and cast (b) alloys (the dashed lines correspond to the minimum creep rate after a temporary increase of load by isothermal creep).

Figure 7.10 a) and b) show the dependence of applied stress on minimum creep rate (for isothermal creep) and maximum creep rate per cycle (for TCC) for the wrought alloys and the cast alloys, respectively. As already mentioned in Paragraph 6.1.1.1, the unreinforced 6061 matrix shows better creep resistance than the PRM alloy. Furthermore, the isothermal creep resistance of both the unreinforced and the particle reinforced matrix is considerably higher than the PRM under TCC. Now, comparing Figure 7.10 a) and b), it is observable that the unreinforced wrought alloy shows approximately the same creep resistance as the unreinforced cast alloy but markedly lower than the SFRM composites, which also present

better resistance under TCC than the cast matrix. The stress exponent n shows values higher than 5 for external stresses higher than 50MPa for both PRM and matrix wrought alloys which may correspond to the region where power law breakdown takes place. For creep rates $< 10^{-8} \text{ s}^{-1}$, the creep exponent n for all materials falls down to approximately three, which is characteristic for viscous dislocation gliding creep mechanism. The apparent $\dot{\epsilon}(\sigma)$ relationship for TCC with $n=3$ for PRM and $n=5$ for the cast alloys will give only $\dot{\epsilon} > 10^{-7} \text{ s}^{-1}$. These Norton's relationships can not be generalized because the creep rate assigned to a primary creep rate will certainly depend on the test conditions of the temperature cycles (frequency and holding time).

8 Conclusions

In the present chapter, the conclusions are summarised after the analysis of the experimental results, correlation to theoretical models and the discussion carried out in Chapter 7.

8.1 Significance of Experimental and Modelling Methods

8.1.1 TCC Tests

1. A more realistic approach is achieved by introducing the effect of the elastic thermal internal stresses ϵ_{ith} during the study of the evolution of plastic strain along TCC tests. The Eshelby's approximation shows to be a suitable tool to estimate ϵ_{ith} produced in the 6061/Al₂O₃/22p PRM during approximately 80% of the cycle (temperature < 240°C) for the TCC test conditions outlined in Paragraph 4.1.2. By means of the applied method, the negative creep periods observed in [2, 3], where no attention was paid to the effects of ϵ_{ith} , are reduced by at least 50%. A modification of the Eshelby's method that could take into account the plastic deformation should be applied in order to evaluate the involved processes more accurately and during the whole temperature cycle.
2. The analysis of the strain evolution during one cycle in a TCC test shows that the representation of the deformation strain rate as a mean value of the cycle does not reflect the actual picture since during a short period of the cycle (temperature > 240°C) plastic deformation takes place and only this part should be taken into account when evaluating the rate of deformation for the investigated material. However, a simple correlation can be made to estimate the actual deformation rate which in this work is taken as a quasi primary creep stage. This is observed to be approximately 5 times the mean deformation rate and about two magnitudes faster than the corresponding stationary creep rate.

8.1.2 HT In Situ Tensile Tests

1. The high temperature In Situ tensile creep tests carried out in this work have demonstrated to be a valuable method to observe the evolution of local strains in comparison with RT tensile tests. From a more qualitative point of view, this tests

have shown good results in clearly depicting the preferential deformation zones on the surface of the studied material. However, in order to increase the resolution of the calculations, a new method for the preparation of the samples would be needed. This method should be focused on the increase of grey values (smoother contrast points), their homogeneous distribution on the surface of the sample and an image acquisition device with a higher resolution.

8.1.3 Isothermal Creep Tests Performing Variations of Load

1. The use of variations of load during the isothermal tensile creep tests carried out for the short fibre reinforced alloys has revealed previously unreported creep properties for this kind of materials. When a SFRM is subjected to an overload period it shows a lower creep deformation rate enhancing thus the creep resistance of these composites. The tested examples promise a reduction of secondary creep rate by a factor of 3-5.

8.2 Significance of Results

8.2.1 Isothermal Creep

1. The PRM shows a creep exponent $n=3$ for a range of loads between 15MPa and 50MPa which corresponds to a mechanism of creep governed by viscous glide of dislocations. On the other hand, the unreinforced matrix presents a “continuous” change of creep exponent since its microstructure is not stabilized and an overaging effect provokes coarsening of precipitates that decrease gradually their strengthening effect for longer exposure times (smaller applied loads). A previous conclusion [115] that the diffusion creep stage is reached at $\sigma < 30\text{MPa}$ has to be revoked.
2. The isothermal tensile creep tests of the unreinforced 6061 alloy and the particle reinforced 6061/ $\text{Al}_2\text{O}_3/22\text{p}$ alloy showed that the minimum creep rate for the matrix is considerably lower than that for the reinforced material. This is caused by a significant enhancement of thermally activated dislocation mechanisms by the microstructure of the investigated PRM. Coarsening of precipitates, increase of the apparent diffusion coefficient, dislocation loop punching from the particles and spinel crystals on the surface of the particles acting as Frank-Read dislocation sources are considered to be responsible for this lower creep resistance of the PRM.

3. For a determined condition of stress and temperature the creep deformation of the unreinforced material is always smaller than the deformation of the composite after the same time elapsed as long as the secondary creep stage is considered.
4. Two different crack formation mechanisms are proposed to take place in the PRM subjected to isothermal creep conditions depending on the level of load: at higher stresses, the development of voids at the edge of a particle leads to the formation of a dimple and fracture occurs as a result of coalescence between dimples formed at individual particles. On the other hand, for small stresses, bigger dimples and the presence of more than one particle per dimple suggest that the crack initiation and consequent fracture is due to the formation of dimples originated from diffusion controlled coalescence of voids generated at two or more adjacent particles.
5. The unreinforced wrought alloy shows slightly better creep resistance than the unreinforced cast alloy (see Figure 8.1).

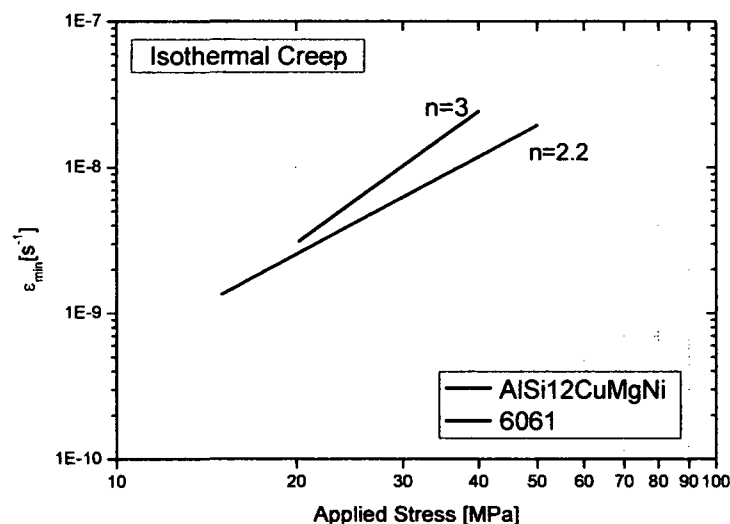


Figure 8.1. σ vs. $\dot{\epsilon}_{min}$ for both unreinforced matrices under tensile creep conditions.

6. The creep resistance of the SFRM corresponds roughly to that of the unreinforced matrix taking less than 50% of the load. Among the SFRM, the highest creep resistance is shown by the 15vol% composite but the difference in minimum creep rate between the SFRM is not as remarkable as it is when the unreinforced and the reinforced cast alloys are compared. The 20vol% SFRM did not show the expected highest creep resistance in comparison with the other two SFRM. This may be due to the presence of microstructural defects such as pores and uninfiltred zones from the fabrication process. Experimental results of the Young's modulus have also

shown a value of E lower than expected for the 20vol% SFRM. Consequently, the application of SFRM with 15vol% Saffil preforms produced by squeeze casting is recommended.

7. When the SFRM are subjected to a change of load during a creep test, the minimum creep rate achieved after a temporary increase of load becomes smaller than before. This is not due to a change in the mechanism of creep deformation. The reason is an effective reduction of the maximum stresses within the internal stress distribution provoked by a localised flow of matter in zones where the yield stress of the matrix surrounding the fibres would be surpassed. The apparent stress reduction in the matrix of about 5% of the external load reduces the secondary creep rate by a factor of 3-5.
8. The unreinforced cast alloy shows that pores due to creep deformation are formed in the Si phase as well as in the interface between the Si phase and/or the intermetallic phases and the matrix. Deep etched samples also revealed many cracks in the Si structure in the direction perpendicular to the tensile axis. On the other hand, and in contrast to the unreinforced matrix, the SFRM materials show a smaller amount of cracks in the intermetallic phases and eutectic Si, but many broken ceramic fibres with the fracture oriented perpendicularly to the tensile direction. In some regions the cracks in the fibres continue along the intermetallic phases and/or eutectic Si. Decohesion between the reinforcement and the matrix was mainly found around fibres aligned perpendicularly to the tensile axis. Fracture of the ceramic fibres or Si and intermetallic phases was not observable during investigations on longitudinal sections of interrupted creep test samples suggesting that the damage of these components begins after the secondary creep stage and may introduce tertiary creep. This work did not investigate the tertiary creep stage of SFRM. The investigation of the damage mechanisms in SFRM subjected to creep needs further specific test series.

9 References

- [1] Muhly J.D.; *The beginnings of Metallurgy in the Old World*, in *The beginning of the Use of Metals and Alloys*, ed. by Maddin R., MIT Press, Cambridge, 1988, 2-20.
- [2] Prader P., *Thermal Cycling Creep Behaviour of Particle Reinforced Aluminium Alloys*, PhD. Thesis, Vienna University of Technology, 2000.
- [3] Prader P., Degischer H.P., *Particle Reinforced AA6061 and A359 Aluminium Alloys Under Cyclic Thermal Loading Conditions*, *Materials Science and Technology*, 16, 2000, 893-896.
- [4] <http://mmc-assess.tuwien.ac.at>
- [5] Tjong S. C., Ma Z.Y., *Microstructural and Mechanical Characteristics of In Situ Metal Matrix Composites*, *Materials Science and Engineering*, 29, 2000, 49-113.
- [6] Degischer H. P., *Innovative light metals: metal matrix composites and foamed aluminium*, *Materials & Design*, 18, 1997, 221-226.
- [7] Birchall J., Stanley D., Mockford M., Pigott G., Pinto P., *The Toxicity of silicon Carbide Whiskers*, *Journal of Materials Science Letters*, 7, 1988, 350-352.
- [8] *Advanced Composite Materials*, Ed. by Navy Environmental Center, Virginia, 1991.
- [9] Degischer H. P., Prader P., Kilian H., Defekte in Stranggepreßtem, teilchenverstärktem Aluminium und die Streuung der Eigenschaften, DVM-Bericht 518 Bauteilversagen durch mikrodefekte, 1998, 135-140.
- [10] <http://www.alcan.com/>
- [11] <http://www.magnesium-elektron.com/>
- [12] Mortensen A., Michaud V., Flemings M., *Pressure-Infiltration Processing of Reinforced Aluminium*, *JOM*, 1993, 36-43.
- [13] Pech-Canul M., Katz R., Makhoul M., *Optimum conditions for pressureless infiltration of SiC_p preforms by aluminum alloys*, *Journal of Materials Processing Technology*, 108, 1, 2000, 68-77.
- [14] Mileiko S., *Metal and Ceramic Based Composites*, Volume 12 Composite Materials Series, Elsevier Science B.V., Amsterdam, 1997.
- [15] Carreño-Morelli E., Cutard T., Schaller R., Bonjour C., *Processing and characterization of aluminium-based MMCs produced by gas pressure infiltration*, *Materials Science and Engineering A*, 251, 1998, 48-57.

- [16] Nolte M., *Entwicklung einer Gieß- und Infiltrationstechnik zur Fertigung von Aluminium-Bauteilen mit selektiver Faserversärfkung*, PhD. Thesis, RWTH Aachen, Düsseldorf, 1997.
- [17] Clyne T., Whithers P., *An introduction to metal matrix composites*, Cambridge Solid State Science series, Cambridge, Cambridge University Press, 1993.
- [18] Yue T., Chadwick G., *Squeeze Casting and their Composites*, *Journal of Materials Processing Technology*, 58, 1996, 302-307.
- [19] Kaczmar J., Pietrzak K., Wlosinski W., *The Production and Application of Metal Matrix Composites Materials*, *Journal of Materials Processing and Technology*, 106, 2000, 58-67.
- [20] Henning W., Neite G. in *Metallische Verbundwerkstoffe*, ed. by Kainer K.U., DGM Informationsgesellschaft, Frankfurt, 1994, 169-191.
- [21] Srivatsan T., Sudarshant T., Laverniaj E., *Processing Of Discontinuously-Reinforced Metal Matrix Composites By Rapid Solidification*, *Progress in Materials Science*, 39, 1995, 317-409.
- [22] Poletti C., Marketz W., Degischer H.P., *Hot Formability of a Particle Reinforced Ti-Alloy*, Proc. 10th World Conference on Titanium.- Ti-2003. July 13-18, Hamburg, 2003.
- [23] Fahlahati A., *Kurzfaserverstärkung für Schnellarbeitsstahl*, PhD. Thesis, Vienna University of Technology, 2001.
- [24] Han B., Agnew S., Dunand D., *High-Strain-Rate Deformation Of Pure Aluminum Reinforced With 25% Alumina Submicron Particles Near The Solidus Temperature*, *Scripta Materialia*, 40, 1999, 801-808.
- [25] Zhigang L., Yong L., Farghalli M., *Creep and substructure in 5 vol% SiC-2124 Al composite*, *Materials Science and Engineering A*, 332, 2002, 330-342.
- [26] Mohamed F., *On Creep Behaviour in Powder Metallurgy 6061 Al*, *Scripta Materialia*, 38, 1998, 457-463.
- [27] Dudek H., Leucht R., *Titanium Matrix Composites*, in *Advanced Aerospace Materials*, Ed by. H. Buhl, Springer Verlag, Berlin, 1992, 124-139.
- [28] Jiang Z., Lian J., Yang D., Dong S., *An Analytical Study Of The Influence Of Thermal Residual Stresses On The Elastic And Yield Behaviours Of Short Fibre-Reinforced Metal Matrix Composites*, *Materials Science and Engineering*, A248, 1998, 256-275.
- [29] Li H., Li J., Wang Z., Chen C., Wang D., *Dependence Of Thermal Residual Stress On Temperature In A Sic Particle-Reinforced 6061Al Alloy*, *Metallurgical and Material Transactions A*, 29A, 1998, 2001-2009.

- [30] Levitt A., *Stresses In Metal Matrix Composites Due To Fibre Matrix Thermal Expansion Mismatch*, Proc. Ceramic Engineering and Science, 7-8A, 1980, 419-423.
- [31] Withers P., Stobbs W., Pedersen O., *The Application Of The Eshelby Method Of Internal Stresses Determination To Short Fibre Metal Matrix Composites*, Acta Metallurgia, 37(11), 1989, 3061-3084.
- [32] Arsenault R., Taya M., *Thermal Residual Stresses In Metal Matrix Composite*, Acta Metallurgia, 35(3), 1987, 651-659.
- [33] Davis L., Allison J., *Residual Stresses And Their Effects On The Deformation In Particle Reinforced Metal-Matrix Composites*, Metallurgical transactions A, 24A, 1993, 2487-2496.
- [34] Roatta A., Bolmaro R., *An Eshelby Inclusion-Based Model For The Study Of Stresses And Plastic Strain Localization In Metal Matrix Composites I: General Formulation And Its Application To Round Particles*, Materials Science and Engineering, A229, 1997, 182,-191.
- [35] Eshelby J. D., *The Determination of Elastic Fields of an Ellipsoidal Inclusion and Related Problems*, Proc. Roy. Soc., A241, 1957, 376-396.
- [36] Levy-Tubiana R., Baczamanski A., Lodini A., *Relaxation Of Thermal Mismatch Due To Plastic Deformation In Al/SiC_p Metal Matrix Composite*, Materials Science and Engineering, A341, 2003, 74-86.
- [37] Heinrich H., Vananti A., Kistorz G., *Strain Fields At Interface Of Al-Based Metal Matrix Composites*, Materials Science and Engineering, A319-321, 2001, 434-438.
- [38] Göbel U., Lefranc G., Pyzalla A., Degischer H. P., *Zerstörungsfreie Untersuchung von Eigenspannungen in AlSi7Mg/SiC/70p Metall-Matrix-Verbundwerkstoffen mit Hilfe von Röntgen- und Neutronenbeugung*, Verbundwerkstoffe, Ed. by H. P. Degischer, Wiley-VCH, Weinheim, 2003, 230-235.
- [39] Whitehouse A., *Creep of Metal Matrix Composites*, in Comprehensive Composite Materials Volume 3, Ed. by Kelly A. and Zweben C., Elsevier, 2000
- [40] Evans R., Wilshire B., *Introduction to Creep*, Ed. by The Institute of Materials, London, 1993.
- [41] Nabarro F., de Villiers H., *The Physics of Creep*, Ed. by Taylor & Francis Ltd., London, 1995.
- [42] Dlouhy A., Eggeler G., Merk N., *A Micromechanical Model For Creep in Short Fibre Reinforced Aluminium Alloys*, Acta Metallurgia Materialia, 43, 1995, 535-550.

- [43] Gariboldi E., Vedai M., *Creep and Creep Damage Tolerance of Al6061-Al₂O₃ Particulate Composites*, Advanced Engineering and Processing, 11, 2000, 737-741.
- [44] Tjong S., Ma Z., *High-Temperature Creep Behaviour of Powder-Metallurgy Aluminium Composites Reinforced with SiC Particles of Various Sizes*, Composites Science and Technology, 59, 1999, 1117-1125.
- [45] Peng L., Zhu S., Ma Z., Bi J., Wang F., Chen H., Northwood D., *High Temperature Creep Deformation of Al₁₈B₄O₃₃ Whisker Reinforced 8009 Al Composite*, Materials Science and Engineering, A265, 1999, 63-70.
- [46] Ma Z., Tjong S., *The High-Temperature Creep Behaviour of 2124 Aluminium Alloys with and without Particulate and SiC-Whisker Reinforcement*, Composites Science and Technology, 59, 1999, 737-747.
- [47] Wakashima K., Moriyama T., Mori T., *Steady-State Creep of a Particulate SiC/6061 Al Composite*, Acta Materialia, 48, 2000, 891-901.
- [48] Nardone V., Strife J., *Analysis of the creep behavior of silicon carbide whisker reinforced 2124 Al (T4)*, Metallurgical Transactions A, 18A, 1987, 109-114.
- [49] Hausselt J., Nix W., *A model for high temperature deformation of dispersion strengthened metals based on substructural observations in Ni-20Cr-2ThO₂*, Acta Metallurgica, 25, 1977, 1491-1502.
- [50] Rösler J., Arzt E., *A New Model-Based Creep Equation For Dispersion Strengthened Materials*, Acta Metallurgica et Materialia, 38, 1990, 671-683.
- [51] Arsenault R., Taya M., *Thermal Residual Stress In Metal Matrix Composite*, Acta Metallurgica, 35(3), 1987, 651-659.
- [52] A. B. Pandey, R. S. Mishra and Y. R. Mahajan, *Steady State Creep Behaviour Of Silicon Carbide Particulate Reinforced Aluminium Composites*, Acta Metallurgica et Materialia, 40(8), 1992, 2045-2052.
- [53] Winand H., Whitehouse A., Whithers P., *An Investigation Of The Isothermal Creep Response Of Al-Based Composites By Neutron Diffraction*, Materials Science and Engineering, A284, 2000, 103-113.
- [54] Whitehouse A., Clyne T., *Effects Of Reinforcement Content And Shape On Cavitation And Failure In Metal-Matrix Composites*, Composites, 24, 1993, 256-261.
- [55] Whitehouse A., Clyne T., *Cavity Formation During Tensile Straining Of Particulate And Short Fibre Metal Matrix Composites*, Acta Metallurgica Materialia, 41(6), 1993, 1701-1711.

- [56] Whitehouse A., Winand H, Clyne T., *The Effect Of Processing Route And Reinforcement Geometry On Isothermal Creep Behaviour Of Particulate And Short Fibre Mmcs*, Materials Science and Engineering, A242, 1998, 57-69.
- [57] Watt D., Xu X., Lloyd D., *Effects of Particle Morphology and Spacing on the Strain fields in a plastically deforming matrix*, Acta Materialia, 44(2), 1996, 789-799.
- [58] Qin S., Chen C., Guoding Z., Wang W., Wang Z., *The Effect of Particle Shape on Ductility of SiC Reinforced 6061 Al Matrix Composites*, Materials Science and Engineering, A272, 1999, 363-370.
- [59] Whitehouse A.; Clyne T., *Critical Stress Criteria For Interfacial Cavitation In Mmcs*, Acta Metallurgica et Materialia, 43(5), 1995, 2107-2714.
- [60] Kilian H., *Personal Communications*, Leichtmetall Kompetenzzentrum Ranshofen, Austria, 1995.
- [61] Aluminiumlegierungen – Knetlegierungen, Standard DIN 1725, 2.1983.
- [62] Duralcan, Duralcan Technical Documents, 1993.
- [63] Polmear I. J., *Light Alloys – Metallurgy of the Light Metals*, Hasted Press, New York, Third Edition, 1996.
- [64] Dutta I., Allen SM., *A Calorimetric Study of Precipitation in Commercial Aluminium Alloy 6061*, Journal of Materials Science Letters, 10, 1991, 232-326.
- [65] Dutta I., Allen S.M., Hafley J.L., *Effect of reinforcement on the ageing response of cast 6061 Al-Al₂O₃ Particulate Composites*, Metall.Trans.A, vol.22A, 1991, 2553-2563.
- [66] Berek H., Zywitzki O., Degischer H.P., Leitner H., *Grenzflächenreaktion in einer Al₂O₃-partikelverstärkten 6061 Al-Legierung*, Z. Metallkd, 85, 1994, 131-133.
- [67] Broeckmann Ch., *Kriechen partikel-verstärkter metallischer Werkstoffe*, Fortschritt-Bericht VDI, VDI Verlag, Düsseldorf, 2001.
- [68] Aluminium Taschenbuch, Aluminium Verlag, Düsseldorf, 1995, 583.
- [69] <http://www.saffil.com>
- [70] Saffil, Saffil Technical Documents, 2003.
- [71] <http://www.iww.tu-clausthal.de/>
- [72] Wang S., Dudek H.J., *Fibre-Matrix Interaction in the Delta Al₂O₃-Fibre Reinforced Aluminium Piston Alloy*, Materials Science and Engineering, A 205, 1996, 180-186.
- [73] W. L. Phillips, *Annotated Equilibrium Diagrams of some Aluminium Alloy Systems*, Monograph and Report Series, Institute of Metals, London, 1959.

- [74] Akbulut H., Durman M., Yilmaz F, *A Comparison of As-Cast and Heat Traeted Properties in Short Fiber Reinforced Al-Si Piston Alloys*, Scripta Materialia, 36, 1997, 835-840.
- [75] Mortensen,-A.; Cornie,-J.-A., *On the infiltration of metal matrix composites*, Metallurgical Transactions A Physical Metallurgy and Materials Science, 18A, 1987, 1160-1163.
- [76] Cseh G., Bär J., Gudladt H.-J., Lendavi J., Juhász A., *Indentation creep in a short fibre-reinforced metal matrix composite*, Materials Science and Engineering, A272, 1999, 145-151.
- [77] Vidal-Sétif M.H., Lancin M., Marhic C., Valle R., Raviart J.-L., Daux J.-C, Rabinovitch M., *On the role of brittle interfacial phases on the mechanical properties of carbon fibre reinforced Al-based matrix composites*, Materials Science and Engineering, A272, 1999, 321-333.
- [78] Dietmar T., *Kriechuntersuchungen an Metallmatrix-Verbundwerkstoffen*, Diploma Thesis, Vienna University of Technology, 2000.
- [79] <http://www.micro-epsilon.de>
- [80] <http://www.hbm.de>
- [81] Pandorf R., *Beitrag zur FE-Simulation des Kriechens Partikelverstärkter Metallmatrix-Verbundwerkstoffe*, Phd Thesis at the Ruhr University Bochum, Germany, 2000.
- [82] Borbely, A., Biermann, H., Hartmann, O., *FE investigation of the effect of particle distribution on the uniaxial stress-strain behaviour of particulate reinforced metal-matrix composites*, Materials Science and Engineering A, A313, 2001, 34-45.
- [83] Soppa E., Doumalin P., Binkele P., Wiesendanger T., Bornert M., Schmauder S., *Experimental and numerical characterisation of in-plane deformation in two-phase materials*, Computational Materials Science, 21, 2001, 261-275.
- [84] Soppa E., Weber U., Schmauder S., Fischer G., *Spannungs- und Dehnungskonzentrationen in Al/Al₂O₃- Verbundwerkstoffen verursacht durch Schädigungsprozesse*, Verbundwerkstoffe, Ed. by H. P. Degischer, Wiley-VCH, Weinheim, 2003, 581-586.
- [85] Tatschl A., Kolednik O., *A new tool for the experimental characterization of micro-plasticity*, Materials Science and Engineering A, A339, 2003, 265-280.

- [86] Gonzalez J., Knauss W. G., *Strain inhomogeneity and discontinuous crack growth in a particulate composite*, Journal of the Mechanics and Physics of Solids, 45, 1998, 1981-1995.
- [87] Nugent E. E., Calhoun R. B., Mortensen A., *Experimental investigation of stress and strain fields in a ductile matrix surrounding an elastic inclusion*, Acta Materialia, 48, 2000, 1451-1467.
- [88] Liu Y. L., Fischer G., *In situ measurement of local strain in a metal matrix composite by the object grating technique*, Scripta Materialia, 36, 1997, 1187-1194.
- [89] Unterwegger K., Kolednik O., *Experimentelle Charakterisierung des lokalen Verformungsverhaltens von partikelverstärkten Verbundwerkstoffen*, Verbundwerkstoffe, Ed. by H. P. Degischer, Wiley-VCH, Weinheim, 2003, 121-126.
- [90] Lasagni F., *Caracterización, Modelado y Estudio de la Deformación Local en Compuestos de Matriz de Aluminio reforzados con Fibras y Partículas de Alúmina*, Diploma Thesis at Vienna University of Technology, 2002.
- [91] Requena G., Lasagni F., Degischer H.P., *Lokale Verformung in diskontinuierlich verstärktem Aluminium*, Verbundwerkstoffe, Ed. by H. P. Degischer, Wiley-VCH, Weinheim, 2003, 171-176.
- [92] <http://www.kammrath-weiss.com/>
- [93] <http://www.gom.com>
- [94] <http://www.tainst.com/>
- [95] Eshelby J. D., *Elastic Inclusions and Inhomogeneities*, Prog. Solid Mech., Ed. by Sneddon I., Hill R., 1961, 89-140.
- [96] <http://www.bleeble.com>
- [97] W. Prohazska, *Das Thermische Ausdehnungsverhalten von AlSiC*, Diploma Thesis, Vienna University of Technology, 2001.
- [98] S. C. Sharama, *Effect of Albite Particles on the Coefficient of Thermal Expansion Behaviour of the Al6061 Alloy Composite*, Metallurgical and Materials Transactions A, 31A, 2000. 773-780.
- [99] Milicka K., Dobeš F., *Creep behaviour of a magnesium alloy AS21 and its fibre-strengthened composite*, Journal of Alloys and Compounds, In Press.
- [100] Liu X., Zhuo Y., *Fracture Surfaces of Al₂O₃/Al-Alloy Composites*, Proc. of the 12th Int. Conf. of Composite Materials in CD-ROM, Ed. by Massard T. and Vautrin A., Paris, 1999

- [101] Schnabl A., *Auswirkungen thermozyklischen Kriechens auf die Eigenschaften einer kurzfaserverstärkten Aluminium Kolbenlegierung*, PhD. Thesis, Vienna University of Technology, 2002.
- [102] Klipfel Y., He M., McMeeking R., Evans A., Mehrabian R., *The processing and mechanical behavior of an aluminum matrix composite reinforced with short fibers*, *Acta Metallurgica et Materialia*, 38(6), 1990, 1063-1074.
- [103] Li Y., Langdon T., *An examination of the effect of processing procedure on the creep of metal matrix composites*, *Materials Science and Engineering*, A245, 1998, 1-9.
- [104] Cadek J., Sustek V., *Comment on steady creep behaviour of silicon carbide reinforced aluminium composites*, *Scripta metallurgica et materialia*, 30, 1994, 277-282.
- [105] Li Y., Langdon T., *Creep Behavior of a Reinforced Al-7005 alloy: Implications for the creep processes in Metal Matrix Composites*, *Acta Materialica*, 46, 1143-1155.
- [106] Evans R. W., Wilshire B., *Introduction to Creep*, The Institute of Materials, 1993, Bourne Press Limited, Bournemouth.
- [107] Arsenault R., Shi N., *Dislocation generation due to differences between the coefficients of thermal expansion*, *Materials Science and Engineering*, 81, 1986, 175-187.
- [108] Vogelsang M., Arsenault R., Fischer R., *An In Situ HVEM study of dislocation generation at Al/SiC Interfaces in Metal Matrix Composites*, *Metallurgical Transactions A*, 17A, 1986, 379-389.
- [109] Dlouhy A., Merk N., Eggeler G., *A Microstructural Study of Creep in Short Fibre Reinforced Aluminium Alloys*, *Acta metallurgica materialia*, 41, No.11, 1993, 3245-3256.
- [110] Hull D., *Introduction to Dislocations*, The Commonwealth and International Library of Science, Technology, Engineering and Liberal Studies, Pergamon Press, Oxford, 1965.
- [111] Xin X., Daehn G., Wagoner R., *Modelling the Generation, Equilibrium, and Emission of Dislocations at Elastically Misfitted Particles*, *Acta Materialia*, 46, 17, 1998, 6131-6144.
- [112] Gehanno H., Brechet Y., Bechet D., Louchet F., *Use Of Internal Variable Models To Predict The High Temperature Behaviour Of A 6xxx Industrial Alloy*, *Materials Science Forum*, 217-222, 1996, 1413-1418.
- [113] Dragone T., Nix W., *Geometric Factors Affecting the Internal Stress Distribution and High Temperature Creep Rate of Discontinuous Reinforced Metals*, *Acta Metallurgica Materialia*, 38, 10, 1990, 1941-1953.

- [114] Roatta A., Bolmaro R., *An Eshelby inclusion based model for the study of stresses and plastic strain localization in metal matrix composites. II. Fiber reinforcement and lamellar inclusions*; Materials Science and Engineering, A229, 1997, 192-202.
- [115] Requena G., Telfser D., Hörst C., Degischer H.P., *Creep of AA6061 alloy and AA6061 metal matrix composite*, Materials Science and Technology, 18, 2002, 515-521.

A. Annex 1: Eshelby's Model

The procedure used in this annex to explain the model developed by Eshelby was taken from the chapter 3 of [17].

Eshelby approached the problem of calculating the stress field provoked by an inclusion within a homogeneous medium by visualising a series of cutting and welding exercises, as illustrated in Figure A.1. A region (the inclusion) is cut from the unstressed elastically homogeneous material, and is then imaged to undergo a shape change (the transformation strain ϵ^T) free from the constraining matrix (so that the strain is “stress free”). The inclusion cannot now be replaced directly back into the hole from whence it came. Instead surface tractions are first applied in order to return it now to its original shape. Once back in position, the two regions are then welded together once more, i.e. there is no movement or sliding along the interface, and the surface tractions are then removed. Equilibrium is then reached between the matrix and the inclusion at a *constrained* strain (ϵ^C) of the inclusion relative to its initial shape before removal.

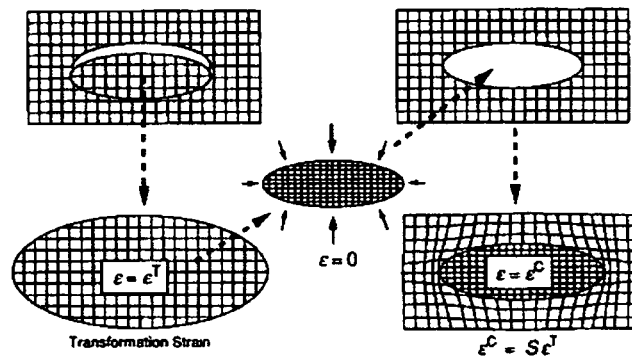


Figure A.1. Eshelby's cutting welding exercises for the uniform stress-free transformation of an ellipsoidal region.

Since the inclusion is strained uniformly throughout, the stress within it can be calculated using Hooke's Law in terms of the *elastic* strain ($\epsilon^C - \epsilon^T$) and the stiffness tensor of the material (C_M)

$$\sigma_i = C_M \cdot (\epsilon^C - \epsilon^T) \quad (A.1)$$

For a specified shape change ϵ^T , all that is now required in order to calculate the inclusion stress is a knowledge of the final constrained ϵ^C . Eshelby found ϵ^C can be obtained from ϵ^T by means of a tensor, termed the Eshelby S tensor, which can be calculated in terms of the inclusion aspect ratio and the Poisson's ratio of the material

$$\boldsymbol{\varepsilon}^c = \mathbf{S} \cdot \boldsymbol{\varepsilon}^T \quad (\text{A.2})$$

The tensor \mathbf{S} thus expresses the relationship between the final constrained inclusion shape and the natural shape mismatch.

Now that the constrained shape is known, the inclusion stress can be evaluated in terms of the stress-free shape misfit by combining equations (A.1) and (A.2) to give:

$$\boldsymbol{\sigma}_i = \mathbf{C}_m \cdot (\mathbf{S} - \mathbf{I}) \cdot \boldsymbol{\varepsilon}^T \quad (\text{A.3})$$

These results can be used to deduce the thermal residual stresses within a single reinforcing inclusion for the case of a differential thermal contraction in a composite. By subtracting the strain of the matrix ($\alpha_m \Delta T$) which takes place on lowering the temperature by ΔT , one can consider the differential thermal contraction misfit as a shape change similar to that used above ($\boldsymbol{\varepsilon}^{T*} = (\alpha_i - \alpha_m) \Delta T$). Similar cutting and welding arguments then allow to write the inclusion stress in terms of the stiffness C_i and the elastic strain of the inclusion:

$$\boldsymbol{\sigma}_i = \mathbf{C}_i \cdot (\boldsymbol{\varepsilon}^c - \boldsymbol{\varepsilon}^T) \quad (\text{A.4})$$

For MMC the matrix and the inclusion normally have different stiffnesses. However, since transformed ellipsoids always give rise to ellipsoidal constrained shapes, it must be possible to imagine a *ghost* inclusion made of matrix material with a shape that, when surface tractions are applied to give it the *constrained* shape of the real inclusion, it will attain the same uniform stress state. In such a case, the actual inclusion and the equivalent inclusion could be interchanged without disturbing the matrix. The inclusion which satisfies this condition is termed the *equivalent homogeneous inclusion*. The trick is then to find the shape of the ghost inclusion (matched in stiffness to the matrix) which is equivalent to the reinforcing inhomogeneous inclusion of interest.

In order to be able to interchange the two inclusions, the stress in the equivalent ghost inclusion must be identical to that given by eqn. (A.4) for the real inclusion

$$\mathbf{C}_i \cdot (\mathbf{S} \cdot \boldsymbol{\varepsilon}^T - \boldsymbol{\varepsilon}^T) = \mathbf{C}_m \cdot (\mathbf{S} - \mathbf{I}) \cdot \boldsymbol{\varepsilon}^T \quad (\text{A.5})$$

from which the appropriate transformation strain $\boldsymbol{\varepsilon}^T$ can be deduced for any shape change $\boldsymbol{\varepsilon}^{T*}$ and the stiffness mismatch ($C_i - C_m$) between the two phases

$$\boldsymbol{\varepsilon}^T = [(\mathbf{C}_i - \mathbf{C}_m) \cdot \mathbf{S} + \mathbf{C}_m]^{-1} \cdot \mathbf{C}_i \cdot \boldsymbol{\varepsilon}^{T*} \quad (\text{A.6})$$

Now that the elastically equivalent ghost problem has been identified, the results shown at the beginning of this chapter can be used directly. The inclusion stress is thus

$$\boldsymbol{\sigma}_i = \mathbf{C}_m \cdot (\mathbf{S} - \mathbf{I}) \cdot [(\mathbf{C}_i - \mathbf{C}_m) \cdot \mathbf{S} + \mathbf{C}_m]^{-1} \cdot \mathbf{C}_i \cdot \boldsymbol{\varepsilon}^{T*} \quad (\text{A.7})$$

In the case that an external load is applied to the composite the analysis is straightforward. The strain arising from the applied load is the same throughout (ϵ^A). Consequently, the stress (and strain) at each point is simply the sum of the applied stress (strain) and the internal stress (strain) already calculated above for the unloaded system. Accordingly, in the homogeneous inclusion

$$\sigma_i + \sigma^A = \mathbf{C}_m \cdot (\epsilon^c - \epsilon^T) + \mathbf{C}_m \cdot \epsilon^A \quad (\text{A.8})$$

where

$$\sigma^A = \mathbf{C}_m \cdot \epsilon^A \quad (\text{A.9})$$

The response of the reinforced composite will be very different from that of the elastically homogeneous one. However, if one is given complete freedom over the choice of the original shape of the ghost inclusion, it must still be possible to select a stress-free misfit (ϵ^T) so as to duplicate the stress in the real inclusion when the composite is under a specific load. In such a case, the real and the ghost inclusions can then be interchanged as before without disturbing the matrix at all. The shape misfit required for the ghost inclusion can be found

$$\epsilon^T = -[(\mathbf{C}_i - \mathbf{C}_m) \cdot \mathbf{S} + \mathbf{C}_m]^{-1} \cdot (\mathbf{C}_i - \mathbf{C}_m) \cdot \epsilon^A \quad (\text{A.10})$$

This can be regarded as the equivalent inclusion transformation strain associated with the misfit between the shapes the reinforcing inclusion and the whole would adopt were the two phases to be subjected to the applied stress independently. As one would expect, it is proportional to the applied stress and increases with disparity in stiffness between the phases.

Now that the transformation strain of the equivalent ghost inclusion has been identified, the inclusion stress can be determined from equation (A.8)

$$\sigma_i + \sigma^A = -\mathbf{C}_m \cdot (\mathbf{S} - \mathbf{I}) \cdot [(\mathbf{C}_i - \mathbf{C}_m) \cdot \mathbf{S} + \mathbf{C}_m]^{-1} \cdot (\mathbf{C}_i - \mathbf{C}_m) \cdot \epsilon^A + \mathbf{C}_m \cdot \epsilon^A \quad (\text{A.11})$$

This deductions are based on a single inclusion embedded within an infinite matrix. The results are therefore applicable only to dilute systems, in which the reinforcement volume fraction is less than a few percent. We will now extend these results to higher reinforcement contents. In Figure A.2 it can be seen that, to maintain the balance of stress in such systems, the composite distorts upon cutting, so as to provide an average matrix stress to oppose the inclusion stress.

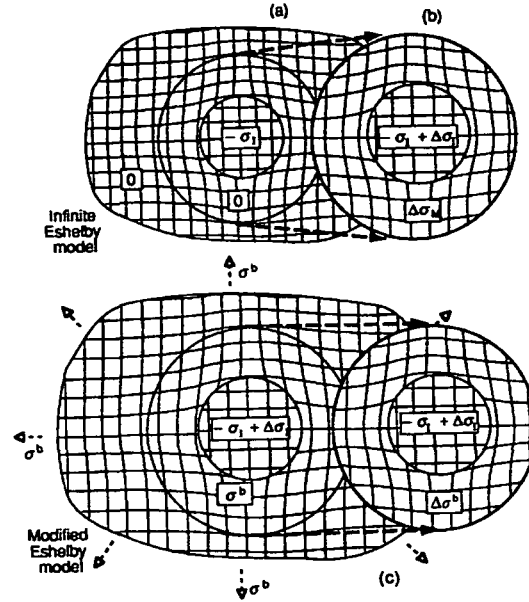


Figure A.2. a) An infinite matrix containing an oversized of the same elastic constants. When a composite is cut as in b) from the infinite, the position of the new external boundary moves outward. This generates a tensile average matrix stress to balance the compressive inclusion stress, so that the internal stresses within the new finite composite sum to zero. This distortion of the composite is modelled in c) by superimposing a tensile background stress (σ^b) upon the infinite solution as if it were externally applied.

One way of incorporating this into the model is to think of it occurring by the superimposition of a background stress (σ^b) which partitions between the phases as if it were externally applied. The balance of stress then becomes

$$(1 - f_{\text{single}}) \cdot \sigma^b + f_{\text{single}} \cdot (\sigma_i + \sigma^b) = 0 \quad (\text{A.12})$$

where f_{single} represents the fraction of the total volume which is occupied by the single inclusion. Through the dependence of (σ^b) on the volume fraction of reinforcement, it communicates to one inclusion the background stress arising from all the others. Consequently, Eshelby's solution can be used to model multiple inclusion composites simply by modifying equation (A.12) to include the volume fraction of all the inclusions

$$(1 - f) \cdot \langle \sigma \rangle_m + f \cdot \langle \sigma \rangle_i = 0 \quad \langle \sigma \rangle_m = -\frac{f}{1-f} \cdot \langle \sigma \rangle_i \quad (\text{A.13})$$

For the case of the thermal misfit, the equations deduced above must be now modified due to the effect of the background stress. Thus

$$(1 - f) \cdot \langle \sigma \rangle_m + f \cdot \mathbf{C}_m \cdot (\epsilon^c + \langle \epsilon \rangle_m - \epsilon^T) = 0$$

$$\langle \sigma \rangle_m = -f \cdot \mathbf{C}_m \cdot (\epsilon^c - \epsilon^T) \quad (\text{A.14})$$

This allows the deduction of the equivalent transformation strain

$$\epsilon^T = -\{(\mathbf{C}_m - \mathbf{C}_i) \cdot [\mathbf{S} - f \cdot (\mathbf{S} - \mathbf{I})] - \mathbf{C}_m\}^{-1} \cdot \mathbf{C}_i \cdot \epsilon^T \quad (\text{A.15})$$

The case of an external load also requires modification for non-dilute composites. In this case the ghost inclusion is stressed by $\sigma_I + \langle \sigma \rangle_M + \sigma^A = \langle s \rangle_I + \sigma^A$ and has a constrained shape corresponding to a strain of $\varepsilon^C + \varepsilon^A + \langle \varepsilon \rangle_M$. Consequently, equation (A.10) becomes

$$\varepsilon^T = -\{(\mathbf{C}_M - \mathbf{C}_I) \cdot [\mathbf{S} - \mathbf{f} \cdot (\mathbf{S} - \mathbf{I})] + \mathbf{C}_M\}^{-1} \cdot (\mathbf{C}_M - \mathbf{C}_I) \cdot \varepsilon^A \quad (\text{A.16})$$

Once ε^T is established, the mean stress can be calculated

$$\langle \sigma \rangle_M = -\mathbf{f} \cdot \mathbf{C}_M \cdot (\mathbf{S} - \mathbf{I}) \cdot \varepsilon^T \quad (\text{A.17})$$

$$\langle \sigma \rangle_I = (1 - \mathbf{f}) \cdot \mathbf{C}_M \cdot (\mathbf{S} - \mathbf{I}) \cdot \varepsilon^T \quad (\text{A.18})$$

LEBENS LAUF

Vor - und Zuname: Guillermo Carlos REQUENA
Argentinisches Reisepass Nr. 24.073.039
Staatsangehörigkeit: Argentinien
Geburtstag: 29. Juli 1974
Geburtsort: Córdoba - Provinz Córdoba - Argentinien
Eltern: Dipl. Buchhalter, Juan Carlos REQUENA, Repsol YPF, Buenos Aires, Argentina.
Antonia Francisca Reviglione, Kassenverwalterin bei OSDE, Neuquén, Provinz Neuquén, Argentina.
Familienstand: Ledig
Adresse: Lederergasse 22-3, A-1080, Wien, Österreich.
Tel Nr.: 0043 1 4024754
E-mail: grequena@mail.zserv.tuwien.ac.at
Arbeitsadresse: Technische Universität Wien, Institut für Werkstoffkunde und Materialprüfung, Karlsplatz 13/308, A-1040, Wien, Österreich.
Tel Nr.: 0043 1 5880130828

1.- AUSBILDUNG:

Grundschule: März 1981 - Dezember 1987
125 Grundschule, Neuquén, Provinz Neuquén
Auszeichnung: Fahnenträger

Gymnasium: März 1988 - Dezember 1993
E.N.E.T. N°1 Gymnasium, Neuquén, Provinz Neuquén.
Abschluss als Elektromechanischer Techniker
Durchschnittsnote: 7,96

Universität: a) März 1994 - Juli 2000:
6 Jahre Elektrotechnik-Ingenieurwesen Studium an der Ingenieurwesen Fakultät, Staatliche Universität der Comahue, Neuquén, Provinz Neuquén, Argentinien.
Durchschnittsnote: 8,00
Titel: Dipl. Ing. Industrie Fachrichtung Elektrotechnik

b) Seit Oktober 2000:
Doktorand am Institut für Werkstoffkunde und Materialprüfung, Technische Universität Wien. Dissertation Thema: „Kriechbeständigkeit von diskontinuierlich verstärkten Aluminium Legierungen“.

2.- LEHRTÄTIGKEITEN:

a) August 1998 - Januar 2000:
Hilfssistent als Student am Fachbereich Mechanik, am Lehrstuhl Werkstoffe, Ingenieurwesen Fakultät, Staatliche Universität der Comahue, Neuquén, Provinz Neuquén, Argentinien.

b) Dezember 1999 – Juli 2000:

Teilnehmer an der Forschungsgruppe von Prof. Dr. Dipl. Ing. Julio A. VIVAS HOHL geleitet für Neue Technologien und Moderne Werkstoffe. Ingenieurwesen Fakultät, Staatliche Universität der Comahue, Neuquén.

c) Mai 2003 – Dezember 2003:

Halbbeschäftigter Universitätsassistent am Institut für Werkstoffkunde und Materialprüfung, TU WIEN, Österreich.

d) Seit Januar 2004:

Wissenschaftlicher Mitarbeiter in Ausbildung am Institut für Werkstoffkunde und Materialprüfung, TU WIEN, Österreich.